A study of the structure and formation of biocompatible mesostructured polymer-surfactant hydrogel films

Holdaway, James

Award date:
2014

Awarding institution:
University of Bath

A study of the structure and formation of biocompatible mesostructured polymer-surfactant hydrogel films

Volume 1 of 1

James Antony Holdaway

A thesis submitted for the degree of Doctor of Philosophy

University of Bath
Department of Chemistry

October 2013

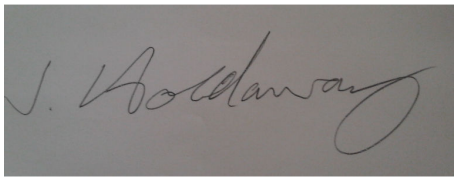

A study of the structure and formation of biocompatible mesostructured polymer-surfactant hydrogel films

UNIVERSITY OF BATH

James A. Holdaway

PhD Thesis

The Edler Research Group

Division of Physical Chemistry

Department of Chemistry

University of Bath

Bath, United Kingdom

October 2013

Table of contents

Abstract

The aim of this work has been to investigate the formation of films and to couple their properties with the bulk behaviour of the film forming components. The primary goal was to improve the biocompatibility of the films, as films are of great interest to the biomedical industry. The investigated films form spontaneous at an air-water interface and some are robust enough to be removed from the surface. The films are formed by mixed surfactants of the cationic CTAB and the zwitterionic SB3-14 together with the polymer PEI, in a short and long form. The film structures are investigated with varying CTAB:SB3-14 ratio. It was found replacing CTAB with SB3-14 reduced mesostructure in the films, however when PEI was used to form the films in its long form there was sufficient polymer network to kinetically trap mesostructure in the films.

To increase biocompatibility, CTAB was replaced with calcium chloride to emulate the cationic charge and present opportunites for complex formation with the polymers. SB3-14 was still present as the surfactant to impart mesostructure with PEI as the polymer. Here it was found that mesostructure could be controlled with calcium chloride concentration due to its hygroscopic nature modulating the amount of water in the films and therefore the resulstant mesophases.

Finally, anionic biopolymers were investigated with the spray coated films. Here it was found that they complexed with calcium chloride more fully than PEI and thus the competition between calcium chloride and SB3-14 for water resulted in more hydrated mesophases than when PEI was used as the film forming polymer.

The bulk solutions and films were investigated mainly with small angle scattering and reflectivity techniques. It was found that as a progression to previous work in the research group that more biocompatible methods could be used to form structured films.

List of abbreviations

AFM	Atomic Force Microscopy
BAM	Brewster Angle Microscopy
CAC	Critical Association Concentration
CMC	Critical Micelle Concentration
CPP	Critical Packing Parameter
CTAB	CetylTrimethylAmmonium Bromide
dsDNA	Double-Stranded DeoxyriboNucleic Acid
DWBA	Distorted-Wave Born Approximation
FDI	Free Induction Decay
FWHM	Full Width Half Max
GIFT	Generalised Indirect Fourier Transformation
GISAS	Grazing-Incidence Small-Angle Scattering
HM Polymer	Hydrophobically Modified water-soluble Polymer
IFT	Indirect Fourier Transformation
LC Phase	Liquid Crystalline Phase
LPEI	Long PolyEthylenImine
MSA	Mean-Spherical Approximation
NMR	Nuclear Magnetic Resonance
NOESY	Nuclear Overhauser Effect SpectroscopY
QCM	Quartz Crystal Microbalance
PDDF	Pair Distance Distribution Function
PEI	PolyEthylenImine
PFG-NMR	Pulse-Field Gradient NMR
RMSA	Rescaled MSA
SANS	Small-Angle Neutron Scattering
SAXS	Small-Angle X-ray Scattering
SB3-14	3-(N,N-Dimethylmyristylammonio)propanesulfonate
SDS	Sodium Dodecyl Sulphate
SLD	Scattering Length Density
SPEI	Short PolyEthylenImine
TEM	Transmission Electron Microscopy
TOF	Time Of Flight
TS-1	Target-Station One
TS-2	Target-Station Two

1.1 An Introduction to Surfactants, Polymers and Polymer-Surfactant Films

The work presented in this thesis is concerned with polymer-surfactant hydrogel films formed from solutions of surfactant, salt and polymer. The polymer-surfactant films exhibit controllable surfactant imparted mesostructure. The films are formed either spontaneously at the air-solution interface or by spray-coating an aerosol of polymer-surfactant solution on a surface.

The main aim of the work was to form and characterise these polymer-surfactant hydrogel films so as to understand the fundamental features of the film forming components. This would enable the exchange of toxic components used in previous studies[1-7] with less or non-toxic components. Reduction of film toxicity enables the films to be used as a basis for further development for biomedical applications, specifically where control of film mesostructure may allow modulation of film properties. This work concentrates on surfactant phases to control the structure of polymer films.

Formation and stability of polymer films is of great importance in many applications in our daily life, as for example paints.[8] The ability to control polymer film structure and subsequent properties opens the possibility for development of more specialised tailored films for particular usages.[9] For instance being able to control properties like the adsorption behaviour of a thin film is important for subjects like anti-fouling[10], protein interaction[11,12] and anti-microbial activity[13]. These are all processes in use today; however, there are also areas within medicine where an improved understanding of films and their properties are of great importance. For instance biocompatible films can be used to release therapeutic drugs in a localised and controlled manner[14]. Furthermore, polymer films can help improve the biocompatibility of implants[15-17]. Therefore, a better understanding of how and why films form and how their properties depend on the components in the film is of great importance for the further development of a wide variety of products.

The contributions of this thesis are that it demonstrates methods of reducing the toxicity whilst maintaining structural control of polymer-surfactant films. First by investigating substitution of surfactant in known film forming solutions[3,5,18] with less toxic zwitterionic surfactant[19]. Secondly, by substitution of the ionic surfactant charge with divalent salt to mimic the polymer-surfactant interactions exhibited by toxic ionic surfactant, which enables less toxic zwitterionic surfactant to be used in film forming solutions. The thesis demonstrates insights in to the model of formation of some previously reported films from the Edler group due to the effect of different surfactant molecular structures on the films. It also demonstrates a new method of

controlling the surfactant imparted structure of the films through variation of salt to surfactant ratio and polymer architecture, including biopolymers. The use of biopolymers further increases the biocompatibility of the films.

In this thesis, several techniques have been employed to undertake this task, including small-angle scattering and reflectivity. These techniques will be described in chapter two. In this chapter, an introduction to the main concepts of surfactants, polymers and thin films is given. Chapter 2 details the analytical methods employed for the investigation. In chapter 3 an experimental study of the spontaneous film formation of a mixture of cationic and zwitterionic surfactants with polymer is discussed. In chapter 4 an experimental study of the spray coated films of a zwitterionic surfactant and polymer in the presence of a divalent salt is presented. In order to increase the understanding of the film formation processes, the behaviour of the components in solution was also investigated.

1.2 Surfactants and polymers

1.2.1 Surfactants

Surfactants (surface active agents) are a class of amphiphilic molecules composed of two distinctly different parts; an ionic or dipolar hydrophilic head and a polar hydrophobic tail, as schematically shown in figure 1.1. Surfactants can either interact with an interface, *e.g.* a liquid-gas interface, or they can self-assemble to form micellar structures in solution. The surfactants are classified by their polar head group, which can be anionic, cationic, zwitterionic or non-ionic which are shown in figure 1.1a, b, c and d respectively. Most commonly, surfactant tails are composed of hydrocarbons, though they can also consist of other chemical moieties[20].

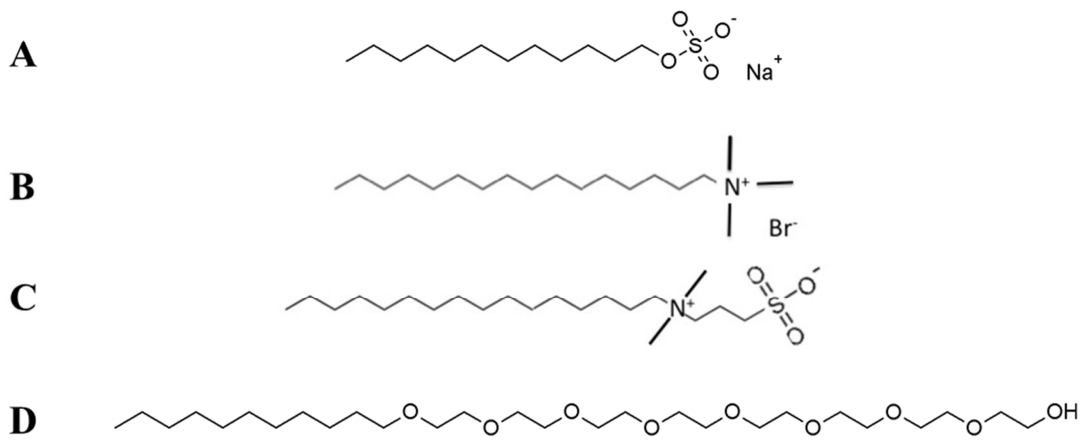

Figure 1.1. Schema of surfactant chemical structures; **A**: Anionic sodium dodecyl sulphate (SDS) **B**: Hexadecyltrimethylammonium bromide (CTAB). **C**: Zwitterionic 3-(N, N-Dimethylmyristylammonio) propanesulfonate (SB3-14). **D**: Non-ionic Octaethylene glycol monododecyl ether ($C_{12}E_8$)

Systems containing surfactants can self-assemble in solution or adsorb to an interface. Adsorption of an amphiphilic molecule, *e.g.* a surfactant, to an interface is driven by the lowering of the free energy of the phase boundary, as the adsorption of amphiphilic molecules lowers the surface tension (interfacial free energy per unit area). This is discussed in greater detail below.

The main driving force in micelle formation however, is the increase in entropy caused by the release of well-ordered water molecules from the hydrophobic part of the surfactant (the hydrophobic effect)[21]. However, micelle formation is opposed by the repulsion between hydrophilic parts of the surfactants, and by their affinity for water.[22] This is also an entropic effect, since a decrease in entropy will arise from forcing the surfactant molecules together. The competition between these two entropic effects governs whether the system phase-separates or the molecules instead form small clusters, like dimers. Micelles are found in between these two states where neither of the effects are strong enough to completely dominate the behaviour[20]. Enthalpic contributions also affect micelle formation. They arise from electrostatic interactions between headgroups of surfactants. Micelle formation does not occur below the critical micelle concentration (CMC), as the free unimers have high entropy of mixing, which is not countered by the energy of having water around the entire surfactant. The CMC is influenced by many parameters; mostly the chemical structure of the surfactant and addition of salt to the system. For example, increasing the size of the hydrophobic region lowers the CMC due to the increase in free energy upon micellization due to the hydrophobic effect.[20,23,24]

For self-assembled micellar structures, the simplest form of aggregate is a spherical micelle. The surfactants aggregate so the hydrophobic region is partitioned from the water so that the hydrophobic part forms a spherical core and the hydrophilic part shields the core from the aqueous solution (figure 1.2a). Considering the spherical micelles, these have an optimal aggregation number, N_{agg}, where all the micelles have minimal free energy.[25] In the case of having an aggregation number smaller than the optimal aggregation number the hydrophobic part will be in contact with water, on the contrary if the aggregation number is larger than the optimal aggregation number, the head groups will be packed too close together and subsequently repel each other. Spherical micelles are therefore found to be relatively monodisperse and with a structure insensitive to changes in concentration above CMC.[23,24]

For cylindrical micelles, no optimal aggregation number is observed where the molecules have a minimal free energy. This is due to end-cap effects, as the molecules at the ends are forced to pack into hemispheres. These molecules will therefore have a head group area larger than the optimal. The molecules away from the cylinder ends are energetically independent of cylinder length and the only limiting factor preventing formation of extremely long cylinders is the increase in entropy arising from adding more surfactant molecules to the cylindrical micelle. The hemispherical end-caps favour growth, as merging two micelles would reduce the energy cost of the end-caps. Cylindrical micelles are therefore found to be polydisperse in length and the length is sensitive to changes in the concentration above CMC.[23,24]

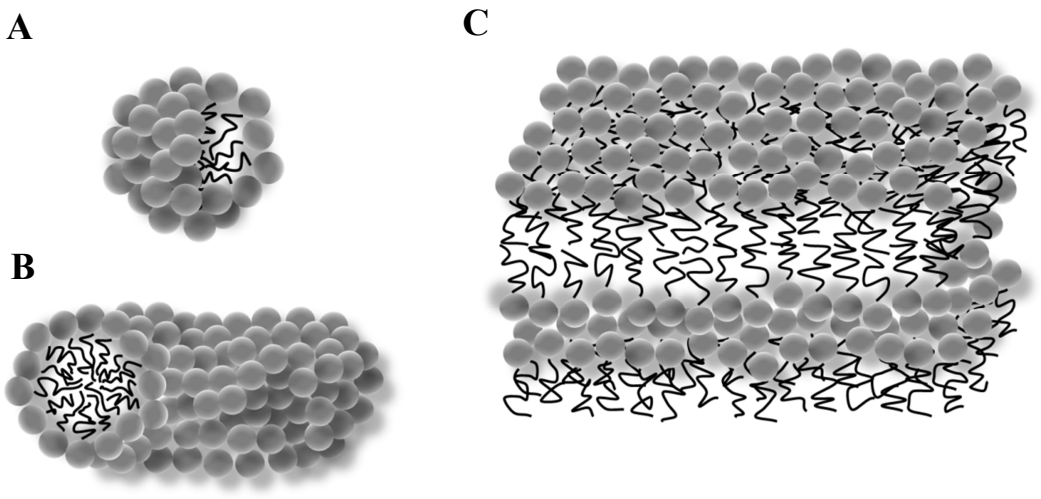

Figure 1.2. Self-assembled structures found in surfactant system. The different geometries are formed dependent on the composition of the amphiphile; the governing factor is the volume ratio between the hydrophilic head and the hydrophobic tail. At large differences spherical micelles are formed (**A**) (for a much larger head group volume), at smaller differences cylindrical micelles are formed (**B**) and finally at no difference bilayers can form (**C**).

An idea of the preferred geometrical shape adopted by the amphiphilic molecules can be obtained by considering the volume ratio between the head and tail group. If one considers the most favourable structure of the micelle as the structure where all the molecules have the minimal free energy of formation. Then by describing the amphiphile with three characteristic parameters; the optimal head group area, a_o, the critical chain length of the tail group, l_c, and the volume of the tail group, v, a characteristic number, the critical packing parameter (CPP), can be evaluated. For a hydrocarbon chain l_c is equal to the maximum chain length for saturated hydrocarbons given by Tanford.[22] The optimal head group area, a_o, originates from a balance between repulsive and attractive forces. The first originates from forcing the head groups too close together and the latter from the unfavourable interaction between the hydrophobic tails and water, observed if the head groups are too far apart.

The ratio, $v/(a_o l_c)$ is the critical packing parameter.[23] The different geometrical shapes depicted in figure 1.2 will fulfil the following criteria for the CPP. Spherical micelles have $(v/a_0 l_c) \leq 1/3$, cylindrical micelles have $1/3 < (v/a_0 l_c) \leq 1/2$ and vesicles or bilayers have $1/2 < (v/a_0 l_c) \leq 1$. When the packing parameter is below 1, the curvature of the interface between the micelle hydrophobic core and aqueous solvent is curved away from the solvent (Type I micelles). For inverted micelle structures the CPP, is given as $(v/a_0 l_c) > 1$. Inverted micelles arise in situations where

the tail volume of the surfactant is very large (as in the case of double chain surfactants), the water volume fraction is low thus reducing the surfactant headgroup area due to low hydration or where the solvent is non-polar.[20,23,24]

Micellization can also be looked upon in a thermodynamic way, where the CMC is considered as the maximum solubility of monomeric surfactant. If more surfactant is added to the solution a micellar phase is apparent. This is known as the phase separation model of micellization.[26] However, here it is only possible to obtain an approximate expression for the free energy of micellization ionic surfactants using the phase separation model, as the Gibbs free energy of micelle formation from ionic surfactant will be affected by the dissociation of counter ions.[27] The Gibbs energy of micelle formation, ΔG_{mic}, is related to the CMC by

$$\Delta G_{mic} = RT \ln(CMC) \qquad (1.1)$$

Where R and T are the gas constant and the absolute temperature, respectively. When the CMC is below 1 M, the Gibbs free energy of micelle formation is negative. Thus, the formation of micelles is a spontaneous process.[20,28,29]

Finally, one has to consider that the micelle shape can be affected by external conditions, such as temperature and the ionic strength of the solution. In the framework of the geometrical considerations the external parameters can change the optimal head group area of the amphiphilic molecule, due to changed interaction between the head groups. Increased salinity strongly affects the head group areas of ionic surfactants, as the optimal head group area will decrease with increasing electrolyte concentration. Effectively, charge screening will weaken the repulsion between the head groups. Considering the optimal head group area of non-ionic surfactants, these are affected by temperature as a_{o} is found to decrease with increasing temperature.

1.2.2 Surfactant Liquid Crystal Phases

After micellization has occurred, increasing the surfactant monomer concentration in solution results in more micelle formation thus increasing the number of micelles in solution. As the volume fraction of micellar aggregates increase, the curvature of the interface at the boundary of the partitioned hydrophobic region and the hydrophilic aqueous environment changes. This is primarily due to changes in the extent of hydration of the hydrophilic headgroups of the surfactant.[30,31]

As hydration of the headgroup decreases, the area occupied by the headgroup will also decrease. In the case of ionic surfactants this phenomena will also cause dissociated counter-ions to associate with the surfactants, further decreasing the headgroup area. Micelle shape changes are driven by the decrease in contact the hydrophobic core has with water due to the headgroup size decreasing. As the headgroup area decreases at the micellar interface, the packing parameter of the surfactant increases, changing the micelle curvature towards water (in the case of Type I oil-in-water surfactants).

As the volume fraction of the micellar aggregates increases, inter-micellar interactions have increasing effect on the solution behaviour of the micellar aggregates. To achieve a minimum energy state, the micellar aggregates pack into arrangements that exhibit orientational and long range order. In the case of spherical aggregates this can be a cubic lattice (figure 1.3a). If the micellar aggregates are anisotropic as in the case of cylinders or lamellar, then they will arrange parallel to each other in distances and directions that minimise the inter-micellar interactions. Therefore, anisotropic micelles form hexagonal (figure 1.3b) and lamellar (figure 1.3c) liquid crystals for cylinders and lamellar micelles respectively. It is possible to form hexagonal and lamellar liquid crystals from micelles that are spherical at the surfactant CMC due to the micellar curvature decreasing with increasing surfactant volume fraction.

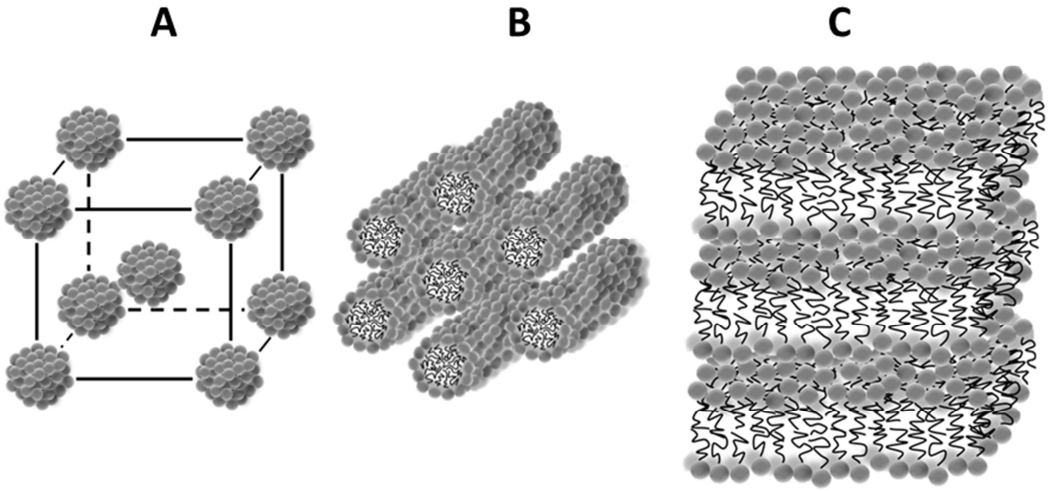

Figure 1.3. Schema of geometries of liquid crystalline phases; **A**: Cubic close packed phase formed by spherical micelles. **B**: Hexagonal phase formed by cylindrical micelles. **C**: Lamellar phase formed by bilayers.

Liquid crystals are phases of matter which lie between that of solids and liquid. In a solid, the constituent components of the phase are spatially fixed, giving the phase long range spatial order. If the solid is a crystal, the components are orientationally fixed, giving the crystalline solid phase orientational order. Liquids are free flowing, with low orientational and spatial order. A liquid crystal is a phase which demonstrates properties of both a crystalline solid and liquid. In a micellar liquid crystal, the micelles and surfactant molecules are fixed in position like a crystalline solid with a mobile liquid solvent phase.[20] Additionally, within the micelles, the hydrophobic core can be considered as fluid at the correct temperature.[30]

Figure 1.4 shows a generalised surfactant water phase diagram. It can be seen that decreasing water content in the system affects the interface curvature of the micellar aggregates that form the liquid crystalline phases. As water content is decreased a normal (Type I) micellar solution decreases interface curvature to form a H_I normal hexagonal phase. When the interface curvature of the micellar aggregates is zero a lamellar liquid crystal (L_α) is formed. When the volume fraction of the micellar aggregates increases beyond this point, inverse micellar aggregates form which pack into inverse surfactant mesophases, such as inverse H_{II} hexagonal. Of course, if the packing parameter of the surfactant is greater than one, then the micellar aggregates will already be of the inverse type in water. It should also be noted that not all phases exist for a given surfactant. At low water content it is often seen that liquid crystal phases cease to exist and the surfactant exists in a solid crystalline phase.

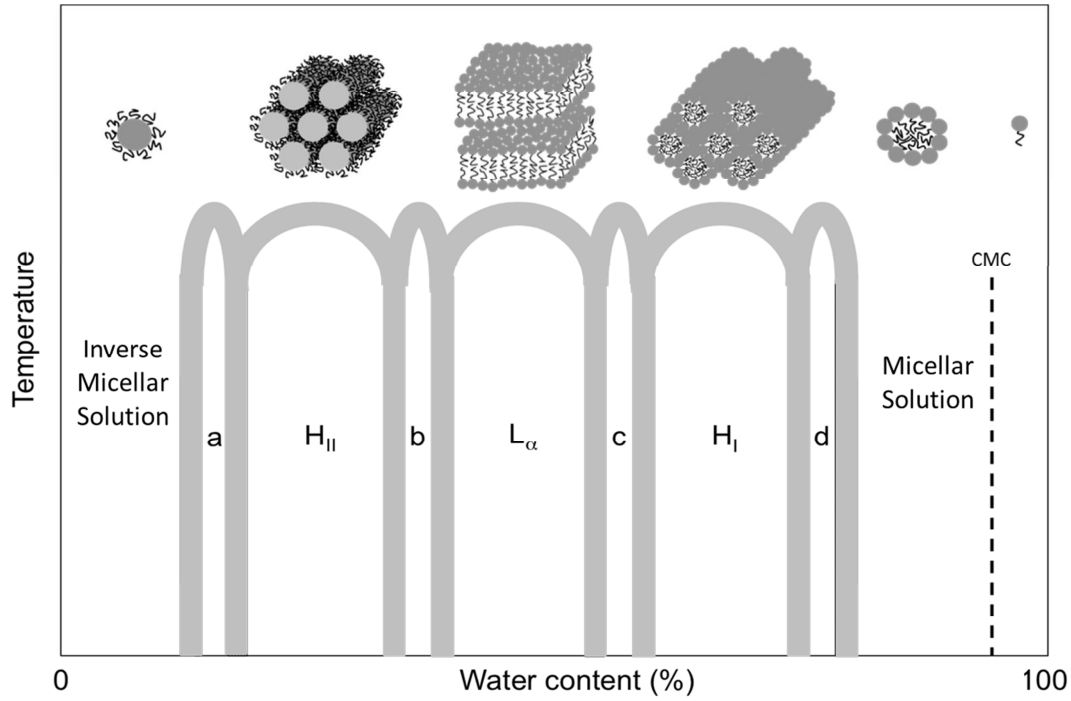

Figure 1.4 Generalised surfactant-water phase diagram. As water content is decreased the surfactant micelles arrange in normal micellar, H_I, L_α, H_{II} and inverse micellar. The letters a, b, c and d represent regions where cubic and bicontinuous regions exist. The grey portions represent regions where phase co-existence is possible. Diagram inspired from reference[32]

Figure 1.4 exhibits breaks between the micellar, hexagonal and lamellar phases. It is at these positions in the phase diagram that cubic phases occur. Cubic liquid crystal phases are either micellar cubic (figure 1.5a) or bicontinuous cubic (figure 1.5b). The grey regions of figure 1.4 represent the positions on the phase diagram where cubic phases and the lesser order liquid crystal phases can co-exist.

Micellar cubic phases (figure 1.5a) are formed as a minimum energy packing of spherical micellar aggregates to lower the inter-micellar interactions. However they can be also be formed from liquid crystal phases of anisotropic micelles such as cylinders where the micelle interface curvature is increased, increasing the energy of solvent-hydrophobe interactions to decrease the energy of inter-micellar interactions.[30] Bicontinuous cubic phases (figure 1.5b) have continuous hydrophobic and solvent phase through the cubic structure. The micellar interface in these phases is said to be a minimal surface. Although the interface has a high curvature, the average curvature through the crystal is equal to zero, therefore at minimal energy. The local energy minima that these phases occupy are further frustrated by changes in the surfactant volume fraction and as the surfactant volume fraction increases the phases more expected curvature as predicted by the packing parameter.[31] This is

primarily due to reduction of the headgroup hydration changing the cross-sectional area of the headgroup.

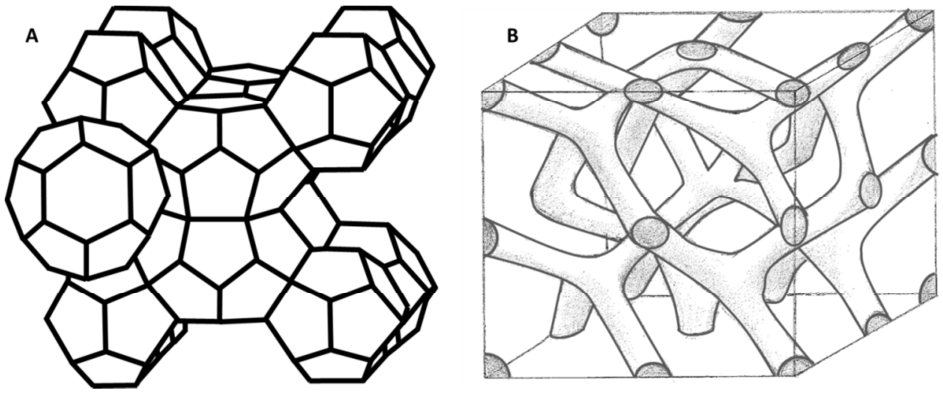

Figure 1.5 Schema showing $Pm\bar{3}n$ micellar cubic (**A**) where the surfactant micelles are contained within the polyhedral and a *Pn3m* bicontinuous cubic phases (**B**) where the surfactants phase is in the grey regions. Schema drawn by author but inspired by Seddon and Templar.[32]

Temperature also affects the surfactant-water phases possible. At a given surfactant volume fraction, changes in temperature modulate the packing of the hydrophobic region of the micelle, causing frustration and exposing the hydrophobic region more to water. This increase in energy often promotes a phase transformation. The effect is more readily seen in double chain surfactants due to the high volume per surfactant molecule they occupy.[30]

1.2.3 Mixed Surfactant Systems

So far, only single component systems have been considered. However by mixing different types of surfactants the properties of the system can be changed. The phase behaviour of mixed surfactants with similarly charged headgroups can be described by applying an average critical packing parameter, which depends on the volume ratios of the surfactant tail and headgroup in the system. Therefore, it will to some extent be possible to predict the behaviour of these systems from the behaviour observed from their individual components.

When mixing surfactants with differently charged headgroups, whether that is anionic, cationic, zwitterionic or non-ionic, the behaviour cannot be predicted by looking to the behaviour of the individual components. When mixing ionic surfactants with non-ionic surfactants, the non-ionic surfactants will effectively act to screen the charges on the micelle surface (figure 1.6) and thereby induce a change

to the effective head group area, thus possibly inducing a shape transition, dependent on volume ratios of the two surfactants.

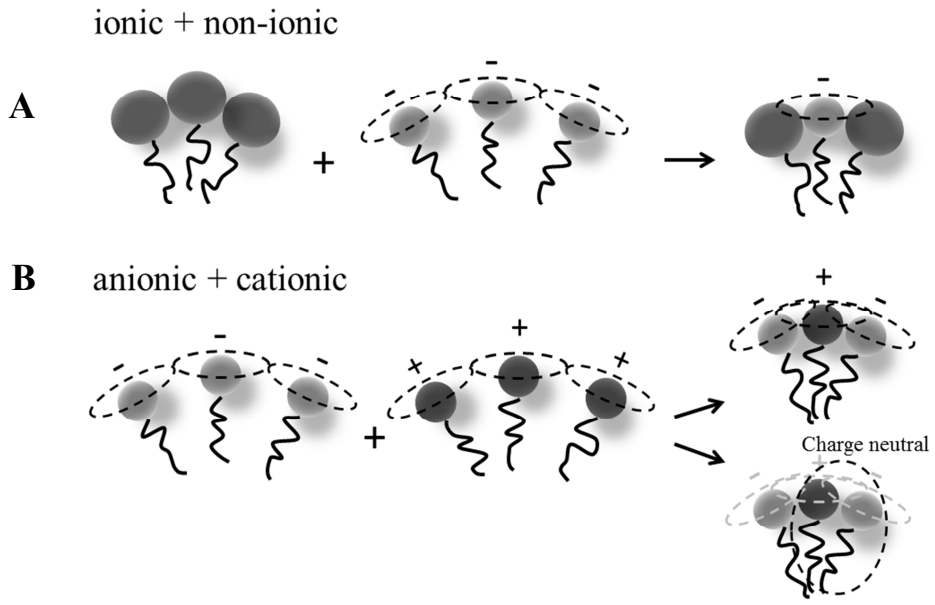

Figure 1.6. A: Mixing of ionic and non-ionic surfactants leads effectively to charge dilution and a subsequent change in effective head group area of the surfactant. **B**: Mixing of an anionic and a cationic surfactant can lead to different behaviours; if counter-ions are present a charge dilution will take place, dependent on mixing ratio. If the counter-ions are removed an overall charge neutral system can occur, provided one-to-one mixing of the charged surfactants occurs and a so called cat-an-ionic surfactant can be formed.

The largest effect is observed in mixtures of oppositely charged surfactants. In a solution of one ionic surfactant the self-assembly is opposed by the lowering of the entropy arising from the counter-ion condensation. However, in a system composed of two oppositely charged surfactants a large increase in entropy is found upon micelle formation as more counter-ions are released from the self-assembled surfactant structures and this is the driving force for micelle formation in mixed ionic surfactant systems. Here, it is not viable to talk about an average critical packing parameter and the behaviour of the system cannot purely be understood form the normal behaviour of the single surfactants.

A property of a mixed surfactant system is that upon removal of the counter-ions, a so called cat-an-ionic (from hereon referred to as catanionic) surfactant are formed (figure 1.6), these have properties similar to those of a double tailed zwitterionic

surfactant. Thus the large differences in the behaviour of the different mixed systems are to a great extent a result of the counter-ions. Thus, addition of a small amount of ionic surfactant to a solution composed of either a mixed non-ionic, zwitterionic or catanionic surfactant solution can have vast effects on the systems.[20]

1.2.4 Surfactant-polymer mixtures

Another important class of molecules for this study are polymers. These are macromolecular structures composed of a large number of monomers, which can be of either natural or synthetic origin. The architecture of a polymer is important for its physiochemical behaviour, which can differ depending on whether the polymer is linear, branched or composed of blocks.[33]

In addition to mixed surfactant systems, the interaction between polymer and surfactant is an important consideration in connection to this work. The interaction between surfactant and polymer can have one of two origins; it can either be electrostatic or hydrophobic in nature. Interactions of the hydrophobic kind are found when the polymer contains hydrophobic regions, as is the case in hydrophobically modified water-soluble polymers (HM polymers) and the hydrophobic regions interact with the hydrophobic micellar cores.[34] Electrostatic interactions govern the interactions in systems where regions of or the whole polymer are ionic or dipolar in electrostatic nature. In this case there is an electrostatic interaction between the polymer and surfactant headgroups.[35]

Different scenarios can occur; the polymer and the surfactant can have similar charge, the polymer and the surfactant are oppositely charged or the polymer is neutral, interacting with a charged surfactant. When considering interaction between polymer and surfactant the critical association concentration (CAC) should be introduced. It is similar to the CMC of the surfactant and describes the concentration where the polymer and the surfactant start to form complexes. This concentration can be much smaller than the CMC by orders of magnitude or lower within the same order. It may thus indicate whether the polymer enhances or suppresses the aggregation tendency of the surfactant.[20]

Ionic surfactants interact with different types of water-soluble polymers, with the most pronounced interaction occurring in the case of anionic surfactants and a lesser interaction observed with cationic surfactants, because the counter-ions are bound more strongly to the cationic headgroups. Dipole-dipole interactions have also been reported[35] with ionic surfactant and neutral polymers, where the ionic surfactant hydrophobic region near the ionic headgroup is itself a dipole. It is only rarely observed that non-ionic surfactants interact with water-soluble polymers, although if the polymer contains hydrophobic regions the surfactants will associate with the polymer due to hydrophobic interactions.[20]

When considering the effect of electrostatic interactions upon surfactant self-assembly the respective charges of the polymer and surfactant must be considered. As discussed previously, release of counter-ions from the micellar surface entropically stabilises the formation of micelles. If the polymer and surfactant are of similar charge then the polyelectrolyte acts as an electrolyte, charge screening the counter-ions and surfactant headgroup and lowering the CMC. The CAC would be lower that the CMC but in the region of the same magnitude of concentration due to the surfactant having a similar effect on the polyelectrolyte and promoting weak aggregation.[20]

However, if the polymer and the surfactant are oppositely charged there will instead be a strong association between the two, causing complex formation by ionic surfactants and homopolymers. Such interactions are described by the 'pearl-necklace model'[36] where the surfactants form discrete micelles along the polymer and the micelle formation in the presence of the polymer resembles that without polymer (figure 1.7 left). If the polymer is slightly amphiphilic, it will be located at the micelle surface, whereby the charge density will be lowered at the micelle surface (charge dilution). This in turn will lower the entropic penalty for forming micelles.[20,37]

Hydrophobically modified polymers resemble surfactants in many ways and the interaction between these and a surfactant species can be looked upon as mixed micelle formation. The polymer can, on its own, form micelle-like structures and it has a strong tendency to form mixed micelles with the surfactant, where the hydrophobic parts of the polymer can be found in the micelle and not just on the surface (figure 1.7 right). Upon interaction with a surfactant there will essentially be no free micelles in solution before all the hydrophobic sites on the polymer are saturated.[20] One should note that the surfactant-polymer interactions depicted in figure 1.4 are speculative and based on how one could envision the interaction could take place. The bead-on-a-string interaction between surfactant and polymer however has been shown experimentally. Associated polymer with surfactant also affects the phase diagram in the liquid crystal regime. This is due to the polymer affecting the inter-micellar interactions by modifying the surface charge of the micelle and introducing packing frustrations due to the mobility of the polymer chains.[38]

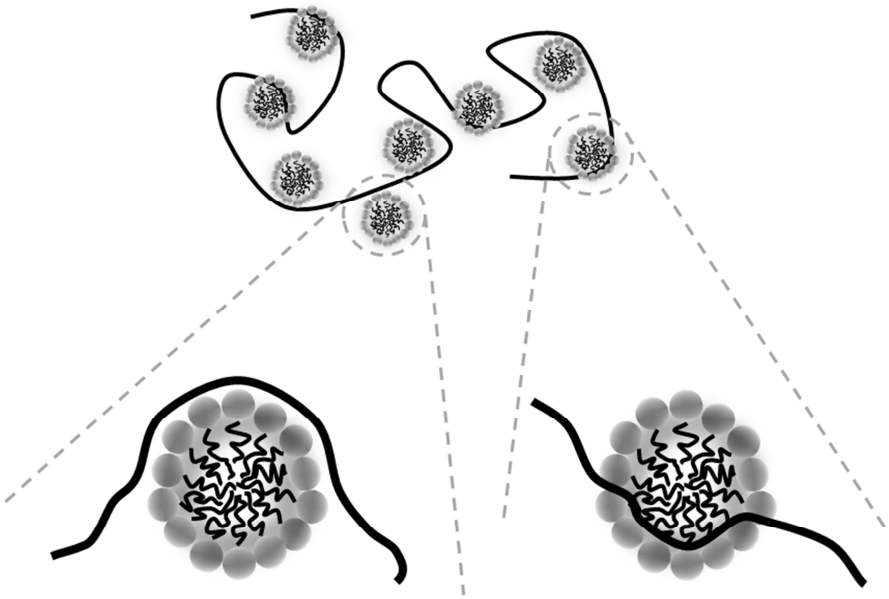

Figure 1.7. Representation of the possible interactions between ionic surfactants and a polymer. Polymer surfactant interactions can be observed between non-ionic surfactants and polymers with hydrophobic domains, where the polymer will have its hydrophobic parts within the micelle (right). Interactions between ionic surfactants and a polymer, which can be either slightly amphiphilic or have a charge opposite to that of the surfactant, result in the polymer being on the surface of the micelles (left). Figure inspired by Holmberg *et al.*[20]

Often discussion of polymer-surfactant interactions concerns synthetic polymers, like poly (acryl amide). However, an important class of natural polymers are also considered in this work. Double-stranded DNA (dsDNA) is a naturally occurring polymer and can be viewed as a stiff and highly charged polyanion. A consequence of the high charge of the dsDNA is that it interacts strongly with cationic surfactants. The strong co-operative interaction between dsDNA and the cationic surfactant leads to a coil-to-globe transition of the dsDNA as a function of surfactant concentration.[39]

1.3 Surfactant templated materials

1.3.1Templated mesostructured materials

Mesostructured materials are of interest as their structural order can give benefits over amorphously structured solids such as increased surface area, size exclusion applications, flow control and controlled release of incorporated species.

Mesostructured materials have structural order spacings in the range of 20-500Å which allows their use to be investigated for applications that would be excluded when using microstructured (<20Å structural order spacing) materials such as zeolites.

One method of controlling the size and geometrical orientation of pores in mesostructured materials is by the surfactant templating of inorganic solids as demonstrated by the discovery of Mobil composite material-41[40](MCM-41). MCM-41 was synthesised via a proposed liquid crystal templating mechanism performed by crosslinking and then calcination of aluminosilicate gels in the presence of hexadecyltrimethylammonium bromide (CTAB). It exhibits a porous structure on the mesoscale which is retained after surfactant removal and the pore size was shown to vary with surfactant used and reaction conditions. The appearance and spacing of the pores in electron micrographs showed structural orientation similarities with hexagonal liquid crystal phases exhibited by CTAB. Other materials synthesised by the same group, MCM-48 and MCM-50, exhibited cubic and lamellar structures respectively[41] by varying the surfactant to silicate ratios.

1.3.2 **Free standing mesostructured surfactant templated silica films**

Self-supporting CTAB templated silica films at the air-solution interface have been formed from aqueous solutions containing CTAB and tetramethyloxysilicate (TMOS). It has been reported that the hydrolysis of TMOS in the presence of surfactants promotes polymerisation and the preferred site of polymerisation is the surface of the CTAB micelles[42] where it can stabilise the elongation of ellipsoid CTAB micelles into cylinders. Although the CTAB micelles and polymeric silica possess the same positive charge in acidic solution, it has been proposed that the interaction is mediated by the counterion bromide from CTAB, allowing the positively charged species to be shielded.[43] The CTAB to TMOS ratio was shown to control the film formation mechanism where intermediate ratios would promote ordered aggregates in the solution which then migrate to the surface while at high and low CTAB:TMOS ratios individual silica coated micelles would migrate to the surface, condense and reorientate.[42]

1.3.3 'Soft templated' Polymer-surfactant hydrogel films

Silica film formation from solutions containing positively charged polymeric silica species and positively charged surfactant micelles led to the substitution of polymeric silica with a positively charged polyelectrolyte. Polyethylenimine (PEI) is an analogous substitute as it possesses amine groups which can be protonated in aqueous solution, therefore behaving as a partial polycation. It also has a hyperbranched structure similar to that formed by polymerising silica in acidic

solutions. Solutions containing CTAB and PEI have been shown to spontaneously form mesostructured polymer-surfactant hydrogel robust films with surfactant imparted structure at the air-solution interface.[43] Compared to surfactant templated films templated by inorganic species, the films are more like a hydrogel with surfactant imparted structure, although they can lock in the surfactant liquid crystal phase and can be considered a soft templated film.

Formation of robust and stable films at the air-solution interface from polyelectrolytes of neutral or like charge to the ionic surfactant is not widely reported in the literature. Addition of polymer to surfactant solutions usually lowers the surface tension further due to adsorption of polymer-surfactant complexes. In systems where the surfactant and polymer are of opposite charge, multilayer films have been reported at the air-solution interface.[35] However these films were unstable and precipitate was found in the solution subphase. In the CTAB-PEI film forming system, it was found that film formation was restricted to the air-solution interface and no periodic mesostructure was formed in the solution subphase at the concentrations investigated.[1-3]

The CTAB/PEI film forming systems were found to primarily exhibit hexagonally close packed cylinder micelles liquid crystal phase. This was determined by neutron reflectivity and grazing incidence x-ray diffraction respectively. It was shown that film formation was dependent on pH, as film formation would not happen below pH 8 however mesostructured films formed at pH 11 where the polymer had 1% of amine groups protonated and at pH 12 where the polymer is residually charged.[2] The decrease in electrostatic repulsion between surfactant micelles and between polymer, and the increased association of amine to cation decreased the spacing between the interfaces of the hexagonal liquid crystal as the polymeric-micelle complexes contracted. The film formation would recur when a film was fractured and it was also reported that the mesostructure exhibited by the films was dependent on the molecular weight of the PEI, as PEI Mw 2000 (SPEI or short PEI) exhibited more ordered mesostructure than hyperbranched PEI Mw 750000 (LPEI or long PEI).[44]

The type and size of the liquid crystal phases exhibited by the CTAB/PEI films could be controlled by surfactant chain length[1,3], PEI molecular weight[1-3] and by cross-linking of PEI.[3] It was found that forming the films from tetradecyltrimethylammonium bromide (TTAB), which forms spherical micelles in solution produced micellar cubic films. This was due to the micellar aggregates having a lower packing parameter than the prolate ellipse micelles of CTAB and therefore packing in to a $Pm\bar{3}n$ phase.[3]

However, structures that could be tentatively attributed to the $Pm\bar{3}n$ space group were also found in films formed from CTAB and PEI where the amount of LPEI present in the film was increased through increasing the pH or where the steric bulk

of the polymeric network was increased through cross-linking of LPEI or SPEI.[3] The increased steric bulk of PEI changed the inter-micellar interactions of CTAB and forced anisotropic micelles to form more spherical aggregates to lower the packing energy as discussed in section 1.2.4.

However the use of CTAB as a component in these film forming systems introduces toxicity to the films.[19] If these film forming systems were to be used for biomedical devices where the surfactant matrix within the films is used to incorporate hydrophobic therapeutic agents as a method of delivery for example, then the toxicity of CTAB would pose a significant problem. The use of a less toxic surfactant as an alternative to CTAB or used a co-surfactant with CTAB could make the films less toxic.

Another film forming system was also discovered which formed films from mixtures of cationic CTAB, anionic sodium dodecyl sulfate (SDS) and a wider variety of polymers such as polyacrylamide[3] and polyethylene oxides.[5] A larger variety of structures could be formed with this system than the CTAB and PEI film forming system and the ability to form structures from different polymers[5] opened up a wide variety of possible uses from the structured films. However, SDS is also a toxic surfactant[19], so as compelling as the variety of structures available within this system was, it was of limited biomedical use.

1.4 Biocompatible films

It has been shown that hydrophobic species can be incorporated into surfactant micelles into CTAB/PEI film forming systems.[6] Whilst changes in micellar phase and film ordering was reported, it was still possible to produce films from these systems. As the lipophilicity of therapeutic agents often has to be modified relative to the intended uptake site such as sub-epidermal cellular surfaces[45], epidermal surface[46] or the intestinal wall.[47] Encapsulation of therapeutic agents may assist in the correct delivery site and controlled release.[48] As one application of mesostructured surfactant templated polymer films may be the encapsulation of therapeutic agents, it is important to find systems that are biocompatible. The systems detailed previously are not biocompatible, mainly due to ionic nature of the surfactants utilised.[49] Although for surfactants of the same headgroup type, the longer tail surfactant will exhibit the greater toxicity[19] PEI toxicity has been reported[50] although it has been shown that derivatised and branched PEI may not show toxic effects and is suitable for use as a drug delivery agent.[50]

One possible route to more biocompatible systems is the use of zwitterionic surfactants in the form filming systems to replace part or all of the catanionicsurfactant mixture in CTAB/SDS solutions. Zwitterionic surfactants

contain both positively and negatively charged substituents in the headgroup, thus mimic the effect of the catanionic pair in one molecule. They exhibit less toxicity than cationic and anionic surfactants of similar chain length.[19,51] The nature of the charged substituents causes the zwitterionic surfactant to be acidic *e.g.* $R^1H_2N^+R^2SO_3^-$, basic $R^1(CH_3)_2N^+R^2CO_2^-$, amphoteric $R^1H_2N^+R^2CO_2^-$ or neither. $R^1(CH_3)2N^+R^2SO_3^-$.[52] Incorporating the zwitterionic sulfobetaine surfactant 3-(N,N-dimethyltetradecylammonio)propanesulfonate (SB3-14)) into the CTAB/PEI film forming systems is proposed in this study due to the nature of the zwitterionic group as it is relatively unaffected by acidic or basic environments allowing it to maintain an ionic nature. The effect of micelle composition using mixed micelles composed of CTAB and the non-ionic surfactant Octaethylene glycol mono-hexadecyl ether on film formation at the air-solution interface with PEI was previously studied.[2] It was reported that increasing the molar ratio of the non-ionic surfactant to CTAB generally decreased film thickness and order based on results from neutron reflectivity experiments. Use of a zwitterionic surfactant that has charged groups may enable substitution of toxic CTAB whilst retaining the liquid crystal phases seen in the CTAB/PEI films.

1.4 Formation of polymer-surfactant films

Formation of thin films can take place at several different interfaces and be the result of several different interactions between molecules like surfactants and polymers. In this work the focus has been on spontaneous film formation at the air-water interface and on films formed at an air-solid interface following spray coating. Spray coating is a way of producing thin films from components, which do not spontaneously form films at the air-water interface. The spray coating is essentially done by creating an aerosol and spraying this on to a surface. The volatile parts of the solution (normally water) within the spray coated layer then evaporate and a thin film is formed.

Considering spontaneous film formation at an interface, adsorption of surfactants at an interface is described by the Gibbs adsorption isotherm (or the free energy of adsorption). The interface is formed between two phases, usually oil/water or air/water. This system can be seen as being composed of several components, *j*. If these components were equally distributed through the two phases, the total Gibbs energy of the system would be the sum of the Gibbs energy of each phase. However, in systems containing surfactants the concentration of these changes throughout the phase as the surfactants can accumulate at the interface. Therefore, the total Gibbs energy of the system differs from the sum of the two phases and must include the surface Gibbs energy. Furthermore, as a consequence of accumulation at the interface the concentration of a component *j* is different at the interface compared to

in the bulk. This can be described by the surface excess, Γ_j. The Gibbs adsorption isotherm is

$$d\gamma = -\sum_j \Gamma_j d\mu_j \tag{1.2}$$

Where Γ is the surface excess (the excess concentration of surfactant at the interface relative to the bulk concentration), γ and μ are the surface tension and chemical potential, respectively. Here, it is seen that the Gibbs adsorption isotherm relates the change in surface tension to the change in chemical potential of the species j.[53]

In the simplest case, a one-component system where the interface is a perfectly flat surface, the Gibbs adsorption isotherm is given as

$$d\gamma = -\Gamma d\mu \tag{1.3}$$

As the assumption of a perfectly flat surface implies that only the surfactant accumulates at the interface and therefore Γ for the two phases, *e.g.* water and oil, is zero. Furthermore, for a dilute one-component system in a solvent the free energy of adsorption can be considered as

$$\left(\frac{\partial \gamma}{\partial \ln c}\right)_T = -RT\Gamma \tag{1.4}$$

Where c is the bulk concentration of the component and R and T the gas constant and the absolute temperature, respectively. It should be noted that in order to obtain the actual surface concentration the bulk concentration must be added to the surface excess. However, as the bulk concentration is significantly lower than the surface excess, this can usually be neglected.[53,54]

From equation 1.4 it is seen that the Gibbs adsorption isotherm describes the relationship between the surface excess, the bulk concentration and the surface tension. Further, from equation 1.4 it is seen that if the surface excess is positive, which it is for surfactants that accumulate at the interface, the left hand side will be

smaller than zero, hence the surface tension decreases with increasing amount of surfactant at the interface[53], until the point where the interface is saturated.

Now considering a film formed spontaneously at the air-water interface: Evaporation of the volatile parts of the solution from the surface, leads to a local increase in concentration at the interface. Thus, due to the difference in concentration in the bulk and at the surface, the system can undergo a phase transition at the interface, where the phases normally seen at high volume fractions can be found.[55] Liquid crystalline phases (LC phases) are observed at the interface. These phases are highly viscous and have long-range order, although still having some short-range disorder and may be apparent as a film The evaporation of water from the interface yields a difference in chemical potential between the bulk solution and the solution close to the interface, so that the solvent close to the interface will have a lower chemical potential than the bulk. The observation of ordered phases close to the interface is in agreement with the higher chemical potential of the polymer-surfactant complexes close to the interface, as these structures form when the chemical potential of the solute in the solution is high.[55] Most of the thin films spontaneously formed, reported to date, have a lamellar[35] phase at the interface, however, examples of films having hexagonal[43] or cubic[5] ordering have also been observed.

In films formed at a solid surface by spray coating it is a matter of debate whether the mechanism behind the formation of dense liquid crystalline phases are the same as for the spontaneously formed films at the air-water interface. If the mechanism is the same as at the air-water interface[55] there would be equal evaporation for the entire surface of the liquid and the dense phase would only form close to the air interface (figure 1.8a). However, other theories have also been proposed. By introducing a surface, the dense phase could also form by interaction with the surface in addition to the dense layer formed at the air-water interface. When the film is dry it will be composed of two layers of ordered hexagonal phases, one formed at the solid-solution interface and one formed at the solution-air interface. Between these two layers a disordered region composed of disordered cylindrical micelles could be observed (figure 1.8a).[56] This is opposed to formation at the air-solution interface where liquid crystals are only apparent at the interface due to the concentration gradient (figure 1.8b).

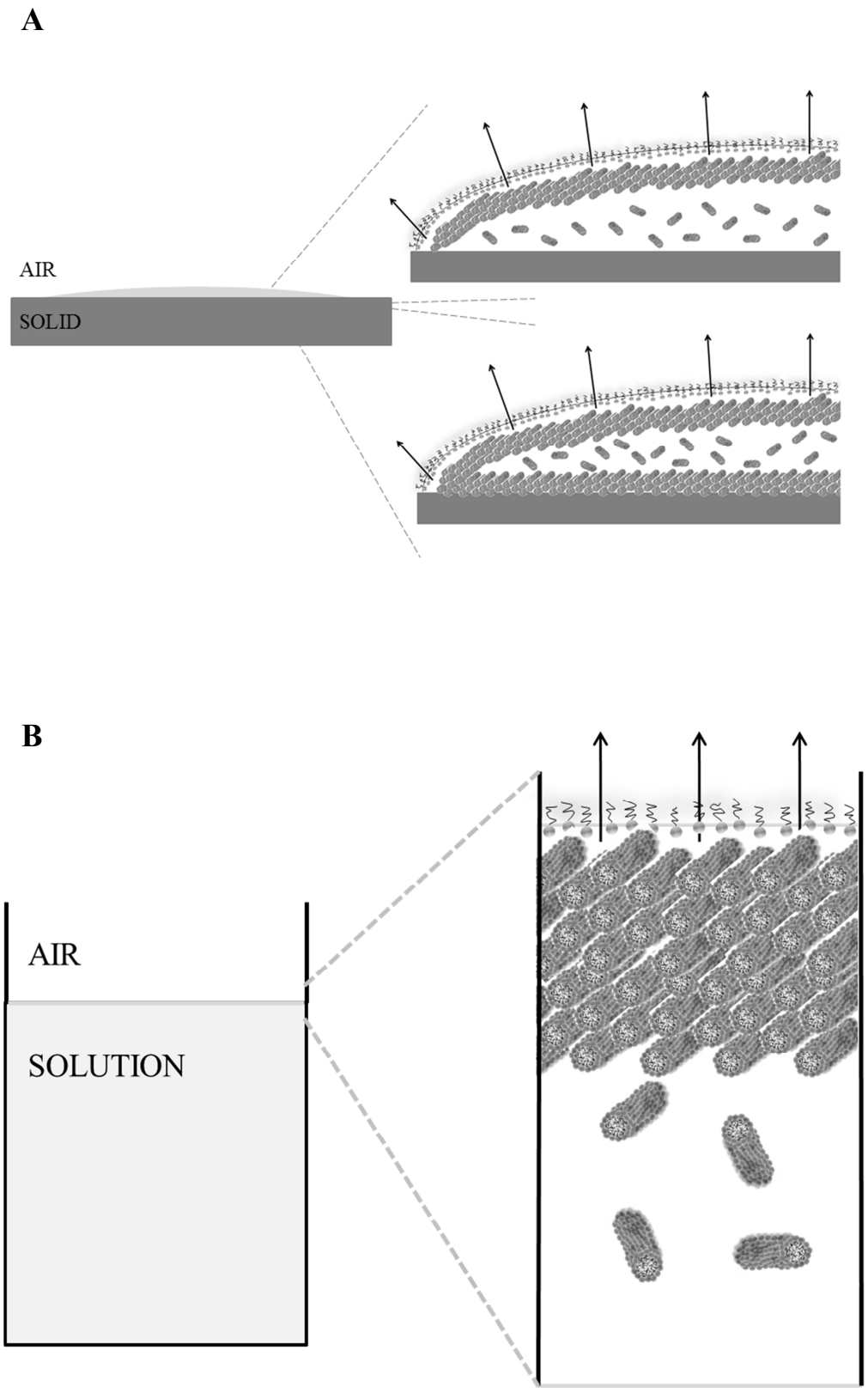

Figure 1.8. A: Film formation at the solid-air interface; the dense hexagonal phase can form in the solution-air interface only or in competition with a dense hexagonal phase formed by interaction with the surface. **B**: Film formation at the air-solution

interface; the dense hexagonal phase forms at the interface due to difference in the concentration in the interfacial layer and in bulk.

Intermolecular forces dominate the physical behaviour of thin films due to the large surface-to-volume ratio in the films.[8] During drying, films formed on a solid surface shrink and since the film is attached to the surface this process will only occur by shrinkage in the vertical direction. Therefore, there is a risk of cracking of the films, as the stress can no longer be relieved by flow. Producing very thin films can circumvent crack formation. In these films the energy needed to crack the film and extend the surface area is higher than the energy gained from relieving the stress. How thin the film has to be to avoid cracking depends on several parameters. However, in general the more elastic the film the less likely it is to crack.[57]

Films formed at the air-water interface do not crack, unlike films on the solid-air interface, due to the ability to shrink in both horizontal and vertical directions and also the amount of water present in the film. However, they can break down, as these films are known to collapse when grown on low concentration solutions. After the film has formed, consisting of homogenous structures in the film and with subsequent loss of lateral mobility, it can become mobile again and hereafter collapse into a thin film without any structure on the meso-scale. The mechanism behind this collapse has been associated with changes in interactions between the film forming species, due to the change in environment as a consequence of water evaporation and interaction with the atmosphere (*i.e.* CO_2 adsorption decreasing the solution pH[58]) and the drying out followed by formation of defects in the upper layer of the film, as a consequence of the difficult or lack of transfer of water through the dense upper layers of the film. These defects could be similar to the crack formation observed in films formed at the solid-air interface.[57]

1.5 References

(1) O'Driscoll, B. M. D.; Milsom, E.; Fernandez-Martin, C.; White, L.; Roser, S. J.; Edler, K. J. *Macromolecules* **2005**, *38*, 8785.

(2) O'Driscoll, B. M. D.; Fernandez-Martin, C.; Wilson, R. D.; Roser, S. J.; Edler, K. J. *The Journal of Physical Chemistry B* **2006**, *110*, 5330.

(3) O'Driscoll, B. M. D.; Fernandez-Martin, C.; Wilson, R. D.; Knott, J.; Roser, S. J.; Edler, K. J. *Langmuir* **2007**, *23*, 4589.

(4) Comas-Rojas, H.; Aluicio-Sarduy, E.; Rodriguez-Calvo, S.; Perez-Gramatges, A.; Roser, S. J.; Edler, K. J. *Soft Matter* **2007**, *3*, 747.

(5) Edler, K. J.; Wasbrough, M. J.; Holdaway, J. A.; O'Driscoll, B. M. D. *Langmuir* **2009**, *25*, 4047.

(6) O'Driscoll, B. M. D.; Hawley, A. M.; Edler, K. J. *Journal of Colloid & Interface Science* **2008**, *317*, 585.

(7) Wasbrough, M. J.; Edler, K. J.; Hawley, A. M.; Holdaway, J. A.; Price, G. J. *Soft Matter* **2012**, *8*, 3357.

(8) Reiter, G.; Sharma, A.; Casoli, A.; David, M.-O.; Khanna, R.; Auroy, P. *Langmuir* **1999**, *15*, 2551.

(9) Wang, Y.; Hosta-Rigau, L.; Lomas, H.; Caruso, F. *Physical Chemistry Chemical Physics* **2011**, *13*, 4782.

(10) Reisch, A.; Hemmerle, J.; Chassepot, A.; Lefort, M.; Benkirane-Jessel, N.; Candolfi, E.; Mesini, P.; Letscher-Bru, V.; Voegel, J.-C.; Schaaf, P. *Soft Matter* **2010**, *6*, 1503.

(11) Schwinté, P.; Ball, V.; Szalontai, B.; Haikel, Y.; Voegel, J. C.; Schaaf, P. *Biomacromolecules* **2002**, *3*, 1135.

(12) Salloum, D. S.; Schlenoff, J. B. *Biomacromolecules* **2004**, *5*, 1089.

(13) Boulmedais, F.; Frisch, B.; Etienne, O.; Lavalle, P.; Picart, C.; Ogier, J.; Voegel, J. C.; Schaaf, P.; Egles, C. *Biomaterials* **2004**, *25*, 2003.

(14) Jewell, C. M.; Zhang, J.; Fredin, N. J.; Wolff, M. R.; Hacker, T. A.; Lynn, D. M. *Biomacromolecules* **2006**, *7*, 2483.

(15) Cai, K.; Rechtenbach, A.; Hao, J.; Bossert, J.; Jandt, K. D. *Biomaterials* **2005**, *26*, 5960.

(16) Chua, P.-H.; Neoh, K.-G.; Kang, E.-T.; Wang, W. *Biomaterials* **2008**, *29*, 1412.

(17) Hu, Y.; Cai, K.; Luo, Z.; Zhang, R.; Yang, L.; Deng, L.; Jandt, K. D. *Biomaterials* **2009**, *30*, 3626.

(18) O'Driscoll, B. M. D.; Fernandez-Martin, C.; Wilson, R. D.; Roser, S. J.; Edler, K. J. *J Physical Chemistry B* **2006**, *110*, 5330.

(19) Sandbacka, M.; Christianson, I.; Isomaa, B. *Toxicology in Vitro* **2000**, *14*, 61.

(20) Holmberg, K.; Jönsson, B.; Kronberg, B.; Lindman, B. *Surfactants and polymers in aqueous solution*; John Wiley & Sons Chichester, **2003**; Vol. 2.

(21) Tanford, C. *Journal of Molecular Biology* **1972**, *67*, 59.

(22) Tanford, C. *The Journal of Physical Chemistry* **1974**, *78*, 2469.

(23) Israelachvili, J. N.; Mitchell, D. J.; Ninham, B. W. *Journal of the Chemical Society, Faraday Transactions 2: Molecular and Chemical Physics* **1976**, *72*, 1525.

(24) Jones, R. A. *Soft condensed matter*; Oxford University Press, **2002**; Vol. 6.
(25) Eriksson, J. C.; Ljunggren, S.; Henriksson, U. *Journal of the Chemical Society, Faraday Transactions 2: Molecular and Chemical Physics* **1985**, *81*, 833.
(26) Shinoda, K.; Hutchinson, E. *The Journal of Physical Chemistry* **1962**, *66*, 577.
(27) Mukerjee, P.; Mysels, K.; Kapauan, P. *The Journal of Physical Chemistry* **1967**, *71*, 4166.
(28) Zana, R. *Langmuir* **1996**, *12*, 1208.
(29) Butt, H.-J.; Graf, K.; Kappl, M. In *Physics and Chemistry of Interfaces*; Wiley-VCH Verlag GmbH & Co. KGaA: **2004**, p 246.
(30) Tiddy, G. J. T. *Physics Reports* **1980**, *57*, 1.
(31) Seddon, J. M.; Templer, R. H. *Philosophical Transactions of the Royal Society of London. Series A: Physical and Engineering Sciences* **1993**, *344*, 377.
(32) Seddon, J. M.; Templer, R. H. In *Handbook of Biological Physics*; Lipowsky, R., Sackmann, E., Eds.; North-Holland: **1995**; Vol. Volume 1, p 97.
(33) Hamley, I. W. *The physics of block copolymers*; Oxford University Press New York, **1998**; Vol. 19.
(34) Bromberg, L.; Temchenko, M.; Colby, R. H. *Langmuir* **2000**, *16*, 2609.
(35) Taylor, D. J. F.; Thomas, R. K.; Penfold, J. *Advances in Colloid and Interface Science* **2007**, *132*, 69.
(36) Kötz, J.; Kosmella, S.; Beitz, T. *Progress in Polymer Science* **2001**, *26*, 1199.
(37) Nagarajan, R. *Colloids and Surfaces* **1985**, *13*, 1.
(38) Ilekti, P.; Martin, T.; Cabane, B.; Piculell, L. *The Journal of Physical Chemistry B* **1999**, *103*, 9831.
(39) Ghirlando, R.; Wachtel, E. J.; Arad, T.; Minsky, A. *Biochemistry* **1992**, *31*, 7110.
(40) Kresge, C.; Leonowicz, M.; Roth, W.; Vartuli, J.; Beck, J. *Nature* **1992**, *359*, 710.
(41) Vartuli, J. C.; Schmitt, K. D.; Kresge, C. T.; Roth, W. J.; Leonowicz, M. E.; McCullen, S. B.; Hellring, S. D.; Beck, J. S.; Schlenker, J. L. *Chemistry of Materials* **1994**, *6*, 2317.
(42) Brennan, T.; Hughes, A. V.; Roser, S. J.; Mann, S.; Edler, K. J. *Langmuir* **2002**, *18*, 9838.
(43) Edler, K. J.; Goldar, A.; Brennan, T.; Roser, S. J. *Chemical Communications* **2003**, 1724.
(44) O'Driscoll, B. M. D.; Fernandez-Martin, C.; Wilson, R. D.; Knott, J.; Roser, S. J.; Edler, K. J. *Langmuir* **2007**, *23*, 4589.
(45) McKeage, M. J.; Berners-Price, S. J.; Galettis, P.; Bowen, R. J.; Brouwer, W.; Ding, L.; Zhuang, L.; Baguley, B. C. *Cancer chemotherapy and pharmacology* **2000**, *46*, 343.
(46) Godwin, D.; Michniak, B. *Drug Development and Industrial Pharmacy* **1999**, *25*, 905.
(47) van de Waterbeemd, H.; Smith, D.; Jones, B. *Journal of Computer Aided Molecular Design* **2001**, *15*, 273.
(48) Zhang, Z.; Feng, S.-S. *Biomaterials* **2006**, *27*, 4025.
(49) Sirisattha, S.; Momose, Y.; Kitagawa, E.; Iwahashi, H. *Water Research* **2004**, *38*, 61.

(50) Bauer, J. A.; Rao, W.; Smith, D. J. *Wound Repair and Regeneration* **1998**, *6*, 569.
(51) Tsubone, K.; Uchida, N.; Mimura, K. *Journal of the American Oil Chemists' Society* **1990**, *67*, 455.
(52) Laughlin, R. G. *Langmuir* **1991**, *7*, 842.
(53) Atkins, P.; De Paula, J. *Physical Chemistry Eight Edition*, Oxford University Press, **2006**.
(54) Lu, J.; Thomas, R.; Penfold, J. *Advances in Colloid and Interface Science* **2000**, *84*, 143.
(55) Åberg, C.; Sparr, E.; Edler, K. J.; Wennerström, H. k. *Langmuir* **2009**, *25*, 12177.
(56) Lu, Y.; Ganguli, R.; Drewien, C. A.; Anderson, M. T.; Brinker, C. J.; Gong, W.; Guo, Y.; Soyez, H.; Dunn, B.; Huang, M. H. *Nature* **1997**, *389*, 364.
(57) Brinker, C.; Hurd, A.; Schunk, P.; Frye, G.; Ashley, C. *Journal of Non-Crystalline Solids* **1992**, *147*, 424.
(58) Campbell, R. A.; Edler, K. J. *Soft Matter* **2011**, *7*, 11125.

2 Experimental Techniques and Theory

In this chapter the focus is on the techniques used to characterise the films and their individual components in bulk. First, the small-angle scattering technique is described, which is used to characterise solution structures of micelles and polymers. Then we move on to the techniques used to characterise the surface structures, the films, which in this thesis are reflectivity and grazing-incidence small-angle scattering. All the scattering techniques are used with both X-rays and neutrons, as there are advantages of employing both methods. Finally, the complementary techniques of Brewster angle microscopy (BAM), densitometry and force tensitometry are briefly described.

2.1 Small-Angle Scattering – Basic principles

Small-angle scattering (SAS) techniques are used for structural investigation of samples. They are based on diffraction, thus information regarding the size and form of structures is dependent on the angle of scattered radiation. The small scattered angles achieved in the technique translate to large structures, *i.e.* larger than the atom to atom distances investigated by X-ray diffraction (XRD). It may be used to investigate liquid or solid samples. In this work, primarily investigation of solutes in aqueous solution will be discussed such as micelles and polymers. The basic principles of small-angle scattering presented here is a summary of theory from Glatter and Kratky[1] and Lindner and Zemb.[2]

A scattering event occurs when a beam of incident radiation interacts with the atoms in a sample. The source of the scattering differs between X-rays and neutrons; the former interacts with the electrons and the latter with the nuclei. Thus, every electron or nucleus becomes the source of a spherical wave.

The interference of the spherical waves gives rise to the observed scattering pattern. In small-angle scattering the incident wave has a wave vector, $|\vec{k}_I| = 2\pi/\lambda$ where λ is the wavelength of the radiation. The scattering vector $\vec{q}$ can be defined for every scattering event. In defining the scattering vector, only elastic scattering is considered where the modulus of the scattered wave, $|\vec{k}_S|$ is equal to the incident wave, $|\vec{k}_S| = |\vec{k}_I|$. The scattering vector is the difference between the scattered and incident wave, $\vec{q} = \vec{k}_S - \vec{k}_I$. Using the definition of the wave vector and following the

expression of q as a function of the wavelength allows comparison of experiments performed on instruments using different wavelengths.

The geometry of the scattering event is shown in figure 2.1. The magnitude of the scattering vector becomes $q = 4\pi \sin\theta/\lambda$, where 2θ is the angle between the incoming and scattered rays.

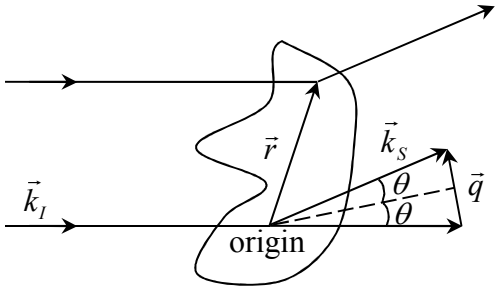

Figure 2.1. Schematic representation of the geometry of a small-angle scattering event. The incident ray, $\vec{k}_I$ hits a particle at $\vec{r}$ and a small part of it is scattered at an angle 2θ. A scattering event occurring at $\vec{r}$, which is the position inside the particle relative to the origin, giving rise to a wave shifted with a phase of $\exp(-i\vec{q}\cdot\vec{r})$.

Scattering from an object consists of the scattering from each atom in the particle. At each scattering event taking place at $\vec{r}$ the waves generated are shifted with a phase of $\exp(-i\vec{q}\cdot\vec{r})$. By introducing the scattering length b_j of the j'th atom, the single particle scattering amplitude can be written as the sum of the spherical waves

$$A_1(\vec{q}) = \sum b_j \exp(-i\vec{q}\cdot\vec{r}) \qquad 2.1$$

In small-angle scattering the positions of the individual atoms are unknown and it is therefore convenient to describe the scattering from a particle as a function of a continuous distribution of the scattering length density (SLD), $\rho(\vec{r})$, where $\rho(\vec{r}) = b(\vec{r})/V_m$, and not as a sum of scattering events at discrete points.

$$V_m = \frac{1}{N_A}\frac{M}{\rho_m} \qquad 2.2$$

Where N_A is Avogadro's number, M is the molar mass and ρ_m is the mass density.

$$\rho = \frac{\sum_{i=1}^{n} b_i}{V_m} \qquad 2.3$$

Where b_i is the bound coherent scattering length of atom i

Experimentally, SLD may be calculated by determining the molecular volume, V_m, which is determined through obtaining the density of a molecule (described under densitometry in section 2.6.3.)

The scattering length of an atom can be defined as the amplitude of the scattered wave vector after interaction with atom i. The bound coherent scattering length specifically is the amplitude of the scattering wave vector from an elastic scattering event from an atom in a molecule. Inelastic scattering events contribute to the scattering amplitude defined by their incoherent scattering length. With X-rays, at the energies and with the species used in this study the incoherent scattering length is insignificant. However, when neutrons are in the incident energy the incoherent scattering length can be significant. It is discussed further in the analysis of small angle scattering data later.

Wave vector dependent scattering amplitude from a particle arises when there is a difference in SLD between the particle and its surrounding medium. In the case of a particle in solution, the excess scattering length density difference, or contrast, $\Delta\rho(\vec{r})$, is the difference between the scattering length density at $\vec{r}$ and the solvent, ρ_s, $\Delta\rho(\vec{r}) = \rho(\vec{r}) - \rho_s$. The single particle scattering amplitude then becomes

$$A_1(\vec{q}) = \int_V \Delta\rho(\vec{r})\exp(-i\vec{q}\cdot\vec{r})d\vec{r} \qquad 2.4$$

However, the detected quantity in a scattering experiment is not the amplitude but the intensity. The single particle intensity is equal to the absolute square of the amplitude, $I_1(\vec{q}) = |A_1(\vec{q})|^2$. Therefore, the single particle scattering intensity can be described as

$$I_1(\vec{q}) = \int_V \gamma(\vec{r}) \exp(-i\vec{q} \cdot \vec{r}) d\vec{r} \qquad 2.5$$

Where $\gamma(\vec{r})$ is the autocorrelation function of the excess scattering length density distribution, $\Delta\rho(\vec{r})$. The autocorrelation function will be further discussed later in this chapter.

For non-interacting isotropically distributed particles, the total scattering intensity can be described by the spherically averaged single particle intensity multiplied by the number density of particles, $I(q) = n\langle I_1(\vec{q}) \rangle$. Thus

$$I(q) = n4\pi \int_0^{D_{\max}} \gamma(r) \frac{\sin(qr)}{qr} r^2 dr \qquad 2.6$$

Here the upper limit of the integration is the maximum distance within the scattering particle, $D_{\max}$, as the particles are non-interacting and the contribution from inter-particle distances can be neglected. The particles investigated in a scattering experiment are randomly orientated and therefore the total scattering intensity is a statistical average over all orientations, as described by the symbol $\langle \ \rangle$ and $\langle \exp(-i\vec{q} \cdot \vec{r}) \rangle = \frac{\sin(qr)}{qr}$. This gives a one-dimensional dependence of the scattering intensity on q. By introducing the pair distance distribution function, $p(r) = \gamma(r) r^2$, equation 2.6 becomes

$$I(q) = n4\pi \int_0^{D_{\max}} p(r) \frac{\sin(qr)}{qr} dr \qquad 2.7$$

The pair distance distribution function will be discussed in the section concerned with indirect Fourier transformation below.

In the systems studied, it is not always the case that the particles do not interact with each other. If inter-particle interaction is present this has to be taken into account as

it introduces a contribution from inter-particle distances. The *r*-vector in equation 2.4, which denotes the point positions, would be a sum of a vector r_j giving the particle *j*'s centre position and a vector *i*. Then the single particle scattering becomes

$$I_1(\vec{q}) = \left| \int_V \Delta\rho(\vec{i}) \exp(-i\vec{q} \cdot \vec{i}) d\vec{i} \sum_j \exp(-i\vec{q} \cdot \vec{r}_j) \right|^2 \qquad 2.8$$

Assuming that the particles are centrosymmetric and monodisperse the expression in equation 2.8 can be re-written.

$$\begin{aligned} I_1(\vec{q}) &= \left| \int_V \Delta\rho(\vec{i}) \exp(-i\vec{q} \cdot \vec{i}) d\vec{i} \right|^2 \times \left| \sum_j \exp(-i\vec{q} \cdot \vec{r}_j) \right|^2 \\ &= \int_V \gamma(\vec{i}) \exp(-i\vec{q} \cdot \vec{i}) d\vec{i} \times \sum_k \sum_j \exp(i\vec{q} \cdot (\vec{r}_k - \vec{r}_j)) \end{aligned} \qquad 2.9$$

The first term is the expression for scattering from a single particle and the second term is the structure factor, which describe the contribution from particle interaction giving rise to preferred or avoided distances between the particles. The structure factor, *S*(*q*), can be written as

$$S(\vec{q}) = 1 - \sum_k \sum_{j \neq k} \exp(i\vec{q} \cdot (\vec{r}_k - \vec{r}_j)) \qquad 2.10$$

By introducing the pair correlation functions, *g*(*r*), the structure factor can be written as

$$S(\vec{q}) = 1 - \int_V g(\vec{r}) \exp(i\vec{q} \cdot \vec{r}) dr \qquad 2.11$$

The pair correlation function is the distribution function of inter-particle distances. $g(r)$ is determined by considering the density of particles in a shell between r and $r+dr$ around a given particle, as illustrated in figure 2.2, and then the average of this distribution is calculated over the entire sample. Therefore, $g(r)$ is the average of the normalised density of particles in a shell from the centre of one particle.

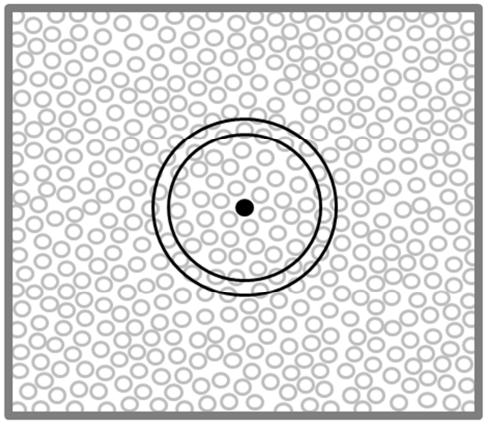

Figure 2.2. Illustration of the pair correlation function, $g(r)$, which is the average of the normalised density of particles in a shell at a distance, r, from the particle centre.

It is only the fluctuations of $g(\vec{r})$ from unity which give rise to scattering, thus $g(\vec{r})$ can be replaced by $\{g(\vec{r})-1\}$ and one gets

$$S(\vec{q}) = 1 - \int_V \{g(\vec{r})-1\}\exp(i\vec{q}\cdot\vec{r})dr \qquad 2.12$$

Furthermore, by assuming an isotropic sample and averaging over all orientations equation 2.12 becomes

$$S(q) = 1 - n4\pi\int_0^\infty \{g(r)-1\}\frac{\sin(qr)}{qr}r^2 dr \qquad 2.13$$

The scattering originating from a monodisperse and isotropic sample with interacting particles gives rise to a total scattering intensity, which is a product of the form factor and the structure factor, as deduced in equation 2.9. The total scattering intensity can then be written as

$$I(q) = n\Delta\rho^2 V_p{}^2 P(q)S(q) \qquad 2.14$$

n being the number density of particles, $\Delta\rho$ the excess scattering length density or contrast and V_p the average volume of the particle. The form factor, $P(q)$, is related to the single particle shape and size and the structure factor, $S(q)$, describes the interference of scattering from interacting particles[3,4]. In the following section the form and structure factors used in this work are presented. For a comprehensive list of form and structure factors the reader is referred to Pedersen 1997.[4,5]

2.2 Analysis of small-angle scattering data

The first step in analysing small-angle scattering data is to evaluate the data independent of models. The scattering data at q approaching zero angle in dilute solutions contains directly obtainable information on the particles giving rise to the scattering. At low q, is the Guinier regime, where, assuming spherical particles, the following applies

$$I(q) \approx I(q=0)\exp\left(-R_g^2 q^2/3\right) \qquad 2.15$$

Two parameters can be obtained directly from the scattering data by displaying it as $\log(I(q))$ versus q^2; the forward scattering, $I(q = 0)$, from the intercept and the contrast weighted root-mean-square radius of gyration, R_g, from the slope.[6] It should be noted that the Guinier approximation is only valid for $qR_g < 1$, as a rule of thumb.

Having obtained the forward scattering for a dilute solution, the scattering intensity at $q = 0$ is proportional to the mass of the particles giving rise to the scattering. From equation 2.14 approaching $q = 0$ for a dilute solution it follows that

$$I(q=0) = n\Delta\rho^2 {V_p}^2 = c\Delta\rho^2 M_p / \left({\rho_d}^2 N_A\right) \qquad 2.16$$

Where n is the number density of particles (concentration in number of particles per volume), c the concentration in mass per volume, average M_p the molar mass of the particles, ρ_d the partial specific density of the particles and N_A Avogadro's number.[7]

In equation 2.16 it was assumed that the particles had a constant SLD throughout the particle, however, for many particles this is not the case. For example, in the case of a micelle, the hydrophobic core may have a different SLD to that of the hydrophilic headgroup. In the case of a non-uniform SLD the expression in equation 2.16 becomes

$$I(q=0) = n\left(\sum_j \Delta\rho_j V_{p,j}\right)^2 = \frac{c}{N_A \sum_j M_{p,j}} \left(\sum_j \Delta\rho_j M_{p,j} / \rho_{d,j}\right)^2 \qquad 2.17$$

Where j denotes the different regions in the particles.

If the different regions have contrasts with opposite signs, which can be the case for micelles, particularly with X-rays, the forward scattering can be suppressed or completely vanish. In these cases the lack of scattering at low q means that it can be difficult or impossible to deduce the molecular mass and the large scale structure of the particles. However, one should note that using a combination of X-rays and neutrons this might be circumvented, as different regions which have opposite signs of contrast when using X-rays may likely not have regions with opposite signs of contrasts when using neutrons.

At intermediate q some particle-specific power laws can be observed, where $I(q) \sim q^{-x}$. The power laws apply above the Guinier regime and below the regime dominated by scattering from the particle cross-section. For a rod-like particle extending in one dimension $x = 1$, whereas for flat particles extending in two dimension $x = 2$. However, $x = 2$ is also observed for polymer chains displaying random walk characteristics. Finally, $x = 1.7$ is found for self-avoiding random walk chains.[3]

Scattering data can also be evaluated with an indirect Fourier transformation (IFT). Here, information on the particle size and shape can be obtained without any model assumptions provided the system consists of non-interacting particles. In the case of

interacting particles the scheme is changed. IFT of interacting particles will be described shortly, but first the case of non-interacting particles is considered.

In equation 2.7 the pair distance distribution functions was defined and it was seen that the intensity is coupled to this by a Fourier transformation. The pair distribution function is given as

$$p(r) = \gamma(r) r^2 \qquad 2.18$$

Here $\gamma(r)$ is the autocorrelation function, which is given as

$$\gamma(r) = \frac{1}{4\pi} \int_0^{4\pi} \int_V \Delta\rho(\vec{r}_1) \Delta\rho(\vec{r}_1 - \vec{r}) d\vec{r}_1 d\Omega \qquad 2.19$$

Where $\Delta\rho(\vec{r})$ is the excess scattering length density distribution at $\vec{r}$ [8,9].

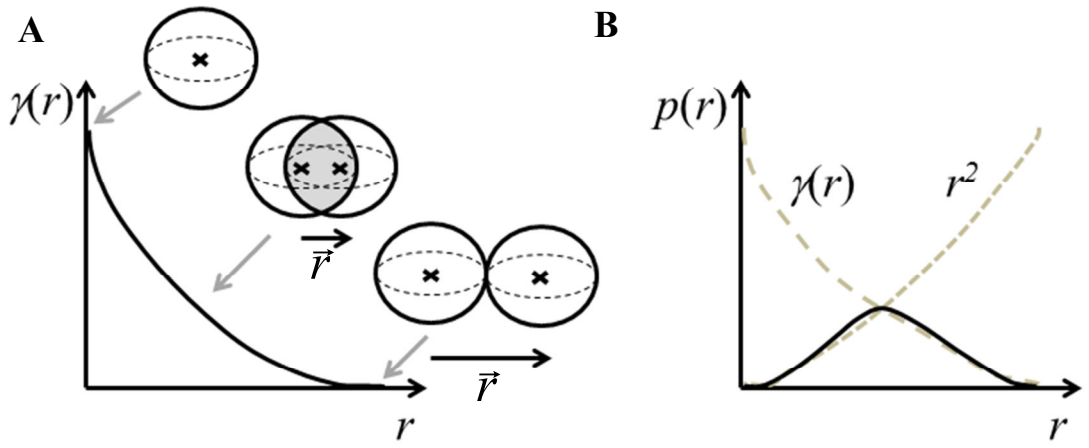

Figure 2.3. A: Autocorrelation function, $\gamma(r)$, for a spherical particle with examples of the overlap between the particle and its ghost. **B**: Pair distance distribution function, $p(r)$, of a spherical particle.

The autocorrelation function is the overlap between a particle fixed in space and its identical ghost shifted at $\vec{r}$, as illustrated for a spherical particle in figure 2.3a. Looking at a particle with a constant electron density the autocorrelation function is

given as the square of the contrast, $\Delta\rho(\vec{r})^2$, multiplied by the overlap volume between the particle and its shifted 'ghost', as stated in equation 2.19. The average over all orientations is the same kind of calculation for a shifted ghost, except that it has to be an average over all possible orientations in space.

The pair distance distribution function can be understood as a histogram of numbers of pair distances inside the particle, weighted by excess scattering length at the points connected by $\vec{r}$.[9,10] In the case of an inhomogeneous particle, with opposite signs of excess scattering length density in different areas of the particle, some distances can have contributions with opposite signs of the excess scattering length at the two points. This will give a negative contribution to the $p(r)$ and this can give negative values of the $p(r)$ at certain r, as shown in figure 2.4. From the $p(r)$ information on the overall size, D_{max}, and the particle shape can be obtained. In figure 2.4 examples of different particle shapes and their corresponding $p(r)$ are shown.

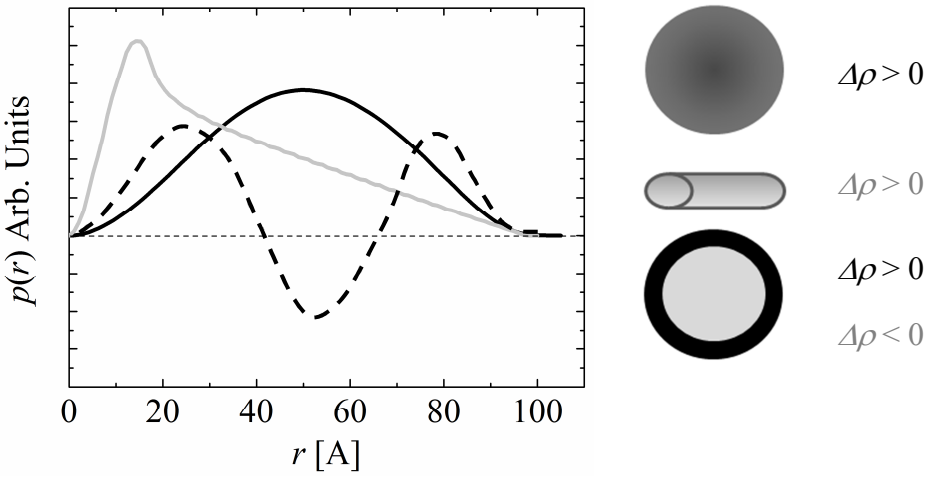

Figure 2.4. The pair distance distribution function for a sphere (black line), a cylinder (grey line) and a spherical particle with opposite signed contrasts (dashed line).

The forward scatting, $I(q = 0)$, and radius of gyration, R_g, are directly obtained from the $p(r)$ as

$$I(q=0) = 4\pi \int_0^{D_{max}} p(r)dr \qquad R_g^2 = \frac{\int_0^{D_{max}} p(r)r^2 dr}{2\int_0^{D_{max}} p(r)dr} \qquad 2.20$$

The forward scattering and the radius of gyration obtained through the indirect Fourier transformation method are more reliable than those obtained from the Guinier approximation, because this procedure uses the entire scattering curve.[11]

The $p(r)$ function can be obtained from experimental data with the IFT method as the $p(r)$ is the Fourier transform of the scattered intensity

$$p(r) = \frac{1}{2\pi^2}\int_0^\infty I(q)qr\sin(qr)dr \qquad 2.21$$

In the IFT method one obtains the pair distance distribution function giving the best fit to the scattering data in a finite q-range without extrapolations. The $p(r)$ can be described using a series of base functions, cubic b-splines, $\varphi_i(r)$, centred at different r-values

$$p(r) = \sum_{i=1}^{M} c_i \varphi_i(r) \quad \text{for } 0 \le r \le D_{\max} \qquad 2.22$$

Where the maximum diameter of the particle, D_{max}, is selected manually and M is the number of b-splines and expansion coefficients, c_i. Fourier transformation of the $p(r)$ gives the expression to be fitted to the scatting data, as $I(q) = P(q) = \sum_{i=1}^{M} c_i \psi_i(q)$ where $\psi_i(q) = 4\pi\int_0^{D_{\max}} \varphi_i(r)\frac{\sin(qr)}{qr}dr$. Due to numerical instability, smoothness constraints are imposed on the $p(r)$. The expression is optimized with respect to the experimental data by use of the weighted linear least-squares procedure. Since the functions are in reciprocal space, smearing effects originating from instrumental broadening like geometry and wavelength effects can also be accounted for.[9-12]

It cannot always be assumed that the particles are non-interacting and in order to perform an indirect Fourier transformation analysis of such system another method must be employed. For homogenous isotropically distributed particles with a spherical geometry the following can be assumed: $I(q) \propto nP(q)S(q)$, where a similar assumption can be made for non-spherical particles. The scattering intensity can now be describe in terms of the form factor, which can be determined in a model free

manor, and a structure factor, which has to be calculated from an adequate model. This leads to a procedure that is no longer model-free, however it still gives valuable information on the form of particles using few assumptions. The method is as follows.

The scattering intensity is

$$I(q) = P(q)S(q,\vec{d}) = \sum_{i=1}^{M} \{c_i \psi_i(q)\} S(q,\vec{d}) \qquad 2.23$$

Where the structure factor depends on q and the vector d, which contains the coefficients d_k with k =1,..,4. These coefficients describe parameters in the structure factor such as the volume fraction and the particle size. In the simple case, where the intensity is given as the form factor times the structure factor, one gets

$$\begin{aligned} \overline{\psi}_i(q,\vec{d}) &= \psi_i(q)S(q,\vec{d}) \\ I(q) &= \sum_{i=1}^{M} c_i \overline{\psi}_i(q,\vec{d}) \end{aligned} \qquad 2.24$$

The coefficients c_i and d_k have to be determined, however, this cannot be done in one coherent procedure as this yields an unstable set of non-linear equations. This problem is circumvented by determining c_i as in the IFT method and determining d_k by a weighted non-linear least squares routine. This is then performed in an iterative procedure, where first the c_i coefficients are determined and then the d_k coefficients until the optimum solution is obtained. Despite the fact that one has to guess a structure factor, this procedure can give valuable information on the system with a minimum of assumptions. A typical structure factor is the hard sphere structure factor.[13] This structure factor yields an effective hard sphere volume fraction and an effective hard sphere radius which defines the limit of the extent particles can encroach on each other.[4,14,15]

Having extracted all possible information on the system independent of models, the data may be evaluated against a model. In model dependent analysis the scattering data is the product of the form factor, $P(q)$ and the structure factor, $S(q)$. The actual form and structure factors used in this work will be presented later in this chapter. In a monodisperse system of isotropic particles the scattering can be written as

$$I(q) = nP(q)S(q) \qquad 2.25$$

Where n is the number density of the particles.

When fitting small-angle scattering data to a model it has to be considered that the information in the data is limited. The extent of information that can be extracted from the data depends on several parameters, the most important being the q-range of the data and the quality of this. The information content is often evaluated by use of Shannon's sampling theorem.[16] Following Shannon, an approximate number of parameters one can include in a model is given by the number of Shannon channels in the data; $N = D_{max}(q_{max} - q_{min})/\pi$, where N is the number of channels (or free parameters). This number rarely exceeds 10-15 in small-angle scattering. The information retrieved from the data can be increased by including *a priori* information or fitting multiple data sets simultaneously.[16,17]

Multiple data sets containing different information on the same system can be obtained by using both X-rays and neutrons. Furthermore, in small-angle scattering, particularly with the use of neutrons, a phenomenon called contrast matching can be used to obtain additional information on the system being investigated.

In neutron scattering the SLD of a region within the system can be changed through isotopic substitution. In small-angle neutron scattering the scattering length of hydrogen is negative and that of deuterium is positive, therefore, one can in many cases match out certain parts of the scattering molecule by using a certain H_2O:D_2O ratio. Sometimes one can also deuterate part of the scattering molecule to make the scattering insensitive to this and thereby effectively see different parts of the molecule dependent on the deuteration.[18] This procedure can increase the information content in a model provided that the data for several similar samples.

Many systems being investigated are not monodisperse and in order to perform model dependent analysis of such systems this must be taken into account. In the case of polydispersity in particle size, this can be included in the modelling. For non-interacting spherical particles the intensity including size polydispersity can be written as

$$I(q) = \Delta\rho^2 \int_0^\infty D(R)V^2(R)P(q,R)dR \qquad 2.26$$

Where $D(R)$ is the number size distribution, $V(R)$ the volume of a particle with radius R and $P(q,R)$ the form factor. To describe the size distribution the Schultz distribution is often used.[19]

Having interacting polydisperse particles in solution, the expression in equation 2.25 is no longer valid and approximations have to be used. Examples of approximation are the decoupling approximation and the average structure factor approximation. In the decoupling approximation the scattering data can be described in a manner similar to that in equation 2.25, however, the structure factor is approximated with an effective structure factor

$$I(q) = nP(q)S_{eff}(q) \tag{2.27}$$

The form factor then becomes an average particle form factor. The effective structure factor is given as[20]

$$S_{eff}(q) = 1 + \beta[S(q) - 1] \tag{2.28}$$

Where β is $\langle A(q)\rangle^2 / \langle A^2(q)\rangle$ and A (q) is the form factor amplitude, giving $P(q) = \langle A^2(q)\rangle$. This approximation is valid for small to moderate polydispersity, of less than 20%.

Using the average structure factor approximation (or the partial structure factor approximation) the scattering intensity can again be described in a manner similar to that in equation 2.25

$$I(q) = nP(q)S_{avg}(q) \tag{2.29}$$

The average structure factor is assumed to be identical to the structure factor of a monodisperse system, with an effective sphere diameter, D_{avg}. The effective diameter is calculated in a way so that the number density of particles and volume fraction in the monodisperse system equals that of the polydisperse system. Therefore, the average particle diameter is calculated as follows

$$D_{avg}{}^{3} = \sum_{i=1}^{p} N_i D_i{}^{3} \Big/ \sum_{i=1}^{p} N_i \qquad 2.30$$

Where p is the number of components in the polydisperse system, N_i the number of particles of the i^{th} size. This approximation allows one to investigate systems with polydispersity greater than 20%, which is the limit of the decoupling approximation.[21]

In the case of anisotropic particles applying a structure factor is complicated, however, for monodisperse systems this may be circumvented by taking the anisotropic particle dimension and converting this to an equivalent sphere radius. This is done by setting the sphere 2nd virial coefficient equal to that of the anisotropic particle.[22] This dimension is then used to calculate the structure factor. This approach, however, becomes more imprecise as the anisotropy of the particle increases. The expression in equation 2.26 does not take particle anisotropy or inter-particle interactions into account. However, it is possible to include size polydispersity of the particles, when these are anisotropic or interacting.[4]

2.3 Small Angle Scattering Models Relevant to this Work

This section describes the actual form and structure factors used in the analysis of the scattering data in this thesis. The first form factor is that of a spherical core-shell particle. A particle is conventionally denoted as a core-shell particle when the scattering length density distribution of the core is significantly different from that of the shell (figure 2.5). The form factor can be written as[23]

$$P_{sph,cs}(q) = \left[\Delta\rho_{shell} V_{total} \Phi(q, r_{total}) - (\Delta\rho_{shell} - \Delta\rho_{core}) V_{in} \Phi(q, r_{in})\right]^2 \qquad 2.31$$

$\Delta\rho_{shell}$ and $\Delta\rho_{core}$ are the excess scattering length density of the shell and the core, respectively, $V_{total} = (4\pi/3)\ r_{total}{}^{3}$ is the volume related to the position of the outer surface r_{total} and $V_{IN} = (4\pi/3)\ r_{in}{}^{3}$ is the volume of the core with radius r_{in}. $\Phi(q, R)$ denotes the form factor amplitude of a spherical particle, which is given by[24]

2.32

$$\Phi(q,r) = \frac{3(\sin(qr) - qr\sin(qr))}{qr}$$

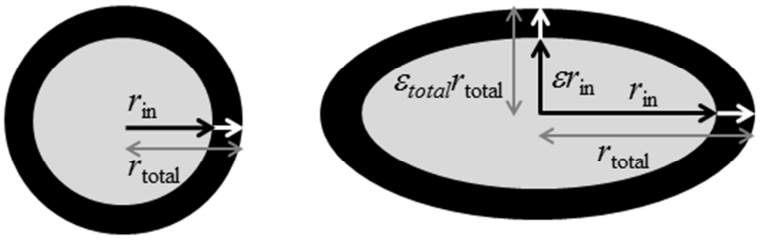

Figure 2.5. Schematic representation of a spherical (left) and an ellipsoidal (right) core-shell particle.

Often the shape of the scattering object cannot be described as a sphere. Therefore, it can be necessary to introduce other geometric shapes. Here, the ellipsoidal shape is described, as this shape is often adopted by micelles. In the ellipsoid of revolution the two axes are related by the aspect ratio, ε. Thus, the length of one axis is related to the other by multiplying it with the aspect ratio, see figure 2.5. The orientationally averaged form factor for a core-shell ellipsoid can be written as[6,25]

$$P_{ell,cs}(q) = \int_0^{\pi/2} \left[\Delta\rho_{shell} V_{tot} \Phi(qR_{tot}) - (\Delta\rho_{shell} - \Delta\rho_{core}) V_{in} \Phi(qR_{in})\right]^2 \sin\phi d\phi \qquad 2.33$$

Where $R_{total} = r_{total}\left(\sin^2\phi + \varepsilon_{total}{}^2 \cos^2\phi\right)^{1/2}$ and $R_{in} = r_{in}\left(\sin^2\phi + \varepsilon^2 \cos^2\phi\right)^{1/2}$, here ϕ is the angle between the scattering vector and the main axis of the ellipsoid. As in the case of a spherical core-shell particle $\Delta\rho_{shell}$ and $\Delta\rho_{core}$ denotes the scattering length density difference for the shell and core, respectively. The volumes are given as follows; $V_{total} = (4\pi/3)\varepsilon_{total} r_{total}^3$ and $V_{in} = (4\pi/3)\varepsilon r_{in}^3$, the first describing the volume of the total ellipsoid and the latter that of the core.

If $\varepsilon_{total} = \varepsilon$ the shell thickness would differ in the two axis directions and if the shell is composed of hydrated head-groups this may not be physical. In that case one would have to use the fact that r_{total}, r_{in} and ε are related by $r_{total} - r_{in} = \varepsilon_{total} r_{total} - \varepsilon r_{in}$ and therefore only three of these parameters can be independently determined.

The particles found in a system may not have a well-defined boundary between the particle and the solvent or in case of core-shell particles between the core and the shell. If this gives a smooth variation in the SLD over the interface it can be modelled by multiplying the form factor amplitudes with $exp(-q^2\sigma^2/2)$, where σ is the width of the interface.[23]

The first and most commonly used structure factor is that of a hard sphere. In many cases the repulsive interaction between particles can be described by introducing hard sphere repulsion between these. The potential will then depend on an effective hard-sphere radius, R_{HS}, and an effective hard-sphere volume fraction, η_{HS}. The structure factor for the hard-sphere repulsion model is given as

$$S(q) = \frac{1}{1 + 24\eta_{HS} G(\kappa)/(\kappa)} \tag{2.34}$$

Where $\kappa = 2qR_{\mathrm{HS}}$. The function $G(\kappa)$ is given by

$$G(\kappa) = \frac{\alpha(\sin\kappa - \kappa\cos\kappa)}{\kappa^2} + \frac{\beta\left(2\kappa\sin\kappa + \left(2-\kappa^2\right)\cos\kappa - 2\right)}{\kappa^3} + \frac{\gamma\left(-\kappa^4\cos\kappa + 4\left[\left(3\kappa^2 - 6\right)\cos\kappa + \left(\kappa^3 - 6\kappa\right)\sin\kappa + 6\right]\right)}{\kappa^5} \tag{2.35}$$

$$\alpha = \frac{\left(1+2\eta_{HS}\right)^2}{\left(1-\eta_{HS}\right)^4},\ \beta = \frac{-6\eta_{HS}\left(1+\eta_{HS}/2\right)^2}{\left(1-\eta_{HS}\right)^4} \text{ and } \gamma = \frac{\eta_{HS}\alpha}{2}.$$

The structure factor is computed using the Percus-Yevick approximation for the closure relation.[13] The hard sphere potential hinders overlay of two particles (figure 2.6a), as two particles cannot occupy the same volume in space at the same point in time.

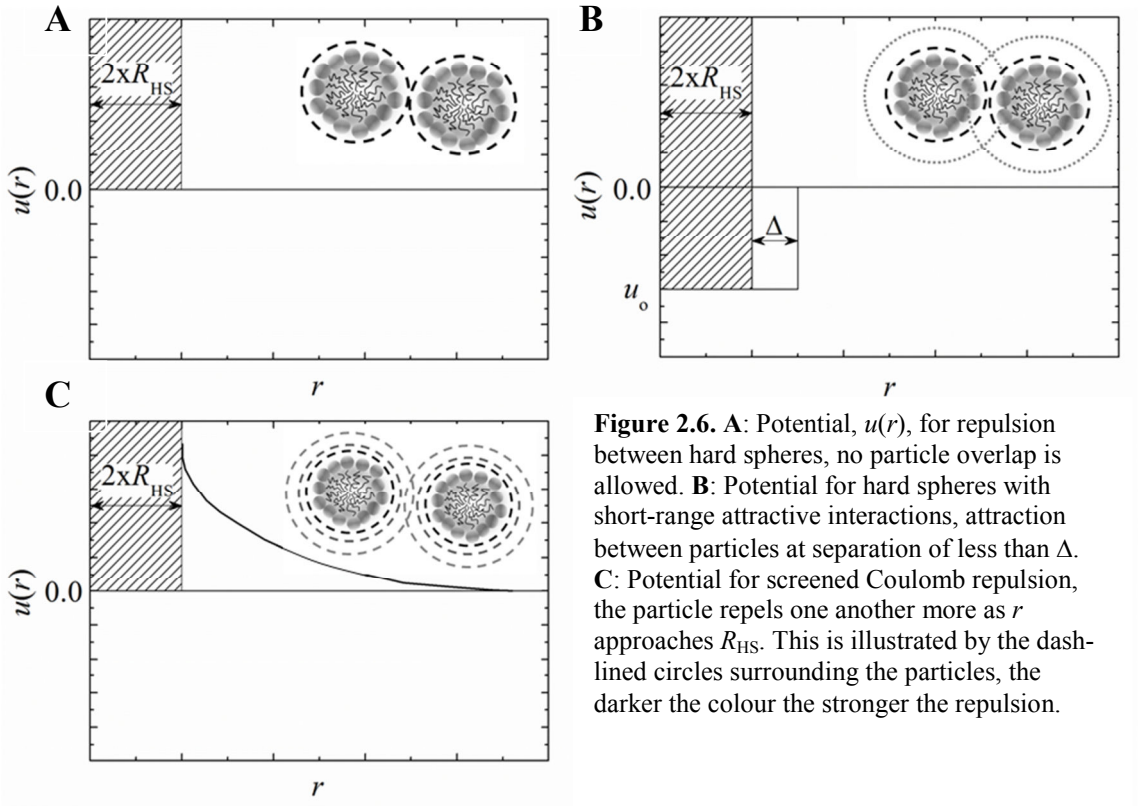

Figure 2.6. A: Potential, $u(r)$, for repulsion between hard spheres, no particle overlap is allowed. **B**: Potential for hard spheres with short-range attractive interactions, attraction between particles at separation of less than Δ. **C**: Potential for screened Coulomb repulsion, the particle repels one another more as r approaches R_{HS}. This is illustrated by the dash-lined circles surrounding the particles, the darker the colour the stronger the repulsion.

If the particles favour interaction with each other the hard sphere structure factor is no longer sufficient. To describe short-ranged attraction, a square-well pair potential can be used. Here the interaction is characterized by a width, Δ, and a depth, u_0, of the potential in addition to an effective hard-sphere radius, R_{HS}, and volume fraction, η_{HS}. In this model the structure factor is given by

$$S(q) = \frac{1}{A^2 + B^2} \qquad 2.36$$

Where the functions A and B are given by

$$A = 1 + 12\eta_{HS}\left(\alpha\frac{\sin\kappa - \kappa\cos\kappa}{\kappa^3} + \beta\frac{1-\cos\kappa}{\kappa^2} - \frac{\lambda\sin\kappa}{12\kappa}\right) \qquad 2.37$$

And

$$B = 12\eta_{HS}\left(\alpha\frac{\kappa^2/2 - \kappa\sin\kappa + 1 - \cos\kappa}{\kappa^3} + \beta\frac{\kappa - \sin\kappa}{\kappa^2} - \frac{\lambda(1-\cos\kappa)}{12\kappa}\right) \qquad 2.38$$

Again $\kappa = 2qR_{HS}$, as for the hard-sphere structure factor. Furthermore, the parameters α, β, γ and μ in A and B are defined as follows

$$\alpha = \frac{1 + 2\eta_{HS} - \mu}{(1-\eta_{HS})^2} \quad : \quad \beta = \frac{-3\eta_{HS} - \mu}{2(1-\eta_{HS})^2}; \qquad 2.39$$

;

$$\lambda = \frac{(1-\eta_{HS}/2)(\tau + \eta_{HS}^2/(1-\eta_{HS}) + \eta_{HS}/12)}{(1-\eta_{HS})^2} \quad :$$
$$\mu = \lambda\eta_{HS}(1-\eta_{HS}) \qquad 2.40$$

Similar to the hard sphere model this structure factor is calculated with the Percus-Yevick approximation for the closure relation. This model was originally introduced by Baxter in 1968[26], later in 1991 Menon *et al.* suggested a procedure using an approximate and explicit expression for the interaction parameter, τ, to simplify the fitting procedure.[27] Here the interaction parameter is

$$\tau = \left(12\frac{\Delta}{(\Delta + 2R_{HS})}\right)^{-1}\exp(u_0/kT) \qquad 2.41$$

In this structure factor the two particles are again excluded from overlay by the hard sphere potential, as in the hard sphere structure factor. Additionally, an attractive force is introduced between the particles, by a square-well pair potential (figure 2.6b), effectively inducing cluster formation when the particles are in the vicinity of another particle.

Another way of describing interparticle interactions is to use a two Yukawa potential. This allows one to introduce both an attractive and repulsive part of varying length to the interactions between the particles. The potential is described as

$$\frac{V(r)}{k_B T} = \begin{cases} \infty & (0 < r < 1) \\ -K_1 \dfrac{exp\left(-Z_1(r-1)\right)}{r} + K_2 \dfrac{exp\left(-Z_2(r-1)\right)}{r} \end{cases} \qquad 2.42$$

Where r, which is that of the hard core, is rescaled with the particle diameter, d_{part}, $r = r/d_{\text{part}}$, Z_1 and Z_2 are decay factors describing the range of the potential and K_1 and K_2 are scaling factors describing the strength of the potential. $K_1 > 0$ and gives the attractive part of the interaction and $K_2 < 0$ giving the repulsive part.[28] This structure factor can be calculated using the Mean-Spherical Approximation (MSA).[29] This structure factor gives interparticle interaction, which can be of long range, and where the interaction decays exponentially with r.

If the particles are charged neither the hard sphere nor the sticky hard sphere structure factor is sufficient to describe the data. In this case a screened Coulomb potential can be introduced between particles in addition to the hard sphere repulsion. The potential is described as follows for $r > R_{\text{HS}}$

$$V(r) = \frac{C_B Z^2}{\left(1 + \kappa R_{HS}\right)^2} \frac{\exp\left(-\kappa\{r - 2R_{HS}\}\right)}{r} \qquad 2.43$$

$C_B = e^2/(4\pi\varepsilon)$, where e is the elementary charge, ε the permittivity of the solvent, κ^{-1} the Debye screening length and Z the number of charges per particle.

The Debye screening length is determined by the concentration and charge of the ions in solution.[30] For large to intermediate particle concentrations the structure factor can be calculated in the MSA.[29] However, at low particle concentration the structure factor should be calculated in the Rescaled MSA (RMSA), where the hard sphere radius is rescaled to obtain physically feasible results.[31]

Using the screened Coulomb potential in addition to the hard sphere potential the particles repel each other above $r = 2R_{\text{HS}}$ by a screened coulomb potential (figure 2.6c), which decays exponentially with r. The repulsion between the particles, thus, becomes stronger the closer these are to each other, until the total repulsion is reached at the hard sphere radius.

2.4 Small Angle Scattering Instrumentation

The small-angle X-ray scattering experiments presented in this work has been performed on a laboratory based facility, a NanoSTAR camera which uses pinhole geometry. The NanoSTAR camera from Bruker AXS is situated in the Chemistry Department at Aarhus University in Denmark. The instrument is optimized for solution scattering and for a more in-depth description than given here, the reader is referred to Pedersen 2004.[32]

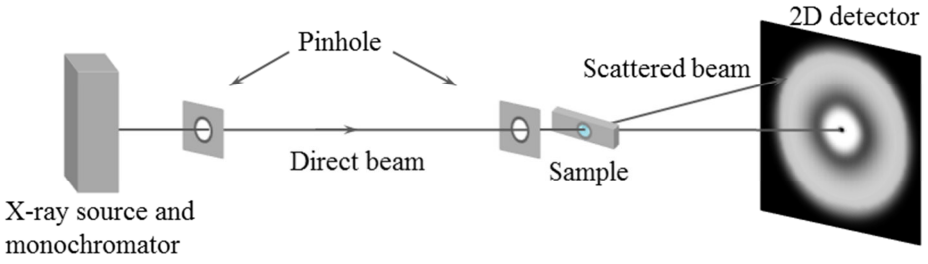

Figure 2.7. Schematic representation of the NanoSTAR setup, where the X-rays are generated with a rotating anode and the beam is reflected and focused by Göbel mirrors and two defining pinholes. Finally, the scattered beam is detected on a two-dimensional gas detector.

The X-rays are generated by a rotating copper anode, with K_α radiation of $\lambda_{K_\alpha} = 1.54$ Å. Two perpendicular Göbel mirrors reflect and focus the beam, before it is passed through two pinholes, which shape and define the beam, as seen from figure 2.7. The second slit does not create any parasitic scattering, as it is made from a single crystal, and thus no further definition of the beam is necessary before it hits the sample. The direct beam is blocked by a semi-transparent beam stop, allowing the intensity to be monitored in situ.

The scattered beam is detected on a two-dimensional position sensitive gas detector (HiSTAR). Here, the scattered photons ionize the gas atoms and the electrons from the ionization process are accelerated towards the anode grid. Close to the anode grid the electrons ionize other atoms and the signal is thus enhanced. The signal from the electrons on the perpendicular anode and cathode grids is used to determine the position of the detected event.[33] To minimise unwanted effects from scattering of air and windows the camera has one integrated vacuum. The sample-to-detector distance gives a q-range from 0.01 to 0.35 Å^{-1} in the standard setup and this can be changed to access smaller or larger q if necessary. The measurements are performed in reusable home-build quartz capillaries with an inner diameter of approximately 2

mm and a wall thickness of 0.01 mm. The sample environment can be temperature controlled in a range from 1 to 90 °C, by a Peltier element (Anton Paar). Water was used as a standard to convert the instrumental intensities to absolute intensities.[32] The scattering intensity was corrected for collimation, wavelength and detector resolution.[34]

In addition to the X-ray scattering experiments performed on laboratory based facilities, small-angle neutron scattering experiment have also been performed. The small-angle neutron scattering experiments presented in this work have been performed at two large-scale facilities, one being the pulsed source facility ISIS and the other the reactor facility ILL. At ISIS the two beam-lines SANS2D and LOQ have been used and at the ILL the beam-line D11 was used. In all cases for small angle neutron scattering measurements, sample solutions were held in 1mm thick quartz Hellma cells. Either double stopper cells (~23 mm wide) or single stopper cells (12 mm wide) were used, holding sample volumes of 0.6 ml or 0.3 ml respectively. In all cases an appropriate solvent background was subtracted from the data prior to further analysis.

The ILL high-flux reactor is a cold source giving a polychromatic neutron beam.[35,36] At the D11 beam-line[37] the neutron beam is monochromated by a helical slot velocity selector, giving $\Delta\lambda/\lambda$ = 9%. A range of neutron guides then collimate the neutrons before the beam interacts with the sample. Neutrons with wavelengths from 4.5 to 40 Å can be obtained. The scattered neutrons are detected on a ^{3}H gas detector (CERCA), which is placed in an evacuated detector tank. The detector can be moved in the detector tank in order to obtain sample-to-detector distances from 1.2 to 39 m to cover different *q*-ranges. This allows one to obtain *q*-vectors in the range from 0.0003 to 1 Å^{-1}. Data was corrected for instrumental factors and normalised to absolute intensities in cm^{-1} using water as a secondary calibration standard.

The LOQ beam-line at ISIS is situated at Target Station one (TS-1).[38] The neutrons are generated by a pulsed source, giving a time-of-flight type instrument. At the beam-line the beam is collimated using two aperture selectors, which allow the apertures to be varied, and a chopper. Furthermore, a supermirror bender, placed at the start of the collimation path, removes short wavelength neutrons and a frame overlap mirror, situated between the chopper and the second aperture selector further defines the beam. This gives a $\Delta\lambda/\lambda$ between 2.6 and 2 %, dependent on choice of wavelength. Neutrons with a wavelength between 2.2 and 10 Å can be obtained. The scattered neutrons are detected on a ^{3}He-CF_4 gas detector (ORDELA), kept in an evacuated tank. The detector is mounted at a fixed position 4 m from the sample position. This setup gives a measurable *q*-range of 0.006 to 0.24 Å^{-1}. SANS data was reduced to one dimension by radial averaging using the Colette program and corrected for the solvent background, detector efficiency and normalized to an absolute scale using a polymer standard.[39]

2.5 Reflectometry and Grazing-Incidence Small-Angle Scattering

2.5.1 Reflectometry

Reflectometry is a technique used to probe surfaces in a direction normal to the surfaces, *e.g.* films typically with a thickness between 0.1 nm-100 μm at a surface. The geometry of a reflectometry experiment is sketched in figure 2.8, where the incoming and outgoing angle are equal, *i.e.* $\alpha_i = \alpha_f$. In a specular reflectivity experiment, the beam reflections are only collected as a function of the z-component of the scattering vector q

$$q_z = 4\pi \sin(\alpha_i) / \lambda \qquad 2.44$$

Where λ is the wavelength of the X-ray and α_i the incoming angle.[40]

The reflectivity measured is dependent on the scattering length density profile perpendicular to the interface. In a medium without layers this would be described by a continuously varying function. However, when layers are present close to the interface this can (often) be approximately described by a layered model. In such a model the scattering length density of the layers, ρ_n, the layer thickness, d_{on}, and the roughness $\sigma_{n,n+1}$ are the parameters used to describe the data.[40,41] In a film the layers are normally not smooth but have a certain roughness, if this roughness is correlated this will give rise to interference fringes in the reflectivity data, also known as Kiessig fringes.[42]

The theory for modelling the specular reflectivity data using a layer model was developed in the 1950's by Parratt[43] and the basic idea is outlined in the following. However, the approach outlined here is different from that developed by Parratt, though it gives identical results. The method is based on Abeles matrix method, which is the method implemented in the program package MOTOFIT[41] implemented in Igor Pro (Wavemetrics).

The scattering vector changes inside the layered medium and the scattering vector in the n^{th} layer can be described as

$$q_n = \sqrt{\left(k_i^2 - 4\pi\{\rho_n - \rho_0\}\right)} \qquad 2.45$$

Where $k_i = 2\pi/\lambda$ and ρ_n and ρ_0 are the scattering length densities of the medium at the n^{th} and 0^{th} layer. The reflectivity from a medium having only one interface (the surface) can be calculated as the Fresnel reflectivity

$$R_F = r^2 = \left(\frac{q_0 - q_1}{q_0 + q_1} \right)^2 \qquad 2.46$$

Here r is the Fresnel reflection coefficient. It should be noted that the reflectivity will decay as q^{-4} at large scattering vectors.[44]

This can be expanded to account for multiple layers near the surface, which is the case for thin films. One can write the generalised Fresnel reflectivity coefficient between layer n and n+1 (see figure 2.8) as

$$r_{n,n+1} = \frac{q_n - q_{n+1}}{q_n + q_{n+1}} \exp\left(-2 q_n q_{n+1} \sigma_{n,n+1}^2\right) \qquad 2.47$$

Here a factor of exp ($-2q_n q_{n+1} \sigma_{n,\,n+1}{}^2$) is included to account for the roughness of the interfaces.

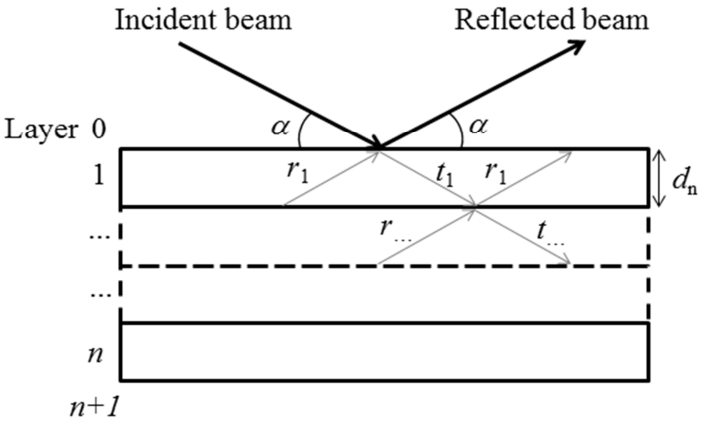

Figure 2.8. Schematic representation of specular reflectivity of a layered medium, where the layers themselves will give rise to reflected waves.

The layers have a finite thickness and in order to take this into account a phase factor can be defined, $\beta = q_n d_n$, which depends on the layer thickness, d_n. The reflectivity profile of a multi-layer film can be calculated by calculating a characteristic matrix for each layer, c_n, and defining a matrix, M, summing up all c_n. These are given in equation 2.48 and 2.49.

$$c_n = \begin{bmatrix} \exp\beta_n & r_n \exp(\beta_n) \\ r_n \exp(-\beta) & \exp(-\beta) \end{bmatrix} \qquad 2.48$$

$$M = \prod_{n=0}^{n} c_n \qquad 2.49$$

Finally, the reflectivity is computed as

$$R = \left| \frac{M_{11}}{M_{12}} \right|^2 \qquad 2.50$$

One can, in many cases, retrieve an optimal amount of information for the specular reflectivity data by using this method in spite of the limited information content in the data.[41]

2.5.2 Grazing-Incidence Small-Angle Scattering

Grazing-Incidence Small-Angle Scattering (GISAS) is used to study surfaces structures, similar to specular reflectivity. This technique is well suited for characterising the lateral structure and surface roughness of the surface layer. In essence the technique it is a combination of small-angle scattering and grazing-incidence diffraction, where the scattering events are similar to those described preciously in this chapter for small-angle scattering.

Contrary, to specular reflectivity the scattering vector, $\boldsymbol{q}$ = (q_x, *qy, qz*), depends on the all of the *x*, *y* and *z* components and not just the *z*-component. However, this also makes the data interpretation more complicated than for specular reflectivity.

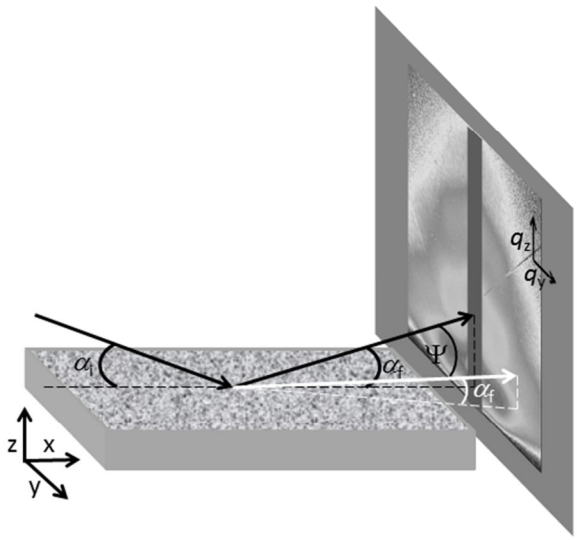

Figure 2.9. Schematic representation of a reflectometry and a GISAS experiment. The reflectometry experiment is characterised by the incoming and scattered angle only, α_i and α_f, respectively. Thus only specular reflections are observed (these are blocked by the vertical beam-stop in this figure). Additionally, GISAS is characterised by an out-of-plane angle Ψ.

Defining the scattering event as in figure 2.9, the components of the scattering vector, *q*, become

$$q_x = (2\pi/\lambda)\{\cos(\Psi)\cos(\alpha_f) - \cos(\alpha_i)\}$$

$$q_y = (2\pi/\lambda)\{\sin(\Psi)\cos(\alpha_f)\} \qquad 2.51$$

$$q_z = (2\pi/\lambda)\{\sin(\alpha_i) + \sin(\alpha_f)\}$$

Where λ is the wavelength, Ψ the out-of plane angle, α_i and α_f the incoming and scattered angle, respectively.

The scattering considered in GISAS is the scattering in the region of total external reflection. The critical angle, $\alpha_c \approx \sqrt{2\delta}$, is the smallest angle where the ray is still refracted. Below the critical angle, total external reflection is obtained and the incoming beam is completely reflected by the sample. The critical angle is a system specific quantity, where δ is the dispersion part of the refractive index. The scattering events taking place at the interface include the normal scattering events, described in the Born approximation, though additionally scattering events followed or preceded by a reflection must also be taken into account. These events are considered in the distorted-wave Born approximation (DWBA). Theoretically describing the scattering intensity arising from this kind of scattering experiment is a highly complex task and is normally only undertaken if the system has a well-known morphology, however, such systems are rarely studied. Thus, different approximations are often applied to simplify the data analysis.[45,46]

In the analysis of GISAS data some features are often encountered, one of these are the Yoneda peak, which is an increase in intensity observed when either the incoming or outgoing angle is equal to the critical angle of the material.[47] Another feature often seen in GISAS data is fringes (or modulations). These can arise from two phenomena; either due to correlated roughness of the surfaces (Kiessig fringes), as described for reflectivity, or by two interfaces separated by a distance which allows these to act as guides for the waves (dynamic fringes).[42,48] From the position of the Kiessig fringes one can retrieve the separation, d_{corr}, of the correlated interfaces, as these fulfil a one-dimensional Bragg law in the q_z-axis

$$q_z = \frac{2\pi}{d_{corr}} \qquad 2.52$$

Bragg peak analysis can also be applied as a simplified way of analysing GISAS data with respect to the internal structure of the film. In structures like lamellar stacks, hexagonal packed cylinders or cubic packed spherical micelles a definite relationship between the Bragg peaks arises and this can be used to determine the internal film structure. However, in doing this one has to note that the normal Bragg peak analysis does not take reflection and refraction effects into account. To account for this the Bragg equation has to be modified, this is done by combining Bragg's law with Snell's laws, which makes it possible to take reflection and refraction into account

and determine the q_z dependence. However, in many cases structural information is retrieved from the GISAS data without using this correction.[45,46]

Another way of analysing GISAS data is to use a simplification, known as the effective surface approximation, where the scattering intensity can be written as[49]

$$I(\bar{q}) = \frac{A\pi^2}{\lambda^4}\left(1-n^2\right)^2 \left|T_i\right|^2 \left|T_f\right|^2 F(\bar{q}) \propto F(\bar{q}) \qquad 2.53$$

If $\alpha_i >> \alpha_c$, q_z is constant and the distorted-wave Born approximation is used.

Here A denotes the illuminated area, λ the wavelength, n the refractive index, T_i and T_f the Fresnel transmission functions and $F(\bar{q})$ the diffuse scattering factor. In the effective surface approximation the data is only analysed in the q_y direction and q_z is kept constant. One should note that this restricts the analysis to the lateral structure in the film. However, this simplifies the data analysis significantly as the Fresnel transmission functions essentially become scaling factors, because α_i and α_f are constant. Using the effective surface approximation the quantity probed is the diffuse scattering factor, which can be approximated by[50]

$$F(\bar{q}) \propto nP(\bar{q})S(\bar{q}) \qquad 2.54$$

When the particles are homogeneous, centrosymmetric and randomly orientated in the sample. Here, N is the number density of particles, $P(\bar{q})$ the particle form factor and $S(\bar{q})$ the structure factor. This is analogous to small-angle scattering and the intensity will be dominated by the Fourier transform of the height-height correlation function of an effective surface.

2.5.3 Identification of concentrated phases: Liquid Crystal Determination

It has been discussed previously how to model small angle scattering data from concentrated surfactant phases in the bulk. In the systems within this work the surfactant volume fraction is large enough so that inter-particle interaction becomes significant. However, in the reflectometry and GISAXS data, the surfactant and polymer volume fractions are often large enough so that the surfactant-polymer

aggregates arrange on to a regular lattice in real space for reasons discussed in chapter 1. The position of the wavevector intensity peaks in reciprocal space is related to the structural spacing of the real space structure.

Lamellar structures are indicated by the scattered intensity exhibiting equally spaced peaks. These are related to the real space dimensions of the lamellar phase by

$$q_h = \frac{2\pi h}{a} \qquad 2.55$$

Where q is the value of the reciprocal space reflection, h indicates the index of the reflection and a is the lamellar unit cell (or d-spacing)

For a columnar 2D-hexagonal *p6mm* the observed wavevector peaks positions should follow a $\sqrt{1}:\sqrt{3}:\sqrt{4}$ ratio relationship in the q-range investigated. This relationship arises from the real space dimension of the *p6mm* unit cell. The relationship between the dimensions of the *p6mm* unit cell and the reflections observed in reciprocal space are described by equation 2.56. From equation 2.56 it can be seen that the predicted peaks relationship of $\sqrt{1}:\sqrt{3}:\sqrt{4}$ would have an *hk* assignment of 10:11:20

$$q_{hk} = \frac{4\pi}{a}\sqrt{\frac{h^2 + hk + k^2}{3}} \qquad 2.56$$

Where q is the value of the reciprocal space reflection, h indicates a reflection that arises from a crystallographic plane described by a distance and direction along one the axes of the *p6mm* primitive unit cell, k indicates a reflection that arises from a crystallographic plane described by a distance and direction along the other axis that originates from the vertices of the *p6mm* primitive unit cell, and a is the unit cell size in real space.

Equation 2.56 is related to the *p6mm* unit cell dimension by basic trigonometry. The *p6mm* primitive unit cell is a parallelogram with an obtuse internal angle of 120º (Figure 2.10Ai). The origin of the *hk* assignments to crystallographic planes are highlighted in figure 2.10 Aii. The primitive unit cell of the *p6mm* phase is related to

the face centred rectangular (FCR) unit cell (Figure 2.10 Aiii). Here the FCR unit cell is defined by a rectangle where the short side is equivalent to the defining dimension, a, of the primitive unit cell and the long side, b, is equal to $\boldsymbol{b = a\sqrt{3}}$. The hexagonal shape of the phase may be visualised by drawing a hexagon along the edges of the primitive unit cells that constitute the FCR unit cell (Figure 2.10 Aiv).

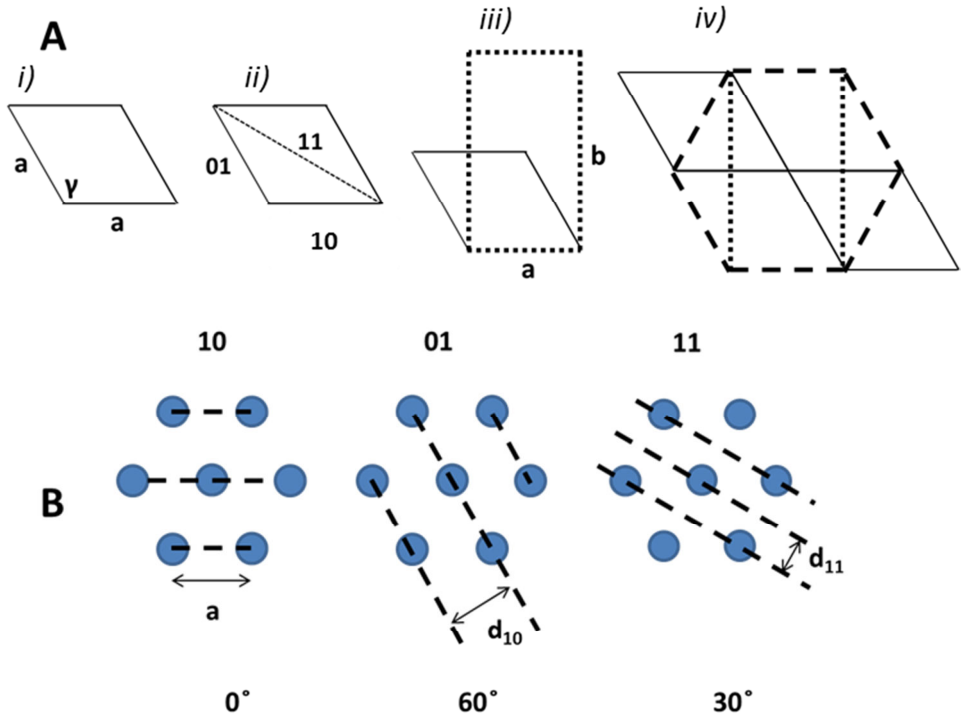

Figure 2.10 Diagram explaining the features of a *p6mm* unit cell. **A:** Representation of a primitive unit cell of the *p6mm* space group (*far left)*. Note that it is a parallelogram with side length *a* and obtuse internal angle of γ=120˚. The directions of the lower order crystallographic planes are noted (*left*) on the primitive unit cell. The spatial relationship between the primitive unit cell and the *p6mm* face centred unit cell is represented (*right*); note that the length of $\boldsymbol{b = a\sqrt{3}}$ from simple geometric considerations. The *p6mm* hexagonal lattice (*far right*) is represented formed from tessellation of the primitive unit cell together with superimposition of the face centred unit cell. **B:** Representation of the *p6mm* unit cell as scattering points placed on the hexagonal lattice where the lattice is orientated with the 10 plane parallel to the substrate. The occurrence of the scattering planes from vectors along the *hk* directions of the primitive unit cell show real space distances resultant in diffraction peaks in reciprocal space, plus it explains the angles of the diffraction peaks normal to the scattering planes which scatter away from the q_z axis *i.e.* away from the film normal.

For a cubic phase, the wavevector peak positions are related to the cubit unit cell by

$$q_{hkl} = 2\pi \frac{\sqrt{h^2 + k^2 + l^2}}{a} \quad 2.57$$

Where q is the value of the wavevector peak; h, k and l are the index of the crystallographic planes and a is the unit cell size.

2.5.4 Instrumentation

The reflectometry and GISAS experiments in this work have been performed at several large scale facilities, as both X-rays and neutrons have been utilised. The experiments involving the use of neutron beams were performed at ISIS and at ILL. Following this the X-ray experiments were carried out at the ESRF and Diamond. For experiments studying film formation at the air-solution interface the solutions were held in a Teflon trough 40×150×5mm in dimensions. For the X-ray experiments the trough was held on a copper block, temperature controlled to 28°C using a circulating water bath. For neutron experiments the trough was placed in an open temperature controlled sample changer using a Eurotherm temperature controller. In all cases the troughs were open to the ambient atmosphere and the relative humidity was measured but not controlled. Humidity was in the range of 50 to 75% when the experiments were performed. Solid spray coated films were deposited on silicon wafers, mounted on a goniometer on the beamline, in ambient surroundings.

The reflectometry beam-line CRISP at ISIS is found at TS-1.[51,52] The neutrons are generated with a pulsed source, giving a time-of-flight type instrument. The beam-line is collimated using a chopper and two guide/collimation sections. Neutrons with large wavelengths are removed using frame overlap mirrors. This gives a wavelength range of 0.5 - 6.5 Å. The instrument was operated in unpolarised mode to maximise the flux and the TOF technique allows for a fixed geometry with constant q resolution. The reflected neutrons are detected on a ^{3}He gas point detector, which was placed in the scattering plane. Therefore, the neutron intensity is integrated over q_y, as q_x is in the scattering plane. Dependent on the incident angle information can be collected at q-vectors between 0.006 and 1.0 Å^{-1}. The data was reduced using scripts written in opengenie to bin the data according to the resolution of the instrumental setup plus the scaling factor calculated from the reflectivity of pure D_2O.

Turning to X-rays, the beam-line I07 at Diamond was used. Diamond is a third generation synchrotron delivering a high brilliance polychromatic X-ray beam. The beam-line I07 is equipped to perform reflectometry and GISAXS. The beam-line has a cryo-cooled undulator, double crystal monochromator and two focusing mirrors ensuring that a well-defined monochromatic beam hits the sample. The instrument is equipped with a flight tube for GISAXS and a diffractometer for reflectometry experiments, which are easily interchangeable. Here the X-rays are detected by a 2D 1K Pilatus detector (GISAXS) or a point detector (XRR).

Another X-ray beam-line used was at the ESRF, which is a third generation synchrotron giving a high brilliance x-ray beam. The ID10B beam-line[53] is suited for reflectivity and GISAXS experiments, where both a vertical and a horizontal scattering geometry can be applied. The polychromatic beam is monochromated by crystals and guided by a double mirror to the sample position. After interaction with the sample the X-rays are detected on a linear detector with 1024 pixels in the q_z plane. This detector is controlled by a goniometer to record scattering outside of the q_z plane, which can vary dependent on experiment.

2.6 Complementary techniques

2.6.1 Brewster angle microscopy

Reflections at an interface depend on the polarisation, p, of the incident light and the angle of incidence, θ. At an interface where the difference in the refractive indices of different media is large normal to the interface, there is no reflectivity at a certain value of p and θ. This is known as the Brewster angle, θ_B. The Brewster angle for an interface is calculated using equation 2.58[54]

$$\tan\theta_B = \frac{n_2}{n_1} \qquad 2.58$$

Where θ_B is the Brewster angle, n_1 and n_2 are the refractive indices of the interfacial media.

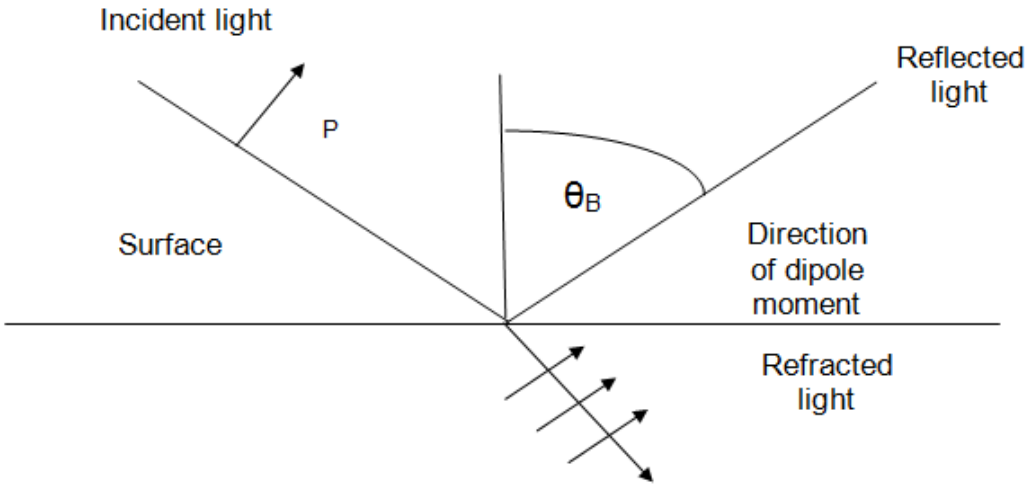

Figure 2.11. Schematic illustrating Brewster Angle Microscopy.

At the Brewster angle, the polarised incident light refracts into the media, as the electric dipole portion of the polarised refracted light is oscillating parallel to the angle of reflection, no light is propagated into the angle of reflection (figure 2.11). When an air-solution interface has species adsorbed at the interface they can be visualised in the angle of reflection as the layer causes a change in the refractive index of the interface, which changes the Brewster angle from 53° (the Brewster angle for and air-water interface).

2.6.2 Force tensitometry

The surface tension, γ, of an interface may be used to determine the CMC of a surfactant in solution. After a certain concentration, added surfactant to the solution contributes to the formation of micelles and do not absorb further to the surface. After this point, the surface tension tends to not decrease further upon addition of surfactant. Determination of the surface excess of a surfactant, Γ, which is the ratio of surfactant at the surface compared to the maximum amount available at the interface allows calculation of the CMC.

The surface excess and surface tension are related by the Gibbs adsorption equation

$$\Gamma = -\frac{1}{RT}\frac{d\gamma}{dC} \qquad 2.59$$

Where R is the real gas constant, T is the temperature and C is the bulk concentration.

It can be seen that the surface excess is proportional to the gradient of the surface tension as a function of the bulk concentration. Determination of the surface excess also allows calculation of the area per surfactant and the free energy of adsorption and micellization, which is discussed in detail in the results section.

Another complementary technique used is force tensitometry. The surface tension of a solution can be determined by use of a force tensitometer. The results presented in this work were obtained by using the Du Noüy ring method and the Wilhlemy plate method. In the Du Noüy ring method a platinum ring is submerged in the liquid and retracted slowly while the force is measured (figure 2.12a). The force it takes to break the interaction between the ring and the liquid is determined. This force is related to the surface tension, γ, of the solution, by $\gamma = f_{\max}/2L$, where $f_{\max}$ is the maximum force exerted before the liquid-ring interaction breaks, where L is the mean circumference of the ring. The factor of two is included to account for the fact that there are effectively two surface areas in the measurement, being the inner and the outer side of the ring.[55,56]

The finite diameter of the ring also gives a contribution to the volume of liquid lifted by the ring, because one side of the ring is in close proximity to the other side (figure 2.12b). This effect should be taken into account, as it affects the accuracy with which the surface tension can be determined and theory describing this effect have been developed.[57] The measurements were performed on a Sigma 701 force tensitometer from Attention.

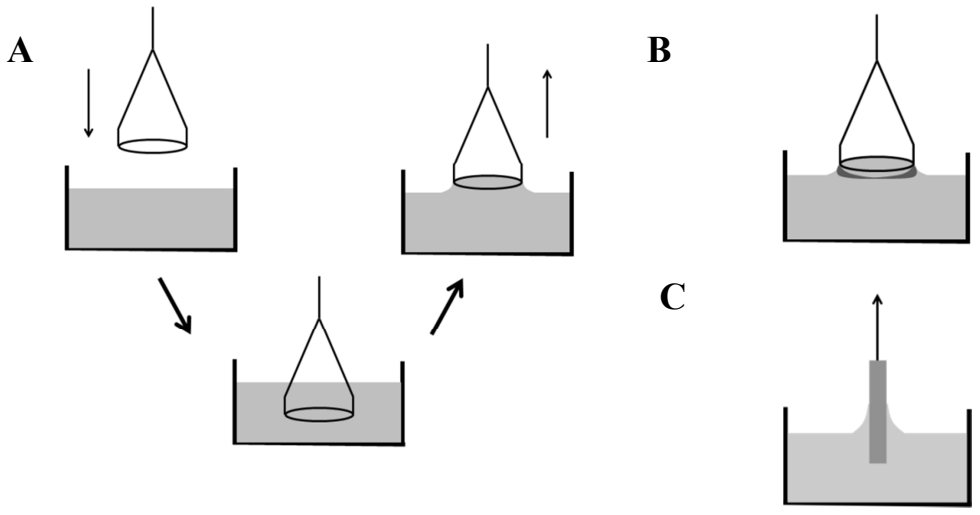

Figure 2.12. **A**: Schematic representations of a surface tension measurement performed by use of a Du Noüy ring. **B**: Wall effects, dark grey, arising from one

side of the ring being in close proximity to the other side which should be accounted for in the measurement. **C**: Schematic representation of the Wilhelmy plate method.

In the Wilhelmy plate method the force, f, exerted on a plate of platinum by the liquid is measured. The surface tension, γ, is related to the force, f, as $\gamma = f/(l\cos(\theta))$, where θ is the angle between the liquid and the plate and l is the wetted perimeter.

2.6.3 Densitometry

Characterising a system using small-angle scattering techniques can give important information on the behaviour of a system. However, as explained previously, an accurate value for the SLD of a molecule is necessary to decrease the variables in a structural model. Determination of the molecular density allows calculation of the molecular volume. The molecular volume can then be used to calculate the SLD, as described in section 2.1.

The density of a liquid sample can be determined by use of the oscillating U-tube technique. The period of oscillation, T, is related to the density, because $T = 2\pi\sqrt{(\rho V)/k}$, where ρ is the density of the system, V the system volume and k the force constant. By oscillating the U-tube and determine its fundamental frequency, f, which is a function of the system mass, the density of the sample can be determined, as shown in figure 2.13. However, effectively the sample will dampen the oscillations, $f = (1/2\pi)\sqrt{(k/m) - (b^2/4m^2)}$, where b is the strength of the dampening. Thus the relation is only valid for samples with a low viscosity where the dampening effects can be neglected.[58,59]

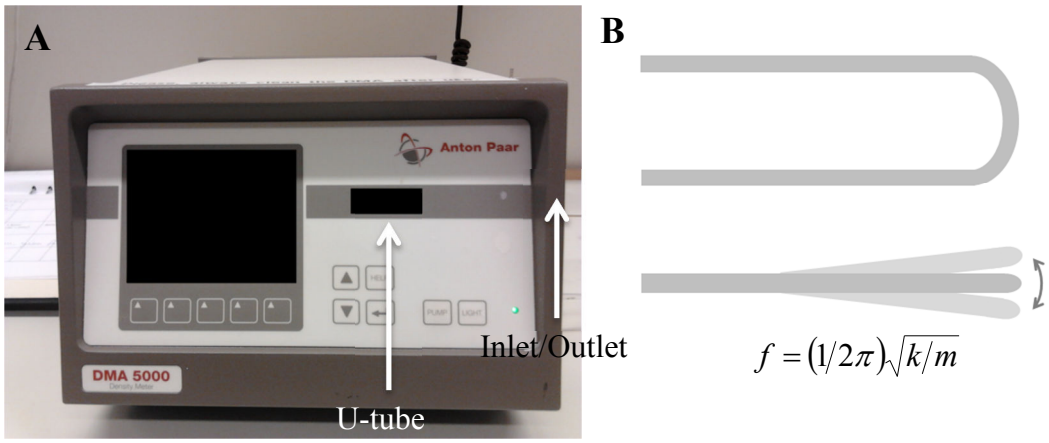

Figure 2.13. A: Densitometer from Anton Paar. **B**: Schematic representation of a U-tube, which is filled with the sample and oscillated during the measurements. When the U-tube is oscillated, indicated by the arrow, it has a frequency, which is a function of the system mass and hence, the density of the system.

From the density measurements the apparent partial specific volume, v_{solute}, can be obtained. The term "apparent" is used for the volume, as the volume obtained for the measurement includes the changes in the solvent molecules close to the solute.[58]

From the apparent partial specific volume one can obtain the apparent partial specific density of the solute. In small-angle scattering this is an important quantity since this together with the density of the solvent can be used to calculate the scattering length density of the scattering molecule, which is necessary for analysing the scattering data on absolute intensity scale.[2,58]

The solution density measurements were performed on a DMA5000 densitometer from Anton Paar situated at University of Aarhus in Denmark. At ambient temperature the accuracy of measurement is 0.000020 g/cm^3, therefore it is estimated that the apparent partial specific volumes have an accuracy of about 0.1-0.3 % due to the relatively low concentration of polymer in the solutions measured in this work.

2.7 References

(1) Glatter, O. K. O. *Small angle X-ray scattering*; Academic press: London [etc.], **1983**.

(2) Lindner, P.; Zemb, T. *Neutrons, X-rays, and light: scattering methods applied to soft condensed matter*; Elsevier Amsterdam, **2002**.

(3) *Neutrons, X-rays and Light: Scattering Methods Applied to Soft Condensed Matter. Chapter 3: General Theorems in Small-Angle Scattering, p. 49-71*; Lindner, P.; Zemb, T., Eds.; North-Holland, Elsvier, **2002**.

(4) *Neutrons, X-rays and Light: Scattering Methods Applied to Soft Condensed Matter. Chapter 16: Modelling of Small-Angle Scattering Data from Colloids and Polymer Systems, p. 391-420*; Lindner, P.; Zemb, T., Eds.; North-Holland, Elsvier, **2002**.

(5) Pedersen, J. S. *Advances in Colloid and Interface Science* **1997**, *70*, 171.

(6) Guinier, A. *Annales de Physique (Paris)* **1939**, *16*, 161.

(7) *Small Angle X-ray Scattering. Chapter 2: General theory. p. 17-52*; Glatter, O.; Kratky, O., Eds.; Academic press, **1982**.

(8) *Small Angle X-ray Scattering. Chapter 4: Data treatment. p. 119-166*; Glatter, O.; Kratky, O., Eds.; Academic press, **1982**.

(9) *Neutrons, X-rays and Light: Scattering Methods Applied to Soft Condensed Matter. Chapter 5: Fourier Transformation and Deconvolution, p. 103-126*; Lindner, P.; Zemb, T., Eds.; North-Holland, Elsvier, **2002**.

(10) *Small Angle X-ray Scattering. Chapter 5: Interpretation. p. 167-196*; Glatter, O.; Kratky, O., Eds.; Academic press, **1982**.

(11) Glatter, O. *Journal of Applied Crystallography* **1977**, *10*, 415.

(12) *Neutrons, X-rays and Light: Scattering Methods Applied to Soft Condensed Matter. Chapter 4: The inverse scattering problem in Small-Angle Scattering, p. 73-102*; Lindner, P.; Zemb, T., Eds.; North-Holland, Elsvier, **2002**.

(13) Kinning, D. J.; Thomas, E. L. *Macromolecules* **1984**, *17*, 1712.

(14) Brunner-Popela, J.; Glatter, O. *Journal of Applied Crystallography* **1997**, *30*, 431.

(15) Weyerich, B.; Brunner-Popela, J.; Glatter, O. *Journal of Applied Crystallography* **1999**, *32*, 197.

(16) SHANNON, C. E.; WEAVER, W. *The Mathematical Theory of Communication*; Third ed.; Urbana, IL: University of Illinois Press., **1949**.

(17) Moore, P. *Journal of Applied Crystallography* **1980**, *13*, 168.

(18) Jacrot, B. *Reports on Progress in Physics* **1976**, *39*, 911.

(19) Schulz, G. V. *Z. Physical Chemistry B-Chem. Elem. Aufbau. Mater.* **1939**, *43*, 25.

(20) Kotlarchyk, M.; Chen, S.-H. *The Journal of Chemical Physics* **1983**, *79*, 2461.

(21) Chen, S.-H.; Lin, T.-L. In *Methods in Experimental Physics*; David, L. P., Kurt, S., Eds.; Academic Press: **1987**; Vol. Volume 23, Part B, p 489.

(22) Isihara, A. *The Journal of Chemical Physics* **1950**, *18*, 1446.

(23) Pedersen, J. S.; Svaneborg, C. *Current Opinion in Colloid & Interface Science* **2002**, *7*, 158.

(24) Rayleigh, L. *Proceedings of the Royal Society of London. Series A, Containing Papers of a Mathematical and Physical Character* **1910**, *84*, 25.

(25) Pedersen, J. *Journal of Applied Crystallography* **2000**, *33*, 637.

(26) Baxter, R. J. *The Journal of Chemical Physics* **1968**, *49*, 2770.

(27) Menon, S. V. G.; Manohar, C.; Rao, K. S. *The Journal of Chemical Physics* **1991**, *95*, 9186.

(28) Liu, Y.; Chen, W.-R.; Chen, S.-H. *The Journal of Chemical Physics* **2005**, *122*, 044507.

(29) Hayter, J. B.; Penfold, J. *Molecular Physics* **1981**, *42*, 109.

(30) Israelachvili, J. *Intermolecular and Surface Forces, Second Edition: With Applications to Colloidal and Biological Systems (Colloid Science)*; {Academic Press}, **1992**.

(31) Hansen, J.-P.; Hayter, J. B. *Molecular Physics* **1982**, *46*, 651.

(32) Pedersen, J. *Journal of Applied Crystallography* **2004**, *37*, 369.

(33) *Modern Aspects of Small-Angle Scattering, Chapter 2: Instrumentation for Small-Angle Scattering, p. 57-91*; Brumberger, H., Ed.; Kluwer Academic Publisher, **1995**.

(34) Pedersen, J. S.; Posselt, D.; Mortensen, K. *Journal of Applied Crystallography* **1990**, *23*, 321.

(35) Schmatz, W.; Springer, T.; Schelten, J.; Ibel, K. *Journal of Applied Crystallography* **1974**, *7*, 96.

(36) Lieutenant, K.; Lindner, P.; Gahler, R. *Journal of Applied Crystallography* **2007**, *40*, 1056.
(37) Lindner, P.; Schweins, R. *Neutron News* **2010**, *21*, 15.
(38) Heenan, R. K.; Penfold, J.; King, S. M. *Journal of Applied Crystallography* **1997**, *30*, 1140.
(39) Wignall, G. D.; Bates, F. S. *Journal of Applied Crystallography* **1987**, *20*, 28.
(40) *X-ray and neutron reflectivity: principels and applications*; Daillant, J.; Gibaud, A., Eds.; Springer, 1999.
(41) Nelson, A. *Journal of Applied Crystallography* **2006**, *39*, 273.
(42) Kiessig, H. *Annalen Der Physik* **1931**, *402*, 769.
(43) Parratt, L. G. *Physical Review* **1954**, *95*, 359.
(44) Zabel, H. *Applied Physics A: Materials Science & Processing* **1994**, *58*, 159.
(45) Müller-Buschbaum, P.; Stamm, M., Ed.; Springer Berlin Heidelberg: **2008**, p 17.
(46) Müller-Buschbaum, P.; Gomez, M., Nogales, A., Garcia-Gutierrez, M. C., Ezquerra, T. A., Eds.; Springer Berlin / Heidelberg: **2009**; Vol. 776, p 61.
(47) Yoneda, Y. *Physical Review* **1963**, *131*, 2010.
(48) Holý, V.; Baumbach, T. *Physical Review B* **1994**, *49*, 10668.
(49) Salditt, T.; Metzger, T. H.; Peisl, J.; Reinker, B.; Moske, M.; Samwer, K. *EPL (Europhysics Letters)* **1995**, *32*, 331.
(50) Naudon, A.; Babonneau, D.; Thiaudière, D.; Lequien, S. *Physica B: Condensed Matter* **2000**, *283*, 69.
(51) Felici, R.; Penfold, J.; Ward, R.; Williams, W. *Applied Physics A: Materials Science & Processing* **1988**, *45*, 169.
(52) Penfold, J.; Ward, R. C.; Williams, W. G. *Journal of Physics E: Scientific Instruments* **1987**, *20*, 1411.
(53) Smilgies, D.-M.; Boudet, N.; Struth, B.; Konovalov, O. *Journal of Synchrotron Radiation* **2005**, *12*, 329.
(54) Hénon, S.; Meunier, J. *Review of Scientific Instruments* **1991**, *62*, 936.
(55) du Noüy, P. L. *The Journal of General Physiology* **1925**, *7*, 625.
(56) Huh, C.; Mason, S. G. *Colloid & Polymer Science* **1975**, *253*, 566.
(57) Huh, C.; Mason, S. G. *Colloid & Polymer Science* **1977**, *255*, 460.
(58) Sommer, C.; Pedersen, J. S.; Stein, P. C. *The Journal of Physical Chemistry B* **2004**, *108*, 6242.
(59) Young, H. D.; Freedman, R. A. *University Physics. Chapter 10: 'Waves/Acoustics'*; Elleventh ed.; Pearson Addison Wesley, **2004**.

3. Investigation of mixed CTAB/SB3-14 surfactant and PEI polymer films

3.1 Introduction

In this chapter the formation and structure of surfactant-polymer hydrogel films are presented and discussed. The films formed from mixtures of cationic surfactant hexadecyltrimethylammonium bromide (CTAB), zwitterionic surfactant 3-(N,N-dimethyltetradecylammonio)propanesulfonate (SB3-14) and basic polymer polyethylenimine (PEI) were studied. These films form spontaneously at the air-solution interface upon mixing and exposure in a non-closed atmosphere. They are robust enough to allow harvesting from the interface when formed from a solution of suitable composition. Variation of the surfactant composition and the polymer molecular weight produces films of different structure and extent of order.

Film formation from mixtures of cationic and zwitterionic surfactant with polymer was chosen for the study as a route towards polymer surfactant hydrogel films that exhibit periodic mesostructure with low toxicity. There has been reported in the literature numerous surfactant-polymer systems that form films at the air water interface from solutions of alkytrimethylammonium bromides and PEI.[1-5]

The study was performed first as an extension of previous work in the group where the initial film-forming system of this type was discovered and second, as an attempt to increase the biocompatibility of the film forming systems. This film-forming system was composed of cationic alkyltrimethylammonium bromide surfactants and polyethylenimine. It was found that the film-forming solutions had to be present in an exposed atmosphere for film formation to occur. If the film-forming solution is present in an enclosed atmosphere it was found that the increase in humidity within the atmosphere prevented film formation from occurring. This is believed to happen because, as no evaporation occurs, the necessary increase in concentration needed to form the film at the surface is absent.[6]

Variation of the surfactant hydrocarbon tail length caused a change in the structure of the films, predominately in the distances between the planes of the structure as seen by neutron and X-ray reflectometry, and it was also found possible to change the film structure by variation of the polymer, PEI, molecular weight. However the use of CTAB as a component in these film forming systems introduces toxicity to the films. If these film forming systems were to be used for biomedical devices where the surfactant matrix within the films is used to incorporate hydrophobic

therapeutic agents as a method of delivery for example, then the toxicity of CTAB would pose a significant problem. The use of a less toxic surfactant as an alternative to CTAB or used a co-surfactant with CTAB could make the films less toxic and the zwitterionic surfactant, SB3-14 is less toxic than CTAB.[7]

Previous work has been done where non-ionic surfactants were used as a co-surfactant with CTAB in the film-forming systems. It was found that up to a threshold mole-fraction the non-ionic surfactant and CTAB mixtures formed films which still exhibited periodic mesophases, thus it was possible to lower the toxicity of the films by decreasing the CTAB mole fraction with a less toxic surfactant.[2,8]

Zwitterionic surfactants are generally less toxic than their cationic counterparts.[7,9] Therefore, it follows that they are worthy of investigation as a co-surfactant in the CTAB and PEI film forming solutions when the main objective is to reduce toxicity in the films. Also, as a zwitterionic surfactant is formed of a cationic and anionic group in the headgroup, it is partially an analogue of the previously reported catanionic surfactant film forming system as both a cationic and anionic charge is present.

3.2 Materials and Methods

Hexadecyltrimethylammonium bromide (CTAB, Acros, purity 99+%), tail deuterated D33-CTAB (CDN 98%-D or Oxford Isotope Facility), and 3-(N, N-dimethyltetradecylammonio) propanesulfonate (Sigma Aldrich, purity 99%) were used without further purification.

Polyethylenimine (PEI, hyper branched form) with molecular weights of ~750,000 Da (LPEI) and ~2000 Da, (SPEI) as 50%wt solutions in water were purchased from Sigma Aldrich. Ultrapure water (purified to 18 MΩ cm using an Elga PURELAB system) or D_2O (99.9%, Sigma-Aldrich) were used to prepare all solutions. Initial separate stock solutions of CTAB, SB3-14 and PEI were prepared in ultrapure water or D_2O prior to mixing to obtain the final solutions of required composition. To prepare film forming solutions, the stock surfactant film were first mixed to make mixed surfactant solutions at the appropriate molar ratio, then the polymer solution was added.

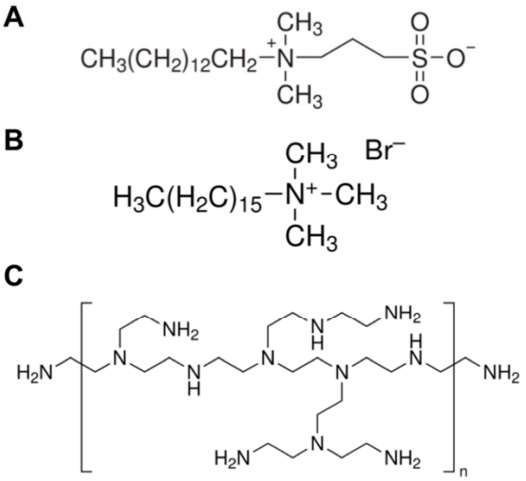

Figure 3.1. Chemical structures of SB3-14 (A), CTAB (B) and branched PEI (C). In the PEI formula *n* denotes the number of repeat units corresponding to the molecular weight of the polymer.

The density measurements were performed on a DMA 5000 densitometer (Anton Paar). A series of measurements on a concentration series of SB3-14 on concentrations ranging from 62.5mM to 1M of pure SB3-14 in water at 25°C were performed in triplicate.

Neutron reflectometry (NR) experiments were performed on the CRISP instrument at ISIS RAL Oxford, UK [10]. Film forming solutions were investigated by 1:1 volume mixing stock solutions of 100mM surfactant and 2%wt PEI to achieve solutions of 50mM surfactant and 1%wt PEI. Neutron scattering length density contrast was achieved by substituting tail-deuterated, d33-CTAB for CTAB. All experiments were performed with D_2O as solvent

Upon mixing the solutions were immediately poured in to Teflon® troughs with dimensions 15cm x 4cm x 0.5cm deep. Films formed at the air-solution interface were grown on ~30ml solutions. The troughs were filled until a positive meniscus formed, raising the film surface above the edge of the trough for reflectivity measurements. Film formation was studied by collecting NR profiles of the solution-air interface. The bottom surface of the troughs were on a sample stage that maintained a constant 28°C to ensure that the solution did not fall below 25°C (this ensured that the solutions did not fall below the Krafft point temperature of CTAB). Films were measured for up to 90 minutes or until there was no observed change in the NR profiles. Film formation was monitored with 15 minute time resolution.

SANS experiments were performed on the LOQ instrument at ISIS RAL Oxford, UK.[11] Film forming solutions were investigated by 1:1 volume mixing of stock

solutions of 100mM surfactant and 2%wt PEI to achieve solutions of 50mM surfactant and 1%wt PEI. Neutron scattering length density contrast was achieved by substituting d33-CTAB for CTAB. All solutions were made in D_2O to make samples of 2ml volume. Solutions were introduced to quartz Helma cells with 1mm beam path and 0.6ml total volume. The incident beam diameter of the LOQ instrument was 12mm. SANS data was collected for a total of 40μA per sample whilst the temperature of the samples was maintained at 28^{o}C.

SAXS measurements were performed on the modified NanoSTAR camera from Bruker AXS at Aarhus University, Denmark. Film forming solutions were, as in the SANS experiments, investigated by 1:1 volume mixing stock solutions of 100mM surfactant and 2%wt PEI to achieve solutions of 50mM surfactant and 1% PEI. Solutions were introduced to quartz capillaries with 2mm path length and approximate 150μl. Water was used as a primary standard to calibrate the instrumental intensity on the detector to absolute units. The reusable quartz capillary was maintained at 28^{o}C in a thermostated sample holder. The SAXS data was collected for 3600 s and so were the corresponding water backgrounds.

Surface tension measurements of CTAB-SB3-14 mixed solutions were performed on a Sigma 701 force tensitometer from Attention using a de Noüy ring. However, the surface tension measurements of pure CTAB alone were performed using the Wilhelmy plate method to enable temperature calibration of the system at 28^{o}C. When the Wilhelmy plate was used it was manually controlled and not controlled by the Sigma 701 apparatus. Stock solutions of the required CTAB to SB3-14 molar ratios were prepared and automatically added to pure water by an autotitrator. After each addition the latency before measurement was 20 minutes. No stirrer was used in the measurements. The final concentration of the stock solutions were determined from test experiments to ensure the inflection arising from the CMC point was approximately central to the concentration range available resulting from the stock concentration. Stock solutions were added to an initial volume of 20ml water.

3.3 Neutron Reflectometry of CTAB/SB3-14/PEI films

3.3.1 Effect of micelle composition and PEI MW on film structure

The structures of interfacial films formed from mixtures of CTAB, SB3-14 and PEI were investigated with NR. The film structures were investigated as a function of [CTAB]: [SB3-14] molar ratio and PEI molecular weight. Film forming solutions were investigated at total surfactant concentration of 50mM for [CTAB]: [SB3-14] ratios of 1:0, 2:1, 1:1, 1:2 and 0:1. Film forming solutions at all surfactant molar

ratios were investigated with LPEI and SPEI at 1%wt. Figure 3.2 shows the final reflectivity profiles of time-resolved series, investigating film formation from solutions of CTAB, SB3-14 and PEI mixtures and the positions of diffraction peaks resulting from periodic mesostructure within the films are presented in Table 3.1.

[CTAB]:[SB3-14] [TOTAL]=50mM	**POLYMER 1%wt**	**Peak q ($Å^{-1}$ ±0.0005)**	**Peak d (Å ±0.05)**
1:0	LPEI	0.111	56.8
		0.125	50.5
	SPEI	0.128	49.1
		0.253	24.8
2:1	LPEI	0.177	53.7
	SPEI	0.128	49.1
1:1	LPEI	0.121	52
	SPEI	NO PEAK	
1:2	LPEI	0.125	50.3
	SPEI	NO PEAK	
0:1	LPEI	NO PEAK	
	SPEI	NO PEAK	

Table 3.1 Peak positions in reciprocal space and calculated real space distances for the diffraction peaks from the NR profiles in Figure 3.3.

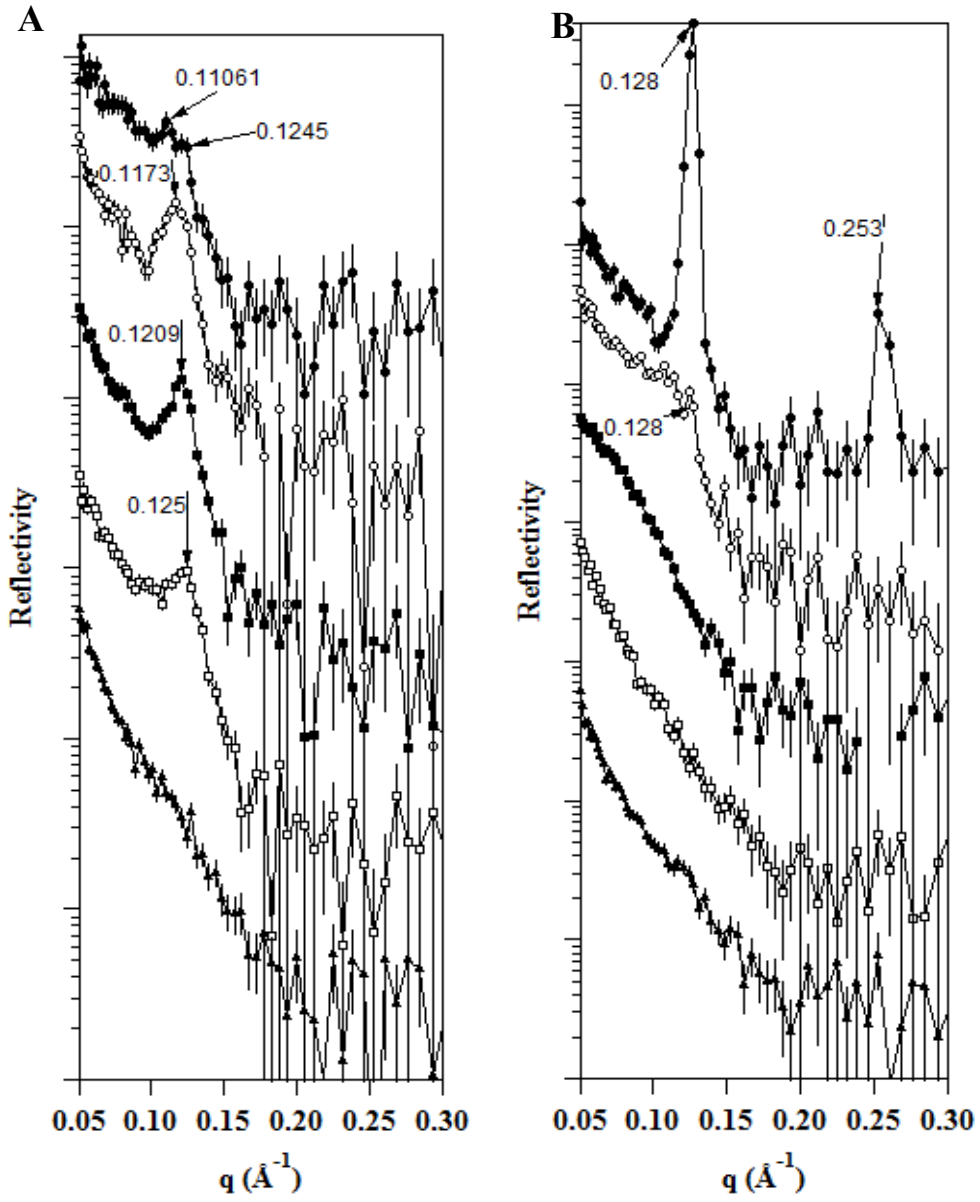

Figure 3.2. **A**: NR profiles of films formed from CTAB: SB3-14 mixtures with LPEI solutions. CTAB and SB3-14 are present in the following molar ratios; 1 CTAB: 0 SB3-14 (filled circles), 2 CTAB:1 SB3-14 (open circles), 1 CTAB:1 SB3-14 (filled squares), 1 CTAB:2 SB3-14 (open squares) and 0 CTAB:1 SB3-14 (filled triangles) **B**: NR profiles of films formed from CTAB:SB3-14 mixtures with SPEI solutions. CTAB and Sb3-14 are present in the following molar ratios; 1 CTAB: 0 SB3-14 (filled circles), 2 CTAB:1 SB3-14 (open circles), 1 CTAB:1 SB3-14 (filled squares), 1 CTAB:2 SB3-14 (open squares) and 0 CTAB:1 SB3-14 (filled triangles) . In all samples total surfactant concentration was 50mM and PEI concentration 1%wt. The patterns have been offset for clarity.

Inspection of the NR profiles in Figure 3.2 shows that for a film to exhibit periodic mesostructure that CTAB must be present when films are formed with LPEI and in molar excess relative to SB3-14 when formed with SPEI. There is no visible film formation from solutions of pure SB3-14 and PEI. For solutions formed with SPEI and SB3-14 in an equimolar or more ratios to CTAB there are no diffraction peaks in the film although there is a broad hump in the NR profile of 1 CTAB: 1 SB3-14 SPEI 1%wt film suggesting a slightly periodic mesostructure at the surface.

3.3.2 The structure of 1 CTAB: 0 SB3-14 with PEI solution films

Whilst it is apparent that films with certain combinations of CTAB, SB3-14 and PEI form periodically mesostructured films, none of the NR profiles provide sufficient information for unequivocal assignment of phase. Films formed from solutions of 1 CTAB: 0 SB3-14 PEI are unique in the series in that the NR profiles exhibit more than one peak suggesting mesophases of greater order than when SB3-14 is present.

Structure of 1 CTAB: 0 SB3-14 50mM LPEI 1% wt. films

Considering films formed from LPEI and CTAB: SB3-14 mixtures, all films formed from solutions that contain CTAB exhibit diffraction peaks, which indicate an ordered surfactant mesophase within the films. In the film formed from 1 CTAB: 0 SB3-14 50mM LPEI 1% (CTAB-LPEI) the two peaks are at q_1 = 0.111 and q_2 = 0.125 (Figure 3.3, Table 3.2). The relative proximity of these peaks suggests that they are from a three dimensionally ordered structure such as a cubic phase. If the peaks are assigned q_{hkl} positions of 210 and 211 for the q_1 and q_2 respectively, which are peaks present in a $Pm\bar{3}n$ micellar cubic phase. The $Pm\bar{3}n$ phase has been reported to exist in the CTAB-polymer phase diagram.[12,13] The ratio of q_1: q_2 should be equal to $\sqrt{5}$:$\sqrt{6}$ or 1.095. The actual ratio is equal 1.028 which is a 2.8% difference however this is near to the error in q from the instrumental resolution so can still be considered significant. The 210 and 211 reflections are not the initial peaks of a $Pm\bar{3}n$ phase, however in the NR profile after 3600 seconds, dislocations due to film formation, interfacial roughness and the presence of less structured regions of the film could dominate the NR profile and obscure certain peaks.

Analysis of time resolved NR profiles collected every 900 seconds to monitor film formation show, as formation progresses, the appearance and disappearance of peaks that can be assigned tentatively to a $Pm\bar{3}n$ micellar cubic structure as √2(110):√4(200):√5(210):√6(211):√10(310) (Figure 3.3 A and B). Peaks identified

are deviations in the reflectivity which are above the magnitude of the error bars and which persist for more than one pattern.

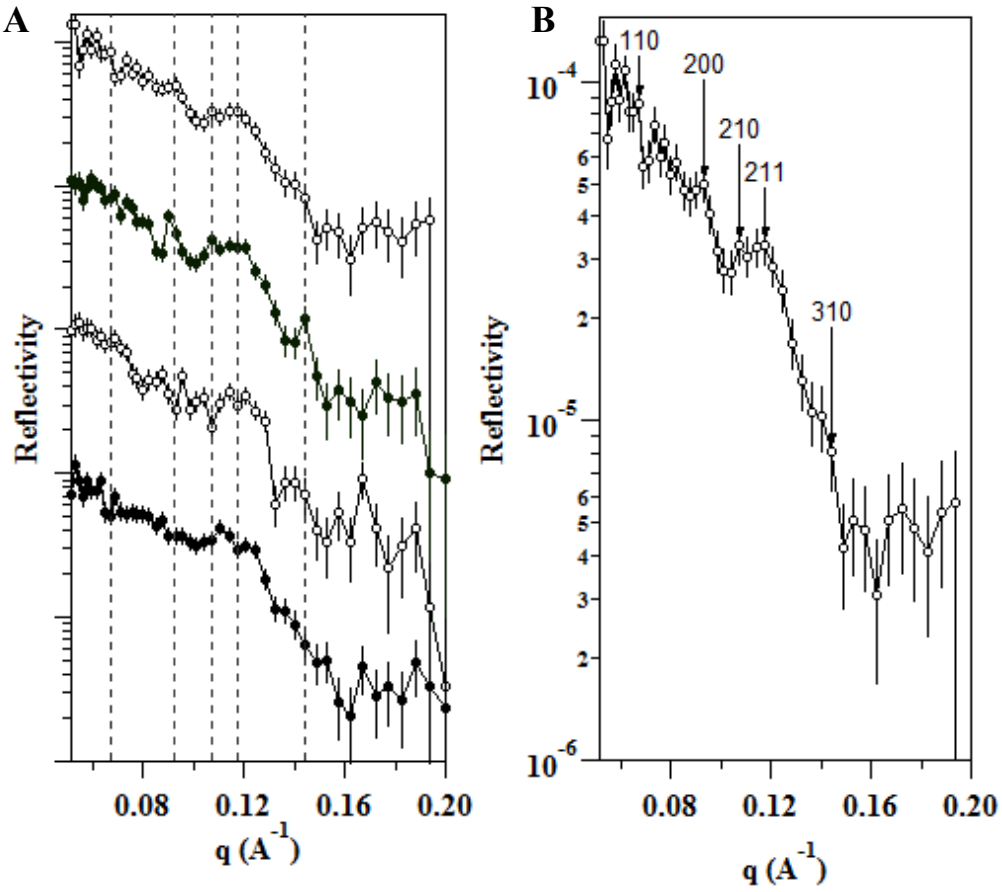

Figure 3.3 A: Time resolved NR profiles of 1 CTAB: 0 SB3-14 LPEI film formation at time=900 seconds (open circles), 1800 seconds (filled circles), 2700 seconds (open squares) and 3600 seconds (filled squares). Dotted lines represent the positions of the q_{hkl} position at √2 (110):√4 (200):√5 (210):√6 (211):√10 (310) for a $Pm\bar{3}n$ micellar cubic on the 900 second NR profile. NR profiles are normalised to total reflection but offset by a factor of 10 for clarity. **B**: Detail of the 900 second NR profile highlighting the $Pm\bar{3}n$ q_{hkl} assignments.

All the peaks are evident in the 900 seconds NR profile (Figure 3.3 A & B) however it is a tentative assignment to a $Pm\bar{3}n$ micellar cubic as the observed order of peaks are not exclusive to a $Pm\bar{3}n$. If a reflection was present that could be indexed to the √3 (111) position then the structure could be assigned to a $Pn\bar{3}m$ bicontinuous cubic. Schematics of $Pm\bar{3}n$ micellar cubic and $Pn\bar{3}m$ bicontinuous cubic were presented in Chapter 1.2.2. However, the absence of this peak could be due to roughness of the

films preventing it from being resolved or the loss of long range order in the film due to movements in the surfactant: polymer complexes. The film at 1800 seconds exhibits a similar set of peaks, but as film formation progresses at 2700 and 3600 seconds the peaks move to higher *q* suggesting a decrease in the unit cell size. This is most likely due to dehydration at the air-film interface, decreasing the volume fraction of the hydrated polymer phase and allowing the interfaces of the surfactant phase in the cubic structure to move closer together. Initially, assuming a $Pm\bar{3}n$-like structure in the film, the unit cell at 900 seconds of film formation has a unit cell of 136 Å with the unit cell of the structure decreasing to 127 Å in the time frame of the experiment.

A $Pm\bar{3}n$ micellar cubic phase was reported for films formed from preparations of PEI and alkyltrimethylammonium bromides in a study by O'Driscoll *et al.*[1] This study investigated the structure and formation of films formed from alkyltrimethylammonium bromides of differing alkyl chain length, molecular weight and type of PEI and the effects of chemical cross-linking of PEI with ethylene glycol diglycidyl ether (EGDGE, Figure 3.4). The structures found in the films were either hexagonally close packed cylinders (*p6mm*) or micellar cubic ($Pm\bar{3}n$) dependent on the curvature of the surfactant micelles within the film.

Specifically, EGDGE was not required for formation of a $Pm\bar{3}n$ phase in the film if the surfactant used was tetradecylammonium bromide (TTAB, 37mM) and the concentration of LPEI was at 60g/L, which is far greater than the concentration of LPEI used in this study (10g/L). A $Pm\bar{3}n$ phase was also observed when the films were formed from CTAB (37mM) and LPEI 15g/L with EGDGE 100mM or SPEI 60 g/L with EGDGE 40mM. Importantly, a $Pm\bar{3}n$ phase was seen when the surfactant micelles were spherical (in the case of the TTAB film) or when there was a significant polymer network in the film (in the case of the cross-linked films). This phenomenon is discussed in detail below.

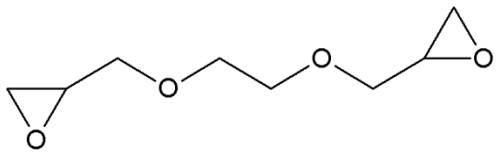

Figure 3.4 Schematic of molecular structure of ethylene glycol diglycidyl ether (EGDGE)

Whilst not explicitly identified in the study due to missing peaks, O'Driscoll *et al*[2] also reported the formation of films that also appear to have a micellar cubic phase structure. In O'Driscoll *et al*[2] (Figure 3.5 A & B) it can be seen that when films are

formed from CTAB 37mM and SPEI a possible $Pm\bar{3}n$ film phase is present. When the concentration of SPEI is at 60, 45 and 30 g/L two peaks are present in the neutron reflectivity data at q_1=0.1109Å^{-1} and q_2=0.1246 Å^{-1}. The ratio of these peaks q position is similar to the ratio of $\sqrt{4}:\sqrt{5}$. In the profiles where q_1 and q_2 are highlighted there also appears to be a small peak at ~0.135. If the structure present is a cubic structure this small peak could be included in the ratio comparison as $\sqrt{6}$ in $\sqrt{4}:\sqrt{5}:\sqrt{6}$. This reflection sequence is expected in the $Pm\bar{3}n$ phase as the 200, 210 and 211 reflections. The unit cell of this structure, if cubic would be 92Å**.**

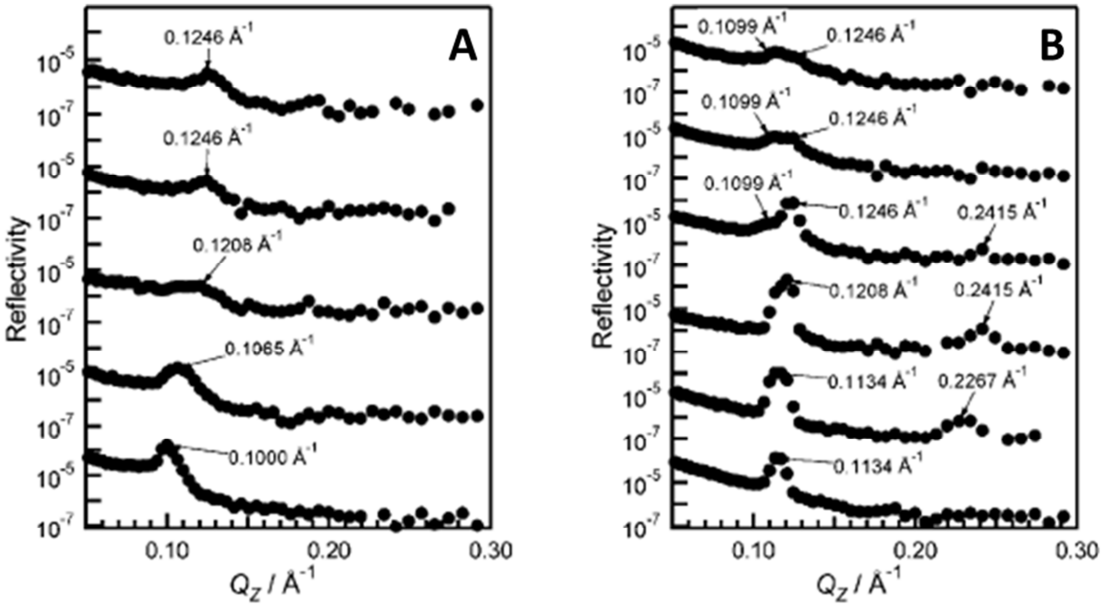

Figure 3.5 Neutron reflectivity of films formed from CTAB and LPEI (**A**) and SPEI (**B**). CTAB concentration 37mM. PEI concentration from top to bottom; LPEI 30g/L, 15g/L, 7.5g/L, 3.75g/L and 1.875g/L; SPEI 60g/L, 30g/L, 15g/L, 7.5g/L, 3.75g/L. Reprinted with permission from O'Driscoll *et al*[2] Copyright 2013 American Chemical Society.

NR profiles of films formed with CTAB (37mM) and LPEI from the O'Driscoll *et al*[2] study (Figure 3.6A) do not exhibit the same structure. At similar polymer concentrations compared to the SPEI, the NR profiles are dominated by a single broad peak centred on q_1=0.1246. If additional peaks exist arising from a similar structure to the SPEI films in the study then they may be too smeared by roughness and disorder in the film.

It should be noted that the experimental conditions of the study in this thesis are different from the O'Driscoll studies. The concentration of CTAB in this study is higher at 50mM compared to 37mM and the concentration of PEI is generally lower than the highlighted film forming preparations from the O'Driscoll studies. However

in each case, the occurrence of $Pm\bar{3}n$ has been seen in systems with a substantial polymer network achieved through high polymer concentration or cross-linking the polymer. The causes of formation of the $Pm\bar{3}n$ mesophase will be discussed next and its relevance to the systems in this study.

It has been reported that the CTAB-water binary phase diagram follows the order of micellar ➔ ordered micellar ➔ hexagonal (*p6mm*) ➔ cubic ➔ lamellar as CTAB concentration is increased[12,14-16]. However CTAB has been shown to exhibit phase transitions of micellar ➔ micellar cubic ($Pm\bar{3}n$) ➔ hexagonal (*p6mm*) in systems of CTAB/polyelectrolyte/water systems.[12,13]

The occurrence of the $Pm\bar{3}n$ phase in the polyelectrolyte-surfactant systems may be attributed to the displacement of tightly bound bromide counter ions from the CTAB micelle surface[12] which allows a higher surfactant aggregate surface curvature. The effect has also been attributed to minimum energy packing considerations through competition between the packing energy and minimal surface considerations brought forth by the presence of polymer dressing the surface of the micelle.[13] This changes characteristic hard sphere of the micellar core to a soft sphere with a compressible soft shell.[13]

The bromide dissociation of CTAB micelles in aqueous solution is estimated to around 10% to 20%[17] largely due to ion-pair formation between bromide and quaternary ammonium ions[18] as the small hydration shell of bromide permits the counter ion to reside close to the micelle surface**.**. However the figure for dissociation has been found to be highly micelle surface curvature dependent, ranging between ~5 to ~40% dissociation for lamellar to spherical curvatures.[19] The resultant charge screening arising from the non-dissociated counter ions reduces charge repulsion between the surfactant headgroups. Therefore the headgroup area remains small enough for the packing of the surfactant molecules within the micelle to favour elongated micelles. In comparison, in hexadecyltrimethylammonium chloride where there is greater counter ion dissociation, the micelles are found to be more spherical.[20]

Displacement of bromide counter ions by polyelectrolyte would remove the charge screening effect and an anionic polyelectrolyte associating with the surfactant micelle can be considered as an analogue of fully dissociated counter-ions (as opposed to partially dissociated bromides). This effect was observed by Ilekti *et al.*[12] However PEI cannot be considered as an anionic polyelectrolyte as it is comprised of primary, secondary and tertiary amines. This causes PEI in aqueous solution to be partially protonated and therefore a cationic polyelectrolyte. It was proposed by Comas-Rojas *et al*[3] that PEI in aqueous solution acted as a moderate electrolyte towards CTAB. PEI in aqueous solution is basic with a pKa of 9.28 for LPEI and 9.56 for SPEI.[2] As PEI is partially protonated in aqueous solution at values of ~3%

and 1% for SPEI and LPEI respectively and SPEI lowers the CMC of CTAB more than LPEI, PEI in general is likely to act as an electrolyte towards CTAB. As it is overall cationically charged it would be initially expected to not have an associative interaction with cationic CTAB micelles. However there are multiple possible interactions of PEI with CTAB.

Regarding the cationic-dipole interaction, it is known that branched PEI[21] forms globular aggregates in aqueous solution above a critical concentration due to a dipole-dipole interaction between the amines of PEI.. Addition of CTAB to PEI solutions causes the aggregates to change shape, incorporating the CTAB micelles[21] and completely screening the charge of the CTAB micelles. This is also seen later in the small angle scattering results in this study discussed below in section number 3.9 Additional evidence of a cation-dipole interaction was reported by O'Driscoll[1] where modulation of the charge density on PEI using NaOH changed the film thickness and characteristic d-spacing with in the CTAB-PEI films. Specifically removal of charge which increased the number of unprotonated lone pairs in PEI increased film thickness and decreased *d*-spacing due to an increased association between CTAB-PEI and a decrease in charge repulsion between ammoniums of both partially charged PEI and CTAB. The opposite was true when the charge was increased.

When considering a counter-ion displacement interaction, the PEI cannot be considered to displace bromide similar to an anionic polyelectrolyte. However the partial cationic charge may stabilise dissociated bromide away from the micellar surface. This would cause an entropically favourable situation favouring micellisation, in particular formation of more spherical micelles, that could constitute a $Pm\bar{3}n$ phase. This effect was reported by O'Driscoll *et al*[22] where decreasing the charge on PEI with NaOH promoted micellar growth into a 2D hexagonal *p6mm* phase, whereas $Pm\bar{3}n$ phases were more likely to form in solutions where PEI was partially charged due to deprotonation of water by PEI amines. The decreasing charge effect and promotion of the *p6mm* phase was most prominent in solution where films were formed with SPEI.

When films were formed with LPEI, it was found that when NaOH was present in the solution, the subphase pH was larger than that of films of similar composition formed from SPEI. It was postulated that this was due to the charge stabilisation of ammonium groups on LPEI displacing hydroxide ions from the film phase and retaining the bromide ions due the enhanced polymeric network of the larger branched polymer compared to SPEI. The displacement of bromide ions from the micellar surface would increase the charge of the micellar surface and therefore increase micellar curvature producing spherical micelles. This may be a possible reason why the $Pm\bar{3}n$ structure is evident in this study and the O'Driscoll *et al* study. However, it is more likely due to packing considerations when the steric bulk

of LPEI, cross-linked LPEI or SPEI and the relative volume fractions of CTAB and polymer network are evaluated.

First of all the conditions needed for CTAB micelles to be in a spherical form need to be considered. It is well known that the association of bromide counter ion quaternary ammoniums is great, estimated at ~90% association.[23] This large association effectively charge screen the quaternary ammonium charge of the CTAB, effectively reducing the equilibrium headgroup volume thus reducing the curvature so bromide association can be said to promote elongated micelles in CTAB. It has been well documented that polyelectrolytes acting as polyions can displace bromide counter ions and act as the counter ion to the surfactant molecules in the micelle.[12] This displacement can induce curvature of the CTAB micelles rather than the lesser curvature of the elongated micelles, as the polyelectrolyte ions are more hydrated than the bromide ions.[24] The more hydrated counter ions allow the surfactant ions to be more hydrated thus they are less charge screened than in the bromide instance.[23] This in turn causes the effective head group area to be larger thus increasing the surfactant surface curvature. However a major difference between this study and the O'Driscoll *et al* study is that the relative volume fractions of CTAB and PEI in the bulk are different.

In the O'Driscoll *et al* study, when $Pm\bar{3}n$ phases were evident with films formed from CTAB the concentration of CTAB was 37mM in the bulk and the concentrations of LPEI and SPEI were 15g/L and 60g/L respectively, whilst both formulation where chemically cross-linked with EDGDE. The salient points are that the CTAB concentration used in the O'Driscoll study was below the sphere to rod transition of CTA.[22] However in this study the concentration of CTAB is 50mM in the bulk. The concentration of PEI in this study is 10g/L. Therefore the relative volume fraction of CTAB to PEI in this study is higher than that of the O'Driscoll study. Interestingly the polymer networks are cross-linked in the O'Driscoll et al study, which would create a polymer network with greater three dimensional steric bulk plus restrict the mobility of the polymer network.

The $Pm\bar{3}n$ structure is an example of tetrahedral close packing. The highest density packing of spheres is achieved through a face centred cubic packing known as the Kepler conjecture. When micelles act as hard spheres they pack in a face centred cubic lattice[25] or a hexagonally close packed structure.[26] When the hard spheres are complemented by a long range repulsive potential then the highest possible density of packing is achieved by packing on a body centred cubic lattice.[27] When spheres are considered as 'soft' *i.e.* polymeric micelles with large coronas or surfactant micelles with associated polymer acting as a corona they are often found to pack in to a tetragonally close packed structure.

The tetragonally close packed structure was found to be the minimal surface area for packing micellar aggregates of two different sizes[28] which was further reinforced by the discovery of a counter example to Keplers conjecture of packing where shapes of equal volume but different shape were found to pack in to a $Pm\bar{3}n$ lattice to achieve the most dense packing.[29] This is relevant to soft spheres and specifically soft spheres that are considered soft due them being comprised of micelles dressed in polymeric species, as it was reported that such micelles pack on to a $Pm\bar{3}n$ like lattice which is not as dense as a face centred cubic to maximise the entropy of the polymer chains by not packing as closely. This is what is most likely seen in the alkyltrimethylammonium bromide films with PEI.

Therefore, it is proposed that the $Pm\bar{3}n$ micellar cubic structures seen in this study and O'Driscoll study are a result of packing due to the polymeric coat of PEI on the CTAB micelles. This packing constraint causes the micelles to adopt a more spherical form as, whilst it may not be energetically beneficial to form the spherical micelles with the bromide dissociation, the overall energy of the system is lowered for this phase. As the CTAB and PEI ratio is lower in this study compared to the O'Driscoll study then there are fewer ammonium groups present to stabilise bromide away from the CTAB micelle surface in this study.

Additionally, as the CTAB to PEI ratio is higher in this study, the CTAB micelles have already undergone the sphere to rod transition and there is more CTAB present. If the Åberg *et al*[6] explanation for the formation of ordered phases at the air-water interface is considered, where stable ordered phases are formed due to evaporation of water from the dividing surface between the solution and air, this phenomenon can be explained. In the case of a low CTAB to cross-linked PEI ratio the CTAB is below the sphere to rod transition concentration and there is cation-dipole associated cross-linked polymer network present imposing its steric bulk at the interface. Therefore, as CTAB attempts to transition due to the increase in concentration the packing constraints imposed by the PEI network cause $Pm\bar{3}n$ packing.

In the case of a larger CTAB to non-cross-linked PEI ratio in this study, the CTAB already exists as a rod in the bulk and the PEI is more mobile imposing less steric bulk at the interface. However as the CTAB has already adopted an elongated micelle conformation, as it attempts to grow due the increase in concentration it encounters enough of a volume fraction of PEI to force the film in to a $Pm\bar{3}n$ phase. This is most likely a combination of the PEI being more associated with CTAB in the interface region (compared to the bulk ratio) due to increased concentration of PEI and also the rate at which the CTAB micelles attempts to grow due to concentration changes. As there is more CTAB present, the increased amount of PEI prevents it packing in to anything apart from a $Pm\bar{3}n$ phase. Another factor to consider is even though the relative amounts of CTAB and PEI are different in the two studies, cross-linked PEI will be less mobile in the bulk and the fact that PEI is

not cross-linked may allow more of it to be present at the interface when film formation occurs.

Structure of 1 CTAB: 0 SB3-14 50mM SPEI 1% wt. films

Considering the film formed from the lower molecular weight polymer, at 1 CTAB:0 SB3-14 SPEI there are two well defined diffraction peaks at q_1= 0.128 and q_2= 0.253Å^{-1} (Figure 3.3 and Table 3.2). These represent real space distances of 49.1 and 24.8 Å respectively. These values can be indexed to both the first and second order of a lamellar (L_α) phase or the 01 and 02 reflections of 2D hexagonal phase (*p6mm*) with the long axis of the cylindrical micelles oriented parallel to the interface. For the reflectivity data to be representative of a lamellar phase the observed peaks should be present in a reciprocal space ratio 1:2:3…*n* relationship. The observation of the peak at 0.253 Å^{-1} suggests that the 1 CTAB: 0 SB3-14 SPEI film exhibits a mesophase with the greatest extent of long range order in the direction normal to the surface of all films investigated.

Reflections from a *p6mm* phase arise from crystallographic planes that are the result of the two dimensional unit cells and the arrangement of micellar aggregates at regular positions defined by the unit cell. The crystallographic planes of the early order reflections are described in section 2.5.3. Consideration of the orientational origins of reflections of the *p6mm* phase allows discussion as to whether the film formed from 1 CTAB: 0 SB3-14 SPEI solutions is a Lα or a *p6mm* phase.

Firstly, if the structure of the 1 CTAB: 0 SB3-14 SPEI is a L_α, the relationship of the reflection peaks is easily attributed to the first and second order of a lamellar structure. The characteristic spacing between planes within the lamellar phase would be 49Å. This *d*-spacing would impose packing considerations upon the CTAB molecules within the lamellae. This structure is possible for a CTAB molecule as an all *trans* conformation of the alkyl tail group would represent a distance of 21.7Å[30] plus the headgroup size of approximately 5 Å[20] so a lamellar phase is possible with minimal inter-lamellar spacing and would have to be a very concentrated Lα according to the lamellar dilution law.[31] This *trans* lamellar would also leave minimal space for SPEI between the micellar aggregates in the lamellar phase.

Lamellar phases have been reported for binary CTAB/water system.[32] However it is reported that the L_α phase is only apparent at CTAB concentration above ~80% and at temperatures above ~40ºC. Clearly, the addition of PEI will have an effect on the phase diagram. As PEI is comprised of dipole amines it is possible that PEI may interact hydrophobically with CTAB micelles by orientating the amine with the aliphatic portion into the micelle.

Ternary phase diagrams of CTAB/alcohol/water have been reported by Fontell *et al.*[33] The effect on the structure of the phases was dependent on the length of the aliphatic region of the alcohol. When the aliphatic region was short it was found that at CTAB concentrations that gave a *p6mm* hexagonal phase in the binary CTAB/water phase diagram there was no occurrence of a lamellar phase. However, when the alcohol was a long chain primary alcohol it was found that the alcohol could incorporate further into the hydrophobic region of the CTAB micelles. This caused a change in the packing parameter of the CTAB micelles producing the lamellar phase. It was also found that the longer chain alcohols could promote tighter packing of the lamellar phase resulting in a smaller *d*-spacing.

However it was reported by Comas Rojas *et al*[3] that PEI does not interact hydrophobically with CTAB. They reported the change in CMC of CTAB/alcohol mixtures as a function of alcohol concentration in pure water and in the presence of PEI. The presence of PEI lowered the CMC of the CTAB/alcohol mixtures compared to CMC of the mixtures not in the presence of PEI. However the trends in CMC as a function of alcohol were similar, suggesting that PEI only interacted with the surfactant electrostatically. It should be noted that the Comas-Rojas *et al* study was performed on systems at CMC concentrations and not in the concentrated state of the films, where mass action considerations may increase the likelihood of hydrophobic interactions.

There is however circumstances where the observed reflections of the *p6mm* phase in a reflectivity pattern appear to have some peaks missing. This may be attributed to either the orientation of the *p6mm* unit cell or in the case of this work, the ratio of the diameter of the cylindrical micelles to the dimension of the unit cell, *a*. Figure 3.7B shows the crystallographic planes of the *p6mm* that arise from distances to micelles arranged on the primitive unit cell along with the angle of the planes from the 10 plane. Thus if a film comprised of a CTAB and PEI internal structure has highly orientated *p6mm* unit cells, the reflections will be orientated at angles away from the film normal. In the neutron reflectivity experiment, only reflections in the q_z plane are investigated, which is normal to the film surface. Therefore only reflections from crystallographic planes which have no angular deviation from the film normal will be apparent.

This is explained schematically in figure 3.6. It can be seen that when the *p6mm* unit cell is orientated in the film with the 10 plane parallel to the film normal, only the 10 reflection and its higher orders will be seen in the NR profile due to the experimental geometry. If the *p6mm* unit cell is orientated with the 11 plane parallel to the film normal, only reflection arising from the 11 planes and its higher orders will be apparent in NR profile. If the *p6mm* unit cells were isotropically orientated then all reflections would be seen in the NR profile. This effect was extensively studied by Hillhouse *et al.*[34]

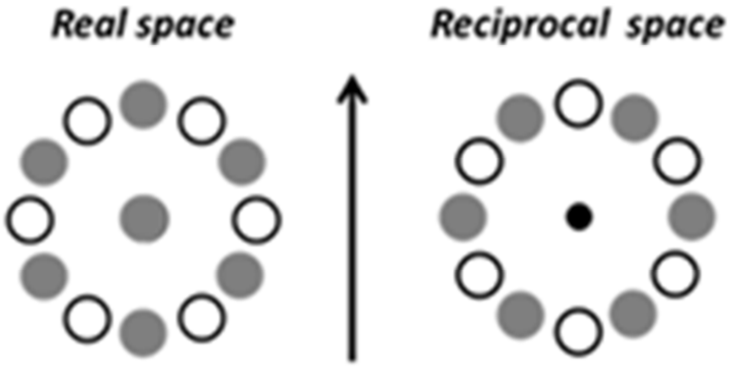

Figure 3.6 Schematic showing the orientation of a *p6mm* unit cell in real space and the respective reflections in reciprocal space. In real space 10 and 11 orientations are shown as open and filled circles respectively. The reflections are shown in reciprocal space with the same colour scheme. The arrow indicates the film normal and the q_z plane for real and reciprocal space respectively.

It has also been reported that missing peaks in the diffraction from a *p6mm* phase may also arise from the diameter of the scattering bodies within the *p6mm* unit cell.[35] It has been shown that when the pore size to unit cell ratio has certain values it is possible to have samples that miss peaks due to destructive interference of scattering from convolution of the form factor of the cylinders and structure factor of the *p6mm* unit cell. However, due to the packing constraints on a lamellar phase formed of CTAB micelles with PEI and the fact that a highly orientated *p6mm* unit cell would have missing reflections in the geometry of the NR experiment; it is likely that the phase exhibited is a *p6mm*. Further supporting evidence is apparent from previous studies on CTAB and SPEI films. Edler *et al*[36] reported a *p6mm* phase for films formed from CTAB 37mM:SPEI 60g/L:NaOH 100mM. This was confirmed by GIXD data where the out of q_z plane scattering exhibited an orientated diffraction 60º away from the out of plane scattering.

The Edler *et al* study[36] also highlighted the influence of the steric bulk of the polymer network on the structure exhibited by the films. With films formed from CTAB 37mM:SPEI 60g/L, the structure exhibited in the NR data appeared to be similar to a $Pm\bar{3}n$ phase. However when charge repulsion between polymer chains and between CTAB and SPEI was reduced by the presence of NaOH the films exhibited a *p6mm* structure. Here the CTAB micelles were able to pack tighter together and grow unhindered in length.

Further supporting evidence came from the 2007 O'Driscoll *et al* study. Here a *p6mm* phase was reported for films formed from CTAB 37mM:SPEI 15g/L. NaOH were not required to form the *p6mm* phase. This can be explained by the reduced steric bulk of the polymer network in the films due to the lower concentration of

SPEI compared to the Edler *et al* study.[36] In the O'Driscoll *et al* study it was found that the characteristic *d*-spacing of the *p6mm* film at the surface was 51Å and 50Å just below the surface. This is similar to the d-spacing for the CTAB/SPEI film in this study at 49Å. As the concentration of SPEI in this study was 10g/L, it is likely that the reduction in spacing in the film is caused by having less SPEI present in between the CTAB micelles in the film.

3.3.3 The effect of mixed CTAB: SB3-14 micelles on film structure

Films formed from mixed micelles and LPEI

As previously discussed it is possible to form films with periodic mesostructure (Figure 3.3 and Table 3.2) when SB3-14 is present in the micelles thus lowering the toxic content of the surfactant within the film. However it was found that replacement of pure CTAB micelles with mixtures of CTAB and SB3-14 has an effect on the structural phase and extent of order exhibited in the films.

When considering the effect mixed micelles of CTAB and SB3-14 have on the structure of the LPEI films it is evident from the data that they also produce periodically structured films. The NR profiles are dominated by a single reflection peak suggesting a repeated layer structure (figure 3.3). However the spacing of the layers within the film decreases with increasing SB3-14 mole fraction (Table 3.2). This can be correlated to the small angle scattering results presented later where the minimum dimension of the mixed CTAB and SB3-14 micelles was found to decrease with increasing SB3-14 mole fraction in the pure surfactant mixtures. No film was formed from solutions of only SB3-14 and LPEI at the interface.

The reduction in d-spacing upon addition of SB3-14 is in contrast to the effect observed when films were formed from CTAB, the non-ionic surfactant octaethylene glycol monohexadecyl ether (C16E8) and PEI.[8] It was reported from SANS measurements that increasing the C16E8 mole fraction increased the minimum dimension of the mixed micelles and this result was repeated in the d-spacing exhibited by the films formed from the mixed micelles and PEI.[8]

The reduction in *d*-spacing of the mesostructure with increasing mole fraction of SB3-14 in the films could possibly be a result of less LPEI being present in the film. Clearly, as no film is formed from pure SB3-14 surfactant when mixed with LPEI, the presence of CTAB in the film forming solution promotes film formation. As the mole fraction of SB3-14 is increased within the micelles there is less CTAB present for the LPEI to interact with. Thus, there is likely a reduction in the amount of LPEI in the film.

The effect of a reduced mole fraction of CTAB in the film is two-fold. Firstly, there is less steric bulk imposed by the polymer on the formation of a mesostructured film when the micellar aggregates pack into the film. Secondly, as LPEI in this solution is slightly protonated, there is less columbic repulsion between the micelles and the matrix of the film. This coulombic repulsion would arise between LPEI and the CTAB-containing mixed micelles as well as inter-polymerically between LPEI molecules. Coulombic repulsion within the film would also be less due to the reduced mole fraction of CTAB as CTAB to CTAB charge repulsion would also be reduced.

Considering the extent of order within the films, compared to films formed from CTAB 50mM with LPEI 1%, there appears to be just one diffraction peak rather than a micellar cubic phase. This would suggest that the amount of surfactant in the film is less as the concentration is not large enough for the mixed micelles to pack into a three dimensionally ordered phase. There are no second order reflections in the NR profiles therefore it is unlikely that the films possess long range periodic order such as the films formed from CTAB 50mM with SPEI 1%wt.

An estimate of the apparent crystal size may be obtained by applying equation 3.1, which is the Scherrer equation[37] converted to reciprocal space[38], to the peaks apparent in the NR profiles of the films formed from mixed micelles. The number of repeating periodic units that comprise the crystallites may be obtained through application of equation 3.2 to the peaks in the NR profiles.

$$Apparent\ Crystallite\ Size = \frac{2\pi K}{\Delta q} \qquad 3.1$$

$$Repeating\ Units = Apparent\ Crystallite\ Size/d \qquad 3.2$$

Where Δq is the full width half maximum (FWHM) of a Gaussian peak, K is the Scherrer constant[37] and d is the repeat spacing of the film structure obtained from $d=2\pi/q_{peak}$

K, the Scherrer constant accounts for peak broadening due to the type of structure within the liquid crystal and the geometry within the liquid crystals.[37] This is normally in the region of 1. For example when the aggregate shape is lamellar, cylindrical or spherical the Scherrer constant is ~0.9, ~1 or ~1.1 respectively.[38] As it is unknown the exact form of the aggregates in the film crystal structure, the Scherrer constant is kept at 1 for this analysis. The FWHM of the peaks related to the mesostructure of the mixed micelle with LPEI films is obtained by fitting a Gaussian distribution to the single peaks. A linear background is applied to the data so that

only the peak position, intensity and FWHM are fitted. The linear background is chosen so that it is fitted between q_{peak}±0.025Å^{-1}. The fits are presented in figure 3.7 and the results presented in table 3.2.

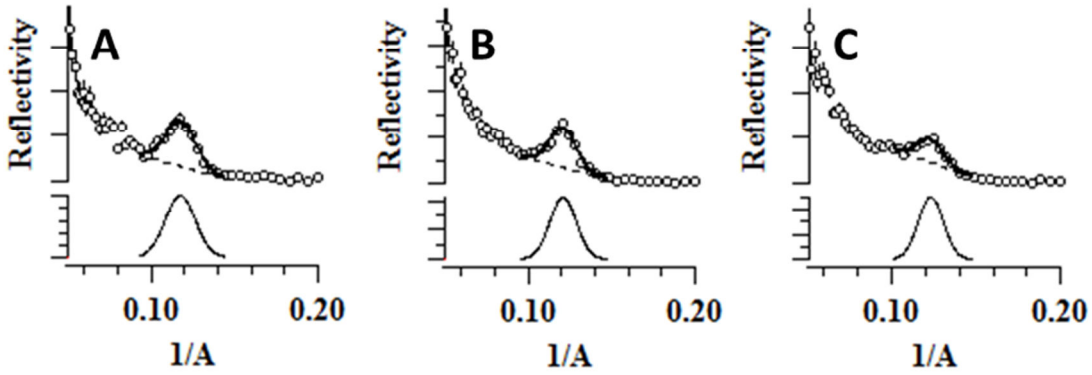

Figure 3.7 Gaussian peaks fitted to the peaks arising from the mesostructure of mixed CTAB: SB3-14 50mM with LPEI 1%wt. films. NR data is open squares (top data), Gaussian peak fit plus linear background is solid black lines (top data), and linear background is dashed black line (top data). Actual Gaussian fitted peak are shown as bottom data. **A**: CTAB mole fraction (x_{CTAB}) = 0.667 **B**: x_{CTAB} = 0.5 **C**: x_{CTAB}=0.333.

x_{CTAB}	q_{peak} (Å^{-1})	d (Å)	Δq	Apparent Crystallite Size (Å)	Number of units
0.667	0.1173±0.0003	53.6±0.2	0.0213±0.0007	295±9	5.5±0.2
0.5	0.1208±0.0004	52.0±0.2	0.0187± 0.001	336±2	6.5±0.03
0.333	0.1232±0.0006	51.0±0.3	0.0173±0.0018	363±35	7.1±0.75

Table 3.2 Results of the Gaussian peaks fitted to the peaks arising from the mesostructure of mixed CTAB: SB3-14 50mM with LPEI 1%wt. films. xCTAB is the mole fraction of CTAB, q_{peak} is the reciprocal space position of the peak, d is the real space distance of the crystallographic planes, and Δq is the FWHM of the fitted Gaussian peak.

It should be noted that application of peak width analysis to determine apparent crystallite size in a reflectivity experiment may be a tenuous analysis. This is due to roughness between the interfaces on the structures within the film possibly smearing out the peak and therefore adjusting the peak size and width. Although for

comparative purposes, some observations may be made from the variation in peak width analysis of the mixed surfactant and LPEI films.

Firstly, the peak fitting confirms the trend in reduction of *d*-spacing of the films as x_{CTAB} is decreased. Previously the peak positions had been taken from the maximum reflectivity data point of the peak. This method could be inaccurate due to the resolution of the data points i.e. the data points are binned and not continuous. Secondly, the apparent crystallite size for all mole fractions of CTAB in the mixed micelle with LPEI films is approximately the same. There is a trend where the apparent crystallite size is proportional to the mole fraction of CTAB. However care should be taken in treating this trend as unequivocal due to factors such as interface roughness which were not taken into account.

This trend could be explained by the reduction of CTAB in the films causing less LPEI to be associated into the films. If there is less of a volume fraction of polymer network in the film it allows the micellar aggregates to pack into a smaller volume. As there is less steric bulk imposed by there being fewer polymers present, the force of packing the micellar aggregates in to the film could cause less buckling as there is less polymer to inhibit the movement of micellar aggregates. This could allow the film to maintain a crystalline structure deeper into the solution.

Overall, the structure exhibited by films formed from mixed CTAB: SB3-14 films with LPEI 1%wt are very similar. It is not known from the data the exact form of the liquid crystal in the film due to only one peak being present. However it can be said there is enough surfactant in the film for an ordered phase to be formed, whether it is lamellae or a concentrated cylindrical micelle phase.

Films formed from mixed micelles and SPEI

It can be seen that the structures formed in films grown from mixed CTAB: SB3-14 50mM with SPEI 1% wt, are vastly different from the films formed with LPEI. The only highly ordered film that is formed when SPEI is the film forming polymer is that from solutions where CTAB is the only surfactant. Inspection of the NR profiles (Figure 3.3) show that when the films are formed from mixed micelles with the mole fraction of CTAB at 0.667 there is a film at the surface of the solution and a small peak at 0.128Å^{-1}, which is in the same position as the first order diffraction in the CTAB and SPEI. This suggests that the film is packed with the same size aggregates as in the CTAB and SPEI film. However, the peak is minimal in size suggesting that the extent of the liquid crystal phase into the bulk is vastly smaller than the structure in the CTAB and SPEI film.

As the mole fraction of CTAB is decreased further to 0.5, there is a broad hump in the NR profile. This suggests that there is some ordering at the surface however

nowhere enough to be considered a repeating periodic mesostructure in previous films. Visible inspection of the surface of the solution showed that no film was present after one hour. As the mole fraction of CTAB is decreased to 0.333 there is no evidence of an ordered phase at the interface. As with films formed from LPEI, there is no film evident when films are formed with just SB3-14 and SPEI.

The NR profiles of the films formed from mixed micelles and SPEI highlight the influence of the polymer form and molecular weight on film formation. As the mole fraction of CTAB was decreased with the films formed with hyperbranched LPEI, the structure exhibited by the films remained relatively constant. However when SPEI is used as the film forming polymer there is a drastic loss of mesostructured film as the CTAB mole fraction is decreased.

This is most likely due to there being a significantly reduced polymer network at the air-solution interface when films are formed with SPEI compared to films that formed from LPEI. Even though clearly the mole fraction of CTAB controls the extent of film formation, an entangled polymer network such as the one possible when LPEI is used as the film forming polymer assists in maintaining film integrity. When SPEI is used as the film forming polymer it is likely that an extensive polymer network is formed in the film. This allows surfactant-polymer aggregates to diffuse more freely and out of the film forming area at the interface.

3.3.4 Film formation and stability

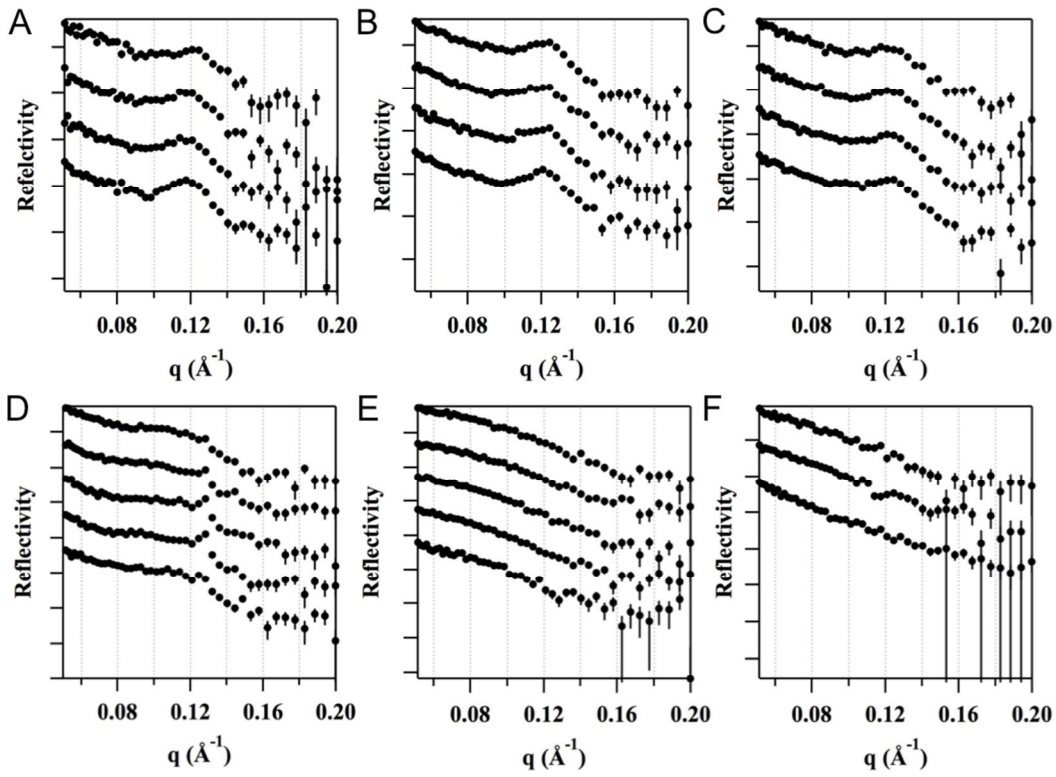

Figure 3.8 Time resolved NR profiles of films formed from mixed micelles of CTAB: SB3-14 50mM and PEI 1%wt. Profiles are offset for clarity. Uppermost NR profiles in each figure are at time = 30 seconds after pouring. Time progresses in 900 second steps sequentially to lowest NR profiles. **A**: X_{CTAB} = 0.667 with LPEI **B**: X_{CTAB} = 0.5 with LPEI **C**: X_{CTAB} = 0.333 with LPEI **D**: X_{CTAB} = 0.667 with SPEI **E**: X_{CTAB} = 0.5 with SPEI **F**: X_{CTAB} = 0333 with SPEI

Over the time frame of the NR experiments performed the structures apparent in the films formed from mixed micelles and PEI remained essentially constant (Figure 3.8). This was particularly true for LPEI films of all surfactant mixtures investigated whereas films made with SPEI only show slight variation in film structure of the time frame of the experiment. When 2 CTAB: 1 SB3-14 was used as the surfactant mixture to form films with SPEI there was variation in the film structure as the experiment progressed. The first 900 second NR profile showed a film structure that exhibited some periodicity such as that of a correlated micellar phase. As the experiment progressed between 900 and 2700 seconds a weak diffraction peak appeared and disappeared after 3600 seconds.

This occurrence of structure and the subsequent loss of structure could be attributed to film collapse or the film being comprised of a surfactant and polymer composition that produces co-existents phases/composition at the phase boundary. In the case of film collapse it has been shown in growth studies of pure CTAB/LPEI films performed at much lower concentration than this study that exposure of the solution to ait over time causes the pH of the solution to decrease enough due to CO_2 adsorption from air, to cause protonation of PEI and the subsequent loss of the cationic-dipole interaction between CTAB and LPEI.[39] However this effect is not seen in any of the other films; the LPEI films are at relatively high polymer concentration and most likely are subject to a large degree of complex entanglement from the LPEI in the films. The SPEI films do not have the same degree of entanglement either the degree of association between surfactant and polymer so it is likely they are more affected by any attenuation of the interaction between polymer and surfactant

As discussed previously film dissolution could also be attributed to the extent to which the polymeric network of the films allows polymer-surfactant aggregates from the films to diffuse back in to the bulk even after the PEI has become more charged from exposure to carbon dioxide. Even though the structure of the LPEI films appears roughly constant, when films are formed from 2CTAB:1SB3-14 and LPEI, it appears that the film is growing more structured with time. A slight increase in the peak height is apparent as the time resolved measurements progress suggesting more

aggregates are packing into the film, or are rearranging within the film to form larger ordered domains. For all other LPEI NR profiles there is minimal change.

3.4 Bulk behaviour of CTAB/SB3-14/PEI solutions

Having considered the effects the composition of mixed CTAB and SB3-14 micelles and the molecular weight of PEI have on the film structure, the bulk behaviour of film forming solutions will now be considered. This is necessary as a more complete understanding of the interactions involved in the solutions will lead to a better understanding of the processes of film formation. Understanding the film formation interactions of the CTAB/SB3-14/PEI film forming system will provide insights which may enable future production of better ordered yet biocompatible films.

3.4.1 Critical micelle concentration of CTAB/SB3-14 mixtures

The critical micelle concentration (CMC) of CTAB, SB3-14 and mixed CTAB:SB3-14 solutions in water were determined by determining surface tension as a function of concentration, the results are plotted in figure 3.9A and presented in table 3.3. This information enables the interactions of surfactant mixing to be studied, by calculating the composition of mixed micelles via the deviation of the mixed CMC from that of ideally mixed micelles. Understanding these interactions may provide insight in to the processes of film formation at the interface.

Surface tension of the air-water interface is inversely proportional to concentration of surfactant. As more surfactant is introduced to the solution the surfactant occupies the interface reducing the surface tension of water at the interface. This results in the reduction of surface tension at the interface and removal of the hydrophobic tail of the surfactant from the aqueous environment. As the concentration of surfactant increases it reaches a point where monomeric surfactant and aggregated surfactant in the form of micelles can co-exist in equilibrium. As increasing the concentration of surfactant after the CMC creates more micelles, the surface tension change with concentration typically exhibits a sharp decrease in gradient, indicating the onset of micelle formation

The CMC was taken from a quadratic fit to the pre CMC region of the plots which represents the adsorption isotherm and a linear fit to the region of the plots post CMC which exhibits a linear gradient with concentration. The CMC was then calculated by numerically solving the derived equations simultaneously to obtain the point of intersection. As the surface tension plots overlap this is represented graphically in figure 3.9B.

If the surface tension profile was non-linear after the CMC point then the linear regression was performed upon the data points where this was necessary, for samples

containing CTAB, as the surface tension decreased with concentration above the CMC inflection. Ionic surfactants have been reported to exhibit this behaviour due to charge screening of the surface associated surfactant by charged micelles in solution. This increases the area available to surfactant at the surface through decreasing charge repulsion as the bulk surfactant concentration increases above the CMC.[40]

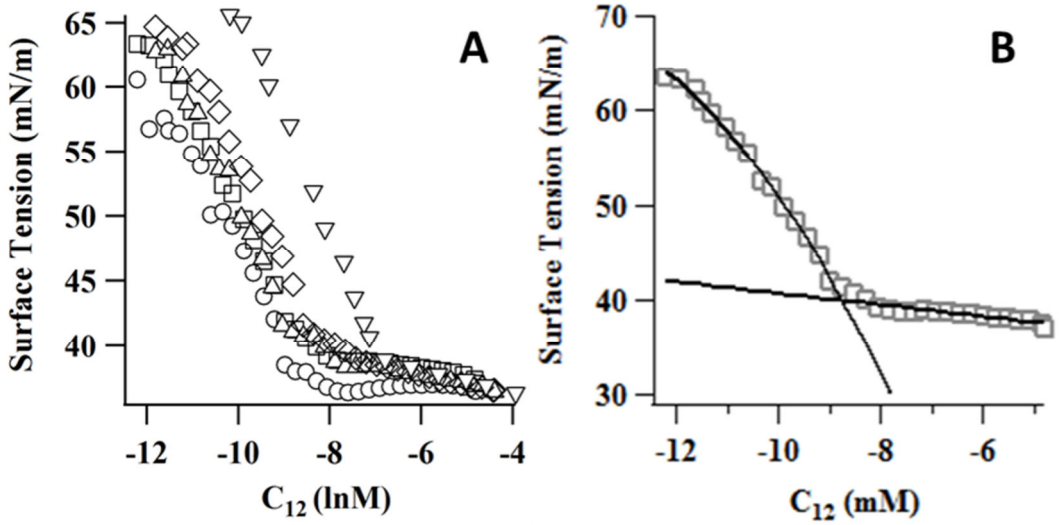

Figure 3.9. A: Graph showing surface tension against surfactant concentration for CTAB (closed triangles), 2 CTAB:1 SB3-14 (open squares), 1 CTAB:1 SB3-14 (closed squares), 1 CTAB:2 SB3-14 (open circles) and SB3-14 (closed circles). **B**: A ln-ln plot to demonstrate how the position of the CMC point is determined from the data, where the CMC point is taken as the intercept of the two lines. The data example shown as open squares is SB3-14. For clarity no error bars are shown on this figure.

Sample	CTAB	2CTAB: 1 SB	1CTAB: 1SB	1CTAB: 2SB	SB3-14
α_1.	1	0.667	0.5	0.333	0
$\boldsymbol{CMC_{12}}$ **[mM]**	0.912±0.052	0.185±0.019	0.149±0.023	0.129±0.009	0.143±0.009

Table 3.3 Results of CMC as a function of x_{CTAB}

The CMC of CTAB is larger than that of SB3-14 (Figure 3.11, Table 3.3). As the free energy of micellisation, ΔG°_{Mic}, is related to to the CMC (Equation 3.3) this result is expected.

$$\Delta G^{\circ}_{Mic} = \ln(CMC)RT \quad 3.3$$

The free energy hydrophobic contribution from the longer alkyl chain[41] of CTAB compared to that of SB3-14 is not large enough to overcome the reduction in free energy headgroup contribution from the larger headgroup area of CTAB due to charge repulsion and the entropy loss due to counter-ion coordination.[42] As the zwitterionic headgroups of SB3-14 have no counter-ion they result in a lower CMC than that for CTAB. The CMC values determined for CTAB and SB3-14 are in good agreement with literature values (Table 3.3).[43,44]

The CMC of the mixed surfactant solutions are a combination of the CMC of SB3-14 and CTAB. If there is no interaction between the two surfactants then the surfactant will mix ideally and the composition of the mixed micelles will be the same as the composition of the bulk of the mixed surfactants solution.[45] The mixed CMC will occur at the total surfactant concentration (CMC_{12}) that corresponds to the comprising single surfactant CMC and the bulk mole fraction of the two surfactants. This relation is described by Clint.[46]

If the micelle is treated as a separate phase from the bulk solution, known as the pseudophase separation model, then at the CMC the surfactant monomers are at equilibrium with the surfactant within the micelle. Therefore the chemical potential must be equal (equation 3.4)

$$\mu_{mono} = \mu_{micelle} \quad 3.4$$

Where μ_{mono} is the chemical potential of the monomeric surfactant and $\mu_{micelle}$ is the chemical potential of the surfactant within the aggregated micelle.

When considering mixtures of surfactant this can be extended by treating the mixed micelle as a mixed phase, with the condition of equations 3.5 and 3.6 for a binary mixture of surfactant

$$c_1 = x_1 CMC_1 \quad 3.5$$

And

$$c_2 = (1 - x_1) CMC_2 \quad 3.6$$

Where c_i is the concentration of monomeric surfactant *i,* x_i is the mole fraction of surfactant i in the mixed micelle and CMC_i is the critical micelle concentration of surfactant *i*.

At the CMC of the mixed surfactant system CMC_{12}, when there are a small number of micelles the bulk surfactant mole fraction of surfactant α_i can be related to c_i

$$\alpha_1 CMC_{12} = x_1 CMC_1 \tag{3.7}$$

and

$$(1-\alpha_1)CMC_{12} = (1-x_1)CMC_2 \tag{3.8}$$

Where α_1 is the bulk mole fraction of surfactant 1 in the solution.

By eliminating x_1, CMC_{12} in the case of ideal mixing of surfactants can be calculated from the bulk mole fractions of the mixture surfactants and the respective pure CMC's.

$$\frac{1}{CMC_{12}} = \frac{\alpha_1}{CMC_1} + \frac{(1-\alpha_1)}{CMC_2} \tag{3.9}$$

The CMC_{12} as a function of α_1 which in this case is the bulk mole fraction of CTAB in the mixed surfactant solution is presented in Figure 3.12 which also has the CMC_{12} for the ideal mixing case from equation 3.9 for comparison. It can be seen from figure 3.10 that the experimental CMC_{12} values fall below the value of the predicted ideal CMC_{12}. This suggests that the two surfactants do not mix ideally and there is an interaction between the surfactants causing non-ideal mixing. For clarity, the experimental and predicted ideal CMC_{12} as a function of α_1 are presented numerically in table 3.4.

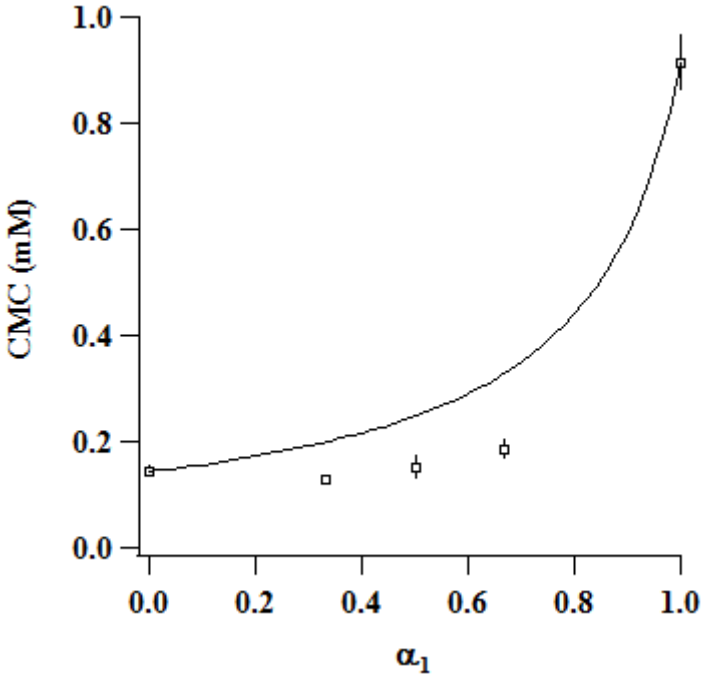

Figure 3.10 Experimental CMC_{12} (square markers) and ideal CMC_{12} (solid line) as a function of the mole fraction of CTAB in the solution, α_1.

Sample	CTAB	2CTAB: 1 SB	1CTAB: 1SB	1CTAB: 2SB	SB3-14
α_1.	1	0.667	0.5	0.333	0
$\boldsymbol{CMC_{12}}$ **[mM]**	0.912±0.052	0.185±0.019	0.149±0.023	0.129±0.009	0.143±0.009
Ideal $\boldsymbol{CMC_{12}}$ **[mM]**	0.912	0.327	0.248	0.199	0.43

Table 3.4. Values of CMC from data presented in Figure 3.2. SB3-14 is abbreviated to SB in the mixed samples. Numeric prefixes signify the molar ratio of the surfactants

If there is any interaction between the two surfactants in the mixture then the mixed CMC will differ from the ideal case. If the interaction is an attractive interaction the mixed CMC will be lower than the ideal mixed CMC and if the interaction is repulsive then the mixed CMC will be greater than the ideal case. The direction of

the deviation of the CMC from the ideal case can be explained by considering the effect the interactions have on the free energy of mixing.

Considering a conceptual model of the contributions towards the free energy of micellisation, it is possible to see how interactions between the surfactants of a binary mixture can lead to non-ideal behaviour of CMC_{12}. In the model proposed by Shiloach and Blankschtein[47], the free energy of micellisation g_{mic} of a two surfactant mixture is described as a summation of several terms including the electrostatic terms for ionic headgroups (Equation 3.10)

$$g_{mic} = g_{tr} + g_{int} + g_{pack} + g_{st} + g_{elec} \qquad 3.10$$

Where g_{tr} is the free energy of transfer of a hydrophobic aliphatic surfactant tail from the hydrophilic aqueous ebnvironment to the hydrophobic micellar core, g_{int} is the free energy contribution of the resultant area of the hydrophobic tail exposed to the aqueous solution due to insufficient shielding by the head group, g_{pack} is the free energy contribution from the packing of the surfactant tails in the micellar core, g_{st} is the free energy contriubution resulting from steric hindrance between surfactant headgroups hindering the transfer of a surfactant from solution to the micelle and g_{elec} is the contribution resulting from electrostatic repulsion and counter-ion association (in the case of ionics) between the surfactant headgroups.

As all the free energy contributions hold for the case of g_{mic} of a single surfactant it is easy to visualise how CMC_{12}.of a binary surfactant system can deviate from ideal behaviour. As the CMC of a system is related to the free energy of micellisation by (Equation 3.3), consideration of the free energy model (equation 3.10) allows changes in the mixed CMC to be attributed to differences in the molecular structure of the constituent surfactants.

In the free energy model (equation 3.10), the only negative contribution to the free energy of micellisation is g_{tr} which is strongly negative due to the hydrophobic effect introduced by Tanford[41] and is the driving force of micellisation. All other free energy contributions are positive and can therefore be considered to hinder the formation of micelles. In the case of the free energy of micellisation all the terms in equation 3.10 are present. In the case of a binary mixture of surfactant they are also present however they are a summation of each instance of monomer of both species. If there is any interaction between the two surfactants for any of the terms in equation 3.10 then this will have an overall effect on the free energy of micellisation of the mixed micelle and therefore the CMC_{12}.

Examples of differences in the free energy contributions of equation 3.10 are mixing surfactants with tails of same chemical type yet different tail lengths for g_{tr}, mixing

surfactant with different headgroup types which affect the g_{int}, g_{st} and g_{elec} terms through differences in the headgroup shielding of the hydrophobic core, differences in headgroup size and form, and differences in the electrostatic nature of the headgroup respectively. G_{pack} will be affected by surfactant tails of different sizes as asymmetry in the tail lengths may cause the surfactant to pack more or less efficiently. In the case of the system of mixed micelles of SB3-14 and CTAB there are differences in the surfactant tails lengths, the size of the headgroups and the electrostatic nature of the headgroups which much be considered to explain the deviation from ideal mixing.

3.4.2 Modeling interactions between species in mixed micelles

Qualitative comparison of the experimental CMC_{12} against the predicted ideal mixing CMC_{12} shows that there is an interaction between CTAB and SB3-14 due to deviation from ideal behaviour. The interaction between surfactants may be investigated through application of a regular solution theory (RST) approximation[48-50] to the pseudophase separation model of micellisation. This allows activity coefficients for each surfactant to be calculated where the activity coefficient for each surfactant in the ideal case is 1. RST also allows the interaction between two surfactants described by one parameter, β. The magnitude of β is an indication of deviation from the ideal mixing case whereas the sign of β indicates the whether the deviation from the ideal case is one of synergistic mixing (a negative β parameter) or antagonistic mixing (a positive β parameter).

In the RST analysis the activity of each surfactant within the micelle deviates from unity which modifies the mixed CMC_{12} from the ideal case. This is demonstrated by the modification of equations 3.11 and 3.12 with activity coefficients. In the case of ideal mixing the activity coefficients are equal to 1

$$\alpha_1 CMC_{12} = x_1 f_1 CMC_1 \qquad 3.11$$

And

$$(1-\alpha_1) CMC_{12} = (1-x_1) f_2 CMC_2 \qquad 3.12$$

Where f_i the activity coefficient for a surfactant and x1 is the mole fraction of CTAB in the surfactant micelle

From elimination of x_1 from equations 3.11 and 3.12 allow the non-ideal mixed CMC_{12} to be calculated from the bulk mole fractions and CMC of the pure surfactants if the activity coefficients are known from equation 3.13

$$\frac{1}{CMC_{12}} = \frac{\alpha_1}{f_1 CMC_1} + \frac{(1-\alpha_1)}{f_2 CMC_2} \quad 3.13$$

The activity coefficients are calculated from the β parameter in equation 3.14 and equation 3.15.

$$lnf_1 = \beta(1-x_1)^2 \quad 3.14$$

And

$$lnf_2 = \beta {x_1}^2 \quad 3.15$$

To calculate the beta parameters it is necessary to first calculate the mole fraction of CTAB within the surfactant micelle. In the regular solution approximation this is achieved by iterative minimisation of equation 3.16

$$x_1^2 \ln\left(\frac{\alpha_1 CMC_{12}}{x_1 CMC_1}\right) = (1-x_1)^2 ln \frac{(1-\alpha_1)CMC_{12}}{(1-x_1)CMC_2} \quad 3.16$$

When a value for x_1 has been calculated, β may be calculated by

$$\beta = \frac{\ln(\alpha_1 CMC_{12}/x_1 CMC_1)}{(1-x_1)^2} \quad 3.17$$

β accounts for the difference in interaction between monomers of similar structure compared to the interaction between surfactants of different structure within the mixed micelle. Specifically it provides an assessment of the stability of the mixed micelle compared to the pure micelles of the mixture components. β can be expressed by accounting all interactions by

$$\beta = (E_{11} + E_{22} + 2E_{12})/RT \quad 3.18$$

Where E_{11}, E_{22} and E_{12} are the interactions between monomers of surfactant 1, between monomers of surfactant 2 and between monomers of surfactant 1 and surfactant 2 respectively.

There are numerous examples of the regular solution approximation and the beta parameter being used as a method of characterising the interaction between sulfobetaine zwitterionic surfactants and ionic surfactants.[51-54] However there has been considerable debate as to whether the regular solution approximation is a valid model for mixed micelle systems containing ionic components where counter-ion binding plays a significant role.[50,55] Also the regular solution approximation treats the mixture as a near ideal regular solution, however when considering counter-ion binding plus the constraints of packing numerous surfactant molecules into a geometric shape then there is serious deviation away from the regular solution model which does not take any of this into account. One significant boundary for the regular solution approximation is that as α_1 is varied, β should be constant for the regular solution approximation to considered valid[56], although this isn't always strictly followed in the literature.

To account for the presence of ionic surfactant in the mixed micelles, Maeda's modified RST analysis[56] was further applied to the CMC data. This modified RST analysis introduces an additional β parameter to describe the addition of ionic surfactant to a non-ionic micelle. According to Maeda[56], the free energy of micellisation of the mixed micelle can be described by

$$\Delta G^{\circ}_{mic} = \beta_0 + \beta_1 x_1 + \beta_2 {x_1}^2 RT \quad 3.19$$

Where x_1 is the mole fraction of the ionic surfactant in the mixed micelle (calculated from regular RST analysis) and β_2 is equal to β calculated from the regular RST analysis.

$$\beta_0 = \ln(CMC_2) \quad 3.20$$

$$\beta_1 = \ln(CMC_1/CMC_2) - \beta_2 \quad 3.21$$

The additional beta parameter β_1 describes the difference in standard free energy associated with the exchange of an ionic surfactant monomer for a non-ionic monomer in the mixed micelle if any change is size is disregarded. Specifically $RT\beta_1$ is equivalent to the difference between the free energy of micellisation of the non-ionic surfactant and the transfer of an ionic monomer into the non-ionic micelles.

The CMC_{12} of the mixed surfactant solutions were first evaluated using Rubingh's regular solution approximation using equations 3.09 to 3.17 to allow analysis by Maeda's modified RST for mixed micelles containing ionic species using equations 3.19. The results are presented in table 3.5. All mixtures of CTAB and SB3-14 exhibited a negative β factor (β_2 in table 3.5) which indicates there is an attractive association between CTAB and SB3-14. Considering the stipulation for the attractive association between the surfactants to be considered synergistic, $\beta > \ln(CMC_1/CMC_2)$ then all exhibit synergism, as the magnitude of the beta factor is greater than 1.85.

Other characteristics of the RST analysis along with the negative β parameter are that the activity coefficient of the non-ionic SB3-14 within the mixed micelle at the CMC is greater than that of ionic CTAB throughout the variation of α1. The activity coefficients are calculated from x and β using equation 3.12. It follows that if the activity coefficient of the ionic surfactant in the micelle is less than that of the non-ionic surfactant then x is smaller than α_1.

	CTAB	2CTAB:1SB	1CTAB:1SB	1CTAB:2SB	SB3-14
α_1	0	0.333	0.5	0.667	1
CMC_{12}(mM)	0.143	0.129	0.149	0.185	0.912
Exp G°_{mic}	-21.92	-22.18	-21.82	-21.29	-17.345
RSTG°_{mic}	-21.92	-22.21	-22.00	-21.73	-17.34
x_1	0	0.259	0.313	0.376	1
β_0			-8.85		
β_1		-1.25	-0.98	-0.78	
β_2		-3.1	-2.83	-2.63	
f_1		0.182	0.262	0.360	
f_2		0.812	0.758	0.689	

Table 3.5 Results of the modified Maeda RST analysis for mixed micelles containing ionic surfactants. Exp G°_{mic} and RST G°_{mic} are the experimentally derived and RST mocelled free energy of micellisation respectively. All other parameters are defined in the text. SB3-14 is abbreviated to SB in the mixed samples. Numeric prefixes signify the molar ratio of the surfactants

One of the stipulations for RST is that the CMC data be fitted to a single beta parameter however a satisfactory fit was unattainable to the data due to their only being three points in $\partial CMC_{12}/\partial\alpha$ which prevents an accurate estimation

of $\partial CMC_{12}/\partial x_1$ and therefore constant beta parameters for the analysis. Therefore the beta parameters were calculated individually for each instance of α. Another consideration is the RST model validity when applied to mixtures containing ionic surfactants. The entropic contribution of associated counter ions and changes in the fraction of associated counter ions with composition suggest that treatment the micelle as mixing of regular solutions may be invalid

Considering the application Maeda's modified RST analysis, which accounts for the presence of ionic surfactant in the mixed, β_1 is negative for all α investigated. As stated by Maeda[56], β_1 accounts for the standard free energy of one ionic surfactant molecule displacing one non-ionic surfactant molecule from the mixed micelle. The free energy change of this process is the sum of the hydrophobic and hydrophilic contributions to the free energy. If the hydrocarbon tails of the surfactants in the mixed micelle are of equal length then the interaction between the ionic and zwitterionic head group will dominate the value of β_1. However, when there is a disparity in the tail length of the surfactants, then the free energy change of transfer of the longer tail dominates. Therefore the β_1 value across all α investigated is negative. As discussed previously ionic surfactant micelles exhibit a decrease in entropy due to the coordination of counter ion relative to non-ionic micelles upon micellisation. Although the β_1 value is negative for all α, it's absolute value decreases as x_1 increases (table 3.5). This is due the increased mole fraction of CTAB in the mixed micelle counteracting the additional transfer of CTAB monomers hydrophobic contribution to the free energy change.

In order to understand the processes leading to the formation of films from solution of CTAB: SB3-14 and polyethylenimine. SANS was performed to study the bulk properties of the solutions.

3.5 Determining constants for modelling of SAS and NR data

Prior to modeling the SANS, SAXS and NR data from CTAB/SB3-14 mixed surfactant and PEI films it was necessary to obtain all independent constants relevant to the datasets such as the volume and scattering length density of each species. In this case the data for CTAB, SB3-14, PEI and water must either be found from previously reported results or calculated. The molecular volume and scattering length densities from CTAB[20], PEI[57] and water (D_2O[20]) are well known. However in the case of the SB3-14 there is not, to the authors' knowledge, reliable data in the literature for the molecular volume and scattering length density. Therefore it was necessary to determine these parameters experimentally. The constant parameters used in modeling the NR data are presented in table 3.6.

Type	Moiety	Volume Å^3	Scattering Length 10^{-12} cm^{-1}	SLD 10^{-6} Å^{-2}

Tail[20]	CH_3	54.3	-0.457	-0.84
	CH_2	26.9	-0.083	-0.31
	CD_3	54.3	2.659	4.91
	CD_2	26.9	1.999	7.43
Headgroup	$N(CH_3)_3^{+20}$	102.3	-0.435	-0.43
	$N(CH3)_2^{+}(CH_2)_3SO_3^{-}$	181.33	1.794	0.099
Counter ion[20]	Br^-	39.3	0.677	1.72
Solvent{Berr 1986)	D_2O	30.2	1.915	6.34
Single Components	CTAB	560.1	-20.72	-0.37
	d33-CTAB	560.1	307.5	5.49
	SB3-14	585.33	2.341	0.04
	PEI[57]	69.4	-0.208	-0.3
Mixtures	2 CTAB: 1 SB3-14	575.2	-13.22	-0.23
	2 d33-CTAB: 1 SB3-14	575.2	209.9	3.65
	1 CTAB:1 SB3-14	577.7	-9.242	-0.16
	1 d33-CTAB:1 SB3-14	577.7	157.7	2.73
	1 CTAB:2 SB3-14	580.1	-5.394	-0.093
	1 d33-CTAB:2 SB3-14	580.1	106.1	1.83

Table 3.6 SLD and molecular volume data for the molecules of interest in this work, collated from Berr *et al*[20] and Wong *et al*[57] plus experimental data. The 'mixtures' values are calculated from equation 3.22.

The values of the SLD of dry surfactant mixtures were calculated from equation 3.22

$$SLD_{MIX} = x_{CTAB}SLD_{CTAB} + (1 - x_{CTAB})SLD_{SB3-14} \qquad 3.22$$

Where SLD_{MIX}, SLD_{CTAB} and $SLD_{SB3\text{-}14}$ are the SLD of the dry mixed surfactant micelle, CTAB and SB3-14 respectively; x_{CTAB} is the mole fraction of CTAB in the mixed micelle.

When calculating the predicted SLD of the dry surfactant mixtures it was assumed that the mole fraction of CTAB in the micelle equaled that of the bulk. As the concentrations investigated were magnitudes greater than the CMC_{12}, it was likely that the compositions would be ideal. This was confirmed later through analysis.

The SLD for mixtures of CTAB and SB3-14 have been presented in table 3.7 without any bromide counter-ion association on the surfactant micelle. Later in

applying a multilayer model to the NR data in the thesis it was concluded that the neutron SLD contribution from an associated bromide ion was too small to show a notable affect when fitting the data. This was confirmed through calculation. Table 3.7 shows the SLD of all compositions of mixed micelle modeled with 0% and 100% bromide association. It can be seen that the SLD difference is minimal, so was too small to be fitted reliably. In the case of modeling the small angle scattering data presented later in the thesis, the shell SLD was fitted freely. Therefore bromide association was accounted for in the fitted SLD value.

Micelle composition	CTAB isotope	SLD 0% Br^- $\times 10^{-6}$ $Å^{-2}$	SLD 100% Br^- $\times 10^{-6}$ $Å^{-2}$	Difference $\times 10^{-6}$ $Å^{-2}$
2 CTAB:1 SB3-14	*h*	-0.227	-0.141	0.086
	d	3.623	3.468	0.156
1 CTAB:1 SB3-14	*h*	-0.159	-0.095	0.064
	d	2.708	2.592	0.116
1 CTAB:2 SB3-14	*h*	-0.091	-0.049	0.042
	d	1.806	1.730	0.077

Table 3.7 Difference in SLD for dry surfactant mixtures with 0% and 100% Br^- association; *h* and *d* represent hydrogen and deuterium

The omission of the bromide counter-ion from the modeling is not an assumption that bromide is completely dissociated from the micellar surfaces. Its omission is due to the relatively minor contribution of the bromide to the neutron scattering length density of the surfactant micelles and the resolution of the NR experiments. Fitting of the bromide associated fraction in a system comprised of two surfactants, polymer and water when only two neutron contrast experiments were performed would not give an accurate value, particularly when neither of the neutron contrast experiments included SLD variation of the headgroup or solvent contrast matching to the headgroup.

The difference between 0% and 100% bromide association decreases as the mole fraction of CTAB is increased. However, in aqueous solution, as discussed in the introduction chapter, bromide dissociation from pure micelles is between 5% and

30%. Assuming that bromide has a coordination number of 4 water molecules[20], the SLD of hydrated bromide would be 5.18×10^{-6} Å^{-2} which is closer to the SLD of D_2O than dry bromide at 1.72×10^{-6} Å^{-2}. Therefore the differences between a fully dissociated and fully associated bromide environment in an aqueous environment is even less than demonstrated in table 3.7, in the case of neutrons.

3.5.1 Determination of SB3-14 volumetric and scattering properties

The molecular volumes[20,41] and scattering lengths[20] of methyl and methylene groups that form surfactant micelle cores are well documented in the literature as well as values for the quaternary ammonium headgroup, plus the bromide ion that comprises trimethylammoniumalkyl bromide salts.[20] However, the molecular volumes of SB3-14 and sulfobetaine surfactants in general are not as extensively reported. Therefore, densitometry was performed to determine the molecular volume of the headgroup and subsequently its scattering length density.

Application of the pseudo phase mode[58,59] to a solution containing surfactant above the CMC can determine the volumetric contribution of the surfactant to the solution volume by

$$V = n_w V_w + n_m V_m + n_a V_a \qquad 3.23$$

Where V is the total volume of the solution, V_w, V_m and V_a are the molar volumes of water, the monomeric surfactant and the aggregated surfactant; n_w, n_m and n_a are the number of moles of water, monomeric surfactant and aggregated surfactant, respectively.

When the surfactant is present above the CMC in solution the surfactant is present as both monomeric surfactant and aggregated surfactant in micelles. Therefore, the partial molar volume of surfactant in solution V_s can be separated out into monomeric and aggregated terms

$$n_s V_s = n_m V_m + n_a V_a \qquad 3.24$$

Where n_m and n_a are the number of moles of monomeric surfactant and aggregated surfactant, respectively; V_m and V_a are the molar volumes of the monomeric surfactant and aggregated surfactant respectively.

For the molar volume of monomeric surfactant to be reliably determined, densitometry experiments should be performed below the CMC of the surfactant where the surfactant is assumed to exist exclusively in a non-aggregated form. However, if surfactant has a low CMC in conjunction with a molecular density near to that of the solvent it is difficult to accurately determine the molar volume of the monomeric surfactant. It is possible with prior knowledge of the CMC of a surfactant to determine the apparent molar volume of both the monomeric and aggregated surfactant. By knowing the dependence of the molar volume of surfactants on concentration, assumptions may be made. The three main classes of surfactant; ionic, non-ionic and zwitterionic, exhibit different relationships of their apparent molar volumes with changes in concentration. They can be split in to ionic and hydrophobic dependencies as shown by equation 3.25

$$\Phi_s = \Phi_s^0 + I + H \qquad 3.25$$

Where Φ_s is the apparent molar volume of the surfactant, Φ_s^0 is the apparent molar volume of the surfactant at infinite dilution, I is the term describing the volume dependency on concentration due to ionic phenomena and H is the term describing the volume dependency with concentration of hydrophobic phenomena.

1:1 ionic surfactants exhibit a volumetric dependency on ionic effects with concentration with terms dictated by Debye-Huckel theory as they show a square root relationship with concentration. In the case of ionic surfactants $I = Am^{\frac{1}{2}}$ where the exponent of molality, m, is a square root according to the literature and A is a parameter that can be calculated form Debye-Huckel theory. Non-ionic surfactants are not affected by ionic effects due to the nature of their headgroup. Therefore contribution of I to the apparent molar volume is unity. Zwitterionic surfactants are ionic surfactants that exhibit no overall charge and by definition are non-ionisable. Of course amphoteric surfactants such as alkyl carboxybetaines are ionisable but true zwitterionic, as the sulfobetaine headgroup are not ionisable. Therefore, examples are found in the literature where zwitterionic surfactants are treated both as non-ionic surfactants and 1:1 ionic surfactants. For the purpose of the volumetric study presented in this work SB3-14 is treated as a non-ionic surfactant due to the fact that treatment as an ionic surfactant resulted in no significant improvement of derived results for the volume of the headgroup and therefore the simplest model was assumed. The H term in equation 3.25 is present to describe the hydrophobic contribution to the apparent molar volume of the surfactant. Therefore, $H=Bm$ where

the adjustable parameter *B* is found to decrease with increasing alkyl chain length in alkyl-chain based surfactants. For a single surfactant *B* is found to be constant.

As the *I* and *H* terms are considered in this study to be constant for the zwitterionic surfactant SB3-14, we can separate the apparent molar volume of the surfactant into monomeric and aggregated contributions according to the pseudophase separation model,[58] and calculate the mean surfactant molar volume from the concentration-weighted amounts of monomeric and aggregated surfactant

$$\Phi_s = p_m \Phi_m + p_a \Phi_a \qquad 3.26$$

Where $p_m + p_a = 1$ and $p_m = m_{CMC}/m$ and $p_m = (m - m_{CMC})/m$; Φ_m and Φ_a are the apparent molar volumes of the monomeric and aggregated surfactant respectively.

The apparent molar volume of the headgroup can then be calculated from iterative solution for Φ_s when equation 3.26 is expressed in terms of contribution of the alkyl chain of the surfactant monomeric and aggregated contributions to the mean surfactant molar volume plus the contribution of the sulfobetaine headgroup to the apparent molar volume, which gives

$$\Phi_s = \left(p_m \Phi_m\right)_{alkyl} + \left(p_a \Phi_a\right)_{alkyl} + \Phi^0_{headgroup} \qquad 3.27$$

Note that the contribution from the headgroup is that of the apparent molar volume of the headgroup at infinite dilution. It is assumed that this contribution is monotonic with respect to concentration. However, it is possible that this is not an accurate representation. Though with no data available below the CMC for SB3-14 and to the best of the author's knowledge no relevant studies performed in the literature, then it is assumed that it is monotonic. Figure 3.11A shows the densitometry profile of SB3-14 aqueous solutions where figure 3.11B (bottom) shows the mean apparent molar volumes of SB3-14 fitted to equation 3.27.

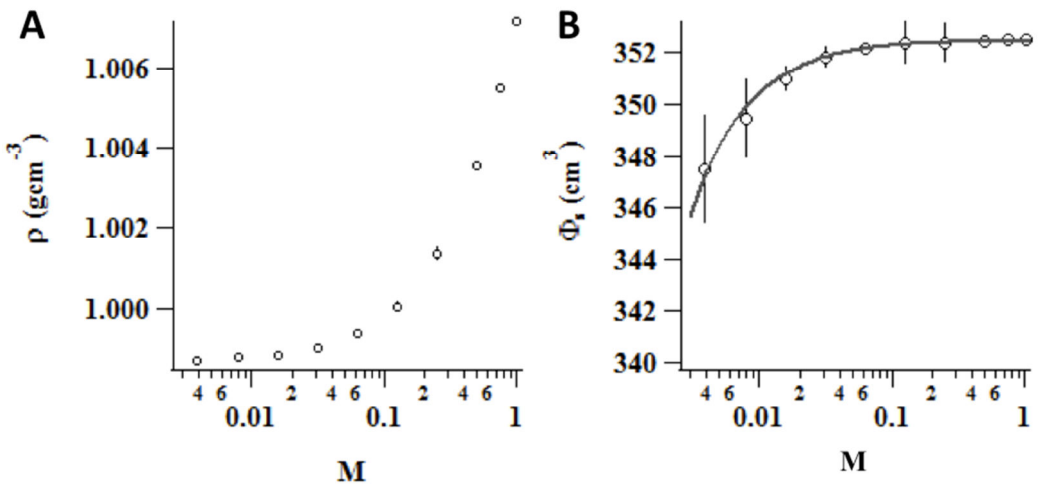

Figure 3.11. The densitometry profile of SB3-14 aqueous solutions (**A**) and the mean apparent molar volumes of SB3-14 fitted to equation 3.5 (**B**).

Solving equation 3.26 for Φ_s iteratively gives fitted values for Φ_m and Φ_a of 219±23 cm^3 and 353 ±0.1 cm^3, respectively. This equates to a molecular volume of 585.33±0.08 $Å^3$ per molecule of SB3-14 in the aggregated micellar state. It is now possible to calculate the molecular volume of the sulfobetaine headgroup of SB3-14 in the aggregated micellar state by firstly employing equation 3.27 to calculate the volume of the alkyl chain in the aggregated micellar state and then subtracting this value from the SB3-14 molecular volume.

$$V_{tail} = V_{CH_3} + n_{CH_2} V_{CH_2} \qquad 3.28$$

Here V_{tail}, V_{CH_3} and V_{CH_2} are the volumes of the whole alkyl chain tail, methyl group and methylene groups and n_{CH_2} is the number of methylenes in the hydrocarbon chain. The values of V_{CH_3} and V_{CH_2} in the micellar aggregated state in the literature show small variation around common values[59], mainly when calculated from surfactants of different electrostatic architecture or when calculated from mixed solvents of different isotopic composition such as heavy water and water mixtures. However, the variation appears to dominate only the apparent molar volume of the methyl groups and when actually summed in to the volume of the whole hydrocarbon chain produce similar results. For the purpose of this study, in the absence of fresh experimental data the molecular volume reported by Tanford[41] of $V_{CH_3} = 54.3$ $Å^3$ and $V_{CH_2} = 26.9$ $Å^3$ are used in the calculation of the SB3-14 headgroup volume. Therefore, for the 14 carbon chain of SB3-14 equation 3.28

calculates a volume of 404 $Å^3$ and equation 3.27 gives a headgroup volume of 181.33 $Å^3$

3.6 Model independent calculation of micellar composition from SANS

It is known from the surface tension data for mixed micelles of CTAB and SB3-14 that 50 mM solution of the mixed surfactants are well above the CMC. At the CMC it was shown that the mixed micelles are rich in SB3-13 compared to CTAB; however at concentration greatly exceeding the CMC it is well known that surfactant mixtures typically approach ideal mixing.[52] To prove this for the current system, composition of the mixed micelles was calculated from SANS analysis using a model independent approach.

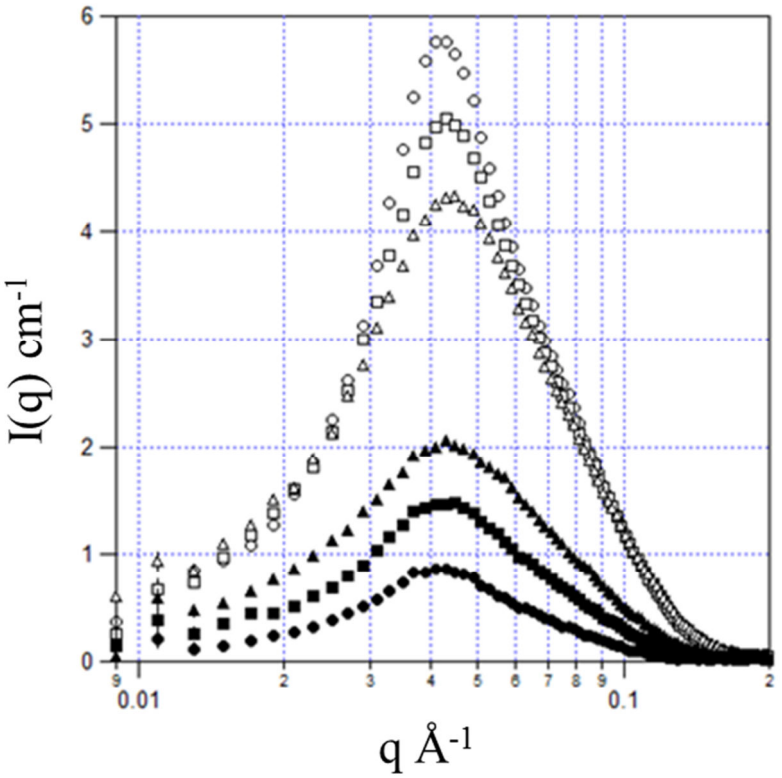

Figure 3.12. Solution small angle neutron scattering data of h33-CTAB: h29-SB3-14 (open points) and d33-CTAB: h29-SB3-14 (closed points) in 100% D_2O. The data were collected at ratios of 2:1 (triangles), 1:1 (squares) and 1:2 (circles).

Collecting SANS data from samples comprised of h33-CTAB: h29-SB3-14 in 100% D_2O and d33-CTAB: h29-SB3-14 in 100% D_2O and comparing the forward scattering intensity of each sample can solve the micelle composition without application of a model. Figure 3.12 shows SANS data from h33-CTAB: h29-SB3-14

in 100% D_2O and d33-CTAB: h29-SB3-14 in 100% D_2O in ratios of CTAB: SB3-14 of 2:1, 1:1 and 1:2. There is an obvious correlation peak in this data originating from interference of the scattering amplitude due to intermicellar interactions, which is accounted for subsequently in the analysis. However, assuming that the structure factor and form factor are congruent for the contrasted samples of the same molar composition, the $I(0)$ value can be used in equations 3.29 and 3.30 to determine the molar fractional composition of the surfactant micelles. In this study due to the noisy data evident at the edge of the instrument detector seen where $q \to 0$ the values used in equations 3.29 and 3.30 were taken as I_{max} where $\Delta q = 0$ between contrasts.

Component	Volume [Å^3]	Scattering Length [Å^{-1}]	SLD [×10^{-6} Å^{-2}]
CH_3	54.3	-11.217	-0.476
CH_2	26.9	-7.478	-0.1018
$N(CH_3)$	102.3	-4.911	-0.48
Br^-	39.3	6.795	0.173
$N(CH_3)_2(CH_2)_3SO_3$	181.33	12.291	0.675

Table 3.8. The scattering length and volume parameters used in the calculation of the composition.

The parameters used in the calculation of the composition are presented in table 3.8 and results in table 3.9. To determine the relationship between scattered intensity and the mole fraction, M_f (Equation 3.30) of CTAB in the mixed micelles surfactants the volume fraction, V_f (Equation 3.29) of CTAB must be calculated first

$$V_f = \frac{(\sqrt{R}-1)(\rho_{hSB3-14} - \rho_{D_2O})}{(\rho_{hCTAB} - \rho_{hSB3-14}) - \sqrt{R}(\rho_{dCTAB} - \rho_{hSB3-14})} \quad 3.29$$

Where $R = I_{h-h\,MAX}/I_{d-h\,MAX}$ with $I_{h-h\,MAX}$ and $I_{d-h\,MAX}$ as the maximum intensity of the scattering from each neutron contrast of the same composition; $\rho_{component}$ is the scattering length density of the indicated component

$$M_f = \frac{V_f/V_{CTAB}}{V_f/V_{CTAB} + (1 - V_f)/V_{SB3-14}} \quad 3.30$$

Where $V_{component}$ is the molecular volume of the indicated component.

Sample	$I_{max,}\ q_1 = q_2$ [Å^{-1}]	V_f	M_f	α	$\frac{M_f}{\alpha}$
2 h33-CTAB: 1 SB3-14	5.77	0.676	0.683	0.667	1.02
2 d33-CTAB: 1 SB3-14	0.85	0.676	0.683	0.667	1.02
1 h33-CTAB: 1 SB3-14	5.05	0.501	0.51	0.5	1.02
1 d33-CTAB: 1 SB3-14	1.47	0.501	0.51	0.5	1.02
1 h33-CTAB: 2 SB3-14	4.32	0.337	0.345	0.333	1.04
1 d33-CTAB: 2 SB3-14	2.04	0.337	0.345	0.333	1.04

Table 3.9. Results obtained from the model independent analysis of the data in figure 3.23. I_{max} is the maximum scattering intensity of a sample, V_f is the volume fraction of CTAB in the mixed micelle, M_f is the mole fraction of CTAB in the

mixed micelle and α is the mole fraction of CTAB of the total mixed surfactant monomers in the bulk solution

It can be seen in the table 3.9 that the calculated mole fractions, M_f, of CTAB within the mixed micelles is close to the mole fraction that was added to the bulk with the discrepancy being 2%, 2% and 4% for 2:CTAB:1 SB3-14, 1 CTAB:1 SB3-14 and 1 CTAB:2 SB3-14, respectively. However, the calculated value for the CTAB M_f has some error associated with it.

Firstly, it is reliant on the calibration of the small-angle scattering intensities to absolute units. Whilst the calibration of small-angle scattering instruments has vastly improved since their inception there is still some error associated with it regarding improvement of absolute correction.[60-63] Also, as the data could not be reliably extrapolated to $I(0)$, the value of I_{max} was chosen to perform the analysis. The point that was chosen for I_{max} may be subjected to errors in binning. This is not to say that the binning was incorrect, but more that the position of one bin from one small-angle scattering curve may not be in the exact same raw data q position of the binned I_{max} data point of the second, contrasting small-angle scattering curve used in the analysis. A final observation is that with a constant instrumental background present in all of the scattering data, as the difference in I_{max} of each corresponding curve tends to zero then the effect of the constant instrumental error will increase the error in the calculated CTAB mole fraction. However, literature states that the error in such an analysis can be as much as 10%[64] when steps have not been taken to analytically determine sources of error. Therefore, the error in the analysis is considered acceptable. It is assumed in further small-angle scattering analysis that the composition of the mixed micelles is that of the bulk composition from sample preparation. However this assumption is only correct if one type of micelle exits in solution. This can be verified with the subsequent analyses.

3.6 Model independent analysis of micelle form and structure factor from SANS data

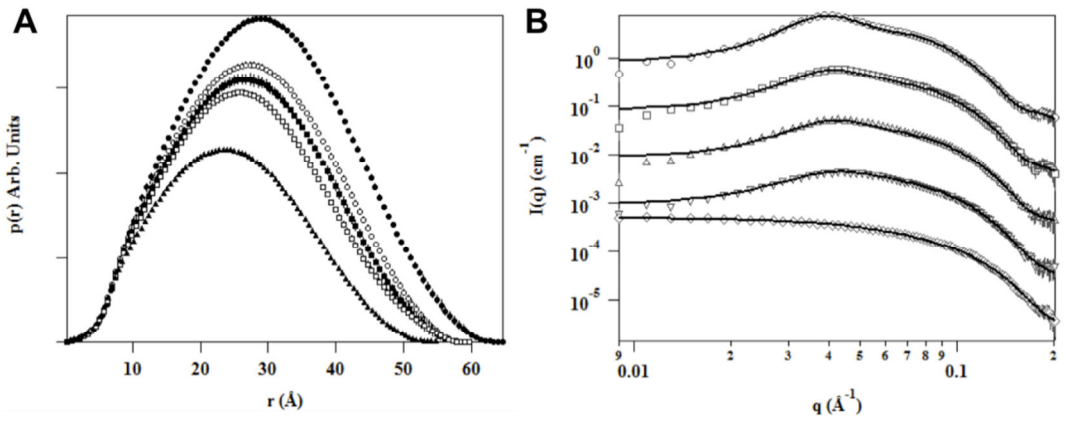

Figure 3.13. **A**: *p*(*r*)'s of CTAB (closed circles), 2 CTAB:1 SB3-14 (open circles), 1 CTAB: 1 SB3-14 (closed squares), 1 CTAB:2 SB3-14 (open squares) and SB3-14 (closed triangles), at 50 mM. **B**: Scattering data with GIFT fits of CTAB (open circles), 2 CTAB: 1 SB3-14 (open squares), 1 CTAB: 1 SB3-14 (upwards open triangles), 1 CTAB: 2 SB3-14 (downwards open triangles) and SB3-14 (open diamonds) at 50 mM. Data has been offset for clarity.

The indirect Fourier transformation (IFT)[65] method, which is a model independent method where only the maximum diameter of the particle is needed as an input value, as described in the theory chapter, was used to analyse the solution structures formed by the surfactant micelles. IFT can give information about the probability of distance correlations between areas of scattering length density contrast, thus giving information about the shape of the micelles, as discussed in the chapter 2. However, if the micelles are subject to inter-micellar interactions, which will be true in the case of non-dilute systems and charged micelles for example, then the scattering data is a product of not only intra-micellar correlations such as core-solvent and core-shell but also inter-micellar correlations. Therefore, a generalised IFT (GIFT)[66,67] analysis is needed, where a structure factor is used to account for these extra correlations in the scattering data. This introduces model-dependent parameters into the analysis, to account for the inter-micellar interactions.

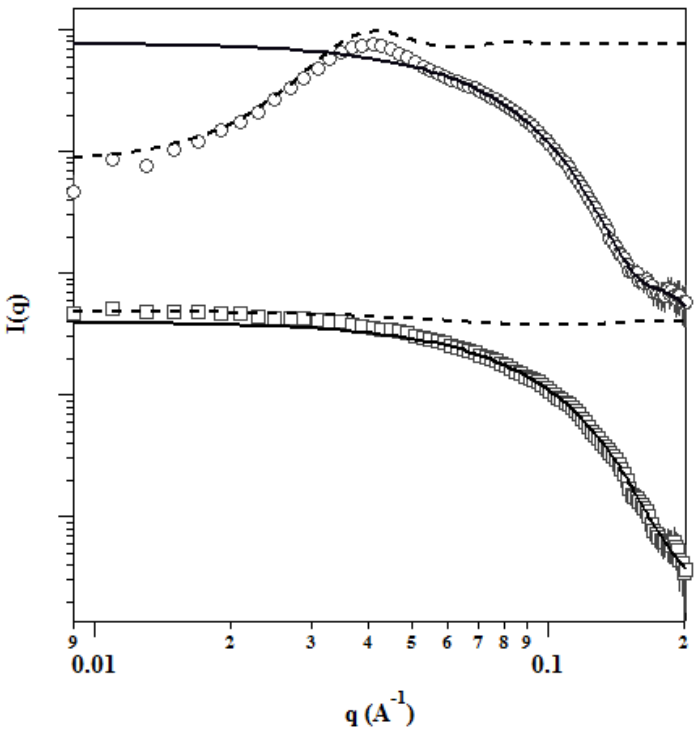

Figure 3.14. Example of fits with form (full line) and structure factor (dashed line) from the GIFT analysis. The two data sets are CTAB (top, open circles) and SB3-14 (bottom, open squares) at 50 mM.

GIFT fitting was performed on the SANS data of micellar solutions of CTAB, SB3-14, 2 CTAB: 1 SB3-14, 1 CTAB: 1 SB3-14 and 1 CTAB: 2 SB3-14 at 50 mM concentration (figure 3.13). Clearly these are not dilute solutions therefore structure factors had to be taken in to account. A micelle with CTAB in it can be considered as charged due to the cationic nature of the CTAB headgroup. A hard sphere structure factor was used for micelles containing CTAB. However, the hard sphere radius was allowed to fit freely to account for the repulsive nature of the micelles, as the charged spheres excluded volume would be bigger than that of a non-charged particle. For pure SB3-14 micelles it was necessary to apply a sticky hard sphere structure factor, as fitting the data with a hard sphere structure factor under-estimated the scattering at low q indicating attractive interactions between the micelles.

The higher scattering amplitude at low q could alternatively be due to micellar growth, however when checked with IFT and hard sphere GIFT this was not the case. That is, the scattering data could not be described simply by increasing the maximum dimension constant of the particles in an IFT analysis.

Figure 3.13A shows the pair distance distribution functions of the SANS data and figure 3.13B shows the GIFT fits to the SANS data. A representative data set is shown in figure 3.14, detailing the form factor and structure factor contributions to the scattering for pure CTAB and pure SB3-14 solutions at a concentration of 50 mM. All SANS data were well-described by use of the GIFT analysis. The results of the fitting are summarised in table 3.10.

Sample	R_g [Å]	R_{HS} [Å]	η_{HS}	τ [e^{-3} $(kT)^{-1}$]	R_{SHS}[Å]
CTAB	22.79±0.25	67.16±0.75	0.294±0.004	-----	-----
2 CTAB: 1 SB3-14	21.33±0.11	59.26±1.06	0.268±0.005	-----	-----
1 CTAB: 1 SB3-14	20.93±0.21	52.4±1.08	0.249±0.003	-----	-----
1 CTAB: 2 SB3-14	20.6±0.12	37±1.14	0.227±0.002	-----	-----
SB3-14	19.11±0.14	20.49±1.16	0.128±0.009	6.73±4.2	21.51±0.27

Table 3.10. Results from the GIFT analysis shown in figure 3.13, where R_g is the radius of gyration, RHS is the radius of the effective hard sphere, n_{HS} is the volume fraction of the hard sphere, τ is the strength of the attractive potential and R_{SHS} is the radius of the sticky hard sphere

As the mole fraction of SB3-14 is increased in the micellar solutions there are visible trends in the fitted parameters, as seen from table 3.4. R_g, R_{HS}, and η_{HS} are all inversely proportional to the mole fraction of SB3-14, whereas pure SB3-14 also exhibits an attractive surface of a certain depth and with a radius that is 5% greater than the R_{HS}. The reduction in the R_{HS} of the micelles when containing CTAB is indicative of the reduced charge as the mole fraction of CTAB is decreased. As the R_{HS} is greater than R_g it is apparent that this effective hard sphere size is indicative of the electrostatic repulsion of the micelles upon each other, preventing the closer contact between micelles that a true hard sphere interaction would allow. Considering the $p(r)$ in figure 3.13 all micelles are spheroid in form. Closer inspection of the $p(r)$ shows that the forms of the micelles exhibit some anisotropy, albeit only slightly as $p(r)_{max}$ is only slightly displaced to the left of $D_{max}/2$. This is seen from the slight skews evident on the right hand tails of the $p(r)$. All pair-distance correlations are of the type ++ meaning that they arise from correlations within the core of the micelle *i.e.* there is no scattering evident from a core-shell scattering in the data although this is likely contributed to by the limited q range of the LOQ instrument that the data was collected on. The GIFT analysis therefore provides some initial starting points for the fitting of the SANS data; any model must include an anisotropic form factor and charged structure factor, for homogenous particles, which decrease in size with a decrease in CTAB mole fraction.

3.7 Model independent analysis of SAXS data

Small-angle X-ray scattering data was collected to complement the existing SANS data. Due to the q range of the instrument and the relative electron density of the surfactants investigated it was possible to perform IFT and GIFT analysis, which showed the particles to have a core-shell structure. The probability densities as a function of distance from micelle centre are presented in Figure 3.15A. The GIFT fits to the SAXS data is presented in Figure 3.15B.

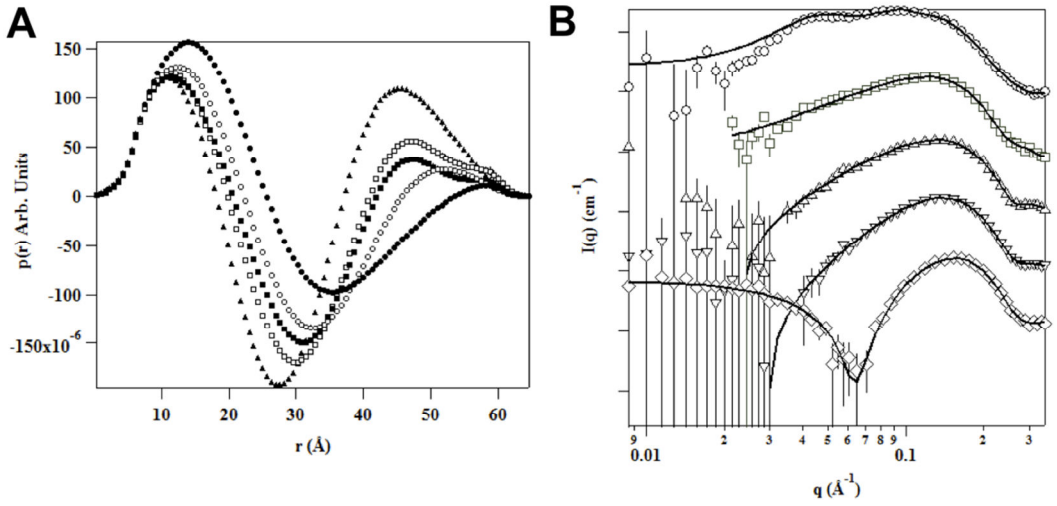

Figure 3.15. **A**: $p(r)$'s of CTAB (closed circles), 2 CTAB:1 SB3-14 (open circles), 1 CTAB: 1 SB3-14 (closed squares), 1 CTAB:2 SB3-14 (open squares) and SB3-14 (closed triangles), at 50 mM. **B**: Scattering data with GIFT fits of CTAB (open circles), 2 CTAB: 1 SB3-14 (open squares), 1 CTAB: 1 SB3-14 (upwards open triangles), 1 CTAB: 2 SB3-14 (downwards open triangles) and SB3-14 (open diamonds) at 50 mM. GIFT fits and SAXS data are offset for clarity

The points to take from this analysis is that in the SAXS experiment, as in the SANS experiment, the particles are anisotropic. It is difficult to determine the true degree of anisotropy due to the changing contribution of the shell to the scattering amplitude as the mole fraction of CTAB is decreased and the mole fraction of SB3-14 is increased. Although the overall size of the particles appears to remain approximately the same, the relative intensity of the shell contribution makes it much more probable for $\Delta\rho > 0$ distance correlations, *i.e.* ++, to be detected in the indirect Fourier transform analysis when the presence of sulfobetaine in the shell increases, thus skewing the $p(r)$.

Interestingly, the shell contribution to the scattering amplitude increases with the mole fraction of SB3-14 and when the micelles are comprised of just CTAB the shell contribution approaches zero. This means that although the CTAB shell consists of quaternary ammonium ions with bromide counter ions the scattering length density of the CTAB shell must be only slightly greater than the scattering length density of the solvent, in this case water. Due to the volume fractions of the surfactants involved, CTAB was fitted with a hard sphere structure factor, where the hard sphere radius was allowed to be greater than the radii of the form factor in the GIFT fitting.

In the case of pure SB3-14 micelles the SAXS data was also fitted using the GIFT method and fitted to a sticky hard sphere structure factor, as the SANS data. However, data from the mixed micelle systems was fitted using an IFT analysis

rather than a GIFT analysis. This is due to appreciably no scattering amplitude being present in the low q region of the data, thus making a structure factor at a concentration of 50 mM surfactant unresolvable for the GIFT method in this data analysis.

This occurrence can be attributed to two factors. The reduction in scattering amplitude is due to the Coulombic repulsion of the micelles containing CTAB, which contributes to a correlation peak, plus the low contribution to the scattering amplitude at low q. However, the main contribution to the scattering amplitude arises from the core-shell contrast of the surfactant micelles and not the core-solvent contrast or the shell-solvent contrast. Thus, there is low scattering amplitude at low q as due to the pair-distances comprising the most probable interfaces. It is also noteworthy that the indirect Fourier transforms of SAXS data from solutions containing mixtures of CTAB and SB3-14 exhibited fluctuations in the shell to shell correlations, which suggest that the electron density throughout the shell is definitely not constant. It can be seen from the fits that the indirect Fourier transforms describe the low q data relative well within the error (Figure 3.15B).

3.8 Model dependent analysis of the SANS data of CTAB: SB3-14 mixed micelles

Taking account of the features suggested by the model free analysis above, SANS data of mixed CTAB: SB3-14 micelles were fitted to a prolate ellipse or polydisperse sphere form factor. The models were described in the preceding theory chapters. The trends in the form and structure factor agree with the GIFT analysis described earlier, namely that all combinations of CTAB:SB3-14 micelles are anisotropic or in the case of SB3-14 a polydisperse sphere, which in the GIFT analysis is deduced as anisotropy and a decrease in the overall size of the micelles.. Additionally, when the CTAB mole fraction is decreased in the mixed micelles the inter-micellar distance, apparent from the increase in q of the peak position, decreases. However, in the fitting of the data to a model the rescaled mean spherical approximation[68] was used rather than the hard sphere radius that exceeded the dimension of the micelle in the GIFT analysis.

The fitting of small angle scattering data for a ternary system is complicated due to increase in the number of volumetric, scattering length and positional parameters involved. It is important that the content of information that the scattering data provides is critically assessed to prevent structural information being obtained where there is no justification for that amount of information, plus the capabilities of the instrument used to collect the data must be considered. In the fitting strategy of the SANS data of CTAB: SB3-14 the following points were considered when constructing a suitable model, with particular emphasis on the relative position of SB3-14 relative to the CTAB in the mixed surfactant micelles.

The scattering length densities of per-hydrogenated CTAB and per-hydrogenated SB3-14 are very similar along the length of the alkyl chain region from the terminal methyl group up to the quaternary ammonium regions of the headgroups. A linear progression along the headgroup of SB3-14 must exhibit an increase in scattering length density of the headgroup as the average neutron scattering length density of the $N(CH_2)_2(CH_2)_3SO_3$ headgroup is 0.099×10^{-6} Å^{-2} which is higher than that of the alkyl tails (table 3.6). However, in the region of the quaternary ammoniums the scattering length density must still be very similar to that of the alkyl chain due to the similarities in chemical composition. The alkyl chains have a scattering length density of -0.44×10^{-6} Å^{-2} and the quaternary ammoniums have a scattering length density of approximately -0.48×10^{-6} Å^{-2}.

The scattering length density of the quaternary ammonium of SB3-14 is difficult to estimate as the volume of the headgroup has only been reliably determined for the whole sulfobetaine headgroup; however the scattering length density of the region would be close to that of trimethylammonium cation due to the relative amount of hydrogen in the moiety. From this lack of contrast between tails and regions of the headgroups it can be seen that it is difficult to determine the exact position of SB3-14 in the core of the mixed micelle using SANS due to the disparity of the alkyl chain lengths between the two surfactants and similarity of the scattering length densities along the length of the surfactant up to and including the quaternary ammonium headgroups.

As stated in the data analysis introduction earlier in this chapter, treatment of the data, and calculation of the volume fraction of the micelles in solution from the aggregation number eliminates the correlation mistakes from assuming a volume fraction and scattering length density for components of the micelle. In this analysis of the SANS data it can also assist in determine the position of SB3-14 in the mixed micelle, despite the fact that the scattering length densities of the tail and headgroup appear to prevent this determination.

If the volume of the quaternary ammonium of the sulfobetaine headgroup does penetrate in to the mixed micelle core, it will be apparent when treating the volume of the micellar core as an aggregate of the weighted average of the core substituents. For example in a “tail only model” the weighted average of a 1:1 mixture of a CTAB 16 methylene chain (458 Å^3) and a SB3-14 14 methylene chain (404 Å^3) is 432 Å^3 and the scattering length density of the tail region is -0.43×10^{-6} Å^{-2}. Whereas in a “penetrating sulfobetaine model” where the SB3-14 penetrates fully to the centre of the micellar core, the weighted average of a 1:1 CTAB:SB3-14 mixture , where the sulfobetaine volume is calculated from an ellipse with a minor radius of 21.7 Å gives a core volume of ~ 455 Å^3. This volume includes the full 19.2 Å of the SB3-14 chain length and 2.5 Å of the sulfobetaine quaternary ammonium. In this case the average scattering length density of the micelle core is -0.44×10^{-6} Å^{-2}. In the case where d33-

CTAB is used in the 1:1 mixture, the 'tail only' model gives a core scattering length density of 2.73×10^{-6} Å^{-2} whereas the 'penetrating sulfobetaine core' model has an average scattering length density of 2.73×10^{-6} Å^{-2}. This is explained schematically in Figure 3.16

The model applied in the fitting is as described above. Namely the core scattering length density of the micelle is treated as an average of the two scattering length densities and volumes of the constituent micellar alkyl regions. The micellar cores may have some of the SB3-14 quaternary ammonium present in the palisade area of the mixed micelle, however, as explained above this is only noticeable from the average surfactant tail volume. Care was taken when applying the model to reduce the number of fitted variable to just three. These were the effective charge of the micellar surface, axial ratio of a prolate ellipse, the shell thickness and the shell SLD. All other parameters were constants. This was achieved by the following procedure.

The micelle core minimum radius was not treated as a free variable; it was treated as a constant. However, to obtain the best fits, different values of the minimum core radius were tested. For each value of the minimum core radius that was tested, the average core volume per surfactant was calculated. Both the 'tail only' and 'sulfobetaine penetration' models were tested. It was found that the 'sulfobetaine penetration model gave the best fits to the SANS data'. The average core volume per surfactant was calculated as follows.

The composition of the micelles had already been calculated from the model independent forward scattering method discussed previously. Therefore, the relative molar ratios of CTAB to SB3-14 were already known and confirmed to be that of the bulk molar ration of surfactants. In the 'sulfobetaine penetration' model the average core volume per surfactant, V_{AVE}, is given by

$$V_{Ave} = x_{CTAB}V_{CTAB\,Tail} + x_{SB3-14}V_{SB3-14\,Tail} \qquad 3.31$$

Where x_{CTAB} and $x_{SB3\text{-}14}$ are the mole fractions of CTAB and SB3-14 in the mixed micelle; V_{CTAB} and $V_{SB3\text{-}14}$ are the volumes of the portions of CTAB and SB3-14 respectively that are present in the micellar core.

V_{CTAB} is kept constant at 458Å. In the 'sulfobetaine penetration' model, $V_{SB3\text{-}14}$ is calculated by assuming the end of the tails of CTAB and SB3-14 is at the same level within the core of the mixed micelle. As discussed previously this would require that part of the SB3-14 headgroup is below that of the CTAB headgroup. Therefore, $V_{SB3\text{-}14}$ is the sum of the SB3-14 tail volume plus the volume of the SB3-14 headgroup that can be considered to be inside micelle core.

$V_{SB3\text{-}14}$ was calculated by subtracting the trans length of SB3-14 tail (19.2Å[30]) from the minimum core radius in the model. The volume of the head group is then calculated from this difference and the radius of the quaternary ammonium of the

headgroup. The radius of the quaternary ammonium is assumed to be that of the trimethylammonium of CTAB. This is calculated from the volume of 102.3Å[320] to be a value of 6.2Å. The volume of the SB3-14 headgroup in the micellar core is then calculated from the equation for the volume of a sphere section, $V_{SECTION}$ (3.32).

$$V_{SECTION} = \frac{\pi(r_{CORE\ MIN} - 19.2)}{6}(3a^2 - (r_{CORE\ MIN} - 19.2)^2) \quad 3.32$$

Where

$$a = \sqrt{\frac{r2(r_{CORE\ MIN} - 19.2)}{(r_{CORE\ MIN} - 19.2)^2}} \quad 3.33$$

and

$$r = \sqrt[3]{\frac{V_{QA}3}{4\pi}} \quad 3.34$$

Where $r_{CORE\ MIN}$ is the radius of the core of the micelle in the minimum axis and V_{QA} is the volume of the quaternary ammonium

The value of $V_{SECTION}$ is then added to the volume of a 14 carbon surfactant tail chain, 404Å^3 to give a value for $V_{SB3\text{-}14\ TAIL}$ and subsequently the average surfactants tail volume? V_{AVE}. From V_{AVE} it is simple to calculate the aggregation number, N_{agg}, of the prolate ellipse surfactant micelle (or in the case of pure SB3-14 micelles a spherical micelle)

$$N_{agg} = \frac{4\pi}{3}r_{CORE\ MIN}{}^2(AR \times r_{CORE\ MIN})/V_{AVE} \quad 3.35$$

From N_{agg}, it is possible to calculate the number of micelles, $N_{micelle}$ in solution and subsequently the volume fraction, $\Phi_{micelle,}$ of micelles in the solution

$$N_{MICELLE} = \frac{C_{BULK} \times N_A}{N_{AGG}} \quad 3.36$$

$$\varphi_{MICELLE} = N_{MICELLE} \frac{4\pi}{3} r_{SHELL\ MIN}{}^2 (AR \times r_{SHELL\ MIN}) \quad 3.37$$

Where $r_{SHELL\ MIN}$ is $r_{CORE\ MIN}$ plus the shell thickness

By testing minimum core radii against the prolate ellipse model, it was possible to fit the effective charge, axial ratio, shell thickness and shell SLD with the volume fraction of the micelles calculated within the model. This removes uncertainty in the fitting as the volume fraction and SLD contrast are equivalent in the effect on the intensity of the form factor and therefore only one instance of either the SLD in the model or volume fraction may be reliably fitted. A similar method was used to determine the volume fraction of spherical micelles in the case of SB3-14 (when all radii of an ellipse are equal the equations reduce to that of a sphere).

Using this method, the volume fraction was also calculated from the form factor volume for the RMSA structure factor described in Chapter 2. The dimension of the ellipsoid was also used to define the hard sphere radius of the effective hard sphere from the 2nd virial coefficient of an ellipsoid with the same volume. Therefore, from the fitting, the start of the charge screening layer begins at the limits of the core-plus-shell radii of the ellipse. The samples containing deuterated CTAB were co-resolved with the fully hydrogenated samples to gain reliable fits for the shell of the mixed micelles

.

x_{CTAB}	N_{agg}	Rcore min (Å)	AR	PD	Shell (Å)	SLD_{Core} ($Å^{-2}$)	SLD_{Shell} ($Å^{-2}$)	V_{tail} ($Å^3$)	Z	R_{HS} (Å)	τ	Head group area ($Å^2$)	Packing parameter
CTAB	159 ± 11,	22.2 ± 0.05	1.59		3.41	−0.43	1.6±0.4	458	24.2±.01	-----		54.9±1.2	0.375
2CTAB: 1SB3-14	140 ± 30,	21.96 ± 1.5	1.52		2.68 ± 1.4	-0.41 / 4.47	2.24 ± 0.7	481	18.2 ± 0.2	-----		58.8±3.8	0.372
1CTAB: 1SB3-14	128 ± 7	21.63 ± 0.4	1.46		2.46±0.5	-0.43 / 3.24	2.06 ± 0.6	480	14.7 ± 0.1	------		60.1±1.1	0.369
1CTAB: 2SB3-14	122 ± 9	21.53 ± 0.5	1.41		2.31±0.2	-0.41 / 1.97	1.9 ± 0.7	483	11.36 ± 0.1	-----		61.2±1.4	0.366
SB3-14	72 ± 11	19.1 ± 1	-----	0.11	5.1 ± 0.5	-0.43	3.67 ± 0.2	404	----	18.1	0.14 ± 0.01	63.5±8.3	0.333

Table 3.11. Fitting results from model dependent SANS analysis. Definitions are in the text

The fitting results agree with the model independent analysis and are presented in table 3.11. The fits are presented in figure 3.16 As the mole fraction of CTAB is decreased, the aggregation number of the mixed micelles decreases. This results in a change in structure of the micelle from a prolate ellipse where pure CTAB is present with an axial ratio of 1.59 which decreases with the decrease in CTAB mole fraction tending towards a sphere. This trend is evident in all samples except for pure SB3-14 where the best fit is achieved with a polydisperse core-shell sphere model. In fact evaluation of the packing parameter shows that when CTAB is present the surfactant molecules are most likely to pack into an elongated micelle.

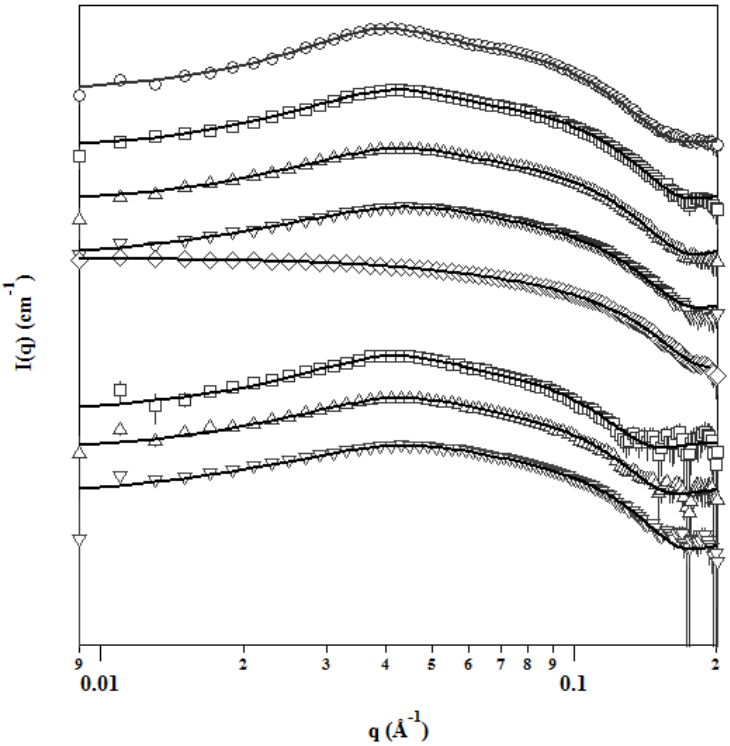

Figure 3.16. Fits data to model of CTAB (open circles), 2 CTAB: 1 SB3-14 (open squares), 1 CTAB: 1 SB3-14 (up triangle), 1 CTAB: 2 SB3-14 (down triangle) and SB3-14 (open diamonds), at 50 mM. Traces have been offset by 1 magnitude of intensity for each data set. Sample containing deuterated CTAB have been offset by 1000.

From a modelling point of view, the shell in the co-resolved data remains approximately at the same thickness and SLD value regardless of the micelle composition. This means that the conformation of the sulfobetaine headgroup is currently unresolvable from this data. However, considering the area per headgroup calculated from the fitting results it can be seen that, as the mole fraction of CTAB is reduced, the average surfactant headgroup area is increased due to the increase in the

mole fraction of the relatively larger headgroup of SB3-14. This can be a result of the quaternary ammonium of the sulfobetaine being more hydrated than the quaternary ammonium of CTAB (as a large fraction of CTAB monomers will have associated bromide). Whilst it does not unequivocally prove it, it is likely that the sulfobetaine headgroup is protruding from the mixed micelles as in rather than lying flat. This is due to the volume linked fitting and the slight increase in headgroup area as the mole fraction of SB3-14 is increased. If the head group was flat against the micelle surface then the average headgroup size might increase more due to the larger surface area of SB3-14.

Analysis of the mixed micelles with SAXS provides greater insight in to the sulfobetaine

Model dependent analysis of SAXS data

The SAXS data was fitted to a core-shell prolate ellipse model when the micelles contained CTAB and a polydisperse core-shell model for pure SB3-14 micelles. To obtain good fits it was necessary to introduce smearing to the core-shell interface and the shell solvent interface, as described in the theory chapter. A schematic of the model used is presented in figure 3.17. This was necessary due to the relatively large scattering length densities of the sulfonate region of the sulfobetaine headgroup and the bromide counter ion. The fitting results are presented in figure 3.18 and the parameters in table 3.12

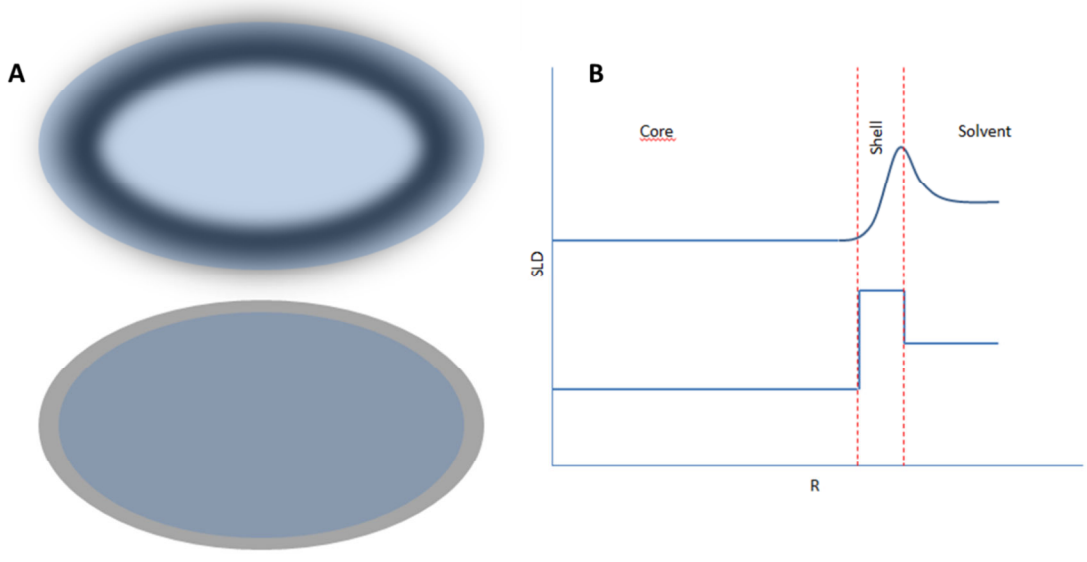

Figure 3.17 Schematic showing the smeared interface model used in the fitting of the SAXS data. A) Plan view of the smeared prolate ellipse model (top) and stepwise prolate ellipse model for comparison (bottom). Black indicates a higher SLD. B) SLD profiles as a function of distance along the minimum radius of the prolate ellipse. Showing the smeared prolate ellipse model (top) where the smearing of the

core-shell interface equals the shell length and the smearing of the shell into the solvent. The stepwise model used in the SANS fitting is shown for comparison (bottom)

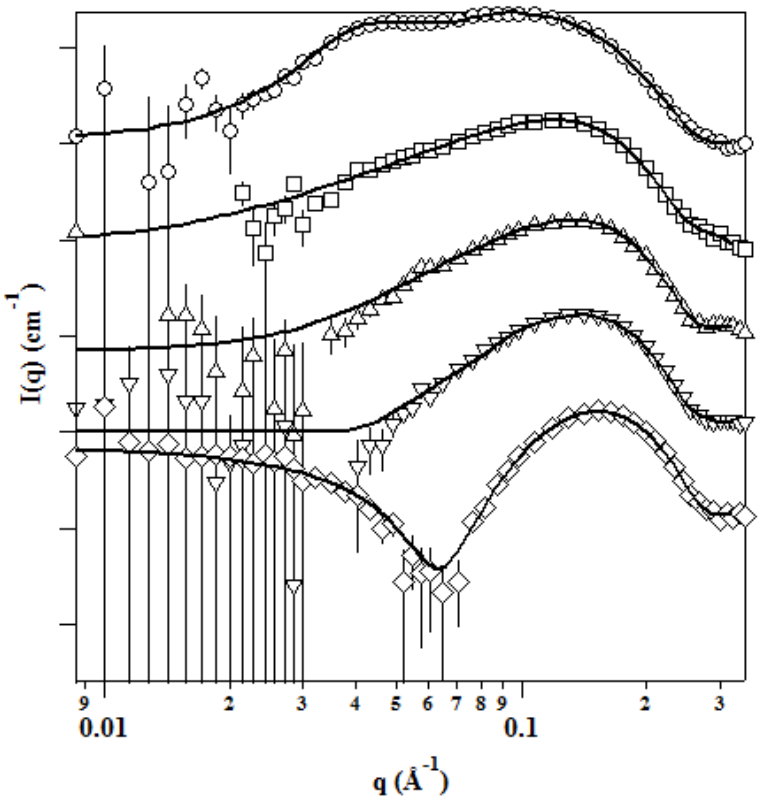

Figure 3.18. SAXS data with fits of mixed micelles at 50mM. Mole fraction of CTAB equals 1 (circles), 0.667 (squares), 0.5 (up triangle), 0.333 (down triangle) and 0 (diamonds). Fits are solid black lines. Data has been offset for clarity.

	CTAB	2CTAB:1SB	1CTAB:1SB	1CTAB:2SB	SB3-14
α_{CTAB}	1.000	0.667	0.500	0.333	0.000
Core Radius (Å)	19.2	19.2	19.2	19.2	16.2
Axial Ratio	1.8	1.6	1.6	1.6	1.0
N_{agg}	132.1	118.1	115.8	113.7	73.4
Shell Thick (Å)	5.1	4.8	4.7	4.3	8.8
ς Core-Shell (Å)	5.1	4.8	4.7	4.3	
ς Shell-Solvent (Å)	3.9	3.2	2.6	2.5	

Core SLD ($Å^{-2}$)	7.50×10 -06	7.50×10 -06	7.50×10 -06	7.50×10 -06	7.50×10 -06
Shell SLD ($Å^{-2}$)	1.15×10 -05	1.17×10 -05	1.19×10 -05	1.23×10 -05	1.05×10 -05
Solvent SLD ($Å^{-2}$)	9.50×10 -06	9.50×10 -06	9.50×10 -06	9.50×10 -06	9.50×10 -06
Z	21.0	5.0	5.3	5.1	

Table 3.12 Fit parameters of fits to SAXS data. Parameter definitions are in text. Sigma is the width of the Gaussian function which was applied to the interfaces to generate the smear.

Due to the relative scattering length densities of the components of the investigated system the scattering amplitude is dominated by the positions of the anionic ions in the surfactant micelles, here both the bromide counter ions and the sulfonate ions of the sulfobetaine headgroup. However, the sulfonate ion is the only ion for which it is possible to determine the concentration as it is covalently attached to the SB3-14 surfactant, whereas the bromide counter ion exists in solution either bound to the surfactant micelle or free in solution.

Much work has been performed to attempt to determine the true nature of counter ion binding to micelles. The convention is that the bound counter ions exist in a Stern layer with the charged surfactant headgroups and the unbound ions exist in a diffuse layer decreasing in concentration outwards from micelle surface.[69,70] However, the distribution of scattering length density throughout the micelle surfaces can give insight to the distribution of ions in the Stern layer and the diffuse layer of the micelle.

As the CTAB mole fraction is decreased the axial ratio of the prolate elliptical micelles decreases, which is also in agreement with the fitting of the SANS data. Also apparent with the decrease in CTAB mole fraction is the increase in the apparent size of the hydrocarbon only core of the surfactant micelles. According to the previously fitted SANS results the cores of the CTAB and CTAB: SB3-14 mixed micelles are appreciably non-hydrated. This is in agreement of other published results of alkyl trimethylammonium surfactants[20] in contrast to other ionic surfactant such as alkyl sulfates where the core penetration of the solvent has been reported as pronounced.[71] It can be seen that the apparent minimum radius of hydrocarbon only core is inversely proportional to the CTAB mole fraction of the mixed surfactant micelles. However, CTAB is the surfactant with the longest hydrocarbon core in the mixed surfactant micelles, so upon initial consideration it could be expected that the minimum hydrocarbon core radius would be proportional to the CTAB mole fraction. The effect can be explained by consideration of the position of the bromide counter ion and the SB3-14 mole fraction in the mixed micelles.

Referring back to the SANS fitting of the mixed micelles, the best fits were obtained by allowing for the quaternary ammonium of the sulfobetaine headgroup of SB3-14

to partially penetrate into the micellar core in the modelling. This minimised the interaction between the constituent surfactant headgroups and probably minimised the conformational energy between CTAB and SB3-14 headgroups. This had negligible effect on the apparent scattering length density of the micellar core in the SANS fitting, as a quaternary ammonium headgroup and a hydrocarbon chain are both largely hydrogenated and therefore, the coherent scattering length are predominately that of hydrogen. Thus this effect was only seen in the apparent average volume of the mixed surfactant micelles. However, when considering the X-ray scattering length densities, the quaternary ammonium groups' electron density is greater than the electron density of the hydrocarbon core. Therefore, penetration of the quaternary ammonium into the micellar core would manifest as a reduction in the apparent micellar core radius.

This phenomenon however cannot explain the reduction in the apparent micelle core radius with the reduction of the CTAB mole fraction, as the apparent micelle core radius is at a minimum in the pure CTAB micelle. However, this can be explained by the position of the bromide counter ion in the surfactant micelle. The fitting of CTAB micelle can only be explained by allowing some of the bromide counter ion to penetrate into the micellar core, whilst still being associated with the quaternary ammonium group. This is apparent in the SAXS analysis as the x-ray scattering length density difference between the micellar core, headgroup, solvent and the bromide counter ion is far greater than the difference in scattering length density in neutron scattering. However, the counter ion in the CTAB micellar core must be non-hydrated as the fitting of the SANS results, which would be very sensitive to water penetration in to the micellar core, indicated that the micelle core remains dry.

As the mole fraction of SB3-14 increases this apparent penetration of the bromide counter ion into the micellar core decreases. This can be attributed to two properties. Firstly, the decrease in the amount of bromide present in the mixed micelles due to the reduction in the CTAB mole fraction of the mixed micelles. Secondly, with the increase in SB3-14 the amount of quaternary ammonium ion species at the micellar core surface also increases as well as the amount of sulfonate ion above this interface or near to it. The relative position of bromide and sulfonate in the Hoffmeister series[72] are close meaning that they exhibit similar affinity for quaternary ammonium. As the two surfactants comprising the mixed micelle are within close proximity to each other it can be proposed that the quaternary ammoniums are effectively redundant to the sulfonate and bromide. As the sulfobetaine is conformationally more restricted to the outer surface of the micelle, although it may be more energetically restricted to the same plane as the quaternary ammoniums.

The degree of relative counter-ion binding of the CTAB remains constant according to the effective charge obtained from the fitting of the SANS results. This means that the presence of sulfobetaine in the surfactant micelle does not displace any more

bound bromide. From the fitting it can be seen that in fact the thickness of the bromide diffuse layer in the surfactant micelle increases with the increasing mole fraction of CTAB. This may be attributed to charge screening from the presence of the sulfonate ion at the micelle surface which increases as the SB3-14 mole fraction increases. The increase in the mole fraction of SB3-14 increases the scattering length density of the densest part of the shell, although it decreases the extent of smearing of solvent into the shell.

This suggests that as the mole fraction of CTAB decreased there is obviously less bromide in the diffuse layer. However, these SAXS results show that the sulfonate ion extends slightly from the shell which the SANS results could not show due to hydration. This conformation of the SB3-14 headgroup is as suggested in the 'sulfobetaine penetration' model. This conformation of the sulfobetaine headgroup may contribute to screening the interaction between CTAB and PEI, further preventing film formation as the CTAB mole fraction is decreased and also preventing formation of the more ordered phases in the film. When the micelles consist of pure SB3-14, the sulfonate in the headgroup adopts a more flat conformation at the surface of the micelle, with some penetration into the core.

Therefore, even though the effective charge of the micelles is reduced due to the reduction of the CTAB mole fraction, the tightly bound sulfonate ion may also contribute to the steric hindrance preventing the coordination of polyethylenimine to the micellar surface. This will further prevent film formation, particularly when SPEI is used as the film forming polymer so that an entangled polymer network cannot be formed in the film.

3.10 Model dependent analysis of the polymer solutions

3.10.1 Scattering contribution of the polymer

SAXS data of the pure polymer solutions at 1%wt was also collected to determine the contribution of the polymer to the scattering amplitude of the mixed surfactant-polymer solutions (figure 3.19). If two components do not interact the scattering pattern obtained from a mixed solution of these will be the linear combination of the scattering from the individual components. However, if the individual components interact, either hydrophobically or electrostatically, in a mixed solution of polymer and surfactant the scattering pattern will no longer be a simple linear sum of that of the polymer and the surfactants, respectively. One can in this way easily test whether or not the polymer and surfactant interact. However, due to the lack of contrasts performed in the experiment it was impossible to resolve exactly how the scattering contribution from the polymer in the mixed solutions affected the scattering from the surfactant micelles.

The scattering pattern from the pure polymer in solution allows the prediction of the general form of the polymer when mixed with the surfactants, assuming the structure of the polymer is unchanged. The polymer scattering was used as a background in fitting the scattering from the mixed surfactant and polymer solutions. This in turn allowed the micellar scattering to be resolved to a greater extent than it would be if no prediction of polymer background was made.

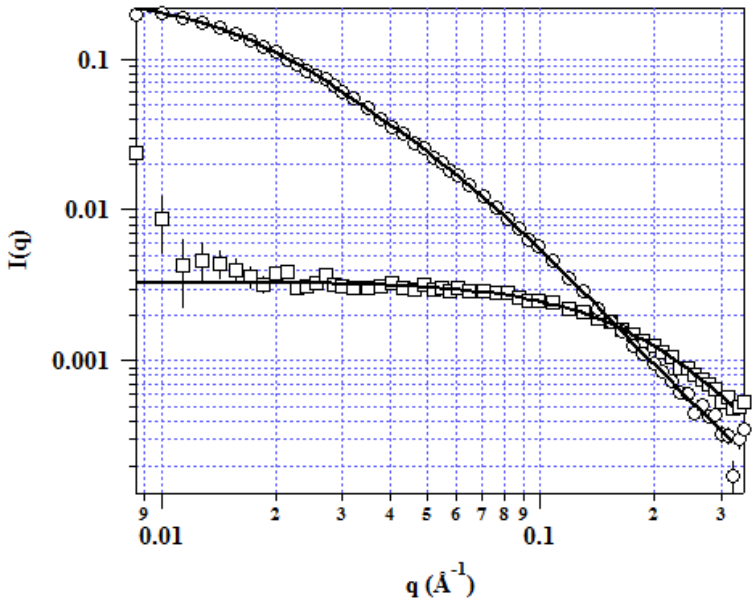

Figure 3.19. SAXS data collected for solutions of SPEI (open squares) and LPEI (open circles) at concentrations of 1%wt with their respective model fits (full lines).

The scattering from the LPEI 1%wt was fitted to a two Lorentzian model and the scattering from SPEI was fitted to a Debye model. The two Lorentzian fit showed that the scattering was made up of two scattering contributions; a 58 Å particle with an exponent of -2.35, which is similar to that expected for a branched polymer mass fractal in a good solvent and a 15 Å component with an exponent of -3.34The scattering from the SPEI 1%wt solution was fitted to a Debye model[73], which fits a -2 exponent for a polymer obeying Gaussian statistics with a radius of gyration of 9.44 Å. The data from these fits was used as a background in the subsequent fitting of the scattering data from the surfactants solutions mixed with polymer.

3.10.2 Model dependent SANS analysis of mixed micelles with PEI

SANS was performed on mixtures of CTAB and SB3-14 with PEI. The data was fitted to the same model that was applied to the SANS data of the mixed micelles without polymer. Specifically, the only free parameters that were freely fitted were the prolate ellipse shell thickness, shell SLD, micellar effective charge and the axial ratio of the prolate ellipse. The aggregation number of the micelles was calculated within the model from the bulk concentration of surfactant and surfactant dimensions. Therefore the volume fraction was not fitted but calculated depending on the form factor of the micelle. Relevant SLD's were taken from table 3.7.

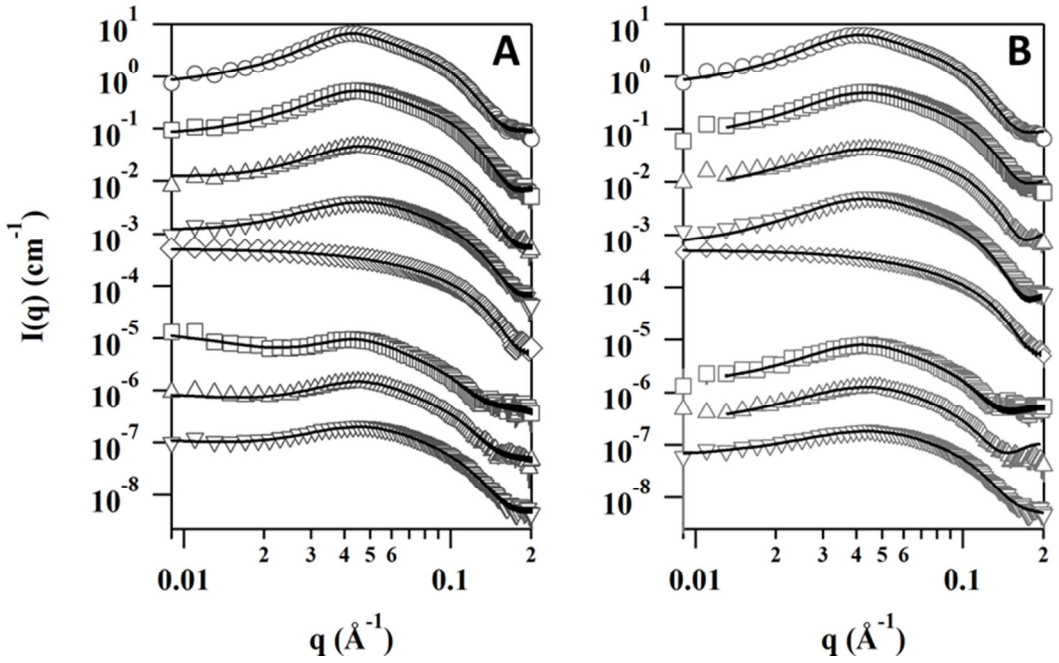

Figure 3.20 **A**: Fits of data to containing LPEI 1%wt model of CTAB (open circles), 2 CTAB: 1 SB3-14 (open squares), 1 CTAB: 1 SB3-14 (up triangle), 1 CTAB: 2 SB3-14 (down triangle) and SB3-14 (open diamonds), at 50 mM. Traces have been offset by 1 magnitude of intensity for each data set. Sample containing deuterated CTAB have been offset by 1000. **B**: Fits of data to containing SPEI 1% wt. model of CTAB (open circles), 2 CTAB: 1 SB3-14 (open squares), 1 CTAB: 1 SB3-14 (up triangle), 1 CTAB: 2 SB3-14 (down triangle) and SB3-14 (open diamonds), at 50 mM. Traces have been offset by 1 magnitude of intensity for each data set. Sample containing deuterated CTAB have been offset by 1000.

The fitting differed from that of the mixed micelles without polymer in that the form factor of the polymer calculated from the fitting of the SAXS data from the polymer in solution was summed to the model for the micelles in solution. Therefore the

dimension of the polymer derived in the last section was used as a constant in the fitting. The form of the polymer was not fitted in this instance; as if it was then the fit could not be relied upon due to too many fitted parameters. This would make it unresolvable which component was contributing to a region of the scattering curve. It should be noted that this is not a statement that the form of the polymer does not change in a solution with the micelles. However with the data available it was unresolvable.

x_{CTAB}	1	0.667	0.5	0.333	0
$r_{COREMIN}$ (Å)	21.74	21.74	21.74	21.74	19.2
AR	1.52	1.49	1.25	1.11	1
N_{agg}	142.84	135.08	111.13	95.07	73.4
Shell (Å)	8.29	6.44	5.99	5.51	3.71
Shell SLD ($\times 10^{-6}$ Å^{-2})	4.10	3.97	4.10	4.17	5.01
Z	17.42	14.12	12.44	9.65	0.00
Packing parameter	0.37	0.37	0.36	0.34	0.33
Area per surfactant (Å^2)	56.57	58.88	62.54	65.89	63.46
PEI Shell VF	0.14	0.07	0.04	0.01	

Table 3.13 Results for the fitting of the SANS data of mixed micelles 50mM with LPEI 1%. Definitions are in text apart from PEI shell VF which is the volume fraction of PEI in the micelle shell

xCTAB	1.000	0.667	0.500	0.333	0.000
$r_{COREMIN}$ (Å)	21.74	21.74	21.74	21.74	19.20
AR	1.66	1.45	1.35	1.17	1.00
N_{agg}	155.62	131.08	120.17	102.23	73.40
Shell (Å)	4.35	2.88	4.34	4.17	4.70
Shell SLD ($\times 10^{-6}$ Å^{-2})	2.65	1.74	3.87	3.47	4.03
Z	14.46	12.12	9.22	5.71	0.00
Area per head group (Å^2)	55.65	59.26	61.35	64.87	63.46
Packing parameter	0.38	0.37	0.36	0.35	0.33

Table 3.14 Results for the fitting of the SANS data of mixed micelles 50mM with SPEI 1%. Definitions are in text.

The SANS data is presented in figure 3.20 with fits to the data. The results are tabulated in table 3.13 and 3.14 for LPEI and SPEI respectively. It can be seen from the SANS data of mixed micelles with LPEI, where deuterated CTAB has been used

in the experiment, that the contribution of LPEI to the scattering in the low q region is significant (Figure 3.33A). It can be seen an increase in intensity before the correlation peak of the structure factor. This confirms that a summation of the polymer contribution with the micelle contribution is the correct model to use. Failing to take in to account the contribution of the polymer to the fitting may result in an incorrect form factor being obtained for the micelles.

Addition of PEI to the surfactant solutions causes the aggregation number to decrease compared to the surfactant only solutions. This is immediately apparent when comparing the axial ratios of the micelles in solution. When PEI is added the axial ratios are lower than that of the equivalent surfactant without PEI. Across the mole fraction range on CTAB, the effect is more pronounced with LPEI. Figure 3.34 shows the axial ratios of solutions of just surfactant, surfactant with LPEI and surfactant with SPEI.

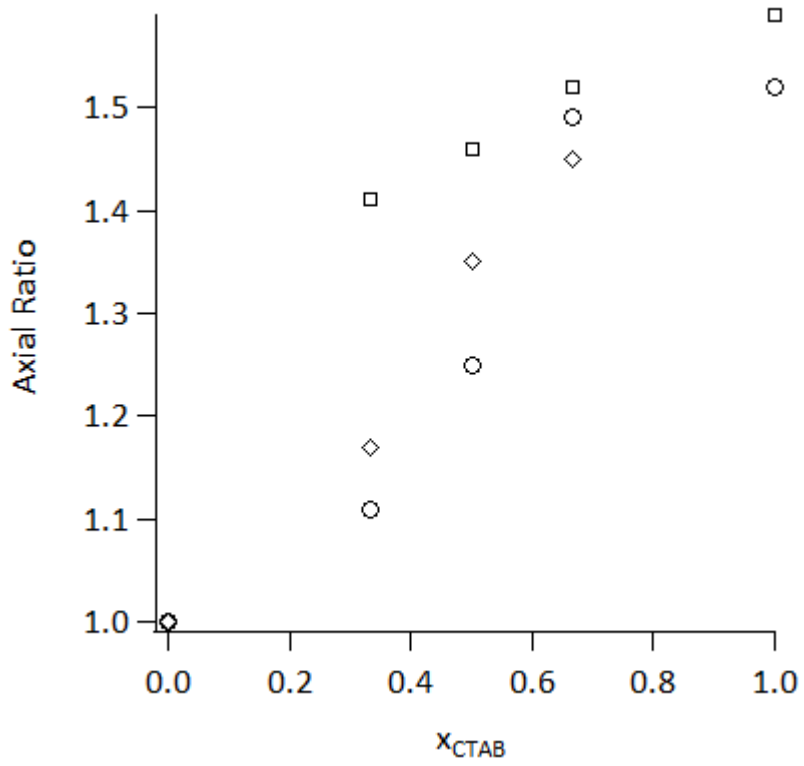

Figure 3.21 The axial ratios of the prolate ellipse micelles in solution as a function of mole fraction of CTAB (x_{CTAB}). No PEI (squares) 1% wt. LPEI (circles), 1% wt. SPEI (diamonds) is there a diamond missing at 100% SB3-14.

When polymer is added to the solutions, the average headgroup area in the micelles increases. The effect becomes more pronounced as the mole fraction of CTAB decreases as can be seen in figure 3.21. If PEI was stabilising bromide away from the surfactant micelle surface then this could explain the phenomena due to increased coulombic repulsion of the CTAB head groups. This could also explain why the

effect appears to be greater with LPEI than SPEI as the larger LPEI network could stabilise bromide away from the micelle surface more effectively than SPEI.

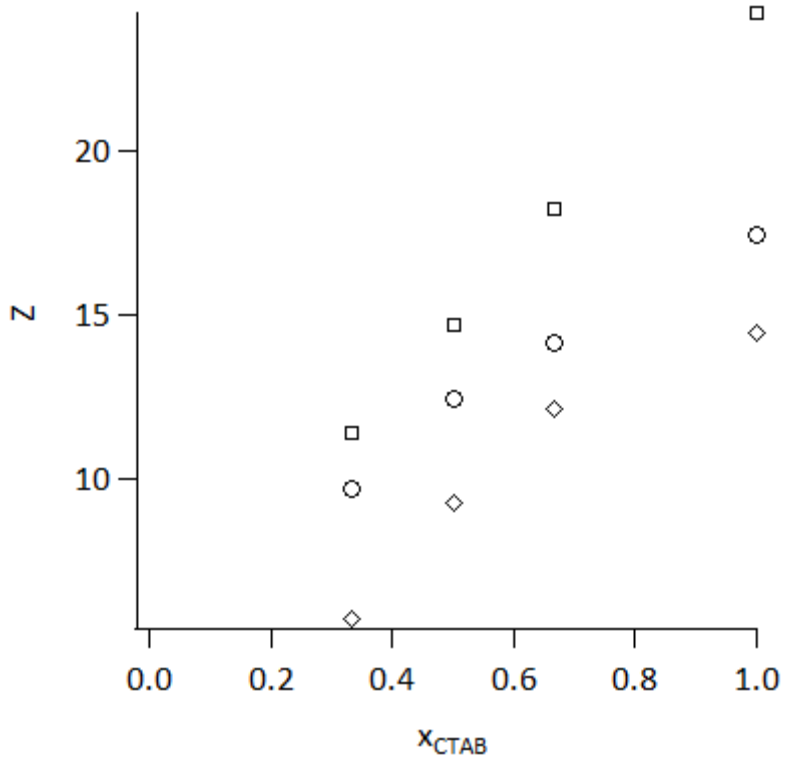

Figure 3.22 Effective charge of the prolate ellipse micelles in solution as a function of mole fraction of CTAB (x_{CTAB}). No PEI (squares) 1% wt. LPEI (circles), 1% wt. SPEI (diamonds)

As the mole fraction of CTAB in the mixed micelle is decreased, the effective charge of the mixed micelles obtained from fitting the data with the mean spherical approximation structure factor[68] also decreased. This is due to the reduction of the amount of CTAB in the mixed micelle. As this is the only ionic component in the micelle this means that the mean distance between the micelles, caused by Coulombic repulsion, also reduces. When fitting SANS data to the mean spherical approximation, the effective charge is equivalent to the degree of ionisation of the micelle, and given by

$$Z_{eff} = \frac{N_{ionized}}{N_{agg}} \tag{3.40}$$

Where Z_{eff} is the effective charge, $N_{ionized}$ is the number of ionized surfactant molecules and N_{agg} is the aggregation number of the surfactant micelle.

Although in the experiment only 4 different molar ratios of CTAB were investigated and caution should be exercised when comparing fitting of the effective charge and placing significance upon the figures as to how many surfactant micelles are ionized, plotting of the effective charge against molar fraction of CTAB of the fits indicates that there is a linear relationship (Figure 3.30) between the effective charge exhibited by the micelles and the mole fraction of CTAB. This suggests that the presence of SB3-14 does not alter the ionisation behaviour of CTAB, which is in agreement with the surface tension results as there is only a slight deviation from ideal behaviour in the CMC of the mixed micelles suggesting that the effective headgroup sizes of both surfactants goes unchanged upon mixing.

Comparing the effective charge of the micelles in solution as a function of CTAB mole fraction shows the effect PEI has on the inter-micellar interactions and also on the dissociation of bromide away from the micellar surface. Figure 3.22 shows the effective charge of the micelles as a function of CTAB mole fraction and PEI. It should be noted that free partially protonated polymer in the bulk can act as a screening polyelectrolyte, decreasing the apparent effective charge of the micelles.

However as the form factor contribution of the polymer was accounted for in the fitting, some observations can be made regarding its effect of the micellar structure factor. As the axial ratio of micelles in the LPEI containing solution is generally the lowest (from the dataset above) yet LPEI causes the effective charge of the micelle to be greater than that of the equivalent mixture with SPEI, it could be said that it displaces and stabilises more bromide away from the micelle headgroups than SPEI.

The trends in the effective charge show that as the mole fraction of CTAB is decreased, the solutions containing polymer are more effectively charge screened. This is most likely to do with the amount of polymer that is free in solution compared to the amount of CTAB in the micelles. When no polymer is present it can be seen in figure 3.22 that the trend in micelle effective charge is linear as a function of mole fraction of CTAB. However the trends with polymer are curved, which is most likely a function, as previously said, of the amount of free polymer in solution (not associated with the micelles) increasing as the mole fraction of CTAB decreases. This can be seen from the volume fraction of LPEI in the shell of the micelles from the SANS fitting (Table 3.13). When fitting the data for SPEI solutions the model fitted a shell similar to the micelles without polymer. Thus it was impossible to make estimates of the amount of polymer in the shell region of the micelles.

Now the bulk structure and extent of interaction has been determined, application of a model to the NR data of the films can be applied.

3.11 Application of multilayer model to mixed micelle and LPEI films

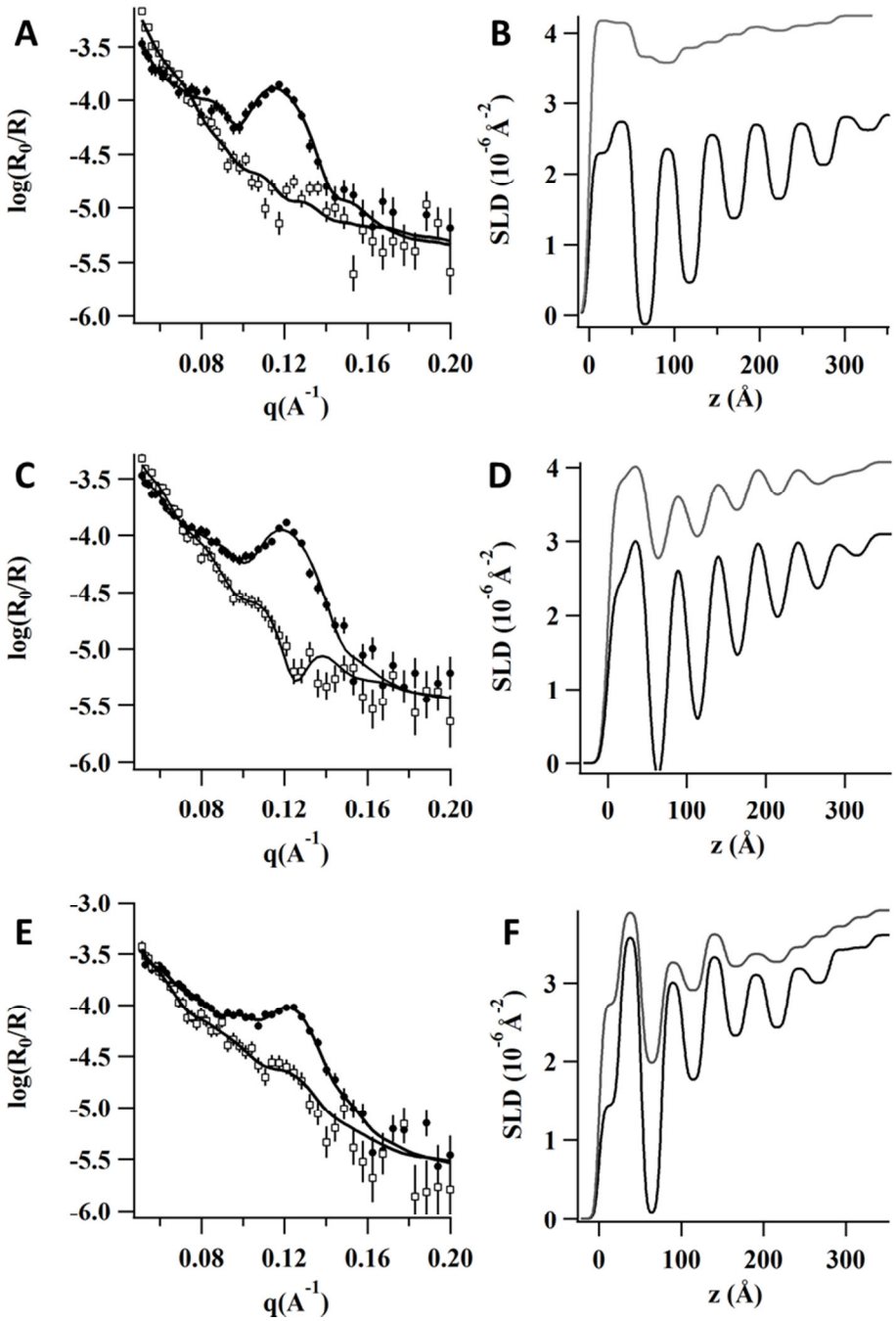

Figure 3.22 Fitted NR profiles (left) and SLD profiles (right) of mixed CTAB:SB3-14 50mM and LPEI 1% films where xCTAB is 0.667 (A + B), 0.5 (C+D), 0.333 (E+F). The lighter grey line in each case is the data corresponding to the sample containing d33-CTAB, while the black data is for samples containing h33-CTAB.

Figure 3.22 shows the reflectivity profiles and calculated SLD profiles of films formed 3600 seconds after mixing from mixed CTAB:SB3-14 50mM and LPEI 1%

wt. solutions. Contrast variation was performed by substituting h33-CTAB with d33-CTAB. This contrast variation experiment was performed to assist in the determination of the micellar composition within the hydrogel film. The reflectivity profiles of the mixed surfactants with LPEI films at different deuteration were co-resolved to determine the fine structure of the interfacial film.

The reflectivity profiles were modeled to investigate the SLD profiles of the films and hence the possible layer structure of the film. This modeling was performed as described in the next paragraph. The layer thickness was initially fixed in the modeling, but this was later allowed to be fitted freely in the fitting procedure, with the restriction that the layer thickness was kept constant throughout the depth of the film, as well as it being kept constant between films of different composition, as the data was co-resolved between the hydrogenated and deuterated CTAB samples. Choosing the layer thickness according to half the characteristic d-spacing exhibited by the diffraction peak in the NR profile effectively allows the modeling procedure to describe the upper and lower side of the surfactant rich layer, as it impinges on the water rich layers of the film, so the thickness of the surfactant layer can be determined from the minima in the SLD profiles in Figure 3.22.

The initial guesses for the SDL parameters in the fit were set so that the SLD profile alternated between layers comprised of 'dry' surfactant and of 'dry' LPEI (Table 3.7). Then the fitting procedure was allowed to fit the volume fraction of these layers, whilst any volume not containing surfactant or polymer in the layers were to be filled with a solvent of water and polymer with a constant SLD. This accounted for the fact that the true film structure was not necessarily lamellar but potentially composed of micelles with a polymer/water solution in between them. However this presented a problem in the fitting, as it was unknown what the correct SLD of the water-polymer solution would be and it was also considered that the water-polymer solution would contain some surfactant, which was not entirely incorporated in to the periodic layers.

The SLD of a D_2O solution containing 1%wt LPEI and 50 mM surfactant is easily calculated. However, what would the SLD of the subphase be near the interfacial film? The film itself is a concentrated phase separating the less concentrated solution phase from the air phase. The presence of the film suggests that there is a chemical potential difference between the air, the air-solution interface and the solution subphase. However, it is unnatural to view this difference in concentration to be a step-wise gradient and therefore it was assumed that the true subphase seen in the reflectivity profile is in fact an arbitrary point in a density gradient of polymer-surfactant composites in D_2O solution. It can therefore differ greatly from the initial solution concentration of surfactant and polymer of the initial film forming solution.

This will be discussed later in depth, but for descriptive purposes on the development of the film model it should be said that the subphase was allowed to be fitted freely to an SLD of between -0.372×10^{-6} Å^{-2} and 6.4×10^{-6} Å^{-2}. This value was not linked between the contrasts. Employing this method of modeling allowed the hydration of the layers to be fitted, whilst accounting for the possibility that adjacent to the film phase there was a phase of surfactant-polymer solution, that while concentrated was unordered like a concentrated micelle phase or gel phase. However, as the SLD of this subphase, which would contribute to the SLD of the layers, was not linked between the contrasts, due to the fact that the surfactant composition, whilst assumed to be the same across the contrasts, would affect the total SLD, as a consequence selective deuteration.

This presents the problem that the SLD of the subphase of each contrast obtained from the fitting, is in fact not correct, that it is just arbitrarily reduced to the fitted value. The SLD value for each contrast obtained from the fit were subsequently compared to a calibration curve, that was calculated from the SLD's of the initial film forming solutions, and plotting the SLD change when reducing the volume fraction of D_2O in the solutions. The final value of the subphase SLD of each contrast were then compared to this calibration curve to check that the subphase SLD value of the hydrogenated CTAB sample was present at the same SLD value projected for the deuterated CTAB sample at the same volume fraction of D_2O. If the value of the SLD gave the same volume fraction of D_2O, then it was assumed that the fit was a fair representation of the film structure.

Another point to note is that with the contrast variation employed in this experiment, it is impossible to determine exactly how much surfactant is present in the layers relative to the amount of polymer. That is why the surfactant rich layers were assumed to have the SLD of dry pure surfactant and the interspersing layers were assumed to have an SLD of dry PEI before fitting.

The interfacial roughness in the films was taken into account by assuming that the interfacial roughness is constant for all layers. This approach may be unphysical, as the extent of thermal fluctuations and interpenetration of the layers would be to some extent dependent on the volume fraction of the layers. However, it is difficult to accurately estimate the true value of interfacial roughness without first knowing the true SLD of the layer that is to be attributed a specific roughness, as a non-smooth interface causes a reduction in the reflected intensity, but so does a reduction in the SLD contrast of the interface.

An experiment employing more extensive contrast variations such as samples performed on air contrast matched water with deuterated surfactant and hydrogenated polymer and on air contrast matched water with hydrogenated surfactant and deuterated polymer, could yield enough information about the true

scattering length density of the surface layer to give a true estimate of roughness. Using these contrasts it would then be possible to eliminate the contribution from reduction of reflectance from that due to contrast. Experiments performed on air-contrast-matched-water with deuterated components give prominence to true surface reflectance, as penetration of the neutrons into the strongly incoherently scattering of the air-contrast-matched-water reduces the coherent reflectance from the subphase. In this case less extreme solution contrast experiments could be performed to assist in the estimation of roughness from the film layers, below the air film interface, to eliminate the effect of contrast on the roughness estimation. However, experimental supply, economics and time constraints meant that the only contrast that could be performed was the substitution of deuterated CTAB for hydrogenated CTAB. Therefore, it was considered more prudent to allow roughness to fit freely, while it remained constant across all layers.

It is apparent from the reflectivity profile of the 2 CTAB: 1 SB3-14:LPEI films that while the h33-CTAB sample exhibits a diffraction peak at q_1 = 0.1173, giving a repeat distance of 53.65 Å, no peak is evident in d33-CTAB sample (Figure 3.22A). It can be seen from figure 3.22 that the fitted model of the films suggests a multilayer structure. There is a top layer of hydrated surfactant and polymer with an effective layer distance of 17 Å. Beneath this layer are repeated layers with effective distance of 53.65 Å calculated from the midpoint of one surfactant layer to the adjacent one, which is in slight disagreement of the repeat layer calculated from the position of q_1. Similarly it can be seen that the film formed from 2 d33-CTAB: 1 SB3-14:LPEI exhibits no peak at q_1 like the film formed from 2 CTAB:1 SB3-14:LPEI. Assuming that the micellar composition within the film is equal to the bulk composition of surfactant, then the lack of a peak can be attributed to the micelles within the film being surrounded by hydrated polymer of similar scattering length density. The scattering length density profile confirms this in figure 3.22B.

The same modeling strategy was followed for films of surfactant composition 1 CTAB: 1 SB3-14 and (Figure 3.22C) 1 CTAB:2 SB3-14 (Figure 3.22E). Fitted reflectivity profiles for 1 CTAB: 1 SB3-14 and their corresponding SLD profiles are presented in figure 3.36D and for 1CTAB:2SB3-14 in figure 3.36F. From figure 3.36C and 3.36E it is immediately append that the film structures of films formed from 1 CTAB: 1 SB3-14 and 1 CTAB:2 SB3-14 are similar to the structure of films form from 2 CTAB: 1 SB3-14, with a single diffraction peak exhibited by the hydrogenated surfactant samples. The trend that is apparent from the hydrogenated samples is that when the mole fraction of CTAB is decreased in the film forming samples so is the repeat distance of the films, as evident from the increase in the q position of the reflection peaks.

Considering the deuterated CTAB containing samples, no strong reflection peak is seen, corresponding to the findings for the 2 CTAB:1 SB 3-14 film forming system.

Assuming again that the composition of the micellar structures in the film is the same as the micellar composition in the bulk, this suggests that the polymer-solvent matrix containing the micellar components has a similar SLD. Although there are no strong reflection peaks apparent in the deuterated surfactant containing samples, the deuterated reflectivity profiles of 1 d33-CTAB:2 SB3-14:LPEI (figure 3.22E) and 1 d33-CTAB:1 SB3-14:LPEI (figure 3.3.22C) do show oscillations, which fit to the model applied, especially for the latter.

Inspection of the SLD profiles for the deuterated CTAB containing samples show that the SLD oscillations between the layers becomes greater when the mole fraction of CTAB is decreased. However, the SLD of the subphase also approaches that of D_2O, due to the fact that there is a lower concentration of surfactant and polymer near the film-solution interface. In addition for the equimolar and excess molar SB3-14 films the samples contain less deuterated material in the contrast samples compared to the excess CTAB film.

Overall, from the NR fitting it can be said that when the mole fraction of CTAB is decreased, the volume fraction of micelles and LPEI is decreased in the films, with decreasingly well-defined interfaces found in the multilayer model. The validity of the fitting was checked by finding a surfactant and polymer volume fraction that accounted for the SLD of the fitted subphase in each contrast of the film. The results are presented in table 3.14.

α_{CTAB}	Subphase SLD CTAB ($\times10^{-6}$Å^{-2})	Subphase SLD d-CTAB ($\times10^{-6}$Å^{-2})	subphase surfactant vf	subphase polymer vf	subphase water vf
0.667	2.83	4.28	0.38	0.16	0.46
0.5	3.20	4.02	0.21	0.27	0.52
0.33	3.61	3.92	0.08	0.33	0.58

Table 3.14 Results of the model validity check. Where vf is the volume fraction of a component

As the mole fraction of CTAB is decreased, the volume fraction of surfactant in the subphase below the film decreases. This is because the CTAB concentration is the main driving force behind film assembly in this system. However it is also seen that the trend is the opposite for the LPEI and water volume fraction. This highlights the extent of the polymer network even when there is less CTAB in the film forming solutions, since the concentrated yet non-ordered subphase beneath the film has a high PEI concentration even when there is less interaction between LPEI and the mixed micelles.

3.12 Summary of results in this chapter

Film formation occurs at the surface of solutions containing PEI with mixed cationic-zwitterionic surfactant micelles at least for mixtures up to equimolar CTAB:SB3-14. As the mole fraction of CTAB is decreased in the mixed CTAB: SB3-14 micelles, the degree of order decreases in the films. This can be seen in films that are formed from pure CTAB with LPEI and SPEI. In the case of LPEI films a $Pm\bar{3}n$ is formed and in the case of SPEI films a *p6mm* phase is formed. As the mole fraction of CTAB is decreased further, there is a loss of order. This is seen in both LPEI and SPEI films, with the effect being more drastic in SPEI films.

The loss of order in films as the CTAB mole fraction is decreased is indicative of the necessity of CTAB being present to form highly structured films. No films are formed when the surfactant used is only SB3-14. Clearly, the interaction between CTAB and PEI is one of the driving forces for film formation. The CTAB and PEI interaction ensures there is sufficient volume fraction of PEI in the films to force the micellar aggregates to pack in an ordered phase. In LPEI films, whilst there is loss of order, the presence of CTAB even at low concentrations appears to ensure there is enough LPEI present to form sufficiently high micelle volume fractions to form films that exhibit periodic mesostructure. However, the loss of the SPEI and CTAB interaction when the mole fraction of CTAB is decreased causes there to be too little SPEI to ensure ordered films are formed.

There is a decrease in the characteristic *d*-spacing of the periodic mesostructure exhibited d by the films as the mole fraction of CTAB is decreased. This is correlated to the decrease in the surfactant-polymer interaction as shown by the small angle scattering results. Also, the micelles formed from mixtures of CTAB and SB3-14 are more stable than pure CTAB micelles and are less likely to interact with PEI as shown by the CMC results. The decrease in the micelle-polymer interaction means there is fewer polymer molecules in the films. This means that in the films there is less steric bulk from the polymer and less Columbic repulsion between the partially charged polymer chains and between the polymer and CTAB containing micelles.

The application of a multilayer model to the NR profiles of filmed formed from CTAB: SB3-14 mixtures and PEI confirms the summary above. When films are formed from LPEI, it is seen that as the mole fraction of CTAB is decreased there are fewer micellar aggregates in the film. Also, in the multilayer modeling, in layers that are predominately PEI, the PEI layers are more hydrated as the CTAB mole fraction is decreased. This is due to the reduced volume fraction of PEI in the films.

The small angle scattering results shows the degree of the micelle and PEI interaction. The results help explain the observed changes in the interactions in the

films. As the mole fraction of CTAB is decreased the packing parameter of the micelles decreases, increasing the curvature, forming more stable micelles. SANS results shows that SB3-14 penetrates into the mixed micelle so that the end of the aliphatic chain of SB3-14 is level with the aliphatic chain of CTAB. SAXS results confirmed that only the sulfobetaine portion of the headgroup of SB3-14 is pointing out from the surface of the mixed micelles. This presents an opportunity to explain the lessened interaction between mixed micelles and PEI and the pure CTAB micelles with PEI. The conformation of the headgroup presents a hindrance to CTAB and PEI interaction. It was seen from SANS of solutions with polymer that there is less of an interaction that can be attributed to the reduced mole fraction of CTAB alone. The SANS results also showed that the addition of polymer to the surfactant increased the surfactant curvature somewhat compared to micelles without polymer. This is most likely due to the presence of PEI stabilizing bromide ions from the micellar surface, particularly for the mixed micelles as the presence of PEI increased the average surface area per headgroup. This likely indicative of a conformation change in the headgroup of SB3-14.

To summarize the effect of PEI molecular weight, the predominate effect is one of the steric bulk of the polymer network in the film. Specifically that LPEI imposes more steric bulk than SPEI due to LPEI promoting the formation of entangled polymer networks. This can be seen in the diffraction peaks of the NR profiles. The first order reflections of the phases exhibited by films formed from LPEI represent a larger *d*-spacing than the equivalent micelle composition films formed from SPEI (where there is a diffraction peak present in the SPEI films).

It is also seen that when films are formed from LPEI, compared to the equivalent surfactant mixture of CTAB and SB3-14 with SPEI that the films are more stable. There is no loss of mesostructure when film formation is monitored with time in the LPEI films. It was postulated that this was mainly due to PEI becoming further protonated as the solution surface was exposed to carbon dioxide. SPEI is has fewer ionisable amines so is less capable of buffering the solution pH. The loss of structure in the SPEI films arose from the lack of a substantial entangled polymer network allowing aggregates to diffuse back into the bulk as the PEI-micelle interaction was decreased. This was not possible in the LPEI films most likely due to the greater entangled polymer network locking the aggregates in place in the film. The more entangled polymer network was seen in the SANS fitting for LPEI as dressing the surface of the micelle. However, the equivalent solutions with SPEOI yielded results that were similar to the SANS fitting of the mixed micelles with no polymer.

3.13 References

(1) O'Driscoll, B. M. D.; Fernandez-Martin, C.; Wilson, R. D.; Knott, J.; Roser, S. J.; Edler, K. J. *Langmuir* **2007**, *23*, 4589.

(2) O'Driscoll, B. M. D.; Milsom, E.; Fernandez-Martin, C.; White, L.; Roser, S. J.; Edler, K. J. *Macromolecules* **2005**, *38*, 8785.

(3) Comas-Rojas, H.; Aluicio-Sarduy, E.; Rodriguez-Calvo, S.; Perez-Gramatges, A.; Roser, S. J.; Edler, K. J. *Soft Matter* **2007**, *3*, 747.

(4) Campbell, M. M.; Jugdaohsingh, R.; White, K. N.; Powell, J. J.; McCrohan, C. R. *Journal of Toxicology and Environmental Health-Part A* **2000**, *59*, 253.

(5) Wasbrough, M. J.; Edler, K. J.; Hawley, A. M.; Holdaway, J. A.; Price, G. J. *Soft Matter* **2012**, *8*, 3357.

(6) Åberg, C.; Sparr, E.; Edler, K. J.; Wennerström, H. k. *Langmuir* **2009**, *25*, 12177.

(7) Sandbacka, M.; Christianson, I.; Isomaa, B. *Toxicol in Vitro* **2000**, *14*, 61.

(8) O'Driscoll, B. M. D.; Fernandez-Martin, C.; Wilson, R. D.; Roser, S. J.; Edler, K. J. *The Journal of Physical Chemistry B* **2006**, *110*, 5330.

(9) Pantani, C.; Spreti, N.; Maggitti, M. C.; Germani, R. *B Environ Contam Tox* **1995**, *55*, 179.

(10) PENFOLD, J. *J. Phys. Colloques* **1989**, *50*, C7.

(11) Heenan, R. K.; Penfold, J.; King, S. M. *Journal of Applied Crystallography* **1997**, *30*, 1140.

(12) Ilekti, P.; Martin, T.; Cabane, B.; Piculell, L. *The Journal of Physical Chemistry B* **1999**, *103*, 9831.

(13) Leonard, M. J.; Strey, H. H. *Macromolecules* **2003**, *36*, 9549.

(14) Auvray, X.; Petipas, C.; Anthore, R.; Rico, I.; Lattes, A. *The Journal of Physical Chemistry* **1989**, *93*, 7458.

(15) Montalvo, G.; Valiente, M.; Rodenas, E. *J Colloid Interf Sci* **1995**, *172*, 494.

(16) Montalvo, G.; Valiente, M.; Rodenas, E. *Langmuir* **1996**, *12*, 5202.

(17) Asakawa, T.; Kitano, H.; Ohta, A.; Miyagishi, S. *J Colloid Interf Sci* **2001**, *242*, 284.

(18) Brady, J. E.; Brady, D. F.; Evans, G. G.; Warr, F.; Grieser, B. W.; Ninham *J Phys Chem-Us* **1986**, *90*, 1853.

(19) Johnson, S. B.; Drummond, C. J.; Scales, P. J.; Nishimura, S. *Langmuir* **1995**, *11*, 2367.

(20) Berr, S. S.; Caponetti, E.; Johnson, J. S.; Jones, R. R. M.; Magid, L. J. *The Journal of Physical Chemistry* **1986**, *90*, 5766.

(21) Kosacheva, E. M.; Kudryavtsev, D. B.; Bakeeva, R. F.; Kuklin, A. I.; Islamov, A. K.; Kudryavtseva, L. A.; Sopin, V. F.; Konovalov, A. I. *Colloid J* **2006**, *68*, 713.

(22) Edler, K. J.; Wasbrough, M. J.; Holdaway, J. A.; O'Driscoll, B. M. D. *Langmuir* **2009**, *25*, 4047.

(23) Pashley, R. M.; McGuiggan, P. M.; Ninham, B. W.; Brady, J.; Evans, D. F. *The Journal of Physical Chemistry* **1986**, *90*, 1637.

(24) Svensson, A.; Piculell, L.; Cabane, B.; Ilekti, P. *The Journal of Physical Chemistry B* **2002**, *106*, 1013.

(25) Hamley, I. W.; Daniel, C.; Mingvanish, W.; Mai, S.-M.; Booth, C.; Messe, L.; Ryan, A. J. *Langmuir* **2000**, *16*, 2508.
(26) Zeng, X.; Liu, Y.; Impéror-Clerc, M. *The Journal of Physical Chemistry B* **2007**, *111*, 5174.
(27) Imai, M.; Kurimoto, M.; Matsuura, F.; Sakuma, Y.; Kawakatsu, T. *Soft Matter* **2012**, *8*, 9892.
(28) Charvolin, J.; Sadoc, J. F. *J. Phys. France* **1988**, *49*, 521.
(29) Weaire, D.; Phelan, R. *Philosophical Magazine Letters* **1994**, *69*, 107.
(30) Tanford, C. *The Journal of Physical Chemistry* **1974**, *78*, 2469.
(31) Tiddy, G. J. T. *Physics Reports* **1980**, *57*, 1.
(32) Wärnheim, T.; Jönsson, A.; Sjöberg, M. In *Surfactants and Macromolecules: Self-Assembly at Interfaces and in Bulk*; Springer: **1990**, p 271.
(33) Fontell, K.; Khan, A.; Lindström, B.; Maciejewska, D.; Puang-Ngern, S. *Colloid and Polymer Science* **1991**, *269*, 727.
(34) Tanaka, S.; Tate, M. P.; Nishiyama, N.; Ueyama, K.; Hillhouse, H. W. *Chem Mater* **2006**, *18*, 5461.
(35) Ishii, Y.; Nishiwaki, Y.; Al-zubaidi, A.; Kawasaki, S. *The Journal of Physical Chemistry C* **2013**.
(36) Edler, K. J.; Goldar, A.; Brennan, T.; Roser, S. J. *Chem Commun* **2003**, 1724.
(37) Patterson, A. L. *Physical Review* **1939**, *56*, 978.
(38) Smilgies, D.-M. *Journal of applied crystallography* **2009**, *42*, 1030.
(39) Campbell, R. A.; Edler, K. J. *Soft Matter* **2011**, *7*, 11125.
(40) Mulqueen, M.; Blankschtein, D. *Langmuir* **1999**, *15*, 8832.
(41) Tanford, C. *Journal of Molecular Biology* **1972**, *67*, 59.
(42) Holmberg, K.; Jönsson, B.; Kronberg, B.; Lindman, B. *Surfactants and polymers in aqueous solution*; John Wiley & Sons Chichester, **2003**; Vol. 2.
(43) Liu, Y.; Chen, W.-R.; Chen, S.-H. *The Journal of Chemical Physics* **2005**, *122*, 044507.
(44) Rosso, F. D.; Bartoletti, A.; Profio, P. D.; Germani, R.; Savelli, G.; Blasko, A.; Bunton, C. A. *Journal of the Chemical Society, Perkin Transactions 2* **1995**, 673.
(45) Khan, R. U.; Anderson, C. W. N.; Loganathan, P.; Xue, J. M.; Clinton, P. W. *Commun Soil Sci Plan* **2012**, *43*, 1412.
(46) Clint, J. H. *J. Chem. Soc., Faraday Trans. 1* **1975**, *71*, 1327.
(47) Shiloach, A.; Blankschtein, D. *Langmuir* **1998**, *14*, 1618.
(48) Rubingh, D. N. In *Solution chemistry of surfactants*; Springer: **1979**, p 337.
(49) Holland, P.; Rubingh, D. *The Journal of Physical Chemistry* **1983**, *87*, 1984.
(50) Hoffmann, H.; Pössnecker, G. *Langmuir* **1994**, *10*, 381.
(51) Rosen, M. J.; Zhu, B. Y. *J Colloid Interf Sci* **1984**, *99*, 427.
(52) Hines, J. D.; Thomas, R. K.; Garrett, P. R.; Rennie, G. K.; Penfold, J. *The Journal of Physical Chemistry B* **1998**, *102*, 8834.
(53) López-Díaz, D.; García-Mateos, I.; Velázquez, M. M. *Colloids and Surfaces A: Physicochemical and Engineering Aspects* **2005**, *270–271*, 153.
(54) McLachlan, A. A.; Marangoni, D. G. *J Colloid Interf Sci* **2006**, *295*, 243.

(55) Maeda, Y.; Jayakumar, R.; Nagahama, H.; Furuike, T.; Tamura, H. *Int J Biol Macromol* **2008**, *42*, 463.
(56) Maeda, H. *J Colloid Interf Sci* **1995**, *172*, 98.
(57) Wong, J. Y.; Majewski, J.; Seitz, M.; Park, C. K.; Israelachvili, J. N.; Smith, G. S. *Biophysical Journal* **1999**, *77*, 1445.
(58) Hetú, D.; Roux, A. H.; Desnoyers, J. E. *Journal of solution chemistry* **1987**, *16*, 529.
(59) Vass, S.; Torok, T.; Jakli, G.; Berecz, E. *The Journal of Physical Chemistry* **1989**, *93*, 6553.
(60) Wignall, G. D.; Bates, F. S. *Journal of Applied Crystallography* **1987**, *20*, 28.
(61) Russell, T. P.; Lin, J. S.; Spooner, S.; Wignall, G. D. *Journal of Applied Crystallography* **1988**, *21*, 629.
(62) Lindner, P. *Journal of Applied Crystallography* **2000**, *33*, 807.
(63) Zhang, F.; Ilavsky, J.; Long, G.; Quintana, J. G.; Allen, A.; Jemian, P. *Metall and Mat Trans A* **2010**, *41*, 1151.
(64) Pedersen, J. *Journal of Applied Crystallography* **2004**, *37*, 369.
(65) Glatter, O. *Journal of Applied Crystallography* **1977**, *10*, 415.
(66) Brunner-Popela, J.; Glatter, O. *Journal of Applied Crystallography* **1997**, *30*, 431.
(67) Weyerich, B.; Brunner-Popela, J.; Glatter, O. *Journal of Applied Crystallography* **1999**, *32*, 197.
(68) Hansen, J.-P.; Hayter, J. B. *Molecular Physics* **1982**, *46*, 651.
(69) Israelachvili, J. N.; Mitchell, D. J.; Ninham, B. W. *Journal of the Chemical Society, Faraday Transactions 2: Molecular and Chemical Physics* **1976**, *72*, 1525.
(70) Israelachvili, J. *Intermolecular and Surface Forces, Second Edition: With Applications to Colloidal and Biological Systems (Colloid Science)*; {Academic Press}, **1992**.
(71) Kamenka, N.; Chevalier, Y.; Zana, R. *Langmuir* **1995**, *11*, 3351.
(72) Zhang, Y.; Cremer, P. S. *Current Opinion in Chemical Biology* **2006**, *10*, 658.
(73) Lundebye, A. K.; Lock, E. J.; Boyle, D.; Ruohonen, K.; Berntssen, M. H. *Aquacult Nutr* **2010**, *16*, 549.

4 Investigation of Spray Coated Films

4.1 Introduction

In the previous chapter it was shown that it is possible to reduce the toxicity of films formed from cationic surfactant and PEI by reducing the relative concentration of the toxic surfactant CTAB. This was achieved via through replacement with less toxic zwitterionic surfactant SB3-14.

When CTAB was replaced with SB3-14 in the mixed micelles, the films formed exhibited a loss of order. However the extent of this loss was dependent on the molecular weight of PEI. When LPEI was the film-forming polymer it was found that ordered films could still be formed due to the entangled polymer network surrounding the polymer-surfactant aggregates. Ordered films could also still be formed when SB3-14 was in excess to CTAB. When SPEI was the film forming polymer, the loss of order was more pronounced upon increasing of the SB3-14 mole fraction. This was due to the relatively small polymer network between the polymer-surfactant aggregates when SPEI was the film forming polymer. Common to all films however was the relationship between CTAB mole fraction and structural order; more ordered films were formed from formulation that contained the most CTAB. It was clear the overall drive for film formation was from the cation-dipole interaction between CTAB and PEI.

This chapter presents work on the substitution of the cationic charge of CTAB micelles with divalent cations, specifically calcium ions (Ca^{2+}) bound to the SB3-14. Calcium chloride was chosen as the source for Ca^{2+} as the salt exhibits low toxicity[1] although in high concentrations may be an irritant.[1] Compared to other divalent cations it exhibits low toxicity[2-4] and may be used as effective displacement therapy in cases of poisoning.[5-7]

Ca^{2+} can also form complexes with LPEI.[8] Therefore it may act in a similar role to CTAB in the formation of films. First by cross-linking the PEI and forming an extended polymer network and secondly as an agent to increase the hydrophobicity of PEI through complexation.

Zwitterionic surfactants show selectivity towards ions in solution. The selectivity could be exploited in the formation of structure polymer-surfactant films. Selectivity towards anions has been demonstrated for sulfobetaine surfactants.[9-13] However it has also been reported that hydronium binding to sulfonate is possible[13] which is dependent on the hydration of the anion. Less specific cation binding is also

reported, where the interaction is dependent on the valency of the cation.[14] Calcium ions have been shown to have a relatively moderate interaction with sulfobetaine micelles.[14] Therefore Ca^{2+} ions could act as a bridging ion in an inter-molecular interaction between the lone pairs of unprotonated regions of PEI and the headgroups of SB3-14 surfactant molecules within micelles. Similar bridging interactions by Ca^{2+} between a zwitterionic lipid and polyelectrolyte, namely DNA have been previously reported.[15] However this was with a phosphocoline based lipid with dipolar amines within the headgroup. This work focuses on anionic-calcium ion interactions

Two methods of film formation were investigated. First the formation of films formed at the air-water interface spontaneously upon mixing and second by introduction of a secondary interface and spray coating the film forming solutions upon them. The effects of adding $CaCl_2$ to previous film forming solutions containing CTAB and SB3-14 mixtures is initially investigated, followed by the total replacement of the CTAB cationic charge within the film forming solution with $CaCl_2$. Finally, the replacement of PEI with completely non-toxic biopolymers is investigated to form non-toxic mesostructured surfactant-polymer hydrogel films, and their effect on the film mesostructure is investigated.

4.2 Materials and methods

3-(N,N-dimethyltetradecylammonio)propanesulfonate (SB3-14, Sigma Alrich, purity of minimum 99%) and tail deuterated D29-SB3-14 (98%-D Oxford Isotope Facility) were used without further purification. Polyethylenimine (PEI, hyperbranched form) with molecular weights of ~750,000 Da (LPEI) and ~2000 Da, (SPEI) as 50 wt% solutions in water was purchased from Sigma Aldrich. Ultrapure water (purified to 18 MΩ cm using an Elga PURELAB system) or D_2O (99.9%, Sigma-Aldrich) were used to prepare all solutions. Initial separate stock solutions of CTAB, SB3-14 and PEI were prepared in ultrapure water or D_2O prior to mixing to obtain the final film forming solutions. A typical film forming solution was prepared at 1 wt% PEI with SB3-14 and Ca^{2+} at 0.05 M in the initial solutions, however to understand the effect of these components on film formation, the SB3-14 concentration was varied between 50mM and 100mM and the Ca^{2+} between 0.5 and 2 times the molarity of SB3-14. Similar SB3-14/Ca^{2+} solutions containing DNA (0.1wt%), or alginate (0.5wt%) were also used to prepare films.

Spray coated films were prepared on 10 cm diameter, 0.5 mm thick (111) silicon wafers which had been precleaned with ethanol, nonionic surfactant and NaOH solution followed by clean water. Films formed at the air-solution interface were grown on 30 ml solutions contained in Teflon® troughs with dimensions 15 cm x 4

cm x 0.5 cm deep. The troughs were filled until a positive meniscus formed, raising the film surface above the edge of the trough for reflectivity measurements.

Spray coated films were prepared using hand-pumped pressurised aerosol bottles loaded with pre-mixed CTAB/SB3-14/PEI solutions for the PEI containing films. This solution was sprayed onto a clean silicon wafer using a uniform spray for 10 seconds followed by drying time of 20 minutes per layer. Where the polymer would cause direct precipitation if mixed with the surfactant solution, the polymer solution was prepared in a separate bottle at the required final concentration noted above and the surfactant solution in a second separate spray bottle. The components were then sprayed onto a silicon wafer alternately for 10 seconds each with no drying time between polymer and surfactant coatings followed by 20 minutes drying time for each combined layer.

Films grown in situ at the air-solution interface were formed by pouring the pre-mixed surfactant/polymer solution into the Teflon trough and allowing it to equilibrate for 5 minutes during search procedures and beamline alignment. The neutron reflectivity experiments were performed on the CRISP reflectometer at ISIS RAL.[16]

Brewster angle microscopy was carried out using a NFT Nanoscope II Brewster angle microscope using 30 mL of solution held in a plastic Petri dish, 62 mm in diameter, open to atmosphere. Light from a diode pumped frequency doubled $Nd^{+}YAG$ laser at 532 nm was used. At the Brewster angle, the reflectivity of polarised light at the interface is zero, so any small changes in interfacial refractive index, such as the presence of a surface film, are clearly visible.[17] Evolution of the film structure was monitored in real time with the aid of a video camera attached to the BAM.

Dry spray coated films with 8 coating layers were prepared in advance of measurements on silicon wafers. Films were measured on the I07 beamline described in Chapter 2 a using an incident beam energy of 8 keV. Kinetic data on film drying was obtained using the Pilatus area detector to collect fast time-resolved data on freshly prepared spray coated films. Clean silicon wafers were mounted on the hexapod and a pump-pressurised spray bottle used to apply SB3-14/PEI/Ca^{2+} solutions, with data collection started as soon as the search procedure could be completed.

The films required ~20 minutes to dry under the conditions in the hutch, allowing data collection in 20 seconds shots to follow mesophase formation during drying. Spray coating was repeated 3 times to study the effect of increasing film thickness on the mesophase, and the effects of re-wetting the initial spray coated film during subsequent applications of solution. After film formation, the sample was scanned across the beam position, taking patterns every 2 mm across 10 mm to probe the

effects of beam damage and film uniformity. Three incident angles were used to obtain GIXD data out to higher *q* than could be obtained at the initial incident angle and to probe deeper into the film. Similar samples were measured on the ID10B beamline at the ESRF using an incident beam energy of 8 keV. In general a reflectivity pattern was measured initially, requiring 30 min followed by a GIXD pattern at grazing incidence, and, if possible, at the angle of the first order diffraction peak. Each GIXD scan required 45 min.

SAXS measurements were performed on the modified NanoSTAR camera from Bruker AXS at Aarhus University, Denmark. Solutions of SB3-14 and $CaCl_2$ were investigated up to concentrations of 1M and 2M respectively to investigate the behaviour in the high concentration regime. Samples were investigated with and without the presence of PEI at 1% wt. Similar SANS experiments were also performed on the D11 beamline at the ILL. In the SANS experiments, contrast variation was achieved through substitution of per-hydrogenated tail SB3-14 with per-deuterated tail SB3-14 in D_2O.

4.3 CTAB/SB3-14/PEI films formed at the air-solution interface

Films formed at the air-solution interface were investigated by NR and BAM to determine the effect variation of the CTAB mole fraction in the surfactant mixtures of film forming solutions along with the $CaCl_2$ concentration. It was found that increasing the CTAB mole fraction in the films caused the increase of surfactant present in the interfacial film whilst also increasing the smoothness of the film. When films are formed from LPEI 1 wt.% and $CaCl_2$ 100 mM (LPEI/$CaCl_2$ film) with no surfactant present, the films formed at the interface are macroscopically rough. This can be seen from the neutron reflectivity profile (Figure 4.1) as well as the BAM image (Figure 4.2) taken of the formed film. The concentration of 100mM CaCl2 was chosen as this was the lowest concentration that produced robust films with LPEI 1%wt.

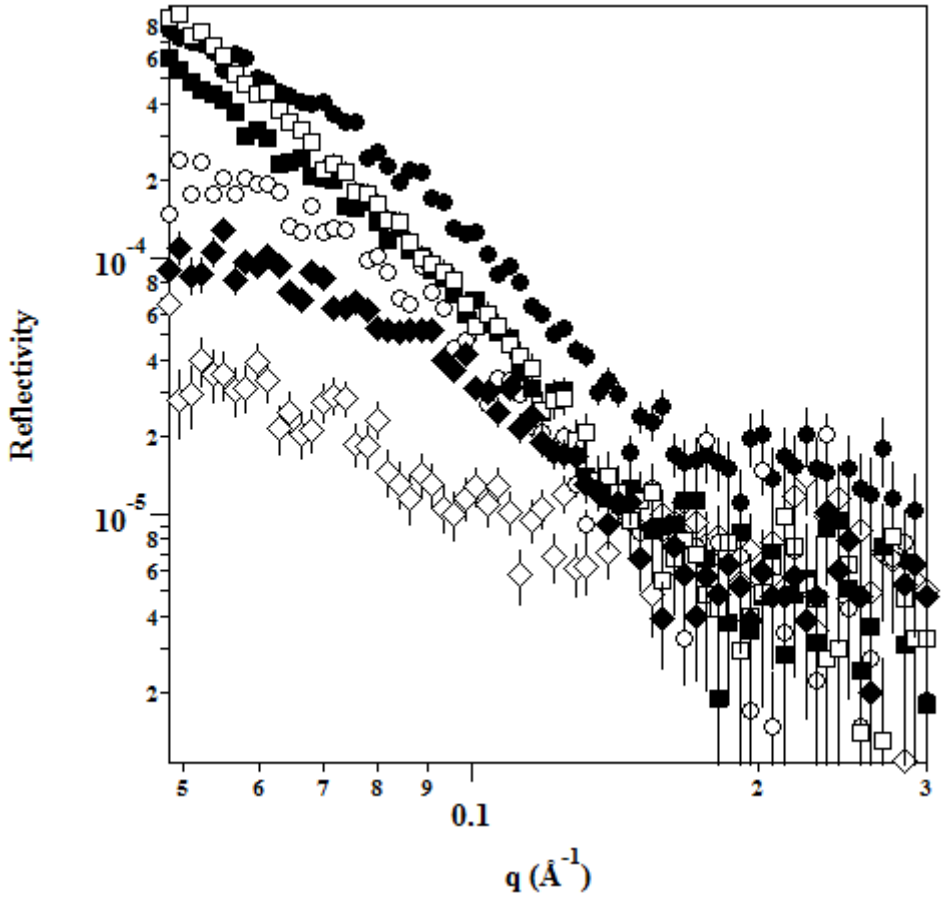

Figure 4.1. Neutron reflectivity data collected from films formed at the air-solution interface formed from LPEI 1 wt%, $CaCl_2$ 100 mM and 50 mM surfactant; CTAB (closed circles), 2 CTAB: 1 SB3-14 (open circles), 1 CTAB:1 SB3-14 (closed squares), 1 CTAB:2 SB3-14 (open squares), SB3-14 (closed diamonds) and no surfactant (open diamonds).

The increase of surfactant content in the film may be observed as an increase in the neutron reflectivity of the film (Figure 4.1) above q = 0.02Å^{-1}. This may be visualised by considering the scattering length density (SLD) of the components within the film. In these experiments as surfactant displaces water in the film, the film scattering length density decreases. This is observable as CTAB, SB3-14 and PEI all have similar scattering length densities when hydrogenated surfactant is considered, due to all three molecules being relatively highly hydrogenated, compared to the essentially pure D_2O or highly hydrated polymer, thus creating greater scattering length density contrast.

The NR profile of the LPEI/$CaCl_2$ film is noisy with respect to intensity below q = 0.2 Å^{-1}, which is less than 1 order of magnitude above the instrumental background of the instrument (as data progresses beyond q = 0.2 Å^{-1} the data becomes more noisy due to the high levels of instrument inherent background and incoherent

scattering from the hydrogenous PEI?). Although the critical edge is not shown in the NR profile it is likely that this low intensity is a consequence of the films roughness causing decay greater in magnitude than the expected $\frac{R_0}{R} \propto q^{-4}$ from an ideal smooth surface. Also the film consists of hydrated polymer and salt, thus having a scattering length density similar to the low concentration LPEI/$CaCl_2$ subphase solution in D_2O. The presence of the macroscopic film is confirmed by inspection of the BAM micrograph in figure 4.2B. It can be seen that the LPEI/$CaCl_2$ film is formed from patches of textured areas of film between areas of smooth film or open water interface.. This is in contrast to the smoother film formed when SB3-14 is present (Figure 4.2A).

LPEI has been shown to complex Ca^{2+}.[8] It was reported that when Ca^{2+} and LPEI are present in a 333:1 molar ratio, 80% of LPEI was present in a Ca^{2+}-LPEI complex at pH 9, which is a similar pH to the solutions in this study.[8] The complexes formed by Ca^{2+} and LPEI are relatively weak, similar to those formed by polyamines and Ca^{2+} ~25 $kgmol^{-1}$.[8] In this present study, the molar ratio of Ca^{2+} and LPEI in the film forming solutions ranges between 3750:1 and 7500:1 at ~pH 9. Therefore it assumed that a large fraction of PEI exists in the Ca^{2+}-LPEI complexed form in this study. So much exists in the complexed formed that the film polymer complexes precipitate out of solution and adsorbs to the air-solution interface.

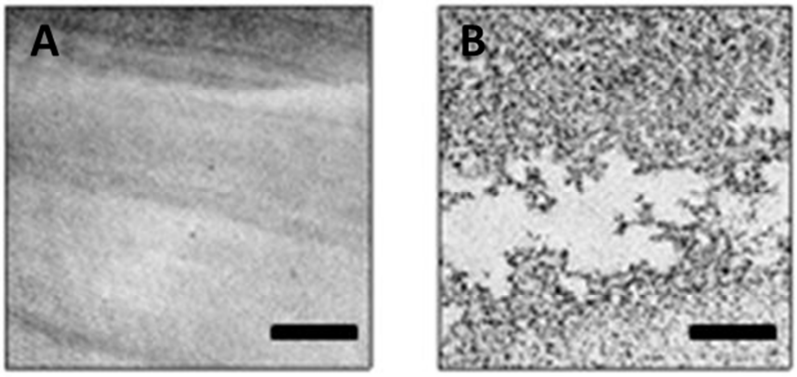

Figure 4.2 Brewster Angle Microscopy images of films formed from [LPEI] =1 wt%, [$CaCl_2$] = 100 mM and **A:** [SB3-14] = 100 mM and **B:** No surfactant. The scale bar is 50μm.

As more surfactant displaces the D_2O, this increased contrast is manifested as increased reflectivity above the normal Fresnel reflectivity. When the surfactant component of the films is purely SB3-14 this observed intensity increase is minor. As the overall charge of the surfactant component is increased, by increasing the mole fraction of CTAB in the surfactant mixtures, the effect becomes more pronounced. This effect is seen in figure 4.1 In the order of No surfactant <SB3-14 < 2 SB3:1 CTAB < 1 SB3-14: 1 CTAB < 1 SB3-14: 2 CTAB< CTAB for the

surfactant component of the film when [$CaCl_2$] = 100 mM, [LPEI] = 1 wt% and [surfactant] = 50 mM. The increase in film smoothness is however also evident when SB3-14, which has no overall charge, is the only surfactant component used to form the films.

Therefore it can be seen that increasing the surfactant micelle charge in the films has a twofold effect, increasing the surfactant content and increasing the smoothness of the film. This may be explained by considering the results in the previous chapter. When films were formed with CTAB/SB3-14 mixtures and PEI with no $CaCl_2$ the correlations in the reflectivity from the film mesostructure, the amount of surfactant in the film and the *d*-spacing of the mesostructure were all proportional to the magnitude of the overall charge of the CTAB/SB3-14 surfactant mixtures *i.e.* the CTAB mole fraction.

The same effect is evident in the NR profiles in the films formed with the addition of $CaCl_2$. As the overall charge of the mixed surfactant micelles is increased, the interaction with PEI is increased. Therefore a greater surfactant charge increases the amount of the surfactant in the film, the film thickness and also increases the degree of order in the films. This is due to the steric repulsion of surfactant micelles when the surfactant component is SB3-14 or the charge-charge repulsion between the micelles when the mole fraction of CTAB is increased. What is not observed is the occurrence of a long range ordered periodic system giving rise to diffraction peaks in the NR profiles. This is explained schematically in figure 4.3.

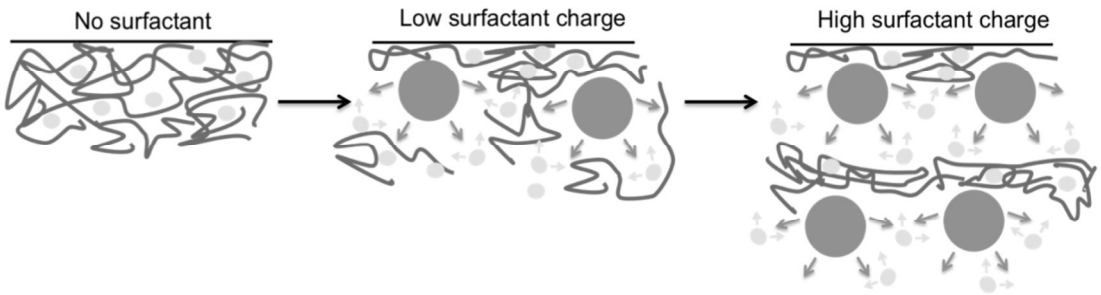

Figure 4.3. Diagram showing the effect of increasing the surfactant charge of the mixed micelles used to form films from CTAB/SB3-14/LPEI and $CaCl_2$. When films are formed with no surfactant and $CaCl_2$ and LPEI the films are a rough collection of salt bound polymer. As surfactant with low or no charge is added (SB3-14) the films are smoothed out due to the steric repulsion between surfactant molecules. As the charge of the micelle is increased by increasing the CTAB mole fraction, the inter-micellar repulsion is increased due to Coulombic repulsion but the interaction with PEI is also increased. This increases the amount of surfactant in the film and increases the film smoothing due to non-charge screened areas of the micelle imposing order in the film.

The absence of diffraction peaks in the films may be explained by the presence of $CaCl_2$ in the film forming solutions. As Ca^{2+} and mixed micelles of CTAB/SB3-14 are both positively charged they compete in binding the PEI to form films. The binding of LPEI by $CaCl_2$ is evident as a film is formed when no surfactant is added to the film forming mixture. As surfactant is added and the surfactant charge is increased there is an increase in the amount of surfactant in the film. However, a fraction of available binding sites on LPEI are taken by Ca^{2+} and protons, as LPEI is basic with a pH of 9-10 in water.[18] The concentration of surfactant in the film may therefore never increase to an amount sufficient to form a periodic mesophase.

As well as the increased competition for binding sites on the PEI, the presence of Cl^- from the $CaCl_2$ will charge screen the surface charge of CTAB-containing micelles. The consequences of this are twofold. The charge screening of CTAB containing-micelles will cause micellar growth, thus reducing the diffusion rate of the micelles and preventing some micelles in reaching the Ca^{2+} complexed polymer matrix film before the polymeric hydrogel matrix become too contracted to allow entry of intact micelles within it. The next consequence is that as the charged micelles are subject to salt screening, the required concentration of surfactant to form a periodic mesophase may be higher as the excluded volume of the micelle decreases due to the lower apparent charge of the micelle. This means that an increased volume fraction of surfactant is required to form the same periodic mesophase as would be required if there was no salt present in the solution.

As films form easily without the presence of surfactant, and the surfactant content of the films is minimal compared to the films formed from solutions of CTAB and PEI with no $CaCl_2$ another approach must be taken to form films that display a controllable periodic mesophase. The presence of $CaCl_2$ in the film forming solutions decreases the concentration of surfactant micelles in the films and the occurrence of periodic mesostructure in the films due to a combination of binding competition and charge screening of the surfactant micelles. The films form without surfactant since the polymeric hydrogel matrix already forms due to binding and charge screening of Ca^{2+}, which may prevent the inclusion of surfactant micelles further due to steric hindrances. The film structure does not change over time suggesting that the structure formed from Ca^{2+} and LPEI is stable and that evaporation of water (if it is able to occur through the polymeric matrix) occurs without changing the concentration of the components within the film. Therefore a change of approach was needed to force the non-toxic SB3-14 to form periodic mesostructured films.

One approach would be to introduce another interface to the film forming solutions. If the film forming solutions were deposited on a solid interface, as water evaporated the number of individual solute molecules within the film forming solutions would stay constant and, thus the solute concentration would increase. This would force a

periodic mesophase to form in the surfactant-polymer hydrogel films as the surfactant concentration within the polymeric matrix would increase.

4.4 Spray-coated films formed at the solid interface

4.4.1 SB3-14/PEI films

Spray coated films formed from solutions of SB3-14 and SB3-14/PEI on a silicon wafer exhibit grazing incidence diffraction patterns corresponding to a solid crystalline surfactant lamellar phase, L_c (Figures 4.1 and 4.2). The occurrence of this phase suggests that when films are formed with no $CaCl_2$ and just the polymer and surfactant components, the loss of water through evaporation occurs to an extent which makes the formation of surfactant mesophase impossible for SB3-14, due to the surfactant volume fraction being too great. If the surfactant volume fraction is too great the surfactant will precipitate out of solution to form solid powdered surfactant crystals. Inspection of the GISAXS data (Figure 4.4) shows that the L_c phase is a powder due to the appearance of Debye-Scherer rings in the diffraction pattern indicating a lack of orientation. When no polymer is present in the film forming solutions and the film is formed from 8 spray-coats of SB3-14 solution (initial concentration 100 mM) there appears to be slight orientation of the lamellar plane parallel to the substrate surface (Figure 4.4a). However when polymer is present qualitative inspection of the out of plane intensity in the GISAXS data show that the planar orientation of the L_c phase is more disordered (Figure 4.4b and 4.4c).

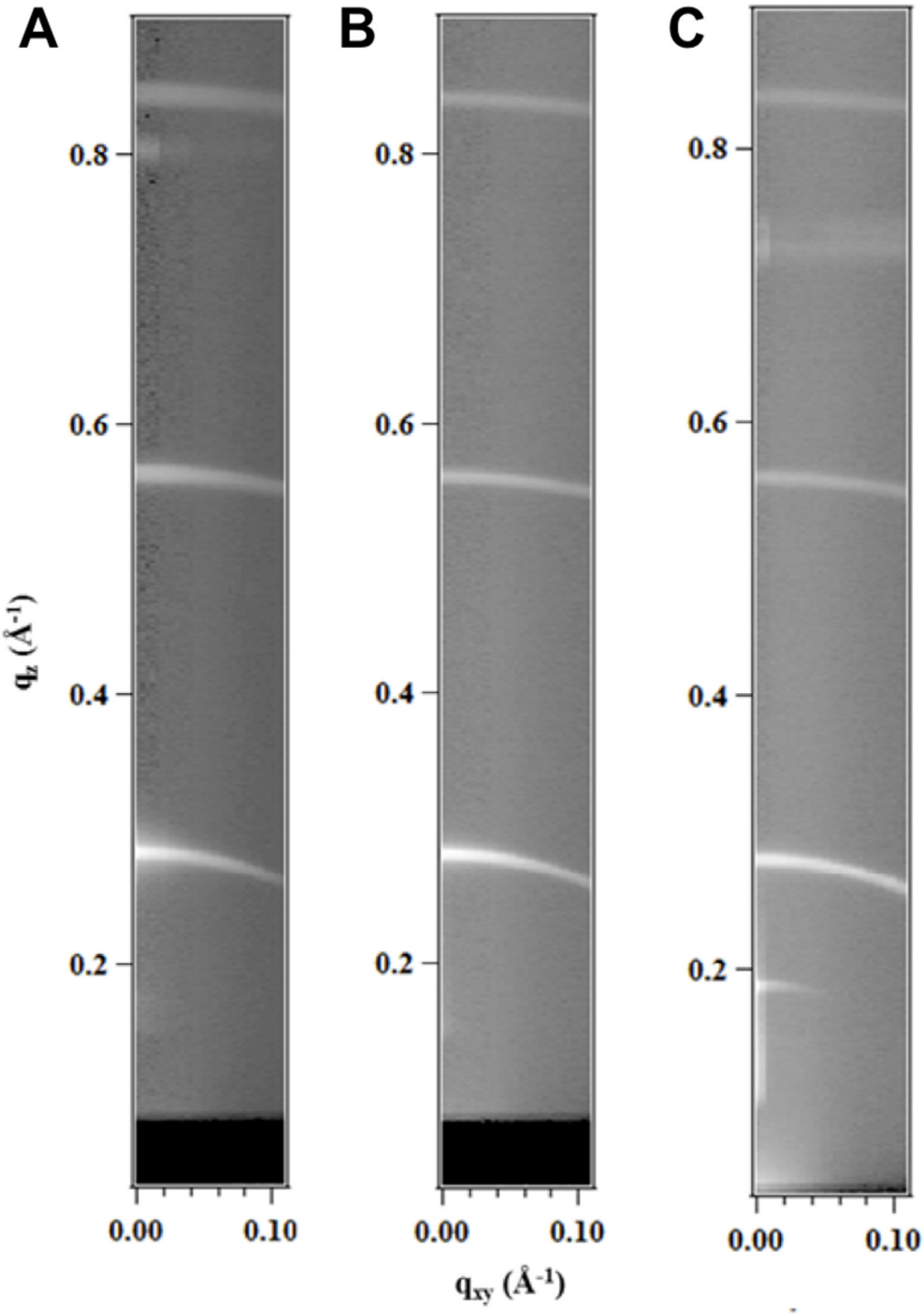

Figure 4.4. GISAXS data of spray coated films formed from SB3-14/PEI mixtures. [SB3-14] = 100 mM in all films, films formed from 8 spray coating applications **A**: No polymer $\alpha_i = 1.96^o$ **B**: [SPEI] = 1 wt% $\alpha_i = 1.98^o$ **C**: [LPEI] = 1 wt% $\alpha_i = 1.31^o$

The effect on the *d*-spacing of the L_c phase when no polymer is present and when polymer is present is minimal (Figure 4.5 and Table 4.1). Analysis of the *d*-spacing

by converting reciprocal space to real space using $d_n = \frac{2\pi}{q_n}$ shows that pure SB3-14 films exhibit a *d*-spacing of 22.4 Å whereas when polymer is present the L_c *d*-spacing increases to 22.7 Å. The x-ray crystal structure of SB3-14 has been reported as a triclinic structure with dimensions *a* = 6.4 Å *b* = 8.6 Å and *c* = 24.7 Å.[19] The maximum dimension of the crystal structures is larger than the lamellar spacing of the spray coated film without PEI. However the crystal formation procedure to obtain crystals of SB3-14 for the reported structure made use of additives to achieve the crystal and the formation procedure was different to the procedure of the spray coated films. The conformation of the L_c phase is explained in greater detail in the next section.

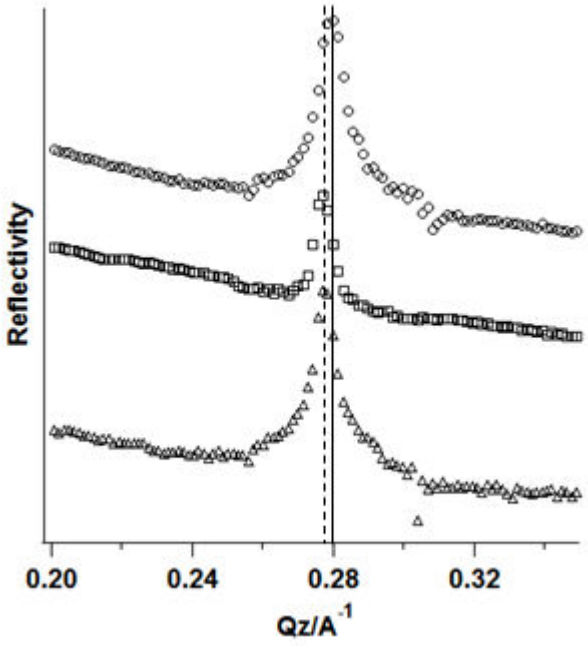

Figure 4.5. XRR profiles spray-coated films formed from SB3-14/PEI mixtures. [SB3-14] = 100 mM in all films, films formed from 8 spray coating applications A) No polymer B) [SPEI] = 1 wt% C) [LPEI] = 1 wt%. The lines at ~0.28 $Å^{-1}$ highlight the reciprocal space position the intensity from the L_c phase

The ~0.3 Å increase with the addition of polymer is too small to be attributed to intercalation of the polymer between the lamellae of the L_c phase although the presence of polymer may be the indirect cause of the *d*-spacing increase. The hygroscopicity of PEI[20-24] may cause more water retention within the film and this in turn whilst not enough to allow the surfactant to form a mesophase is enough to affect the conformation of the head group of SB3-14 thus resulting in the expansion of the lamellar phase. This effect is explained in greater detail in the SB3-14/$CaCl_2$/PEI film results below.

However, when films are formed from solutions of SB3-14 and solutions of SB3-14/PEI, no surfactant mesophase is evident in the film. This can be attributed to the lack of water content of the film preventing the formation of an ordered surfactant mesophase and the film comprising structures of essentially precipitated surfactant.

Film components	***q* of initial Bragg diffraction ($Å^{-1}$)**	**Lamellar Spacing (Å)**
SB3-14 100 mM	0.280±0.0005	22.4±0.01
SB3-14 100 mM, SPEI 1 wt%	0.277±0.0005	22.7±0.01
SB3-14 100 mM, LPEI 1 wt%	0.277±0.0005	22.7±0.01

Table 4.1. Positions of the first order diffraction and *d*-spacing of the L_c phase formed by spray coated solutions of SB3-14 and PEI

4.4.2 SB3-14/$CaCl_2$ films

Films formed from solutions of SB3-14 with $CaCl_2$ with no polymer do not form a periodic mesophase however they do form a mesophase. The XRR profile (Figure 4.6) exhibits a broad peak in the reflectivity profile. The peak is centred on q = ~0.12 $Å^{-1}$ with a peak start of q = ~0.09 $Å^{-1}$ and a peak end of q = ~1.6 $Å^{-1}$. This would give an average periodic spacing of ~52 Å.

The data was not fitted due to the lack of other information on the film structure. The reflectivity profile could equally arise from a distribution of scattering length density that was just 1 or 2 layers on top of an amorphous layer of high scattering length density or from a distribution of scattering length density profiles consisting of different thicknesses of layer. It is more likely that the origin of the broad peak is from a correlated micellar phase seen in time-resolved measurements presented later, although this cannot be directly demonstrated.

Regardless of the origin of the broad peak in the reflectivity profile, it can be seen that the addition of $CaCl_2$ to the film-forming solutions with SB3-14 promotes the formation of a liquid crystal mesophase rather than a solid crystalline surfactant film. The promotion of formation of a surfactant mesophase may be attributed to the hygroscopicity of $CaCl_2$, which has been shown to increase the total water uptake of matrices where it is present.[25-27] Although the surfactant film in this case is not present as part of a cross-linked matrix it is assumed to be a similar phenomenon

here, where the presence of $CaCl_2$ modulates the water content of the film, preventing less water desorption through evaporation than would occur if the film forming solution just contained SB3-14.The presence of $CaCl_2$ in solution has been shown to modulate the humidity of closed atmospheres through it's hygroscopicity,[28,29] particularly in situations where low toxicity is required such as in food packaging[30] and direct application to food[31,32] in enclosed packaging.

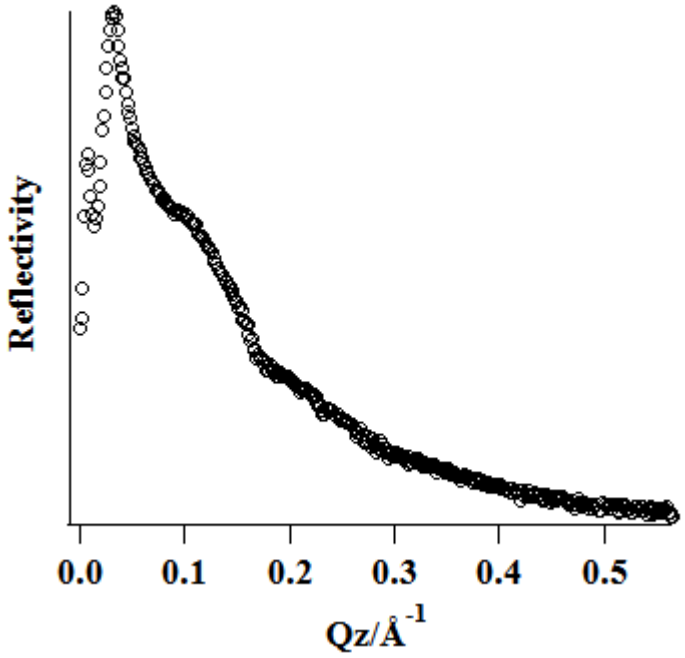

Figure 4.6. XRR profile of film formed from spray coated solution of SB3-14 and $CaCl_2$. [SB3-14] = 100 mM, [$CaCl_2$] = 100 mM in the initial film forming solution. Film formed from 8 spray coating applications.

4.4.3 SB3-14/$CaCl_2$/PEI films

2 [SB3-14]:1 [CaCl2] films

Films formed from solutions containing SB3-14, $CaCl_2$ and PEI exhibit a periodic mesophase. When the ratio of surfactant to $CaCl_2$ is 2 [SB3-14]:1 [$CaCl_2$], [SB3-14] = 100 mM and [PEI] = 1 wt% the resultant mesophase structure in the film is a mixture of L_α and L_c. GISAXS and XRR profiles of films formed are presented in Figure 4.7. XRR data (Table 4.2) and the radial integration of GISAXS data (Figure 4.9C) was fitted to Lorentzian peak models to obtain the unit cell sizes of the film structures formed and the Scherrer equation applied to obtain information about the

apparent crystallite size of the periodic mesostructure in the film (Table 4.3). Instrumental resolution is not included in the Scherrer analysis so the quote crystallite sizes are the lower limits

GISAXS and XRR (Figure 4.7A & 4.7C) of SPEI and LPEI films (Figure 4.7B & 4.7D) formed with this surfactant with $CaCl_2$ exhibit the same mixed mesophase. Analysis of the GISAXS data shows that the phases exhibited by the films are one dimensional and that further structures are not present. Although the presence of PEI polymers of different molecular weight does not cause different mesophases to be present in the films, the films do display subtle differences in the degree of order in the film. When LPEI is used as the film forming polymer there is a slight increase in the unit cell of the mesophases compared to SPEI. On average this is approximately 0.5 Å, which is too small to be attributed to a change in the intercalation of polymer.

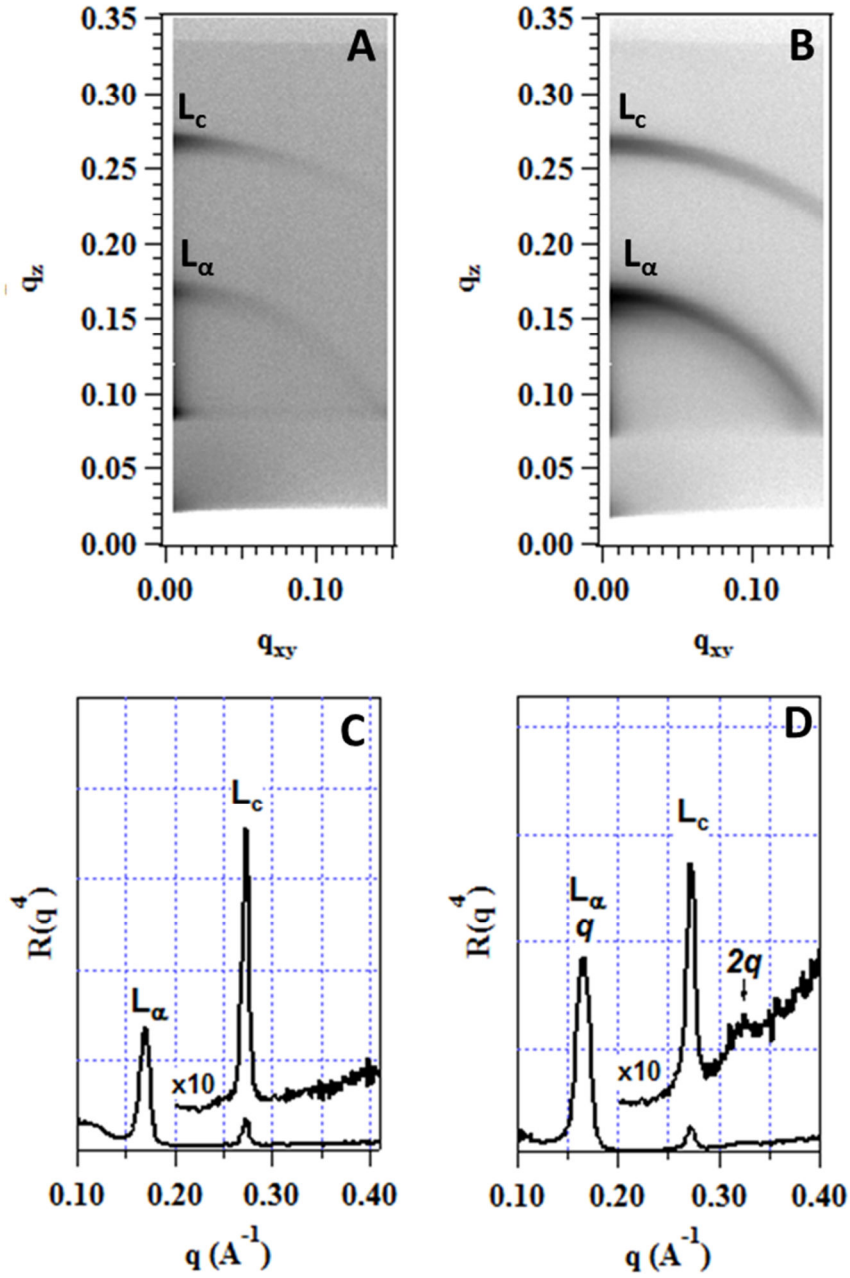

Figure 4.7. GISAXS and XRR of films formed from spray coated solutions of 2 SB3-14:1 $CaCl_2$ [SB3-14 100 mM] with 1 wt% PEI. **A**: GISAXS plot of film formed with SPEI as PEI component, $\alpha_i = 1.1^\circ$. **B**: GISAXS plot of film formed with LPEI as PEI component, $\alpha_i = 0.96^\circ$. **C**: XRR profile of film formed with SPEI as the PEI component. D) XRR profile of film formed with LPEI as the PEI component. GISAXS plots show log intensities for clarity. XRR profile intensities are presented as $\boldsymbol{I = \frac{R_0}{R} q^4}$ to remove the Fresnel reflectivity trend. Maxima resulting from the structures in the films are annotated; L_α liquid crystalline lamellar, L_c solid crystalline lamellar, *nq* order of liquid crystalline lamellar peak.

The main effect of the polymer molecular weight used in the film forming process is on the lateral planar disorder of the film. When the films are formed with SPEI as the polymeric component, the films exhibit a preferred orientation with the lamellar planes relatively parallel to the substrate surface. When films are formed with LPEI, the orientation of the lamellar planes is also predominately parallel to the substrate surface. However azimuthal integrations of the GISAXS data show that LPEI containing films exhibit more deviation away from the orientation parallel of the substrate surface than SPEI containing films. This trend is evident in both the L_α phase (Figure 4.8a) and L_c phase (Figure 4.8b) for films formed from SPEI and LPEI, since the integrated azimuthal intensity decays with no maxima apart from the $q_z = 0$ (substrate normal axis), with the q_y range investigated.

XRR	[SB3-14]=100mM		[CaCl2]=50mM	[PEI]=1%wt
Polymer	**Phase**	**Index**	**XRR peak ($Å^{-1}$)**	**Unit cell (Å)**
SPEI	L_α	1.00	0.170±0.0005	37.0±0.01
	L_c	1.00	0.273±0.0005	23.0±0.01
LPEI	L_α	1.00	0.166±0.0005	37.9±0.01
		2.00	0.325±0.002	38.6±0.03
	L_c	1.00	0.272±0.0005	23.1±0.01

Table 4.2. XRR peak positions, films phases and unit cell dimensions. Composition of spray coating solution provided in top row of table

GISAXS	Solution =		[SB3-14]=100mM		[$CaCl_2$]=50mM	[PEI]=1%wt	
Sample	**Phase**	**Index**	**GISAXS peaks ($Å^{-1}$)**	**Unit cell (Å)**	**FWHM (10^{-2})**	**Size (Å)**	**Area ($Å^2$)**
SPEI	L_α	1	0.167	37.5±0.1	1.15±0.04	546±18	2.24±0.07
	L_c	1	0.268	23.4±0.1	0.712±0.03	883±34	2.47±0.09
LPEI	L_α	1	0.165	38.1±0.1	1.20±0.04	525±18	45.7±0.02
		2	0.266				
	L_c	1	0.170	23.6±0.1	0.873±0.03	720±24	11.9±0.04

Table 4.3. GISAXS peak positions, film mesophase assignments, unit cell size, peak widths, apparent crystal size and integrated area from fits of Lorentzian peaks to the data. Composition of spray coating solution provided in top row of table

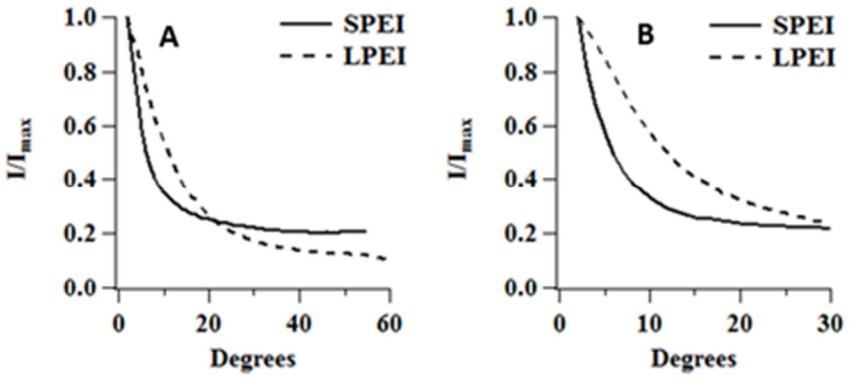

Figure 4.8. Azimuthal and q_z slice integrations of GISAXS plots from films formed from 2SB3-14:1 $CaCl_2$ [SB3-14] = 100 mM. **A:** Azimuthal integrations of L_α peak from GISAXS data. **B:** Azimuthal integrations of L_c peak from GISAXS data.

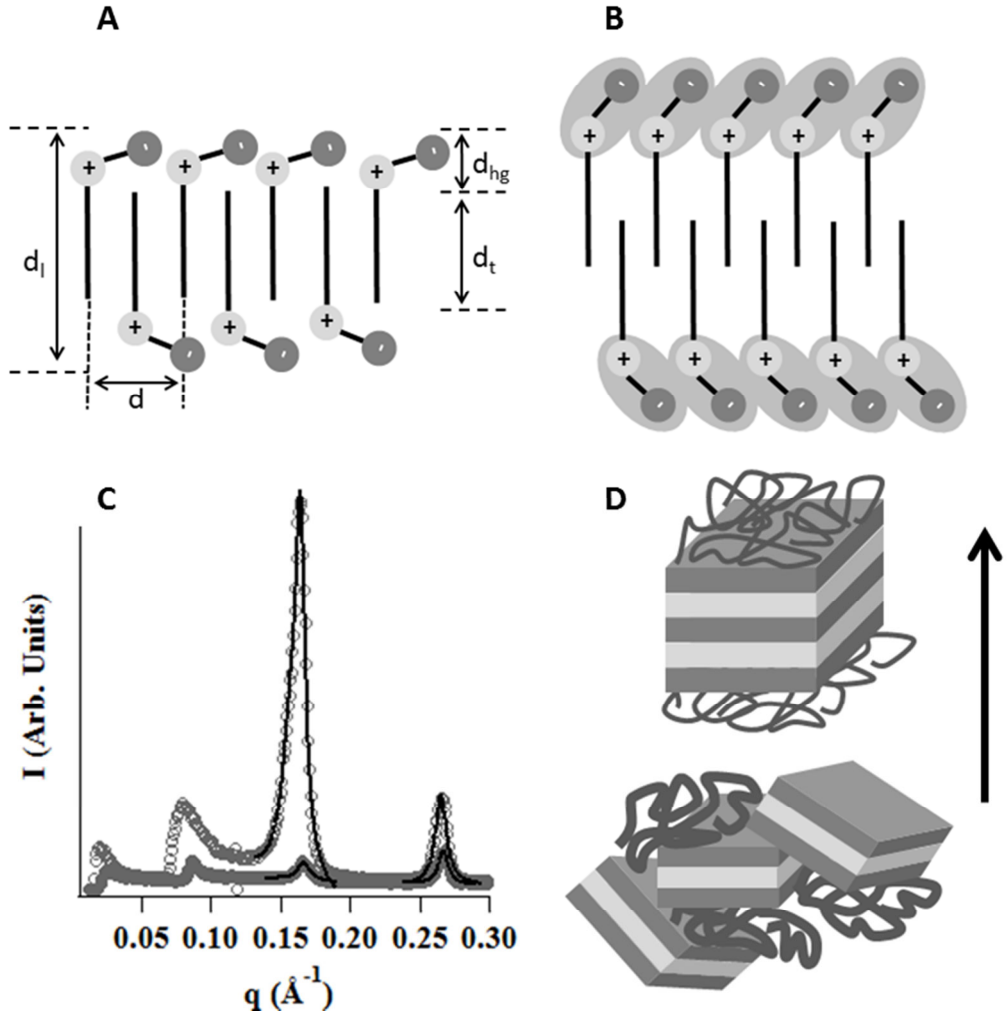

Figure 4.9. A: Diagram of the L_c crystalline solid surfactant phase of lamellar thickness ~23Å present in films formed from SB3-14/PEI solutions and 2 [SB3-14]:1 [$CaCl_2$]/PEI solutions; lamellar thickness, surfactant headgroup thickness, hydrophobic tail thickness and lateral surfactant tail spacing are denoted by d_l, d_{hg}, d_t and d respectively. **B:** Diagram of the suspected L_α phase present in films formed from 2 [SB3-14]:1 [$CaCl_2$]/PEI solutions. The grey region surrounding the surfactant headgroups highlights the increased hydration of the headgroups compared to the L_c phase surfactant headgroups. **C:** GISAXS intensity along q_z from q_y = 0.05 Å^{-1} of films formed from 2 [SB3-14]: 1 [$CaCl_2$]/SPEI (closed circles) and 2 [SB3-14]: 1 [$CaCl_2$]/LPEI (open circles). Solid black lines represent Lorentzian peak fits with linear background to peak data between $\boldsymbol{q_{max} \pm 0.025 Å^{-1}}$. **D:** Diagram showing difference in orientation in both L_α and L_c phases in films formed with 2 [SB3-14]: 1 [$CaCl_2$]/SPEI (upper image) and 2 [SB3-14]: 1 [$CaCl_2$]/LPEI (lower image). The arrow highlights the direction of the substrate normal.

The *d*-spacing's exhibited by the two lamellar phases present in the film are quite small compared to the expected spacing of extended C_{14} chain[33,34] surfactants in a lamellar phase. [34] The small *d*-spacing of the lamellae suggest there is some

intercalation of the alkyl surfactant chains (Figure 4.9B) as an all trans conformation of the surfactant chains would cause the alkyl component of the L_α surfactant mesophase alone to have a *d*-spacing of ~38 Å.[33] It is unlikely that there is any intercalation of polymer between the L_α crystallites indicated by the *d*-spacing's of the unit cell of both the L_α and L_c phase which are respectively ~37 Å and ~23 Å. The increase in spacing between the SPEI and LPEI samples for the same surfactant and $CaCl_2$ composition is approximately 5 Å in both XRR and GISAXS (table 4.3 & 4.4). It is unclear as to whether the increase in unit cell size for samples that contain $CaCl_2$ compared to samples without $CaCl_2$ is due to hydration of the headgroup or intercalation of polymer.

The *d*-spacing of the L_c phase at ~23 Å is small enough to be considered to be the length of the SB3-14 molecule with the headgroup arranged so that it is in a low energy conformation, with the headgroup charges associating with other adjacent molecules of the surfactant in the L_c phase. This is because if the headgroup was fully extended along with a fully extended alkyl chain the surfactant molecule would be expected to have a length longer than ~23 Å. The tri-methyl quaternary ammonium head group of CTAB is ~6 Å in length.[35] Therefore, as the sulfobetaine headgroup is comprised of a quaternary ammonium, propyl group and sulfonate ion it is unlikely that this group fully extended would be less than ~4Å (where the value of 4 Å is calculated from L_c *d*-spacing of 23 Å minus the extended length of a 14 carbon chain, ~19 Å[36]).

The arrangement of the molecules in this L_c phase is difficult to determine without any wide angle scattering information to confirm the conformation of the alkyl surfactant tail group or indeed any higher order peaks at smaller angles of the lamellar phase. It is assumed that the surfactant molecules are in the conformation indicated in figure 4.9Å due to the d-spacing involved. This structure is similar to the one reported in Yokoyama *et al.*[19]

By considering this structure of the L_c phase it is possible to postulate the steric cause of the L_α phase which is of quite a short *d*-spacing at ~38Å compared to the expected minimum *d*-spacing of SB3-14 molecules in a L_α phase, with the alkyl surfactant tails in a trans conformation. If the head groups of the surfactants contained in the L_c phase are non-hydrated then, to lower the energy of the anionic and cationic charges, the headgroups are most likely arranged so that they are as near to an opposite charge as is sterically possible. This immediately rules out an intra-headgroup ion-ion interaction due to the bending restrictions imposed by the inter-charge propyl group. It has been shown in numerous studies that the inter-charge alkyl group must be above 5 methylene group long to exhibit appreciable inter-zwitterion charge association.[37] Due to the non-hydrated state of the headgroups and the likely charge interaction between headgroups it is likely that the surfactants are in fact in a conformation highlighted in Figure 4.9A; the L_c phase, where the

surfactant alkyl tails are in an alternating inter-digitating conformation [34] This structure is comparable to the crystal structure for SB3-14 reported by Yokoyama *et al*[19] however it should be noted that the crystallisation conditions are different to the crystallisation conditions present in this study.

When more water is present in the system the headgroups become more hydrated. This hydration will lead to hydration shells developing around the ions of the zwitterionic headgroup and thus change the conformation of the headgroups due to the steric factors of the hydration shell. If the headgroups extend away from the lamellar plane due to their increased hydration then they may impose less lateral pressure on the surfactant molecules in the lamellar. This in turn may decrease the opportunity for inter-digitation in the hydrophobic core of the lamellar and produce a phase a shown schematically in Figure 4.9B.

Central to these structural changes is the presence of water. The presence of $CaCl_2$ as discussed previously promotes water retention.[25-27] Therefore, in the formation of the spray coated films when they undergo evaporation the presence of a L_α phase can be explained by the presence of a little water compared to just the L_c phase when no $CaCl_2$ is present. Further to this, the effect on the polymer type on the structures exhibited by the spray coated films may be explained by the amount of water present.

All components of the film are in fact hygroscopic with the PEI showing significant hygroscopicity.[21-24] When the film components such as the surfactant and $CaCl_2$ contents are the same between SPEI and LPEI formed films, then any change in the unit cell of the surfactant mesophase must come from the contribution of the polymer. As explained above the change in unit cell sizes may be too small to postulate that it comes from intercalation of the polymer between the lamellar sheets, therefore the change in unit cell size must come from a difference in the degree of hydration of the surfactant headgroup. As explained above this will also change the apparent size contribution of the surfactant alkyl chain tails to the lamellar spacing due to the headgroup conformation allowing less inter-digitation.

This water retention effect from PEI can be seen when considering the relative distribution of the L_c and L_α phase in the spray-coated films. When films are formed from 1 [SB3-14]: 1 [$CaCl_2$] with [SB3-14] = 100 mM and the polymer component is SPEI 1 wt% the ratio of the relative scattering volume obtained from the integrated area of a Lorentzian fitted to a near specular q_{xy} slice of the GISAXS data (Figure 4.9) of the L_α phase to the L_c phase is 2.24:2.47 (table 4.3) or approximately close to 1 suggesting there is a near equal amount of scattering volume in the two phases. However when films were formed from the same surfactant and $CaCl_2$ composition but using LPEI 1 wt% as the polymer component, the relative scattering volume of the L_α to L_c phase is 45.69:11.64 which is approximately 4 times greater scattering

volume of the L_α phase compared to the L_c phase. As the occurrence of the L_α phase is dependent on the water content of the film, it can be said that there is greater water content in the film containing LPEI. The greater water content with LPEI is seen from the slight increase in the unit cell size of both the L_α and L_c phases which can be put down to the increase in size due to a change in the conformation of the head groups and also in the relative amounts of the two different phases in the films.

So, use of LPEI in the film forming solutions causes an increase in the amount of the hydrated L_α-like phase from analysis of the integrated peak areas in the GISAXS patterns. Further analysis of the peak of the GISAXS patterns reveals that there is minimal change in the relative size of the crystallites comprising both phases, with the apparent crystal size of the L_α phase being 546 Å and 525 Å for the SPEI and LPEI containing film samples respectively. For the L_c phase the apparent crystal sizes are 883 Å and 720 Å for the SPEI and LPEI containing films, respectively. Thus the presence of more water in LPEI containing samples shows that whilst the number of the L_α phase crystallites increase, the size of L_α phase remains essentially unchanged.

The presence of more water in LPEI containing films could also be a steric consequence of the fact that LPEI is a large hyper-branched polymer rather than a small short brush like polymer as in SPEI. As the polymeric matrix interacts with Ca^{2+} ions it probably forms a cross-linked polymeric matrix through forming complexes with Ca^{2+}. When either SPEI or LPEI is used in the film forming solutions there is the same number of monomers in the solution. LPEI is slightly more basic suggesting a different distribution of primary vs. secondary or tertiary amines however the same number of amines are available for coordination to the Ca^{2+} ions. Due to the increased linear and branching length of the LPEI polymer the polymeric matrix of the LPEI containing samples will be able to cross-link inter-polymerically to a greater degree, simply due to the increase size of the polymer, increasing the likelihood that it come into contact with another polymer molecule. The resulting, more cross-linked structure, would hinder water loss through evaporation by hindering transport of water.

The effect of polymer on the mesostructural order present in the film is schematically represented in figure 4.9D. From the azimuthal integrations in figure 4.8A and B, it can be seen that films formed with SPEI as the polymeric component display less planar disorder than films formed with LPEI.. This is likely due to the size of LPEI compared to the size of SPEI. The steric impositions of the larger LPEI polymer cause the planar growth of the L_α phase and L_c phase as the water is dehydrated from the film forming solution. The smaller crystallite size plus the volume occupied by the LPEI-water-Ca^{2+} complex cause the smaller crystallites to be distributed more widely around the substrate normal axis. This is further evidence that the polymeric components are not incorporated in to the surfactant mesophase

and that the surfactant crystallites probably exist in a phase separated, surfactant-rich state.

1 [SB3-14]:1 [$CaCl_2$] films

When films are formed from a mixture of 1 [SB3-14] : 1 [$CaCl_2$] with 1 wt% PEI there is an increase in the surfactant micelle curvature in the micelles which comprise the ordered surfactant mesophase in the film. Inspection of the GISAXS data (Figure 4.10a and 4.10b) shows that films containing SPEI 1 wt% or LPEI 1 wt% both form films containing a clear columnar two dimensional space group in this case a *p6mm* which is a two dimensional hexagonal structure. In Figures 4.10A and 4.10B the GISAXS data are annotated with the *p6mm* scattering maxima in white bold type. As well as both films exhibiting a *p6mm* phase when films are formed from SPEI containing solution, the GISAXS patterns show the presence of the L_α and L_c () also present in the films formed from solutions with a surfactant to $CaCl_2$ molar ratio of 1:2 as described previously. The L_α and L_c phases are annotated on figure 4.10a in bold black type. The unit cell dimensions calculated from the XRR and GISAXS are presented in Tables 4.6 and 4.7 respectively.

The XRR profiles of the films (Figure 4.10C and 4.10D) made from this 1:1 surfactant to $CaCl_2$ ratio show the same structures as the GISAXS profiles. However it is possible to determine the degree of orientation of the crystallites normal to the substrate plane by analysis of the GISAXS data. Initial inspection of the XRR from the SPEI containing film suggests that the structure is a *p6mm* structure of mixed planar orientation *i.e.* the 10 and 11 crystallographic planes are in a mixture where both planes are parallel to the substrate surface. The orientational dependence of observed peaks in the q_z scattering plane from a *p6mm* crystal was discussed in Chapter 3. In the film containing LPEI the only peaks apparent are what appears to be a first and second order of a lamellar phase or *p6mm*. This initially suggests that the film containing SPEI exhibits more planar disorder in the crystallite orientation normal to the substrate than for the film containing LPEI, which is opposite to the polymer dependent orientation seen in film comprised of a 1:2 surfactant to $CaCl_2$ ratio. However the GISAXS data shows that *p6mm* crystals exist in both films and the orientation of the films may not be as straightforward as it initially seems.

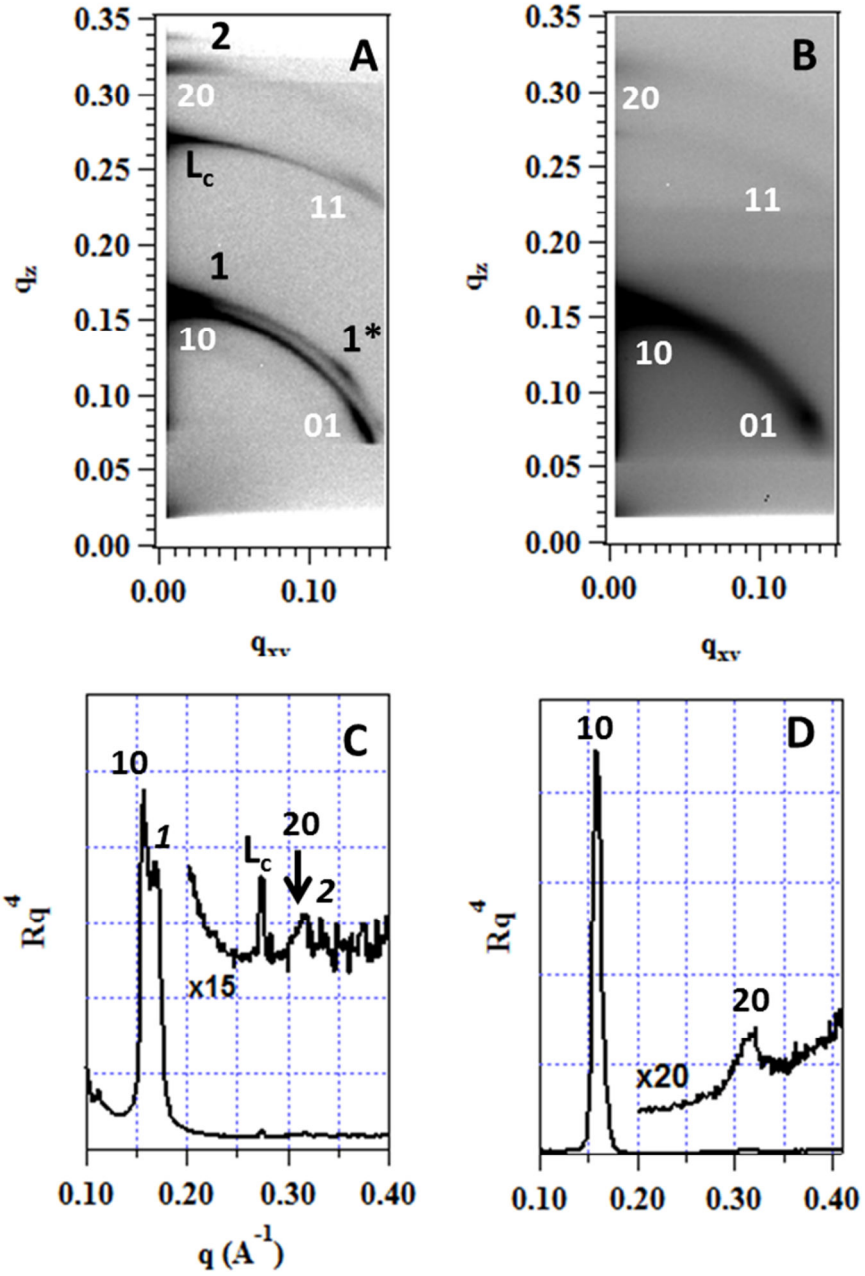

Figure 4.10. GISAXS and XRR of films formed from spray coated solutions of 1 [SB3-14]:1 [$CaCl_2$] [SB3-14] = 100 mM with 1 wt% PEI. **A:** GISAXS plot of film formed with SPEI as PEI component, α_i=1.1˚. **B:** GISAXS plot of film formed with LPEI as PEI component, α_i=0.96˚. **C:** XRR profile of film formed with SPEI as the PEI component. **D:** XRR profile of film formed with LPEI as the PEI component. GISAXS plots show log intensities for clarity. Reduction in intensity at high q_z values is from a blade above sample to reduce air scatter. XRR profile intensities are presented as $\boldsymbol{I = \frac{R_0}{R} q^4}$ to remove the Fresnel reflectivity trend. For clarity low reflectivity high q regions in the XRR profiles are multiplied and factor is shown. Maxima resulting from the structures in the films are annotated and explained in text. The effect of using SPEI or LPEI as the polymeric component in the formation of films formed from 1 SB3-14:1 $CaCl_2$ is twofold. Firstly as described previously the

use of the lower molecular weight SPEI shows that two liquid crystalline structures are formed, a L_α phase and a *p6mm* phase made up of cylindrical micelles plus a lamellar phase formed from hydrated solid surfactant. The larger molecular weight LPEI forms only a *p6mm* phase. As the *p6mm* phase exhibits greater individual micelle surface curvature than a L_α phase, the headgroups of the surfactant comprising the *p6mm* phase must have a larger cross-sectional area in the surface, causing forcing the micelles to develop a curved cylindrical structure. Therefore as the concentration of the non-surfactant components in the film are constant over both films, *i.e.* polymer at 1 wt% and $CaCl_2$ at 100 mM in the initial film forming solution, it is likely that the increase in micelle curvature seen in the *p6mm* phase is caused by more water being present in the film.

Secondly when the films are formed with LPEI as the polymeric component it is seen that the films exhibit more planar disorder in the film structures than films formed with SPEI regardless of the structure phase. This effect is similar to that seen in the films formed from 2 SB3-14:1 $CaCl_2$ where the presence of LPEI rather than SPEI was found to cause planar disorder in the lamellar phases in the films.

The true orientation of the *p6mm* liquid crystals can be seen qualitatively by inspecting the out of plane scattering in the figures 4.11A & B for films formed from SPEI and LPEI respectively. Azimuthal integration of the Debye-Scherer rings on GISAXS patterns from these films show the planar disorder present in the films (figure 4.13).

Inspection of the change in relative intensity in the azimuthal integration as the angle increases from the zero angle, defined by the q_z direction, shows the orientation of the structures in the films. Figure 4.11A shows the azimuthal intensity of the 10 and 11 reflections from the *p6mm* structure. There is a decrease from maximum intensity as the angle increases, rising to additional maxima at 60 and 30 degrees from the 10 and 11 reflection, respectively. This confirms that the *p6mm* is predominately orientated with the 10 crystallographic planes parallel to the substrate as, from figure 4.11, these are the expected angular positions of the out of plane scattering for a 10 oriented *p6mm* phase.

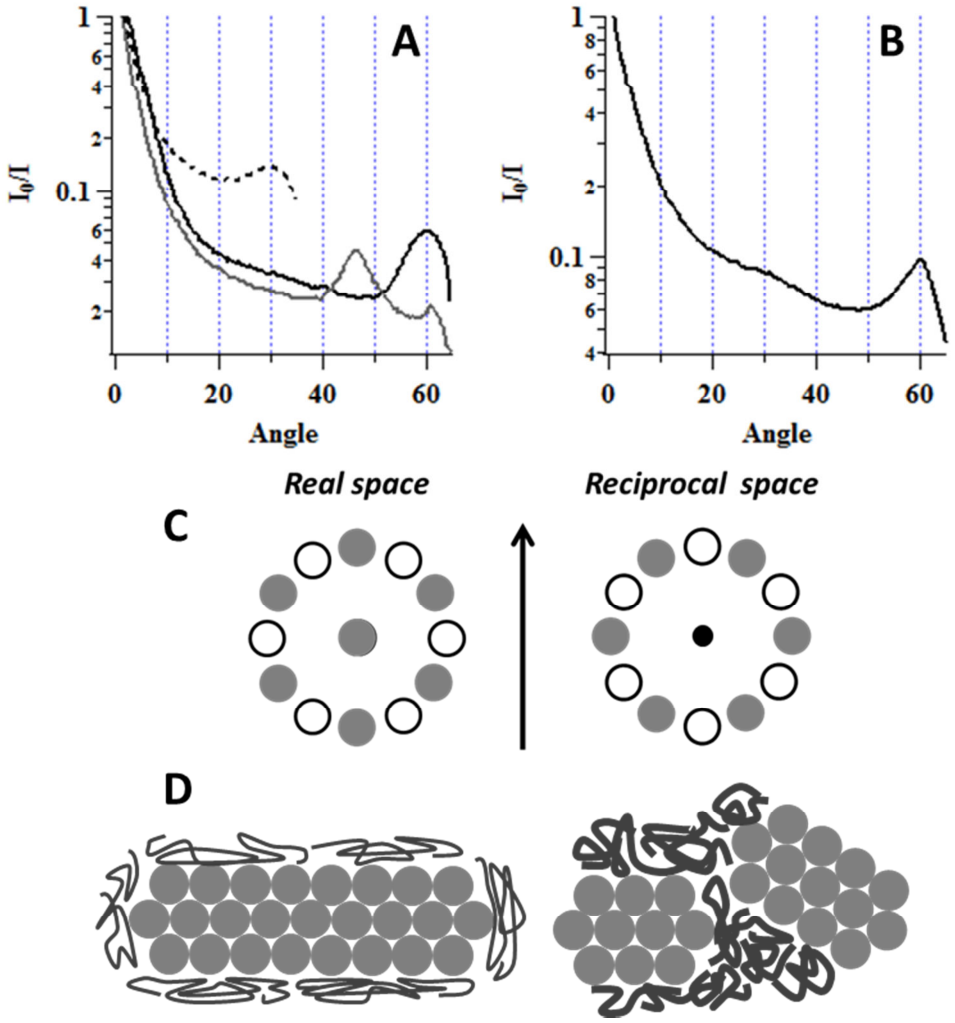

Figure 4.11. A & B: Azimuthal integration of GISAXS data from films formed from 1 SB3-14:1 $CaCl_2$ [SB3-14] = 100 mM with [SPEI] = 1 wt% (**A**) and [LPEI] = 1 wt% (**B**). The SPEI azimuthal integrations are of the Debye-Scherer rings of the *p6mm* reflection from the 10 (black) and 11 (dashed black) diffraction planes and the first order reflection from the Lα phase. The LPEI azimuthal integrations are from the *p6mm* 10 reflection. **C:** Graphical representation of the orientation dependence of diffraction maxima from the real space distances and direction of the *p6mm* unit cell showing the unit cell orientated with the 10 plane (filled grey circles) and the 11 plane (open circles) parallel to substrate plane. The reciprocal space diffraction positions follow the same colour scheme. The vertical axis represents the direction normal to the substrate. **D:** Diagram showing the possible orientation of the *p6mm* crystallites observed in the GISAXS data from the films, showing film formed with SPEI (left) and film orientation from LPEI film (right). The SPEI film is more orientated formed from laterally large crystallites which are orientated with the 10 plane parallel to the substrate surface whereas the LPEI crystallites are laterally smaller and hence form a multiply orientated state of crystallites where the 10 and 11 plane are parallel to the substrate as seen by the multiple maxima in the azimuthal integration shown in figure **B**.

The azimuthal intensity of the 10 reflection of the LPEI containing film shows that there is some variation in the orientation of the *p6mm* structure in the film (figure 4.11b). Firstly, inspection of the azimuthal intensity shows that away from the maximum at zero angle shows the decrease in intensity is not as pronounced as the decrease in intensity of the azimuthal intensity of the SPEI containing films (figure 4.11a). In the SPEI films the azimuthal intensity had a 25-fold decrease in intensity at 20 degrees, compared to the maximum at 0 degrees, whereas the azimuthal intensity the 10 reflection in the LPEI film at the same 20 degree position only decreases by approximately a factor of ten. Closer inspection of the azimuthal intensity reveals that there is a small maximum between the maxima that represent the 10 and 01 reflection of the LPEI *p6mm* structure. This is situated at 30 degrees and must be a result of a mixed orientation of the *p6mm* crystallites, which have the 10 and 11 plane both parallel to the substrate. This is represented in figure 4.11C where the real space orientation of a *p6mm* crystal is shown with the 10 and 11 planes parallel to the substrate. Translating the real space structure into reciprocal space shows that the occurrence of reflections from the 10 plane are still spaced 60 degrees apart, however as both orientations are present, reflections will be seen that are spaced 30 degrees apart due to the contribution from both orientations.

This can be visualised by the presence of LPEI causing a disruption in the extent of the lateral growth of the *p6mm* crystallites, presumably due to its steric bulk and also preventing long range order in planes through imposing the polymer volume on the orientation of the crystallites causing the crystallites to be rotated and orientate with the 10 and 11 crystallites parallel to the substrate surface. This is explained graphically in figure 4.11d and it can also be seen in the apparent crystal size and relative scattering volumes from Table 4.7. Films formed with SPEI as the polymeric component form *p6mm* crystallites with longer range order than films formed from LPEI.

Figure 4.12 shows the GISAXS data for 1:1 LPEI and the representative unit cell in real space. Determination that this phase is indeed a *p6mm* symmetry face-centred unit cell is achieved by confirming the relative positions of the out-of-plane scattering, where $q_{xy}>0$, to the scattering in the q_z plane, where $q_{xy}\sim0$. It can be seen that the 01 reflections occur at half the wave vector in the q_z direction compared to the 10 reflection and these q_z wave vectors of the 10 and 01 reflections translate to real space distances of 40.4 Å and 80.42 Å respectively. Comparing these dimensions on figure 4.12A for the reciprocal scattering and figure 4.12B for the real space representation it can be seen how the reciprocal space and real space features relate to each other. The 10 reflection arises from the crystallographic plane formed by cylindrical micelles packing tightly in offset layers whereas the q_z wave vector of the 01 reflection occurs from the position of the boundaries of the face centred unit cell at exactly twice the spacing of the 10 reflection. The centre-to-centre vector of the nearest micelles forming the 10 crystallographic plane are in a direction 60

degrees away from the 10 reflection plane which also explains the direction of the 01 reflection as this is the direction where this exact spacing can again be seen. The q_{xy} spacing reveals information about the real space unit cell in the other dimension of the 2 dimensional face-centred cell. The reciprocal wave vector in the q_{xy} direction of the 01 reflection is 0.135 $Å^{-1}$ which relates to a real space distance of 46.4 Å. This distance is smaller than the longest dimension the face centred unit cell by a factor of $\sqrt{3}$, confirming that the unit cell has *p6mm* symmetry, as the q_{xy} position of the 01 reflection represents the spacing of the real space position of the boundaries of the smaller *b* axis of the face centred rectangular unit cell.

Therefore it can be seen there isn't much space between the surfactant micelles for polymer however there may be space between the channels created by the surfactant aggregates. A polymer bridging effect has been reported for liquid crystals formed of PEI and anionic surfactants where the unit cell size is smaller than the pure surfactant liquid crystal[38]. A similar effect may be occurring here, plus if PEI displace water from between the micellar aggregates there may be space for polymer. However, for the cross-section of the micelles shown from SANS and SAXS analysis later, the unit cell of 46.4 Å leaves little room for polymer.

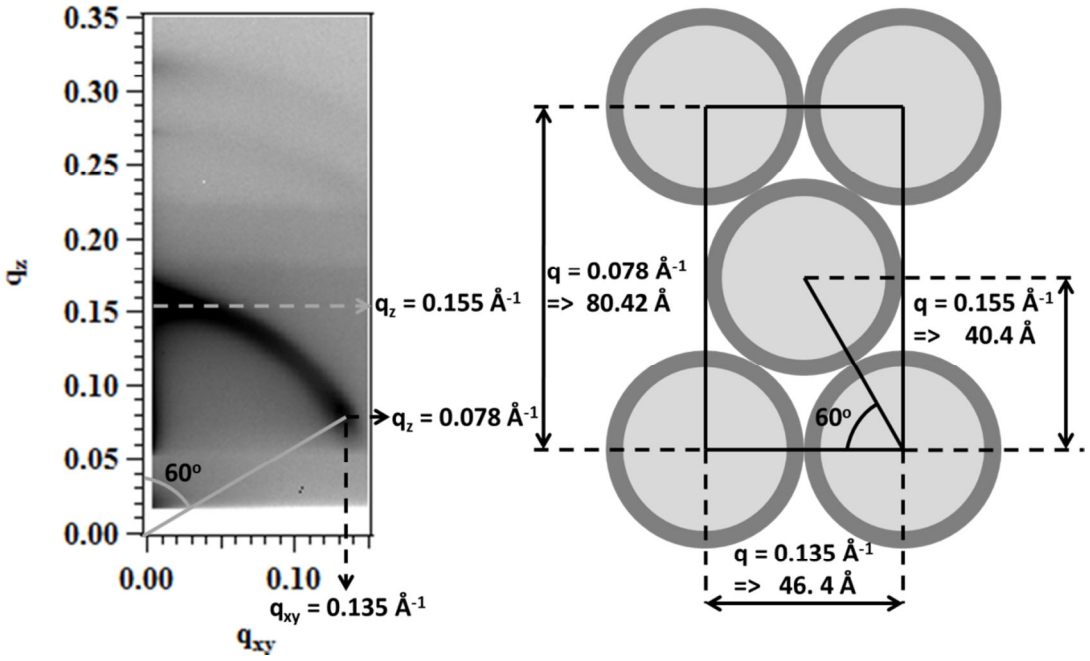

Figure 4.12. A) GISAXS data with labelling showing the relationship of the out of plane scattering to the unit cell in real space. To confirm the existence of a face centred unit cell, the reciprocal space locations of the out of plane scattering maxima have direct relationships with the real space dimensions that can only occur if the structure is a face centred unit cell. By inspection of the q_z and q_y positions of the out of plane scattering it can be seen that the 01 reflection occurs at a q wave vector half the value of the q position of the 10 reflection. It can also be seen that the q_y position of the 01 refection is exactly half the q value of the 11 $q_{||}$ value. It can be seen by

relating the q_z and q_{xy} values of the 01 reflection that the a and b dimensions of the 2d hexagonal unit cell can be derived and the ratio between them are $\boldsymbol{a/b = \sqrt{3}}$.The q_z and q_{xy} positions of the 01 reflection. **B)** Diagram highlighting the features of the *p6mm* unit cell. Linking the reciprocal space diffraction maxima with the dimensions of the *p6mm* unit cell in real space. It can be seen that the 01 reflection occupies half of a unit cell dimension and the 11 q_{xy} reflection represents the full b dimension. The 60^o degree angle of the 01 away from the q_z direction occurs from the angle between the long axes of the face centred unit cell to the micellar origin of the centre micelle of the *p6mm* face centred unit cell.

Polymer	$\frac{[CaCl_2]}{[SB3-14]}$	Phase	*hkl*	q_{hkl} (Å^{-1})	d_{obs} (Å)	d_{calc} (Å)	d_{obs} - d_{calc} (%)	d_{cell} (Å)
SPEI	1	*p6mm*	100	0.157	39.99±0.04			45.85±0.21
			210	0.275	22.89±0.08	23.09	0.88	
			200	0.318	19.74±0.09	20.00	1.3	
		L_α	100	0.168	37.31±0.07			37.55±0.09
			200	0.333	18.90±0.03	18.66	-1.28	
		L_c	100	0.275	22.89±0.007			22.89±0.08
LPEI	1	*p6mm*	100	0.159	39.64±0.02			45.88±0.09
			200	0.316	19.92±0.04	19.82	-0.47	

Table 4.6. Table showing the fitted peak parameters from XRR profiles of films formed from spray coated solutions of 1 [$CaCl_2$]:1 [SB3-14]; [SB3-14] = 100 mM. d_{obs} were obtained by fitting the XRR data with a Lorentzian peak model with linear background between $0.025<I_{max}>0.025$ Å^{-1} of q_{hkl}. d_{calc} was obtained by multiplication of the first order peak of the crystallographic phase with the product of $\boldsymbol{s_{hkl} = h}$ and $\boldsymbol{s_{hkl} = \sqrt{h^2 + k^2 + hk}}$ for lamellar and *p6mm* respectively. $\boldsymbol{d_{cell} = \frac{2\pi}{s_{hkl} q_{hkl}}}$

Sample	Phase	Index	GISAXS peaks ($Å^{-1}$)		d-spacing (Å)	unit cell (Å)	FWHM	apparent crystallite size (Å)	Area ($Å^2$)
			qz	qxy					
SPEI	*p6mm*	10	0.1575±3.10E-05		39.9±0.008	46.1±0.009	0.00519±0.0001	1210±25	32
		11	0.2735±1.30E-05		23±0.001	45.9±0.002			
		20	0.31672±5.50E-05		19.8±0.003	45.8±0.008			
	L_α	1	0.1675±1.09E-04		37.5±0.02	37.5±0.02	0.004247±0.000365	1480±127	6.5
		2	0.3367±3.14E-02		18.7±1.7	37.3±3.5			
	L_c	1	0.2698±9.60E-06		23.3±0.0008	23.3±0.0008	0.0067±0.00032	940±45	7.7±0.06
LPEI	*p6mm*	10	0.15583±9.60E-06		40.3±0.002	46.6±0.003	0.0136±0.0004	463±13	
		11	0.2674±3.13E-02		23.5±2.75	47±5.5			
		20	0.31356±1.09E-04		20.±0.007				

Table 4.7. GISAXS peak positions, films phases, unit cell size, peak widths, apparent crystal size and integrated area from fits of Lorentzian peaks to the data for films formed from PEI, SB3-14 100mM and $CaCl_2$ 100mM

1 [SB3-14]:2 [CaCl2]/PEI Films

Solutions containing 1 [SB3-14]:2 [$CaCl_2$] with [SB3-14]= 100 mM form films that exhibit pure *p6mm* structures when formed with either 1 wt% SPEI or 1 wt% LPEI. No other structures are evident in the GISAXS data or XRR profiles (Figure 4.11). The dimensions of the *p6mm* unit cells and fitted parameters are presented in Table 4.11. All peaks in the GISAXS data can be indexed to a *p6mm* Table 4.12) with the 10, 11 and 20 reflections being present. When $CaCl_2$ is in excess concentration compared to SB3-14 the unit cells of the *p6mm* structures exhibit a slight increase in unit cell size compared to the *p6mm* unit cell sizes exhibited by films formed from 1 [SB3-14]:2 [$CaCl_2$] as the film forming solution (Table 4.12). The increase is slight though, in the order of ~0.5 Å when SPEI is used as the polymeric component, with no change observed when LPEI is the polymeric component. This suggests there is no significant change in the headgroup conformation of the micelles of the *p6mm* mesophases or the amount of polymer between the micelles comprising the phase under these conditions.

When comparing the effect the polymeric component has on the unit cell of the *p6mm* phase when the films are formed from 1 [SB3-14]:2 [$CaCl_2$] the trend is the same for the 1 [SB3-14]:2 [$CaCl_2$] as it is for the 1 [SB3-14]:1 [$CaCl_2$] films; LPEI as the polymeric component produces films of *p6mm* films of unit cell size 46.6 Å, which is a slight increase of the unit cell size compared to the 45.5 Å unit cell size of the films formed with SPEI as the polymeric component (table 4.7). This increase is similar to the previous films of surfactant and salt composition of 2 [SB3-14]:1 [$CaCl_2$] and 1 [SB3-14]:1 [$CaCl_2$] and is unlikely to be due to intercalation of the polymer as the increase is under 1 Å in size and more likely to be due to the increase of water content within the films, due to LPEI being present arising from the increased polymer network formed by LPEI as discussed previously.

The effect of polymer on the orientation of the *p6mm* crystallites is similar to the previous films, in that LPEI causes the mesophase to exhibit greater planar disorder than films formed with SPEI. The XRR profiles suggest that films formed from SPEI and LPEI are completely orientated with the 10 crystallographic plane parallel to the substrate due to the 11 reflection of the *p6mm* phase not being present (Figure 4.16 A & B). However inspection of the GISAXS data suggests that films formed from LPEI exhibit more planar disorder than films formed with SPEI due to there being more diffracted intensity between the maxima resulting from the 10 orientation on the Debye-Scherrer rings of the 10, 11 and 20 reflections of the *p6mm* unit cell.

Inspection of azimuthal integrations (Figure 4.17A) confirms that LPEI containing films contain a mixture of *p6mm* orientations with the 10 and 11 crystallographic

plane being parallel to the substrate whereas SPEI containing films only exhibit 10 orientated *p6mm* crystallites. This is confirmed by the LPEI 10 azimuthal integration exhibiting maxima at 30 and 60 degrees in addition to the zero degree maxima whereas the SPEI containing film only exhibits a maximum at 60°on the 10 reflection. The azimuthal integration of the 11 reflection of both LPEI and SPEI containing films show the expected maxima at 30° from the zero angle maxima. However the 30° maximum of the LPEI containing film has less intensity relative to the zero degree maximum than the corresponding maximum in the SPEI containing film. This is in agreement with there being 10 and 11 orientated *p6mm* crystallites present in the LPEI film as the 11 orientated film would be expected to have a maximum at the zero angle rather than at 30°for the 11 reflection of a 10 orientation.

Another effect of different molecular weight PEI as the polymeric component is the apparent size of the crystallites with SPEI allowing *p6mm* crystallites of greater size to form than LPEI (Table 4.12 and figure 4.17 B and C). This is likely due to the same effect which causes the LPEI containing films to exhibit more planar disorder than the SPEI films; the higher molecular weight polymer prevents formation of large crystallites due to steric bulk The presence of pure *p6mm* phases suggests that the excess $CaCl_2$ compared to SB3-14 prevents enough water from evaporating from the film in the formation process for the films to be sufficiently hydrated to form a liquid crystal mesophase.

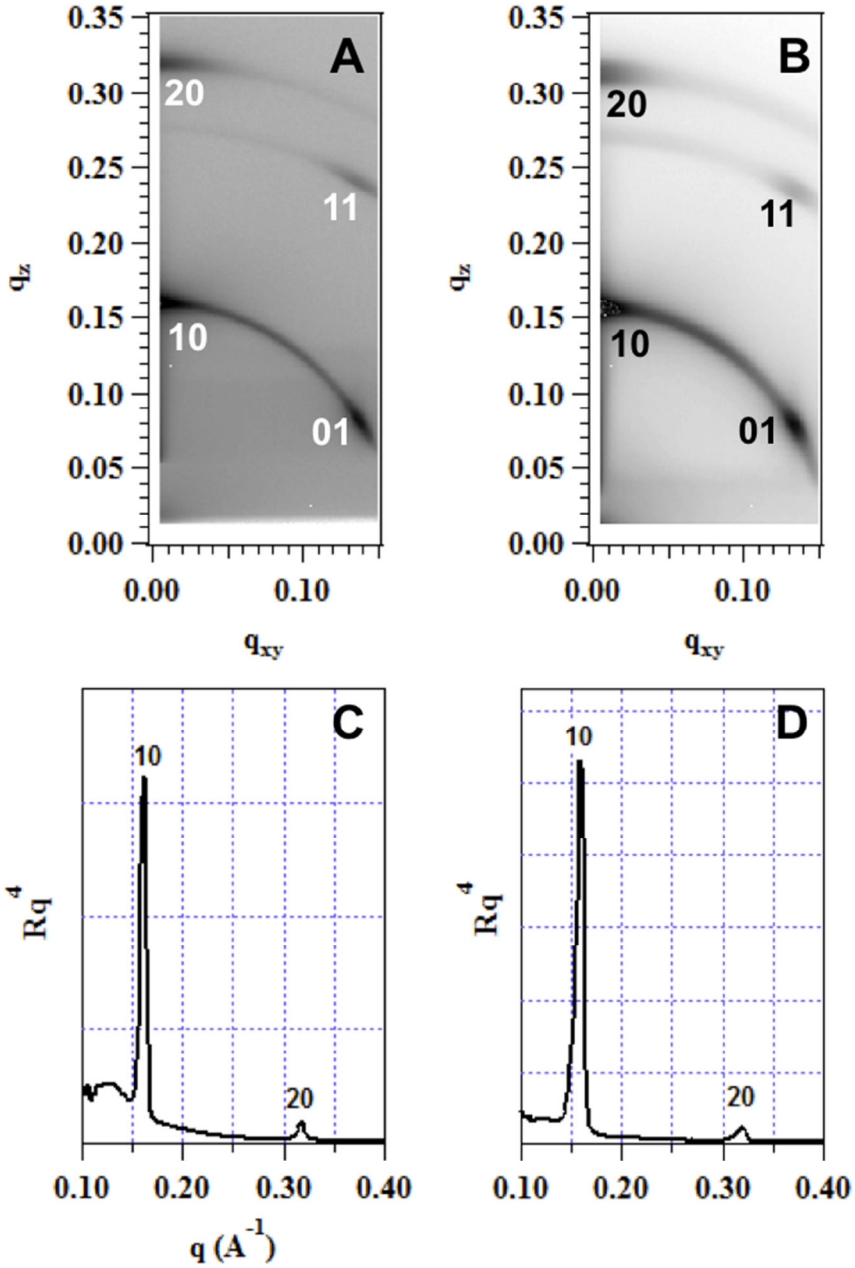

Figure 4.13. GISAXS and XRR of films formed from spray coated solutions of 1 SB3-14:2 $CaCl_2$ [SB3-14 100 mM] with 1 wt% PEI. **A)** GISAXS plot of film formed with SPEI as PEI component, α_i=1.1˚. **B)** GISAXS plot of film formed with LPEI as PEI component, α_i = 0.96˚. **C)** XRR profile of film formed with SPEI as the PEI component. **D)** XRR profile of film formed with LPEI as the PEI component. GISAXS plots show log intensities for clarity. XRR profile intensities are presented as $\boldsymbol{I = \frac{R_0}{R} q^4}$ to remove the Fresnel reflectivity trend. Maxima resulting from the structures in the films are annotated; L_α liquid crystalline lamellar, L_c solid crystalline lamellar, *nq* order of liquid crystalline lamellar peak.

Sample	Phase	Index	XRR peak ($Å^{-1}$)	*d*-spacing (Å)	average unit cell ($Å^3$)	unit cell ($Å^3$)
			0.161±0.00019	38.9±0.02	45.4±0.03	44.9±0.02
SPEI	*p6mm*					
			0.316±0.0001	19.8±0.006		45.7±0.01
			0.158±0.00025	39.6±0.037	45.6±0.05	45.7±0.04
LPEI	*p6mm*					
			0.319±0.0002	19.6±0.012		45.3±0.02

Table 4.11. XRR data of films formed from 2 $CaCl_2$:1 SB3-14 and PEI

Sample	Phase	Index	GISAXS peak ($Å^{-1}$)		*d*-spacing (Å)	average unit cell ($Å^3$)	unit cell ($Å^3$)	FWHM	apparent crystallite size ($Å^3$)
			q_z	q_{xy}					
			0.16±0.0001		39.1±0.008	45.5±0.016	45.2 ±0.0093	0.0041±0.001046	1530±390
SPEI	*p6mm*		0.274±0.0013		22.9±0.005		45.8±0.01		
			0.318±0.0017		19.7±0.003		45.6±0.008		
						46.5±0.032			
			0.155±0.001		40.3±0.02		46.5±0.02	0.008579±0.00034	732±30
LPEI	*p6mm*								
			0.269±0.001		23.3±0.008		46.7±0.01		
			0.309		20.2		46.		

Table 4.12. GISAXS data of films formed from 2 $CaCl_2$:1 SB3-14 and PEI

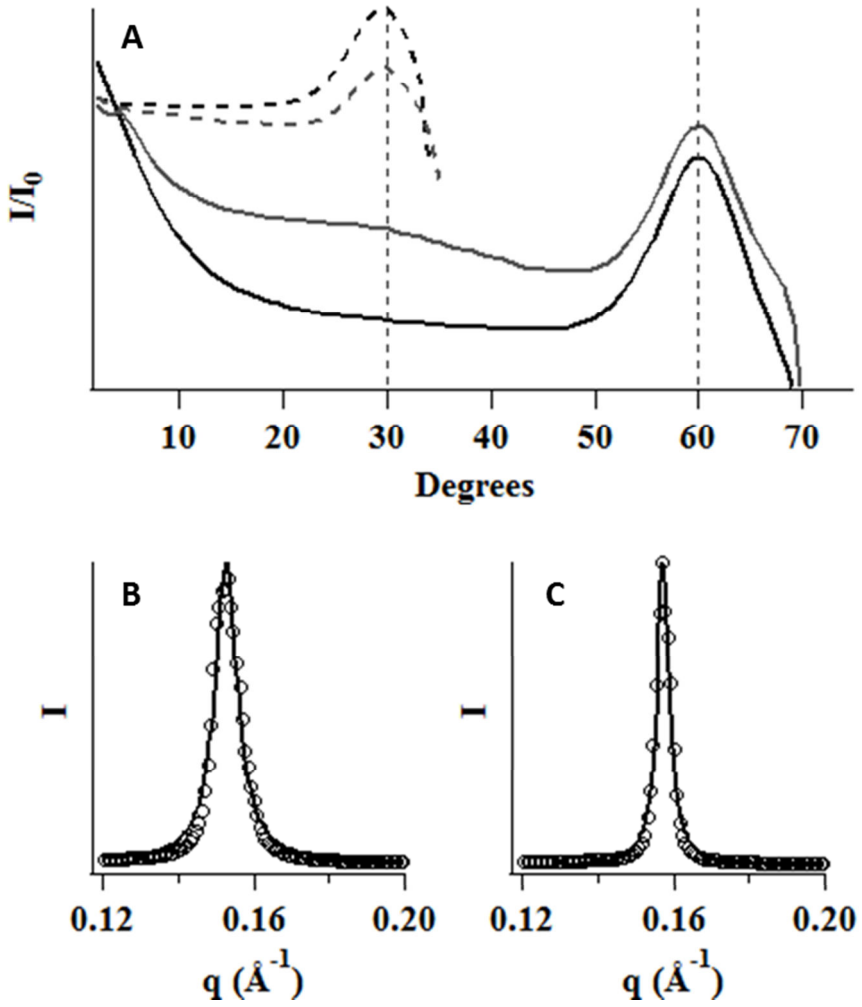

Figure 4.14. A) Azimuthal integration of the *p6mm* 10 (solid) and 11 (dashed) reflections from GISAXS data for films formed from 1 [SB3-14]: 2 [$CaCl_2$]/SPEI (black) and 1 [SB3-14]: 2 [$CaCl_2$]/LPEI (Grey). **B)** GISAXS intensity along q_z from q_y = 0.05 $Å^{-1}$ of film 1 [SB3-14]: 2 [$CaCl_2$]/LPEI. Solid black lines represent Lorentzian peak fits with linear background to peak data between q_{max} = ±0.025 $Å^{-1}$. **C)** GISAXS intensity along q_z from q_y = 0.05 $Å^{-1}$ of films formed from 1 [SB3-14]: 2 [$CaCl_2$]/SPEI . Solid black lines represent Lorentzian peak fits with linear background to peak data between q_{max} = ±0.025 $Å^{-1}$.

4.5 Bulk Behaviour

4.5.1 SB3-14 micelles with no $CaCl_2$

Modelling of SANS and SAXS measurements of a concentration series of SB3-14 reveal that the micelle form factor is that of a sphere (Figure 4.18) with fit

parameters presented in table 4.13 & 4.14. It was found that the aggregation number is independent of concentration, which is in agreement with the literature on sulfobetaine surfactants[37]. The insensitivity of the aggregation number to concentration was found throughout the concentration series, which was from 62.5 mM to 1000 mM, with the concentration increased by 2 for each concentration point. This concentration series was chosen to emulate the behaviour of the film forming solution where evaporation of the solvent causes the surfactant concentration to increase.

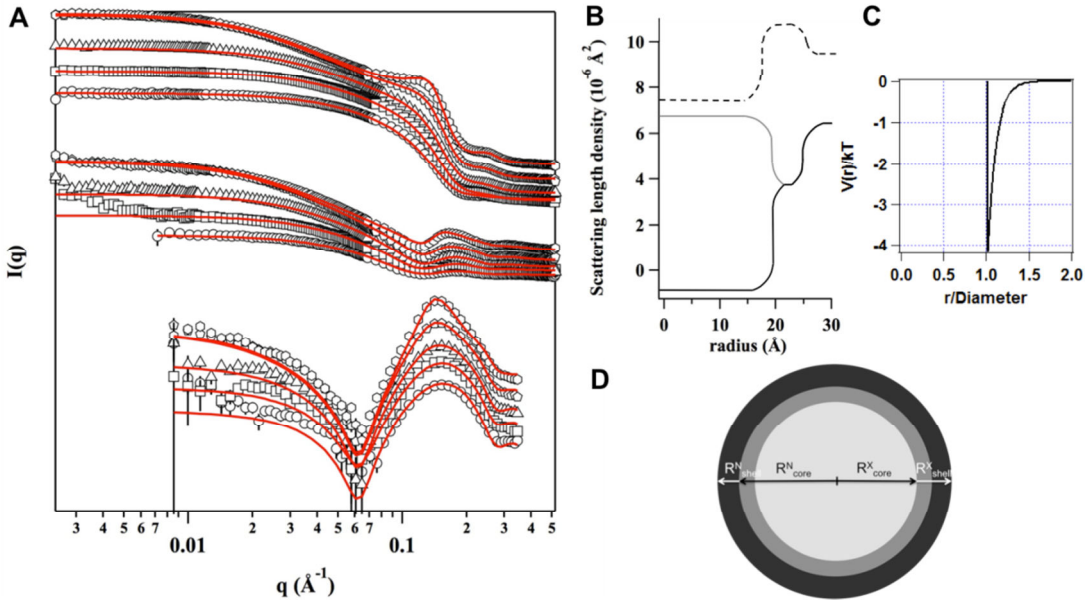

Figure 4.15. A) SANS and SAXS data of SB3-14 at concentrations of 1 M, 500 mM, 250 mM, 125 mM and 62.5 mM. SB3-14 SANS data was collected with D_2O as the solvent and SB3-14 and d29-SB3-14 as the surfactant. SB3-14 SAXS data was collected with H_2O as the solvent and SB3-14 as the surfactant. Data is plotted on an absolute scale but offset for clarity; SB3-14 in D_2O no intensity offset, d29-SB3-14 in D_2O intensity offset by a reduction factor of 10, SB3-14 in H_2O (SAXS) offset by a reduction factor of 200. Within each scattering contrast set there is no intensity offset, the observed relative intensity differences within a contrast being due to the difference in volume fraction from the concentration difference with 1 M SB3-14 being the highest intensity and 62.5 mM being the lowest intensity. **B)** Representative SLD profiles of the SB3-14 micelle for SB3-14 in D_2O (SANS, black), d29-SB3-14 in D_2O (SANS, grey) and SB3-14 in H_2O (SAXS, dotted black). The positions of the core-shell and shell-solvent boundaries are to scale however the curvatures of the boundaries, which represent smeared interfaces arising from polydispersity are not to scale. **C)** Plot showing the magnitude and extent of the Yukawa potential used to fit the $S(q)$ to the data which accounted for the increase in low q scattering due to aggregation. **D)** Schematic representing the SB3-14 micelle from fitting the small angle scattering data to a polydisperse core-shell sphere with an attractive two Yukawa potential term. The diagram highlights the different boundaries for the cores for the SANS data and the SAXS data.

Considering the fits to the SANS data: As the aggregation number of the micelle was found to be constant across all concentrations, the micelle form factor was also found to be constant. The best fit was achieved by fitting the data to a polydisperse core-shell sphere[39] and locking the core radius of a core shell form factor described by the alkyl surfactant chains to a radius of 19.5 Å.[33] The shell thickness and scattering length density were allowed to fit freely. This length was chosen as it is the extended length of an alkyl chain. Across all concentrations this gave a shell of thickness 4.8 Å. The SLD profiles of the micelle show that the shell is hydrated with 50% of the headgroup volume being water. The thickness of the shell suggests that the surfactant headgroups are lying flat on the surface of the micelle. The volume fraction of the solutions was held to the dry volume fraction of the surfactant in solution calculated from the density of the surfactant and the amounts weighed out when preparing samples. To obtain satisfactory fits it was necessary to fit the data with a structure factor to describe an attractive interaction between the micelles. In this case a Two Yukawa potential[40] was found to best fit the data, with noticeably better fits than using another attractive potential such as a sticky hard sphere structure factor[41]. This is likely to be due to the two Yukawa structure factor being more robust for high volume fractions compared to the sticky hard sphere structure factor.
The two Yukawa potential was found to be completely attractive in character beyond the hard sphere radius with no repulsive potential present. The hard sphere term was fitted separately as the dry volume fraction of the surfactant in solution was a locked parameter. This allows for the hard sphere to be defined differently to the dimension of the form factor of the micelle since this could possibly give erroneous results for the size of the micelle if the fitting procedure forced the micelle form factor to fit the hard sphere volume. The hard sphere volume can deviate from the form factor for the micelle due to phenomena such as ordered hydration layers surrounding the micelle. With this in mind the two Yukawa structure factor was found to have a hard sphere radius of 24.3 Å, identical to the form factor radius of the micelles. The attractive potential exhibited by the SB3-14 micelles has been reported for other sulfobetaine headgroup surfactants[37]. The origin of the attractive interaction is still unclear according to the literature.

To investigate the effect $CaCl_2$ has on the SB3-14 micelles, solutions were prepared that emulated the film forming solutions. For example SB3-14 was investigated at increasing concentration with $CaCl_2$ solution where the concentration of $CaCl_2$ was present in molar ratios of 1:2, 1:1 and 2:1 as previously investigated in the film forming solutions. Good fits were obtained by fitting the data to the same polydisperse core-shell sphere model that was used to fit the SB3-14 data with no added salt. Fits are presented in figure 4.15. As the aggregation number was defined as $\frac{V_{core}}{V_{tail}}$ and the core was locked to the same radius of 19.5 Å thus the aggregation number also remained constant. The quality of the fits to the data suggests that there

is no micellar growth even at high surfactant and salt concentration. It should be noted that anisotropic models were also fitted to the data to determine whether there was micellar growth. It was found that the data could be fitted to an oblate ellipsoid, however the anisotropy was only a factor of ~1.1 times the minor radius of the ellipsoid. Anisotropy this small is impossible to distinguish from a polydisperse sphere[42]. Therefore it was decided to use a polydisperse sphere as this model solved the form factor with an analytical solution for the core-shell decoupling and thus was more convenient to use. Also the polydispersity described by the model was convenient as the core shell interface, evident from the SANS data of d29-SB3-14 in D_2O samples along with the SAXS data of SB3-14 in H_2O, was also smeared due to polydispersity.

As before, when fitting the data of SB3-14 against salt, the core radius was locked to 19.5 Å for the SANS data but was allowed to fit freely for the SAXS data. This is because the scattering length density of the core in the SAXS data is more sensitive to penetration of the sulfonate region of the headgroup into the micellar core than the SANS data is. The fit parameters are presented in table 4.13 & 4.14 and presented graphically in Figure 4.16, 4.17 & 4.18 to highlight the trends. As the data is fitted to a simple core shell sphere, the trends highlighted focus on the effect adding $CaCl_2$ has on:

- Total radius of micelle
- Hard sphere radius of micelle
- Shell thickness
- Shell scattering length density
- Solvent scattering length density
- Core radius of the micelle from the SAXS data

Sample			SANS					
[SB3-14] (mM)	**[CaCl2] (mM)**	**Dry VF**	**R_{Core} (Å)**	**R_{Shell} (Å)**	**Pd**	**R_{HS} (Å)**	**SLD_{Shell} (10^{-6} Å^{-1})**	**$SLD_{Solvent}$ (10^{-6} Å^{-1})**
1000	0	0.2606						
500	0	0.154						
250	0	0.08097	19.5	4.28±0.04	0.20	24.33±0.12	3.88±0.0226	6.33
125	0	0.0422						
62.5	0	0.02155						
1000	2000	0.2509	19.5	4.76±0.03	0.18	26.22±0.02	3.82±0.02	6.29
1000	1000	0.2561	19.5	4.40±0.02	0.16	26.04±0.02	3.55±0.02	6.32
1000	500	0.2585	19.5	4.16±0.02	0.17	25.57±0.01	3.35±0.02	6.33
500	1000	0.1469	19.5	5.16±0.02	0.18	26.15±0.03	3.80±0.02	6.32
500	500	0.1484	19.5	4.74±0.03	0.16	25.18±0.03	3.41±0.01	6.33
500	250	0.1492	19.5	4.48±0.02	0.17	24.09±0.04	3.02±0.01	6.33
250	500	0.08017	19.5	5.41±0.02	0.18	25.38±0.06	4.08±0.008	6.33
250	250	0.0806	19.5	5.25±0.02	0.17	24.41±0.07	3.99±0.008	6.33
250	125	0.08084	19.5	4.53±0.02	0.18	21.96±0.09	3.85±0.01	6.33

Table 4.13. Table presenting the sample characteristics and the fitting parameters obtained from the SANS fitting.

Sample			SAXS					
[SB3-14] (mM)	**[CaCl2] (mM)**	**Dry VF**	**R_{Core} (Å)**	**R_{Shell} (Å)**	**Pd**	**R_{HS} (Å)**	**SLD_{Shell} (10^{-6} Å^{-1})**	**$SLD_{Solvent}$ (10^{-6} Å^{-1})**
1000	0	0.2606						
500	0	0.154						
250	0	0.08097	16.90±0.02	7.34±0.04	0.13	24.33±0.12	10.8±0.01	9.44
125	0	0.0422						
62.5	0	0.02155						
1000	2000	0.2509	19.27±0.04	5.34±0.04	0.15	26.13±0.03	12.4±0.03	10.7
1000	1000	0.2561	18.85±0.03	5.24±0.03	0.15	25.80±0.02	11.9±0.02	10.1
1000	500	0.2585	18.17±0.03	5.66±0.03	0.15	25.04±0.02	11.3±0.01	9.77
500	1000	0.1469	18.64±0.03	5.32±0.08	0.16	25.80±0.05	11.9±0.04	10.1
500	500	0.1484	16.91±0.04	10.34±0.12	0.15	25.79±0.10	10.6±0.01	9.77
500	250	0.1492	16.71±0.04	9.49±0.09	0.15	24.11±0.10	10.5±0.01	9.60
250	500	0.08017	16.57±0.08	11.10±0.23	0.15	25.23±0.34	10.5±0.02	9.77

250	250	0.0806	16.71±0.06	9.42±0.15	0.15	24.43±0.31	10.5±0.02	9.60
250	125	0.08084	16.44±0.07	9.39±0.16	0.15	23.48±0.39	10.4±0.03	9.49

Table 4.14. Table presenting the sample characteristics and the fitting parameters obtained from the SAXS fitting.

4.5.2 Effect of CaCl2 on SB3-14 micelles

The total size of the SB3-14 micelle without salt is 24.3 Å which is calculated from a core size of 19.5 Å and a shell size of 4.8 Å from the SANS data and a core of 16.9 Å with shell of 7.4 Å from the SAXS data. As discussed previously in Chapter 3 the differences in core length are due to the relative sensitivity of the SAXS data to the sulfonate headgroup compared to the SANS data. However from the SANS data it can be seen that the headgroup conformation is flat to the surface of the micellar core and this conformation will make the sulfonate headgroup penetrate into the micellar core slightly due to the dynamic nature of micelles in solution.

1000mM SB3-14 with added CaCl2

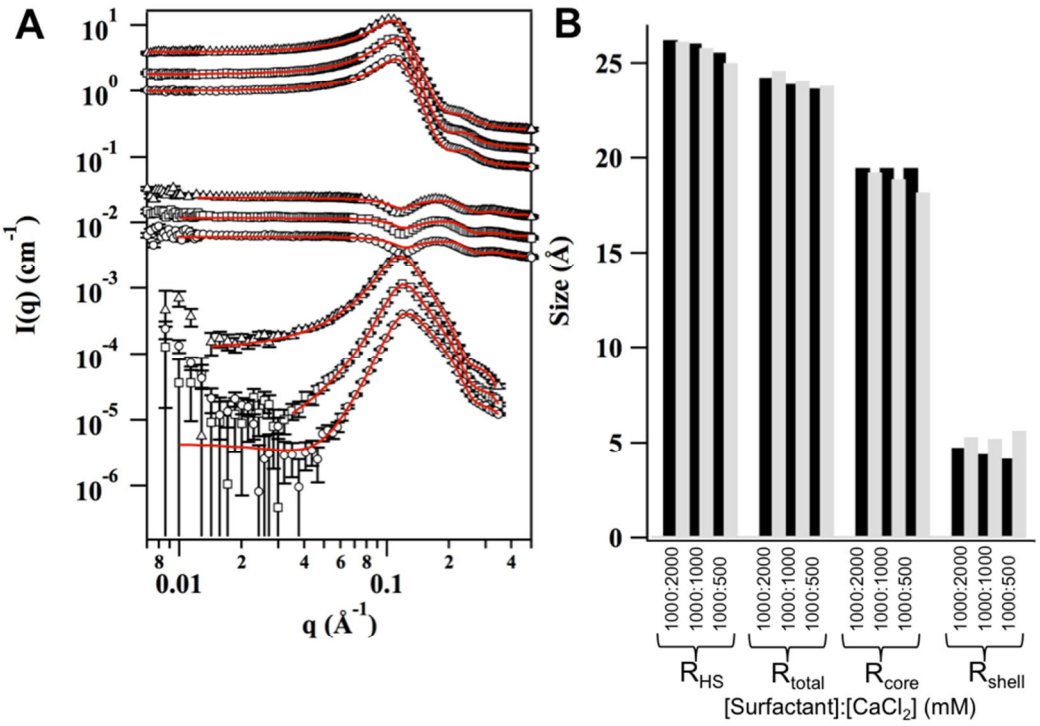

Figure 4.16. A) SANS and SAXS data of SB3-14 at concentrations of 1000 mM with $CaCl_2$ concentrations of 2000 mM, 1000 mM and 500 mM to give [SB3-14] to [$CaCl_2$] ratios of 1:2, 1:1 and 2:1.. Data is plotted on an absolute scale but offset for clarity; SB3-14 in D_2O no intensity offset, d29-SB3-14 in D_2O intensity offset by a reduction factor of 10, SB3-14 in H_2O (SAXS) of set by a reduction factor of 200. In each scattering contrast set there is no intensity offset, the observed relative intensity differences within a contrast being due to the concentration series. **B)** Graphical representation of the fit parameters; R_{HS}, R_{total}, R_{core} and R_{tail}.Black bars are for SANS, grey bars for SAXS

The fits of SB3-14 at a concentration of 100 mM with $CaCl_2$ at concentration of 2000 mM, 1000 mM and 500 mM to give [SB3-14] to [$CaCl_2$] ratios of 1:2, 1:1 and 2:1 are presented in Figure 4.19A and the fitted parameters are present graphically in Figure 4.19B. The chosen $CaCl_2$ concentrations emulate the different SB3-14 to $CaCl_2$ ratios used in the film forming solution and study the surfactant at high concentration which is an approximation of the process that the film forming solutions undergo when the solution is spray coated on a silicon wafer and the solvent allowed to evaporate.

For clarity all trends will be discussed in the order outlined above so that the trends will follow the order 1:2, 1:1 and 1:2 respectively. The SANS data will be discussed initially followed by a discussion of the SAXS data.

Increasing the ratio of $CaCl_2$ to SB3-14 decreases the micellar size as seen from the decrease in the shell thickness of the SANS fit parameters. The total diameter of the micelle is 24.3 Å, 23.9 Å and 23.7 Å for solutions with SB3-14 to $CaCl_2$ ratios of 1:2, 1:1 and 1:2 respectively which correspond to shell thicknesses of 4.8 Å, 4.4 Å and 4.2 Å when the hydrophobic core of 19.5 Å is removed from the total thickness. For the SAXS data the corresponding parameters are 24.6 Å, 24.1 Å and 23.8 Å for the total micelles radius and with 19.3 Å, 18.9 Å and 18.2 Å for the micellar core radius and 5.3 Å, 5.2 Å and 5.7 Å for the shell.

Comparing to the SB3-14-only solutions shows that dimensions of the micelle are relatively similar, with no extensive headgroup conformational changes to an extended conformation in the presence of Ca^{2+}. However there are some changes to the internal conformation of the micelle. Firstly the dimensions of the shell suggest that the headgroup is packed flat against the micellar core, however there is a reversal of trends for the shell thickness in the SANS data compared to the SAXS data. However as the change is slight and is most likely due to the SAXS data sensitivity to the salt concentration in the headgroup which will be discussed later.

The hard sphere radius R_{HS}decreases in size as the surfactant to $CaCl_2$ ratio decreases. The parameters are 26.2 Å, 26 Å and 25.6 Å for SB3-14 to $CaCl_2$ ratios of 1:2, 1:1 and 1:2 respectively from the SANS data. The corresponding R_{HS} for the SAXS data are 26.1 Å, 25.8 Å and 25 Å for the SAXS data. These values are ~2 Å larger than the total micelles radius for the SANS data. The R_{HS} values for the SAXS data follow a similar trend albeit the difference from the total micelle radius is less pronounced due to the total micelle radius being slightly larger in the SAXS data.

From these results it can be seen that the hard sphere radius exceeds the total radius of the micelle when $CaCl_2$ is equimolar or in excess, suggesting that at these concentrations the micelles adsorb sufficient salt to become slightly charged. This suggests that in the formation of the film, where the amounts of solutes are greater, interactions between SB3-14 and partially charged PEI may occur. As the interaction

would be electrostatic it may explain the small liquid crystal unit cell sizes due to compaction of the polymer due to charge screening. Also, when salt are in excess, the shell thickness decreases relative to the other compositions, providing further evidence to the cause of the liquid crystal sizes in the films. The large shell thicknesses at lower $CaCl_2$ concentrations suggests that when it is in excess to SB3-14 that it may contract due to the headgroup beginning to be salted out at the concentrations.

500mM SB3-14 with added CaCl2

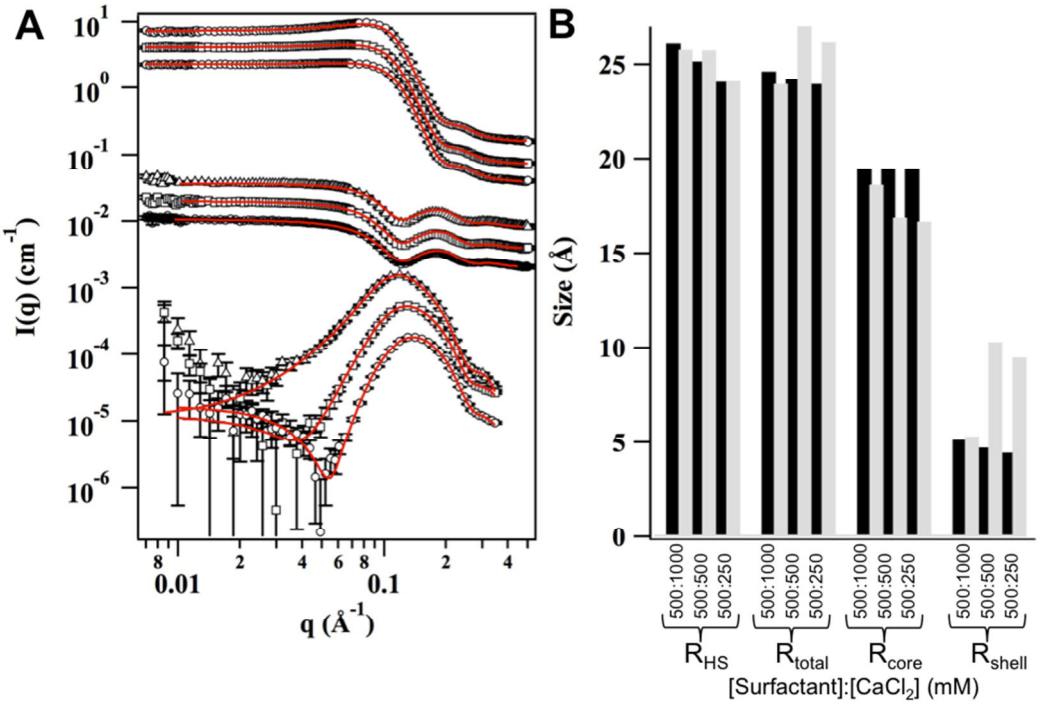

Figure 4.17. A) SANS and SAXS data of SB3-14 at concentrations of 500 mM with $CaCl_2$ concentrations of 1000 mM, 500 mM and 250 mM to give [SB3-14] to [$CaCl_2$] ratios of 1:2, 1:1 and 2:1.. Data is plotted on an absolute scale but offset for clarity; SB3-14 in D_2O no intensity offset, d29-SB3-14 in D_2O intensity offset by a reduction factor of 10, SB3-14 in H_2O (SAXS) of set by a reduction factor of 200. In each scattering contrast set there is no intensity offset, the observed relative intensity differences within a contrast being due to surfactant concentration. **B)** Graphical representation of the fit parameters; R_{HS}, R_{total}, R_{core} and R_{tail}. Black bars are for SANS, grey bars for SAXS

When comparing 250 mM SB3-14 against $CaCl_2$ at ratios of 1:2, 1:1 and 2:1 as before, similar trends are observed with SANS and SAXS as well as some significant differences. Firstly when comparing the changes in the total micelle size

with the SANS data there is a decrease in size, similar to the 1000 mM SB3-14 solution, the values being 24.7 Å, 24.2 Å and 24 Å which corresponds to shell thicknesses of 5.2 Å, 4.7 Å and 4.5 Å. These are slightly larger than the values for the shell thickness in the 1000mM SB3-14 samples and the difference is above experimental error. Consideration of the SAXS data values for total micelle radius and shell thickness shows a different trend where the total micelle radius 24 Å, 27.3 Å, 26.2 Å and shell thickness of 5.32 Å, 10.34 Å and 9.49 Å. these measurements correspond to core radii Of 18.6 Å, 16.9 Å and 16.7 Å respectively.

Increasing the ratio of $CaCl_2$ to SB3-14 increases the micellar size as seen from the increase in the shell thickness of the SANS fit parameters. The total radius of the micelle is 24.3 Å, 23.9 Å and 23.7 Å for solutions with SB3-14 to $CaCl_2$ ratios of 1:2, 1:1 and 1:2 respectively.. For the SAXS data the corresponding parameters are 24.6 Å, 24.1 Å and 23.8 Å for the total micelles radius and with 19.3 Å, 18.9 Å and 18.2 Å for the micellar core radius and 5.3 Å, 5.2 Å and 5.7 Å for the shell. However the trend for the hard sphere radius R_{HS}decreases in size as the surfactant to $CaCl_2$ ratio decreases. The parameters are 26.2 Å, 25.2 Å and 24.1 Å for SB3-14 to $CaCl_2$ ratios of 1:2, 1:1 and 1:2 respectively from the SANS data. The corresponding R_{HS} for the SAXS data are 25.8 Å, 24.11 Å and 24.11 Å for the SAXS data.

In the 500 mM data there is a change observed when the ratio of surfactant to $CaCl_2$ goes from 1:2 to 1:1. The SANS data follows the same trend as the 1000 mM data with a reduction in a micelle size that may be directly attributed to a reduction in the shell thickness. However in the SAXS data, the shell thickness increases in relative size along with a reduction in core radius. This will be discussed fully in the next section where the data for the scattering length density within the micelle shells is discussed along with the reduction of the R_{HS} compared to the micellar dimensions.

250mM SB3-14 with added $CaCl_2$

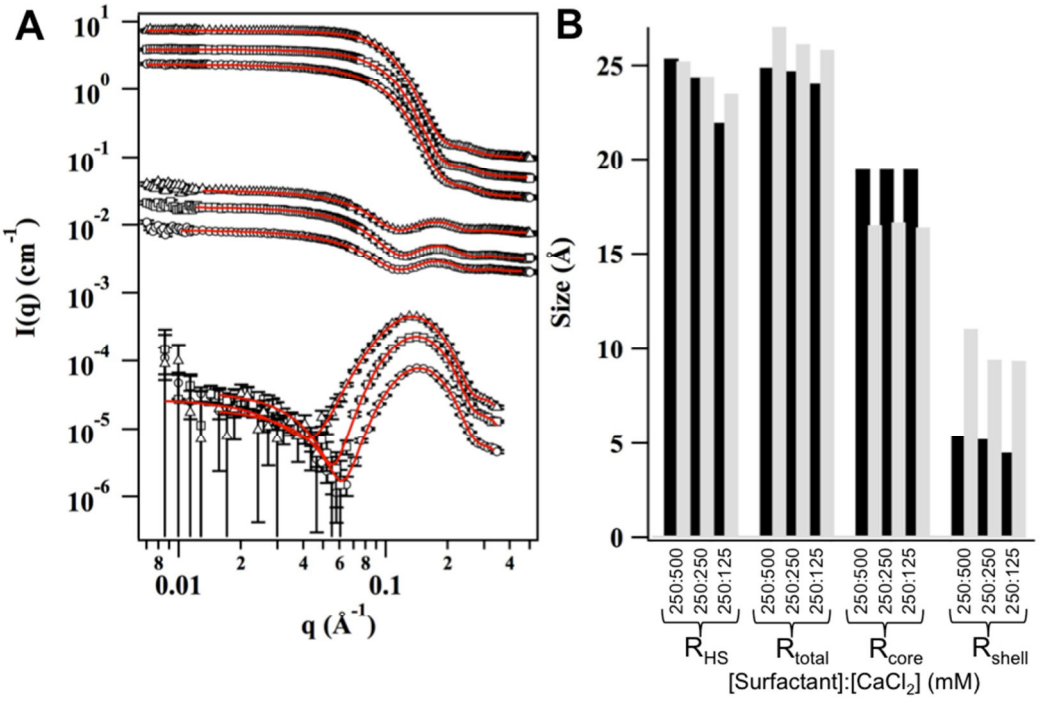

Figure 4.18. A) SANS and SAXS data of SB3-14 at concentrations of 250 mM with $CaCl_2$ concentrations of 500 mM, 250 mM and 125 mM to give [SB3-14] to [$CaCl_2$] ratios of 1:2, 1:1 and 2:1.. Data is plotted on an absolute scale but offset for clarity; SB3-14 in D_2O no intensity offset, d29-SB3-14 in D_2O intensity offset by a reduction factor of 10, SB3-14 in H_2O (SAXS) of set by a reduction factor of 200. In each scattering contrast set there is no intensity offset, the observed relative intensity differences within a contrast. **B)** Graphical representation of the fit parameters; R_{HS}, R_{total}, R_{core} and R_{tail}.

SANS and SAXS analysis of SB3-14 at 250 mM shows the same trend in reduction of the size of micelles in the SANS data with values of 25.3 Å, 24.4 Å and 22.0 Å with shell thicknesses of 5.4 Å, 5.3 Å and 4.5 Å when the SB3-14 to surfactant ratios are 1:2, 1:1 and 2:1 respectively. The SAXS data is follows the same trend albeit with larger dimensions compared to the SANS data with 27.7 Å, 26.6 Å and 25.8 Å for the micelle dimensions corresponding to shell thicknesses of 11.1 Å, 9.4 Å and 9.4 Å and core thickness of 16.6 Å, 16.7 Å and 16.4 Å when the ratios of surfactant and $CaCl_2$ are 1:2, 1:1 and 2:1 respectively. The trend here is that the shell thickness is increased at all $CaCl_2$ concentrations compared to no $CaCl_2$ being present. This suggests that $CaCl_2$ and SB3-14 headgroup interactions are concentration dependent, a mass-action effect where they interact purely due to diffusion and no long range electrostatic interaction.

4.5.3 The effect of CaCl2 on SB3-14 headgroup and inter-micellar interactions

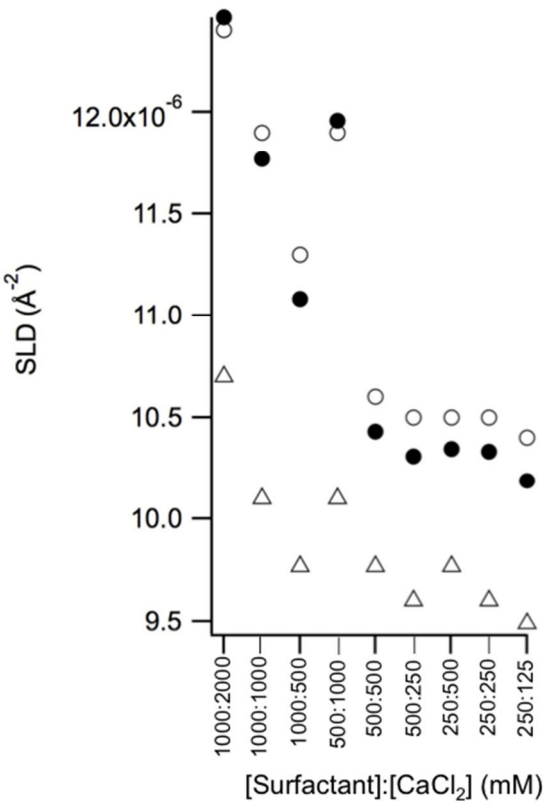

Figure 4.19 Parameters for the SAXS scattering length densities of the shell (open circles), solvent (open triangles) and shell void (closed circles). The shell void is defined as the shell volume minus the SB3-14 headgroup volume.

The small angle scattering results of SB3-14 with $CaCl_2$ shows that when SB3-14 is at the 1000mM and all concentrations of $CaCl_2$ and at 500mM and $CaCl_2$ is in excess, the hard sphere diameter is greater than the diameter of the whole micelle, particularly when considering the SANS results. When considering the SAXS results, which are more sensitive to the large SLD of the sulfonate ion of the sulfobetaine headgroup, it is seen that when the hard sphere radius is below the dimension of the micelles it is likely due to a change in the headgroup conformation. Specifically, the dimensions of the headgroup appear to extend for composition including 500mM SB3-14 with 500mM $CaCl_2$ and below these concentrations for both SB3-14 and $CaCl_2$.

The effect is seen when calculating the SLD of the void volume within the headgroup shell of the SAXS data. The void volume is defined as the volume not occupied by the volume of the headgroup SB3-14. It is calculated by calculating the shell volume and dividing through by the aggregation number. This gives the shell volume per surfactant; subtracting the volume of the SB3-14 headgroup plus any hydrocarbon core that the SAXS fitting defines in the shell gives the void volume. The SLD of the void volume is calculated by the volume fraction weighted SLD of the fitted shell SLD and the SLD of the SB3-14 headgroup.

Figure 4.19 shows the solvent, fitted shell and void volume SLD for all compositions of SB3-14 and $CaCl_2$ investigated by SAXS. It can be seen that at concentrations that

for SB3-14 and $CaCl_2$ compositions where the sulfobetaine headgroup is not in an extended conformation, the void volume SLD is relatively high compared to the void volume SLD when the headgroup appears to be extended. In all compositions of SB3-14 and $CaCl_2$, the void volume SLD is greater than the solvent SLD. This suggests that the concentration of $CaCl_2$ is greater in the shell region of the SB3-14 micelles than in the bulk solvent. Therefore SB3-14 micelles do exhibit an attraction to $CaCl_2$. It is not known from the SAXS data the exact position of each ion but it is logical to assume that anionic chloride is associated with the quaternary ammonium and cationic calcium is associated near the sulfonate ion of the sulfobetaine.

Interestingly though, the void volume SLD shows that when SB3-14 and $CaCl_2$ are in compositions that exhibit the longest range repulsive interactions the headgroup is collapsed and the solvent in the shell of the micelles contains the most salt. As the compositions that exhibit this behaviour are the highest SB3-14 concentrations investigated (1000mM) with all salt concentrations and 500mM with 1000mM $CaCl_2$. This suggests that there is a mass action requirement for enough $CaCl_2$ to be adsorbed to the shell to exhibit longer range repulsive interaction greater than the dimension of the micelle. Also, it shows that salt is required to screen the attractive interactions. As discussed previously, the nature of the attractive interactions is presently unknown. However it is possible that there occur due to hydrophobic regions of the core being exposed when there is no salt present and may be hydrophobic consequence. When $CaCl_2$ is present, the extra hydration of the headgroups and the increased coordination of water in this region due to the presence of salt may screen these hydrophobic interactions.

4.5.4 The effect of LPEI on theSB3-14 micelles

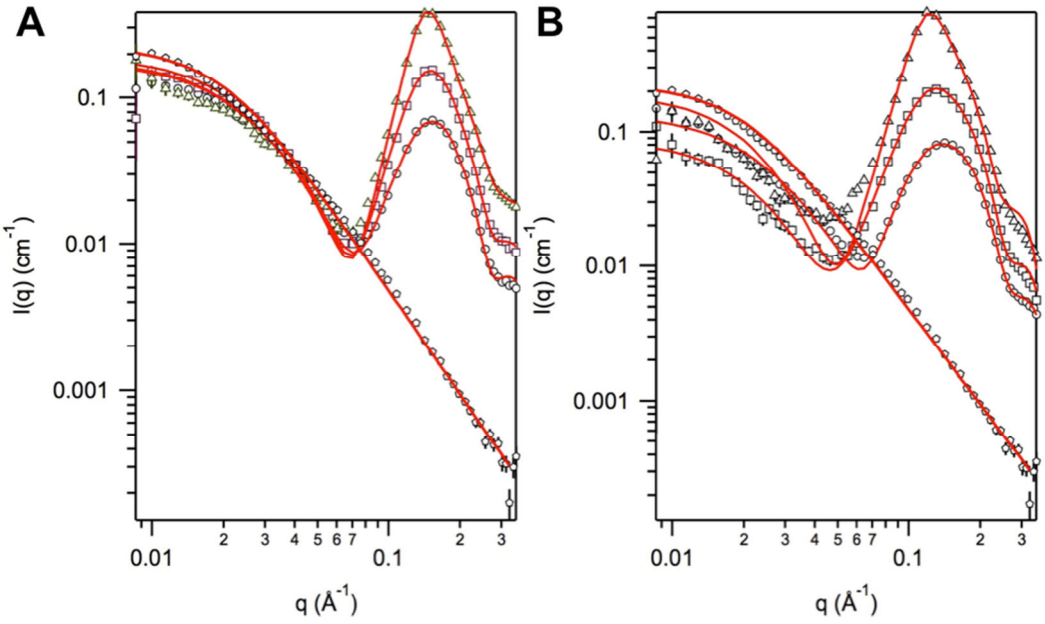

Figure 4.20. SAXS data of SB3-14 in H2O with 1 wt% LPEI. [SB3-14] = 250 mM (circles), 500 mM (squares), 1000 mM (triangles). LPEI 1 wt% (pentagons). Fits to a summed model of polydisperse core-shell sphere with excluded volume polymer

model are presented by a solid red line. **A)** No $CaCl_2$ present and **B)** $CaCl_2$ present [SB3-14] = [$CaCl_2$].

When LPEI 1 wt% is added to SB3-14 fitting of the SAXS data shows there is minimal change to the size of the micelle and the conformation of the headgroup. SB3-14 was investigated at concentrations of 250 mM, 500 mM and 1000 mM with LPEI 1 wt% with no added salt and with equimolar $CaCl_2$ to SB3-14 so that the surfactant to $CaCl_2$ ratio is a molar ratio of 1:1. Fits to the data used a summed model similar to that presented in Chapter 3, of an excluded volume polymer plus the polydisperse core-shell sphere model previously used to model the micelle only data, are presented in Figure 4.20.

To model the data, the parameters for the micelle were the same as the parameters from the fits used for the corresponding micellar solutions with and without salt, discussed above. The parameters used in the model for the excluded volume polymer are a radius of gyration R_g of 77.6 Å and a Porod exponent of 2.35. The 2.35 Porod exponent was chosen for the fits as this was the exponent that best fit the pure polymer solution scattering data discussed previously in Chapter 3 and an exponent of 2.35 is also the expected exponent of a branched polymer mass fractal [43]

Initially the data was not fitted and the model was just compared with the data. The high q region of the scattering which is dominated by the core-shell structure of the SB3-14 was described well by the unchanged model suggesting that the presence of LPEI 1 wt% has no effect on the shape of the micelle, both when no salt is added and when $CaCl_2$ is present in equimolar concentration. However to achieve better fits, the structure factor used to fit the micelle data was changed. To fit the low q data in the mixtures with PEI, but with no added salt, the structure factor fitting allowed a less attractive potential. This did not describe the data perfectly however the fits were better. The parameters describing the polymer were not allowed to fit, although it is likely that the presence of such high concentration surfactant in the solution will change the solution state of the solvent and therefore the conformation of the polymer chains. However, it was decided that without more contrast data, such as from SANS experiments, allowing the polymer parameters to fit would give the model too many parameters relative to the amount of data available, and would be likely to give an erroneous fit. For the PEI/SB3-14 solutions with added salt, the structure factor remained the same as in the micelle and salt only fits, as it was found that the summed model without additional fitting described the data well.

In summary it was found that the addition of polymer has no effect on the size and SB3-14 micelles apart from partially screening the attractive interactions seen in SB3-14 solutions when no $CaCl_2$ is present. Additionally the hard sphere character of SB3-14 solutions containing salt was found not to change significantly from the parameters derived from the solutions where there was LPEI present. This suggests

that the presence of LPEI at these surfactant, salt and polymer concentrations does not significantly alter the water structure around the SB3-14 micelles and therefore does not change the shape or the behaviour of the micelles at the investigated concentrations. This suggests that the primary influence on SB3-14 micelle behaviour in the film forming solutions is the $CaCl_2$ concentration and the relative SB3-14 concentration to $CaCl_2$.

4.6 Mechanism of formation

4.6.1 Time resolved GISAXS

The mechanism of film formation was investigated by time resolved GISAXS (Figure 4.18). The only film forming solution investigated by time resolved GISAXS was 1 [SB3-14]:1 [$CaCl_2$]:[SPEI] with [SB3-14] = 100 mM and [SPEI] = 1 wt% due to experimental time constraints. Although this gives limited information regarding the mechanism of film formation in comparison to the full spectrum of SB3-14 to $CaCl_2$ ratios and polymer combinations in film forming solutions investigated above, this solution is the most interesting to investigate as the final film structure exhibits both a *p6mm* and Lα mesophase plus a L_c phase consisting of solid hydrated surfactant.

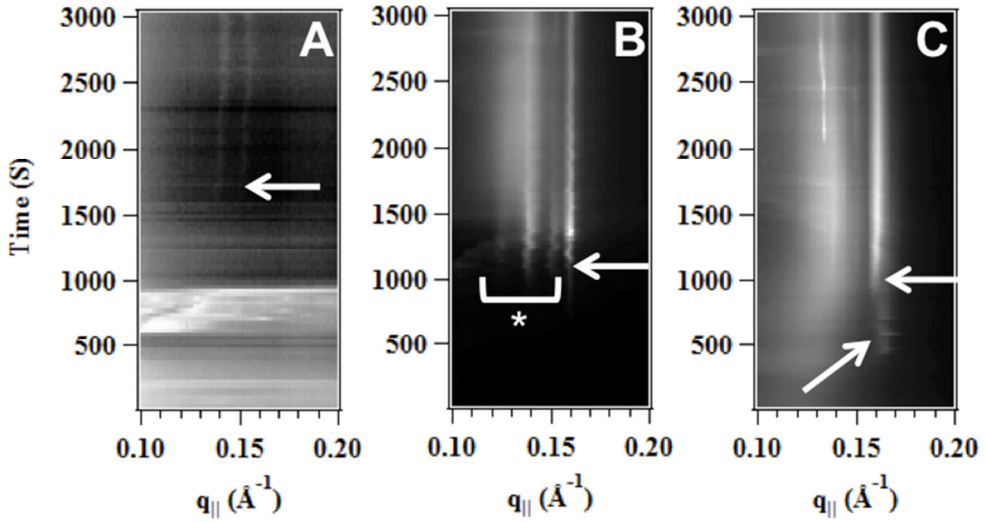

Figure 4.21 Time resolved GISAXS measurement of film formation from spray coated solutions of 1 [SB3-14]:1 [$CaCl_2$]:[SPEI] with [SB3-14]=100mM and [SPEI]=1%wt. Time resolution is 30 seconds and $q_{||}^{||}$ data is obtained from the radial integration of each two dimensional GISAXS plot. The three plots are the time resolved GISAXS plots of successive spray applications of film forming solutions.

Each spray application was monitored for 50 minutes, subsequently another spray application of solution was made and the changing film structure was monitored A) 1 spray coat B) 2 spray coats C) 3 spray coats

The time resolved measurements show that the film formation goes through a series of phases of micellar cubic to *p6mm* as the concentration of the surfactant mesophase increases, due to the solvent evaporates from the substrate. These phases are apparent as a pure micellar cubic phase (Figure 4.21A) and then as a mixed phase with a *p6mm* (Figure 4.21B) plus regions where a micellar phase is apparent (figure 4.21C). The structures and transitions are discussed in more detail below

1st spray coated layer

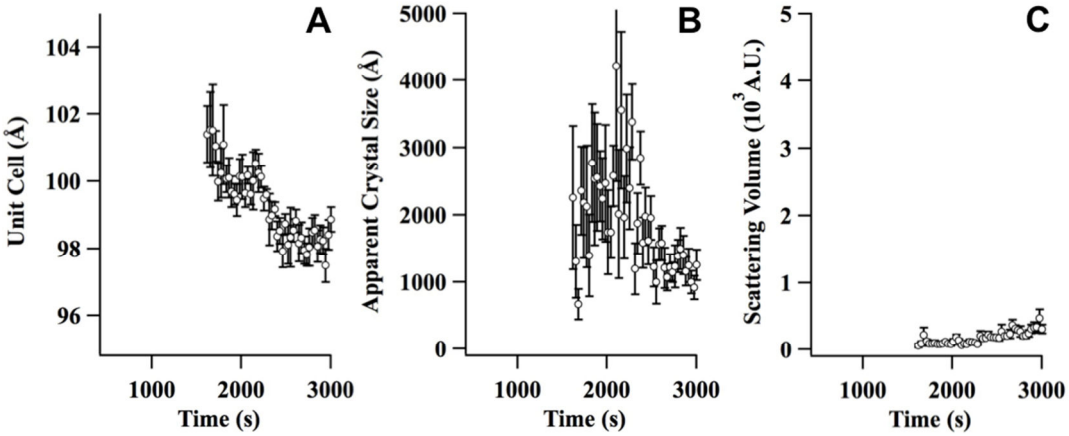

Figure 4.22 Unit cell (A), apparent crystal size (B) and relative scattering volume (C) calculated from the radial integrations of time resolved measurement of film formation from 1st spray coated film formed from 1 [SB3-14]:1 [$CaCl_2$]:[SPEI] with [SB3-14]=100mM and [SPEI]=1%wt. The unit cell dimensions were calculated from the 210 reflection of a $\boldsymbol{Pm\bar{3}n}$ unit cell by $\boldsymbol{d_{cell} = d_{hkl}\sqrt{s}}$. The apparent crystal size was calculated from $\frac{\boldsymbol{2\pi}}{\boldsymbol{\Delta q}}$ and the relative scattering volume is calculated from the integrated intensity if a Lorentzian fitted between $\boldsymbol{q_{max} \pm 0.025}$ $\boldsymbol{Å^{-1}}$ of the 210 reflection of the $\boldsymbol{Pm\bar{3}n}$ unit cell.

The structure evident in the first spray coating of the film forming solution was indexed to a $Pm\bar{3}n$ micellar cubic (Figure 4.22 A). The appearance of this mesophase occurred approximately 900 seconds after the application of the 1st layer of film forming solution. For clarity the onset of the $Pm\bar{3}n$ mesophase is highlighted with an arrow on Figure 4.22 A. There was no other structure evident before the appearance of the $Pm\bar{3}n$ mesophase with the 200, 210 and 211 all appearing simultaneously in the GISAXS measurements albeit weakly. Inspection of the individual radial integrations of the experiment suggest that the $Pm\bar{3}n$ phase is co-existent with a correlated micellar phase due to a broad hump encompassing the 200,

210 and 211 reflection of the $Pm\bar{3}n$ phase however this is not very apparent in Figure 4.22 A due to the intensity scale being logarithmically spaced for clarity of the peak intensities. Indexing of the structure to the $Pm\bar{3}n$ mesophase is not unequivocal from the three peaks evident in this experiment however the structure appears in subsequent experiments and is discussed further later in the text.

The $Pm\bar{3}n$ structure decreased in size from a unit cell of ~101 Å at onset of appearance of to a final size of ~98 Å (Figure 4.22 A) at the end of the time resolved run. This is consistent with the solvent from the bulk phase evaporating, reducing the volume between the micelles that pack on in to the $Pm\bar{3}n$ unit cell. Approximation of the apparent size of the micellar cubic crystallites is difficult due to the low resolvability of the $Pm\bar{3}n$ peaks in the data however it is found that the apparent size of the crystallites appears to decrease as the time resolved run of measurements progresses (Figure 4.22 B) although this data is extremely noisy. However if the apparent size of crystallites decreases this could be a result of two mechanisms; 1) The exchange of water within the film-forming layer dissolving already formed cubic crystallites due to water diffusing from the subphase to the film surface and 2) the increase in the stress caused by the dehydration of water from the film. However as the integrated peak intensity of the $Pm\bar{3}n$ 211 peak increases with time(Figure 4.22 C) this suggests that the amount of the $Pm\bar{3}n$ crystallites increases in the film forming solution which is again consistent with dehydration of water from the film forming solution. It is most likely that the decrease in crystallite size is caused by the stress of solvent dehydration imposing stress fractures on the crystallites due to changes in the solution surface curvature and forcing already formed crystallites together through reduction of volume between them.

2nd spray coated layer

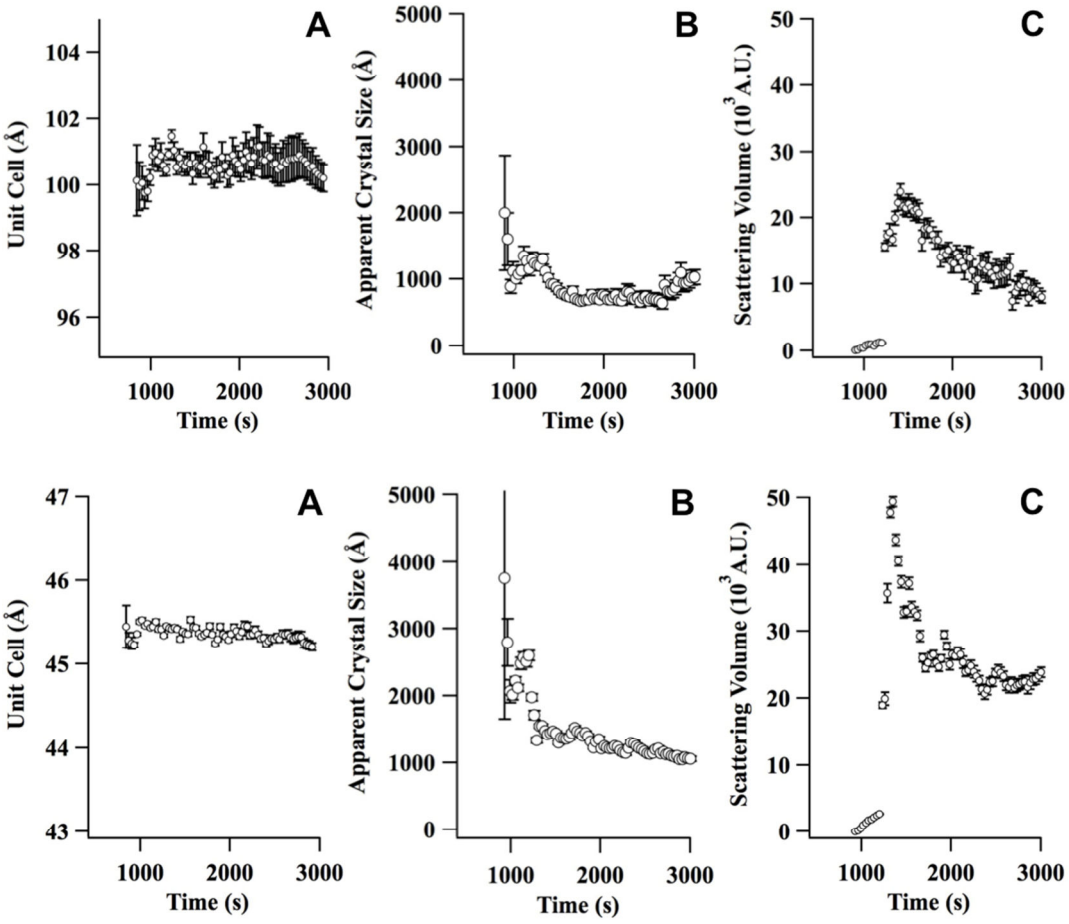

Figure 4.23 Data for the 2nd spray coated film formed from 1 [SB3-14]:1 [$CaCl_2$]:[SPEI] with [SB3-14]=100mM and [SPEI]=1%wt This film contains two mesophase structures Top row: for the $\boldsymbol{Pm\bar{3}n}$ phase Unit cell (A), Apparent Crystal Size (B) and Relative Scattering Volume (C) calculated from the radial integrations of time resolved measurement of film formation from . The unit cell dimensions were calculated from the 210 reflection of a $\boldsymbol{Pm\bar{3}n}$ unit cell by $\boldsymbol{d_{cell} = d_{hkl}\sqrt{s}}$. The apparent crystal size was calculated from $\frac{\boldsymbol{2\pi}}{\boldsymbol{\Delta q}}$ and the relative scattering volume is calculated from the integrated intensity if a Lorentzian fitted between $\boldsymbol{q_{max} \pm 0.025}\text{Å}^{\boldsymbol{-1}}$ of the 210 reflection of the $\boldsymbol{Pm\bar{3}n}$ unit cell. The 211 reflection was chosen as it was considered the most distinct reflection of the cubic unit cell away from the correlated micellar scattering. Bottom row for the *p6mm* phase: Unit cell (D), Apparent Crystal Size (E) and Relative Scattering Volume (F) The radially integrated data was fitted by fitting a linear background and fitting multiple peaks to all maxima in the scattering. The constraints for the linear background was $0.025<q_{hklmin}$, $q_{hklmax}>0.025$ where the min and max is defined as the lowest q scattering peak and q_{hklmax} is the highest q scattering peak

Application of a second spray coating of the film forming solution and the subsequent time resolved GISAXS shows that there is a onset of both the micellar

cubic $Pm\bar{3}n$ phase with the columnar phase 2D hexagonal *p6mm* at the same time. Therefore the dehydration of the film due to solvent evaporation must cause environments to exist which are of the optimal concentration for both the micellar cubic $Pm\bar{3}n$ and the *p6mm* (Figure 4.23A) to exist at the same time. Therefore there must be regions of different water content in the film. The $Pm\bar{3}n$ is the phase which requires the greater water content to form as shown in the first coating of the film forming solution where the water content of the film was greater. It has also been reported for lower surfactant volume fractions before the p6mm phase in sulfobetaine surfactant phase dioagrams[44].The water content of the film was greater as, even though during the 2nd spray coating application more water was added to the film forming system, so was more surfactant, $CaCl_2$ and SPEI. This causes the concentration of the structure forming constituents of the film to achieve a greater concentration sooner, as the film contents were already at a greater concentration due to evaporation of the first spray coating solution.

Features of the evolution of both the structures over the time frame of the 2nd time resolved experiment are that the unit cells of the $Pm\bar{3}n$ and *p6mm* phase remain relatively constant. The data from the radial integrations (Figure 4.23A) is noisy for the unit cell determination of the $Pm\bar{3}n$ phase however there is no significant change in size throughout the experiment, remaining approximately constant at ~100.5 Å. Interestingly it does not reduce in size as the $Pm\bar{3}n$ phase did in the first experiment, as the solvent evaporates from the surface. The *p6mm* unit cell data is significantly (Figure 4.23D) less ambiguous in for the determination of the unit cell due to there being less error. The apparent crystallite sizes of both structures (figure 4.23B and figure 4.23E) decreases over time, as does the integrated peak intensities of the chosen representative peaks.

The reduction of the apparent crystallites sizes and the peak intensities can be attributed to the appearance of a disordered micellar phase. Interestingly the mesophase crystallites appear first suggesting that the films form with an ordered mesophase first. This is most likely due to ordered phases forming at both interfaces initially; at the air-solution interface through evaporation and the solution-surface interface through adsorption and displacement of water. A similar phase transition was seen by Cagnol *et al*[45]. They reported that the denser 211 planes of the $Pm\bar{3}n$ phase in an evaporative grown silica-surfactant film, were situated at the solid-film interface and this plane experienced growth of the micellar aggregates into a *p6mm* phase, along the 10 plane at the same d-spacing of the $Pm\bar{3}n$ 211 phase.

However in this system the *p6mm* phase 10 d-spacing is not the same distance as the $Pm\bar{3}n$ 211 spacing. Therefore it is likely that they occupy different depths in the film. Assuming that water loss is greater at the air-solution interface than the solid-film interface due to evaporation, it is likely that the $Pm\bar{3}n$ phase is at the solid-film interface and the *p6mm* is at the air-solution interface. The disordered micellar phase

is in between these two phases. This is probably due to there being the highest water content at this intermediate depth due to a lack of adsorption causing no water displacement or evaporation events as there are no interfaces here. This is shown graphically in Figure 4.24.

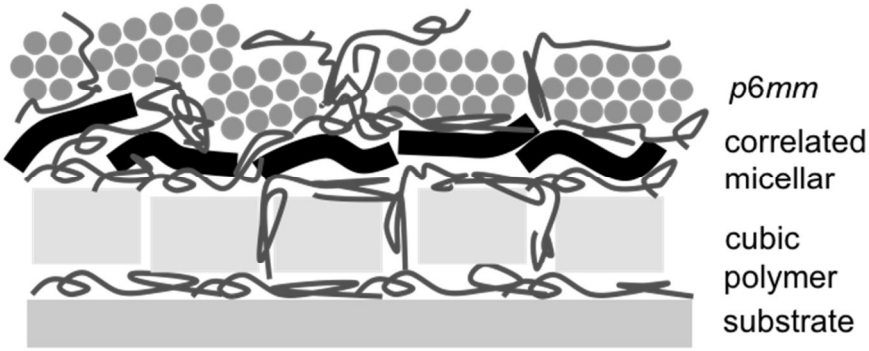

Figure 4.24 Proposed separation of phases in the formation of the spray coated films

The structures appear to be in a steady state in d-spacing but also in orientational order. Figure 4.25A shows the index of the $Pm\bar{3}n$ phase and the *p6mm* phase. The $Pm\bar{3}n$ phase is orientated with the 120 and 121 planes parallel to the substrate surface which shows that the *p6mm* phase could not come from growth of an orientated $Pm\bar{3}n$ crystal. It suggests that the cubic phase possibly grows out of the correlated micellar phase which is less orientated. Figure 4.25B shows that after 2000 seconds, the structures in the film do not appear to exhibit any compression due to evaporation from the film. Figure 4.26 shows that throughout the experiment the orientation of the crystals remain unchanged for both the $Pm\bar{3}n$ phase (4.26A) and the *p6mm* phase (4.26B).

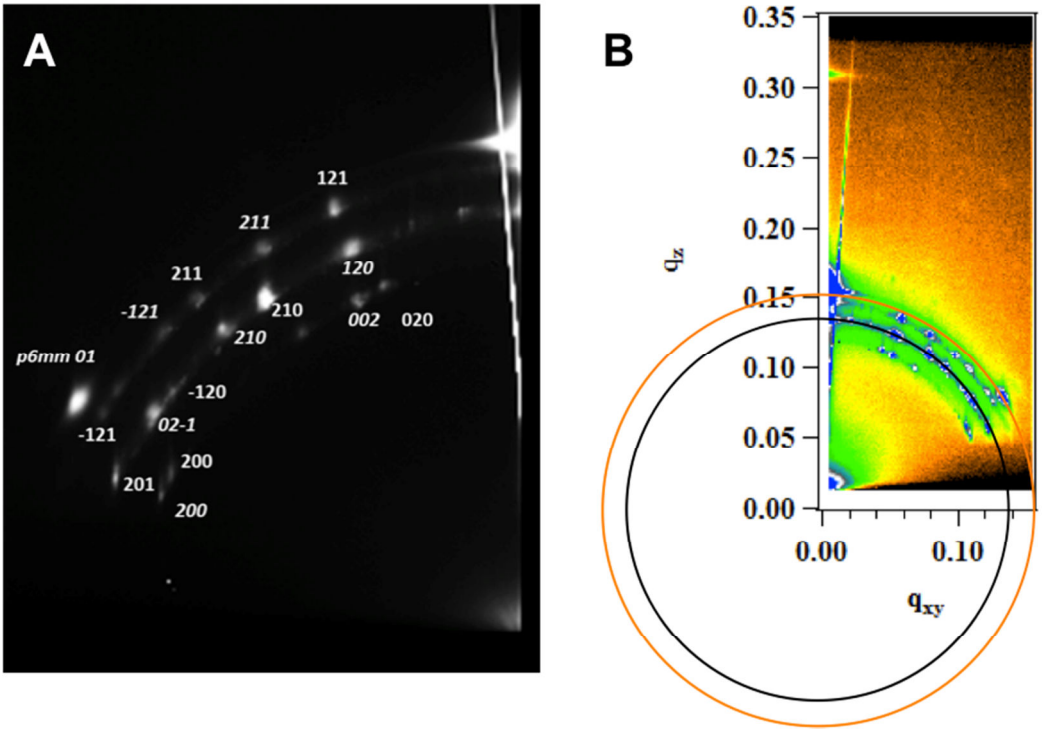

Figure 4.25- A) GISAXS data from t=2000 of 2nd spray coat of film forming solution 1 [SB3-14]:1 [CaCl2]:[SPEI] with [SB3-14]=100mM and [SPEI]=1%wt. The scattering maxima are indexed to a *p6mm* and ***Pm$\bar{3}$n*** unit cell. The *p6mm* unit cell 10 scattering plane is parallel to the film substrate whereas the ***Pm$\bar{3}$n*** unit cell is present with both the 120 and 121 planes parallel to the substrate surface. For the ***Pm$\bar{3}$n*** unit cell the maxima present from 120 plane alignment are identified with normal typeface whereas maxima resulting from 121 alignment are identified with italic indexing B) the same GISAXS data with 2 circles superimposed on the GISAXS data. The circles are centrosymmetric around $q_{||}^{||}$=0 $Å^{-1}$. The coincidence of the diffraction rings with the circles in both the in plane and out of plane scattering show that *p6mm* and ***Pm$\bar{3}$n*** structures are not subject to vertical or lateral distortion

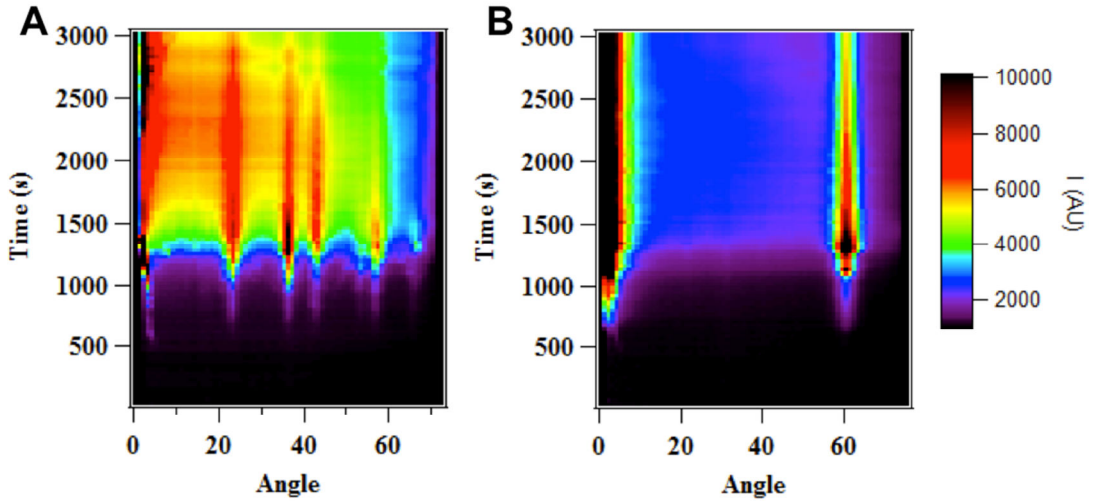

Figure 4.26 Time dependent occurrence of scattering maxima from diffraction planes away from the substrate normal from GISAXS data of 2nd spray of film forming solution 1 [SB3-14]:1 [$CaCl_2$]:[SPEI] with [SB3-14]=100mM and [SPEI]=1%wt. A) $Pm\bar{3}n$ B) p6mm. The data shows that after formation of the structures in the time resolved data there is no change in the orientation of the unit cells of the periodic mesostructure.

3rd spray coated layer

.

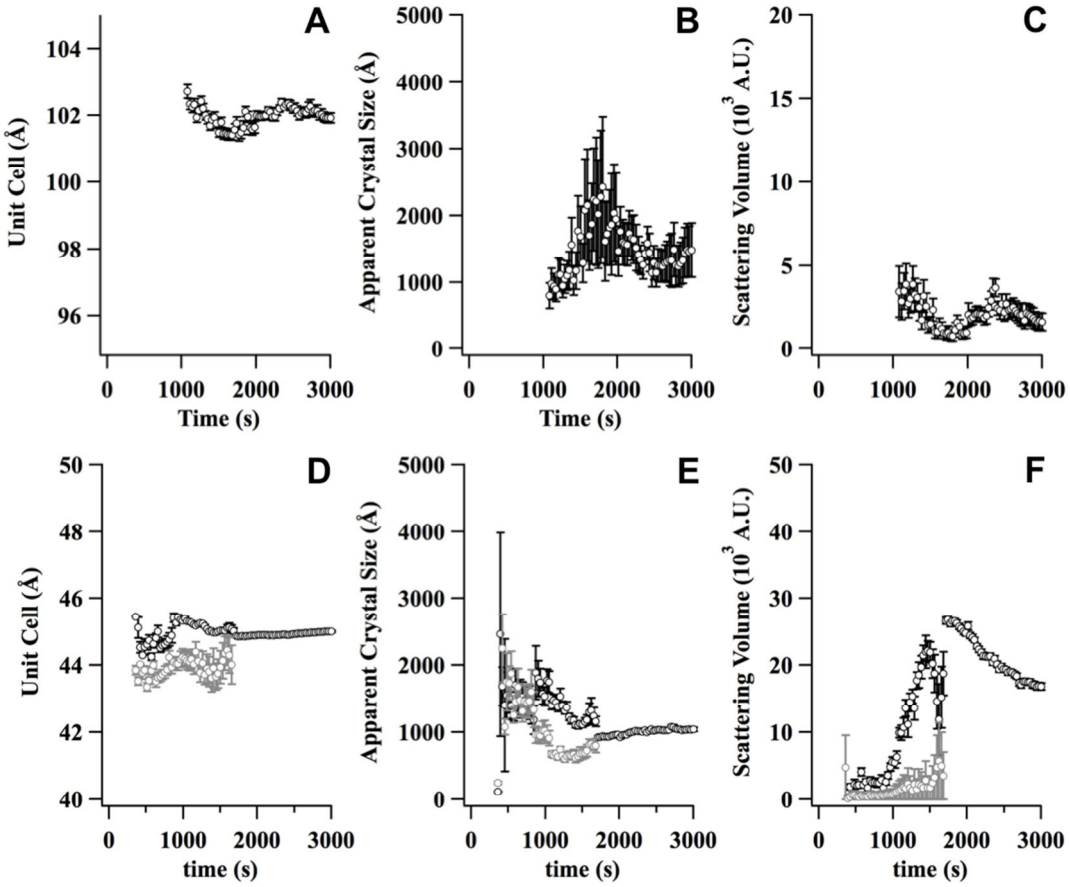

Figure **4.27** Film formation from 1st spray film formed from 1 [SB3-14]:1 [$CaCl_2$]:[SPEI] with [SB3-14]=100mM and [SPEI]=1%wt. Data for the $\boldsymbol{Pm\bar{3}n}$ phase: Unit cell (A), Apparent Crystal Size (B) and Relative Scattering Volume (C) calculated from the radial integrations of time resolved GISAXS measurement The unit cell dimensions was calculated from the 210 reflection of a $\boldsymbol{Pm\bar{3}n}$ unit cell by $\boldsymbol{d_{cell} = d_{hkl}\sqrt{s}}$. The apparent crystal size was xcalculated frm $\frac{\boldsymbol{2\pi}}{\boldsymbol{\Delta q}}$ and the relative scattering volume is calculated from the integrated intensity if a Lorentzian fitted between $\boldsymbol{q_{max} \pm 0.025}$ $\boldsymbol{Å^{-1}}$ of the 211 reflection of the $\boldsymbol{Pm\bar{3}n}$ unit cell. The 211 reflection was chosen as it was considered the most distinct reflection of the cubic unit cell away from the correlated micellar scattering. Data for the p6mm phase: Unit cell (D), Apparent Crystal Size (E) and Relative Scattering Volume (F) The radially integrated data was fitted by fitting a linear background and fitting multiple peaks to all maxima in the scattering. The constraints for the linear background was $0.025 < q_{hklmin}, q_{hklmax} > 0.025$ $Å^{-1}$ where the min and max is defined as the lowest q

scattering peak and highest q scattering peak what are the two different colour dots on the graphs.

On the final time-resolved data set a 3rd spray coated layer was investigated. Here the structure is dominated by a micellar phase and a *p6mm* phase. A $Pm\bar{3}n$ phase is slightly evident in the region of the micellar phase. The unit cell, apparent crystal size and relative scattering volume are presented in figure 4.27 A to C respectively. Compared to the second layer it appears that a micellar phase is more dominant here suggesting more disorder and more hydration. This follows as even though there is more solute in the film due to the addition of an extra layer it is likely that there is enough volume of solution that a *p6mm* phase, if present at the air-solution interface, is preventing evaporation of solvent.

As the cubic phase is most likely forming at the solid-film interface (due to more water being present), the presence of added water appears to disrupt this more. Whereas at the air-solution interface there appears to be initially a smaller *p6mm* phase which undergoes a transition to a larger *p6mm* phase (Figure 4.27D). The appearance of a larger *p6mm* phase is attributed to initial formation of a smaller *p6mm* phase due to the evaporation of water. However as the volume fraction of all components increases, there is likely to be greater intercalation of polymer between the micelles. This is seen in Figure 4.27F, where the relative volume of the larger *p6mm* phase increases over time, taking longer to form than the smaller *p6mm* phase which may be due to the time it takes for the polymer to rearrange.

4.7 Films formed from biopolymers

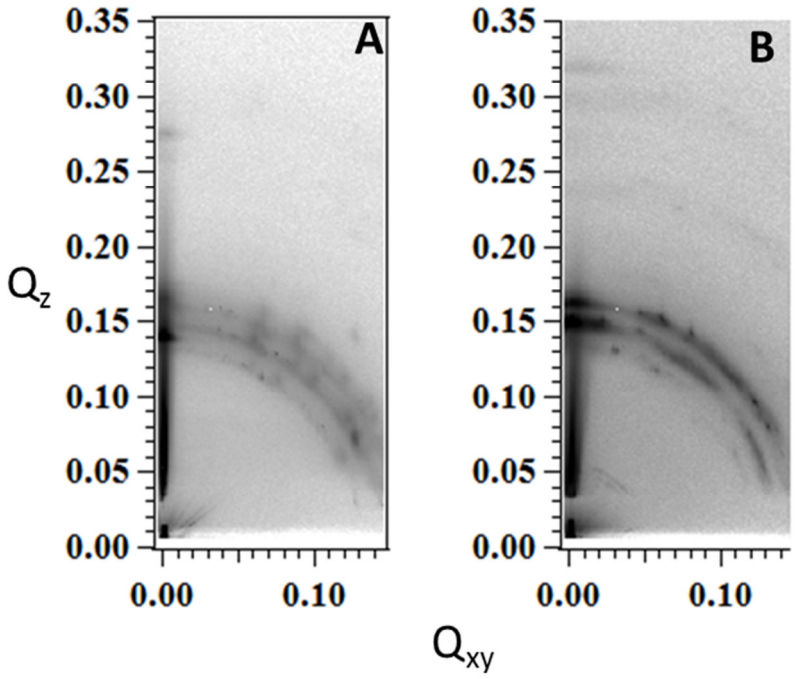

Figure 4.28 GISAXS data of films formed from SB3-14 100mM, CaCl2 100mM and A) Sodium Alginate 0.5% wt and B) DNA 0.2% wt. All data is at 0.45 degrees incident angle and plotted in reciprocal Angstroms.

Figure 4.28 shows GISAXS data formed from biopolymers and SB3-14 and CaCl2 (surfactant and salt in equimolar quantities). At these compositions it is shown both films exhibit a $Pm\bar{3}n$ structure that appears the same as the structure observed in the time resolved measurements of films formed from SB3-14/CaCl2/PEI. The presence of a predominate $Pm\bar{3}n$ phase suggests that there is more water in the films compared to the PEI films according to accepted sulfobetaine surfactant phase diagrams[44]. However it could also be indicative of the polymer having more interaction with the surface of the micelle, dressing it and causing packing consideration like pure CTAB and LPEI structures discussed in chapter 3.

It should also be noted that the polymer concentration is less than when films were formed from PEI. The polymer concentration was reduced due to being able to apply the spray solutions with the spray bottle. The biopolymer were also applied in alternating stages with the surfactant and salt solution due to complexes being formed in the bulk solutions. When the polymers were at 1% wt they were too

viscous to apply evenly on a substrate with the spray bottle. Therefore, as less polymer is present it is likely that there is less competition for water to hydrate the surfactant. A final consideration is that as the polymers are both ionic they will associate more with the calcium ions than PEI. This could sequester more calcium from the film solution and therefore introduce less competition for hydration than in the PEI films, when calcium is more likely to be unbound. This could contribute to the surfactant being more hydrated than in the PEI films.

There are differences between the films is that when films are formed from alginate the $Pm\bar{3}n$ phase has a slightly larger unit cell compared to DNA (95.2 compared to 94 angstroms respectively). Also when films are formed from alginate the GISAXS shows that there is also a *p6mm* phase present, where the 10 reflection of the hexagonal phase occupies the same region as the 210 plane of the $Pm\bar{3}n$ phase. This is similar a previously reported transition when the phase transition is reversible along this phase[45]. Importantly it suggests that unlike what is observed in the time resolved PEI films, the hexagonal and micellar cubic phase occupy the same region of the film as they a distance redundant and the film shows a mixture of phases that are transforming from eachother. It also suggests that the alginate film is drier than the DNA film. However, due to the differences in polymer concentration this could be attributed to more salt being associated with the polymer or even the polymer competing for water. However, both films exhibit the micellar cubic phase after the same drying period of the equivalent PEI film suggesting that the presence of a steady state micellar cubic film can be controlled by the use of biocompatible anionic biopolymers.

4.8 Summary of results in this chapter

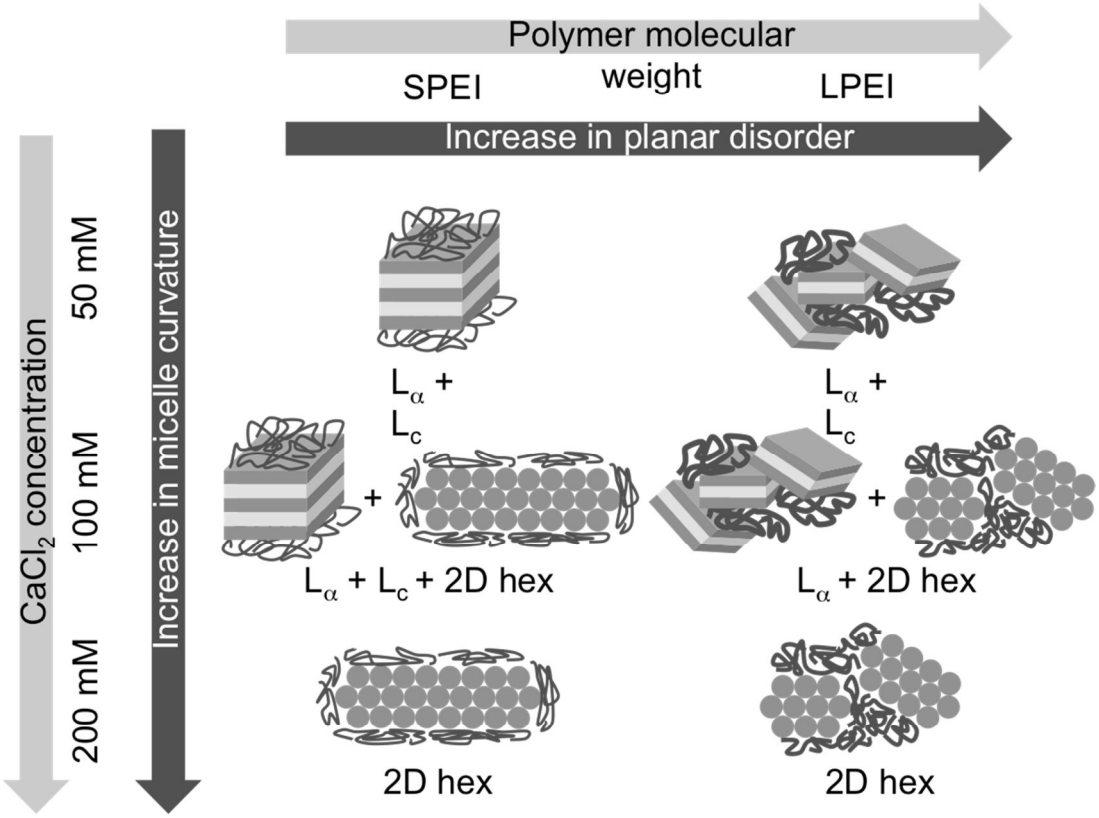

Figure 4.29 Schematic showing the effect PEI molecular weight and $CaCl_2$ concentration has on the films.

The main effects of the components in the film can be attributed to increasing the surfactant micelle curvature from $CaCl_2$ concentration and the increase in planar disorder of the films with PEI molecular weight. Small angle scattering results show that at high surfactant and salt concentrations the inter-particle interactions go from attractive to repulsive to the extent that the micelles can be considered to be slightly charged. This can explain the small unit cell of liquid crystals when polymer is present due to electrostatic attraction between the polymer and surfactant. It may also explain increased surfactant curvature as the $CaCl_2$ concentration is increased along with increased water content thus increasing the packing parameter by increasing the head group size. The main result is although the presence of $CaCl_2$ increased the curvature of SB3-14, it can be seen in figure 4.29 how the increased hydration due to hygroscopic $CaCl_2$ promoted the formation of locally curved mesophases, from solid crystalline lamellar to liquid crystal lamellar to two dimensional hexagonal. The molecular weight of PEI imposed itself that the LPEI prevented sterically prevented the formation of long range order mesophases compared to SPEI. When films were formed with anionic biopolymers it was shown

that it is possible to produce steady state micellar cubic films. This could be attributed to the surfactant being more hydrated due to less competition from sequestered $CaCl_2$ which is more associated with polymers.

4.8 References

(1) Mathieu, L. G.; Pelletie.Rp *Canadian Journal of Comparative Medicine and Veterinary Science* **1966**, *30*, 35.

(2) McCarty, P. L.; McKinney, R. E. *Journal (Water Pollution Control Federation)* **1961**, *33*, 399.

(3) Tatara, C. P.; C. Newman, M.; McCloskey, J. T.; Williams, P. L. *Aquatic Toxicology* **1998**, *42*, 255.

(4) Handlogten, M. E.; Shiraishi, N.; Awata, H.; Huang, C.; Miller, R. T. *American Journal of Physiology - Renal Physiology* **2000**, *279*, F1083.

(5) Angle, C. R.; McIntire, M. S. *Archives of Pediatrics & Adolescent Medicine* **1964**, *108*, 436.

(6) Bruening, K.; Kemp, F. W.; Simone, N.; Holding, Y.; Louria, D. B.; Bogden, J. D. *Environmental health perspectives* **1999**, *107*, 431.

(7) Markowitz, M. E.; Sinnett, M.; Rosen, J. F. *Pediatrics* **2004**, *113*, e34.

(8) Battaglia, G.; Crea, F.; Crea, P.; De Stefano, C.; Sammartano, S. *Journal of Chemical & Engineering Data* **2008**, *54*, 502.

(9) Hu, W.; Hasebe, K.; Tanaka, K.; Haddad, P. R. *Journal of Chromatography A* **1999**, *850*, 161.

(10) Beber, R. C.; Bunton, C.; Savelli, G.; Nome, F. In *Surface and Colloid Science*; Springer Berlin Heidelberg: 2004; Vol. 128, p 249.

(11) Fritz, J. S. *Journal of Chromatography A* **2005**, *1085*, 8.

(12) Marte, L.; Beber, R. C.; Farrukh, M. A.; Micke, G. A.; Costa, A. C. O.; Gillitt, N. D.; Bunton, C. A.; Di Profio, P.; Savelli, G.; Nome, F. *The Journal of Physical Chemistry B* **2007**, *111*, 9762.

(13) Priebe, J. P.; Satnami, M. L.; Tondo, D. W.; Souza, B. S.; Priebe, J. M.; Micke, G. A.; Costa, A. C. O.; Fiedler, H. D.; Bunton, C. A.; Nome, F. *Journal of Physical Chemistry B* **2008**, *112*, 14373.

(14) Priebe, J. P.; Souza, F. D.; Silva, M.; Tondo, D. W.; Priebe, J. M.; Micke, G. A.; Costa, A. C. O.; Bunton, C. A.; Quina, F. H.; Fiedler, H. D.; Nome, F. *Langmuir* **2012**, *28*, 1758.

(15) Ainalem, M.-L.; Kristen, N.; Edler, K. J.; Höök, F.; Sparr, E.; Nylander, T. *Langmuir* **2009**, *26*, 4965.

(16) PENFOLD, J. *J. Phys. Colloques* **1989**, *50*, C7.

(17) Hénon, S.; Meunier, J. *Review of Scientific Instruments* **1991**, *62*, 936.

(18) O'Driscoll, B. M. D.; Milsom, E.; Fernandez-Martin, C.; White, L.; Roser, S. J.; Edler, K. J. *Macromolecules* **2005**, *38*, 8785.
(19) Yokoyama, T.; Murakami, G.; Akashi, H.; Zenki, M. *Analytical Sciences: X-ray Structure Analysis Online* **2004**, *20*, x31.
(20) Thiele, H.; von Levern, H. S. *Journal of Colloid Science* **1965**, *20*, 679.
(21) Chatani, Y.; Tadokoro, H.; Saegusa, T.; Ikeda, H. *Macromolecules* **1981**, *14*, 315.
(22) Chatani, Y.; Kobatake, T.; Tadokoro, H.; Tanaka, R. *Macromolecules* **1982**, *15*, 170.
(23) Cross, G. H.; Ren, Y.; Swann, M. J. *Analyst* **2000**, *125*, 2173.
(24) Choi, H. S.; Ooya, T.; Lee, S. C.; Sasaki, S.; Kurisawa, M.; Uyama, H.; Yui, N. *Macromolecules* **2004**, *37*, 6705.
(25) Aristov, Y. I.; Tokarev, M. M.; Cacciola, G.; Restuccia, G. *Reaction Kinetics and Catalysis Letters* **1996**, *59*, 325.
(26) Aristov, Y. I.; Restuccia, G.; Cacciola, G.; Parmon, V. N. *Applied Thermal Engineering* **2002**, *22*, 191.
(27) Zhang, X. J.; Qiu, L. M. *Energy Conversion and Management* **2007**, *48*, 320.
(28) Hopp, H. *Botanical Gazette* **1936**, 25.
(29) Winston, P. W.; Bates, D. H. *Ecology* **1960**, *41*, 232.
(30) Shirazi, A.; Cameron, A. C. *HortScience* **1992**, *27*, 336.
(31) Anantheswaran, R. C.; Beelman, R. B.; Roy, S. *Journal of Food Science* **1996**, *61*, 391.
(32) Cisneros-Zevallos, L.; Saltveit, M. E.; Krochta, J. M. *Journal of Food Science* **1997**, *62*, 363.
(33) Tanford, C. *Journal of Molecular Biology* **1972**, *67*, 59.
(34) Tiddy, G. J. T. *Physics Reports* **1980**, *57*, 1.
(35) Berr, S. S.; Caponetti, E.; Johnson, J. S.; Jones, R. R. M.; Magid, L. J. *The Journal of Physical Chemistry* **1986**, *90*, 5766.
(36) Tanford, C. *The Journal of Physical Chemistry* **1974**, *78*, 2469.
(37) Kamenka, N.; Chorro, M.; Chevalier, Y.; Levy, H.; Zana, R. *Langmuir* **1995**, *11*, 4234.
(38) Ren, B.; Cheng, Z.; Tong, Z.; Liu, X.; Wang, C.; Zeng, F. *Macromolecules* **2006**, *39*, 6552.
(39) Guinier, A. *Annales de Physique (Paris)* **1939**, *16*, 161.
(40) Liu, Y.; Chen, W.-R.; Chen, S.-H. *The Journal of Chemical Physics* **2005**, *122*, 044507.
(41) Menon, S. V. G.; Manohar, C.; Rao, K. S. *The Journal of Chemical Physics* **1991**, *95*, 9186.
(42) Gapiński, J.; Szymański, J. d.; Wilk, A.; Kohlbrecher, J.; Patkowski, A.; Hołyst, R. *Langmuir* **2010**, *26*, 9304.
(43) Beaucage, G. *Journal of Applied Crystallography* **1996**, *29*, 134.
(44) Faulkner, P. G.; Ward, A. J.; Osborne, D. W. *Langmuir* **1989**, *5*, 924.
(45) Cagnol, F.; Grosso, D.; Soler-Illia, G. J. d. A. A.; Crepaldi, E. L.; Babonneau, F.; Amenitsch, H.; Sanchez, C. *Journal of Materials Chemistry* **2003**, *13*, 61.

5. Conclusion

The main aim of this work was to develop was to develop methods of producing low toxicity films that exhibited surfactant imparted mesostructure. Further aims were to determine which experimental conditions would produce periodic mesostructure and the applicability of sulfobetaine surfactant in producing polymer-surfactant hydrogel films that exhibit periodic mesostructure.

The aims were achieved by investigating polymer-surfactant hydrogel films that were formed from cationic surfactant CTAB, zwitterionic surfactant SB3-14 and PEI. The research then proceeded with the replacement of cationic charge in the films with divalent calcium ions, leading to the complete replacement of CTAB. Lastly, PEI was replaced as the film forming polymer by anionic biopolymers such as DNA and sodium alginate. This work has resulted in less toxic films than previously reported films in the Edler group, being formed from mixtures of zwitterionic and cationic surfactant. Films were formed with periodic mesostructure, depending on the PEI molecular weight used. The size of the mesostructure was controlled by the mixed micelle composition. Low toxicity films were also formed from a spray coating method, where films were formed from mixtures of SB3-14, calcium chloride and polymer. Here the type of mesostructure formed was controlled by the calcium chloride concentration and polymer electrostatic architecture. Both film types reported in this work contribute to the field of structured polymer-surfactant by introducing possible low toxicity variants. Some insight into the film formation mechanisms was derived, plus mechanistic models for their formation were proposed. Relationships between the bulk processes and film formation were also proposed.

5.2 Main research areas

The main research areas in this work were investigating the following effects on the polymer-surfactant hydrogel film structure and formation.

- Mixed micelle surfactant composition
- Polymer molecular weight
- Divalent cation salt concentration relative to surfactant concentration
    - Initially with cationic CTAB present
    - Later as complete replacement of the cationic charge of CTAB
- Polymer electrostatic architecture
    - -dipoles versus ions

Mixed micelle surfactant composition was investigated through mixtures of CTAB and SB3-14. This was primarily to reduce the amount of toxic CTAB in the films. Films were formed with mixtures of CTAB and SB3-14 in molar ratios of 1:0, 2:1, 1:1, 1:2, 0:1 at total surfactant concentration of 50mM. Films were formed with PEI

at 1% wt at two different molecular weights, 750,000 g mol^{-1} and 2000 g mol^{-1}. The mixtures were investigated with neutron reflectometry to determine the film structure and small angle scattering techniques to determine the bulk behaviour. When neutrons were used as the incident radiation, contrast variation was achieved through substitution of per-hydrogenated tail CTAB with per-deuterated tail CTAB. This gave insight into the composition of the mixed micelles. Composition was also determined at the CMC by investigating the surface tension of a concentration series of the surfactant mixtures also showed the relative position of the surfactant within the mixed micelles at the hydrophobic-hydrophilic interface, with the SB3-14 having significant penetration of the sulfate moiety into the micelle cores. Model dependent and independent analysis was applied to the small angle scattering results. This gave insight in to the composition, form, and micellar charge and aggregation number of the mixed micelles. Model dependent and independent analysis was applied to the neutron reflectometry results which gave insight in to the effect mixed micelles had on the form and internal mesostructure on the films.

The effect of the polymer molecular weight was investigated by forming films from mixed surfactant micelles with PEI at a molecular weight of 750,000 (LPEI) and 2000 gmol-1(SPEI). All molar ratios of CTAB and SB3-14 above were investigated in the presence of either LPEI or SPEI as the film forming polymer, so that the effect of polymer molecular weight was able to be determined for these ratios. These solutions were investigated with neutron reflectometry and small angle scattering techniques which demonstrated that substitution of CTAB with SB3-14 resulted in the loss of mesostructure due to loss of cationic charge although the polymer network of LPEI kinetically trapped enough surfactant to create a concentrated syrfactant mesophase. The effect of polymer molecular weight was also investigated in spray coated films. Here solutions were formed from calcium chloride, PEI and SB3-14, and the film structures were investigated by GISAXS and XRR. The molecular weight of PEI was shown to influence the formation of long range structure in the resultant mesophases due to LPEI imposing more steric bulk than SPEI.

The effect of divalent cations on the film formation was investigated by two methods. Initially calcium chloride was present in film forming solutions that comprised both CTAB and SB3-14 with PEI. Film formation at the interface was monitored with neutron reflectometry. The second method of investigating the effect that divalent cations had on the formation of structured polymer-surfactant films when calcium chloride completely replaces the cationic charge from cationic CTAB. These films were investigated by spray coating film forming solutions as films that exhibited periodic mesostructure were not present at the air-solution interface. Therefore, another interface was introduced in the form of a silica wafer. Here the calcium chloride concentration was varied relative to the SB3-14 concentration in the initial film forming solutions. The final film structures and mechanism of

formation was investigated by GISAXS and XRR. These showed that generally the films had a lamellar to 2D hexagonal structure, where curvature of the micellar aggregates was dependent of calcium chloride concentration.

Finally the polymer electrostatic architecture was investigated by then substitution of PEI with the anionic biopolymers DNA and sodium alginate. Substitution of the amine dipole polymer PEI with the anionic biopolymers was only investigated with the spray coated films and not the spontaneously forming films at the air-solution interface. This was primarily because the main aim of this work was to produce films that exhibited periodic mesostructure plus low toxicity and films did not form spontaneously in these systems. Due to the anionic architecture of the polymers it was necessary to apply the spray coated films in stages where solutions of mixed SB3-14 and calcium chloride were alternately applied with solutions of biopolymers. This was to prevent complexes being formed in the bulk solution before spraying, and to allow restructuring when the polymer and salt interaction occurred at the film formation interface. Here it was found than anionic biopolymers remove more $CaCl_2$ from solution, decreasing competition for water with the surfactant and resulting in a more hydrated micellar cubic phase compared to when films are formed with PEI and the resultant hexagonal phases.

5.3 Significance of these results

The significance of this work is that methods of the formation of mesostructured polymer-surfactant films with controllable mesostructure. The films have lower toxicity compared to previously reported films from the Edler group. Therefore they may have some application in biomedical applications. Additionally, their method of formation is relatively easy compared to other film forming techniques such as layer by layer deposition.

5.4 Future Work

The next studies to be performed would be to incorporate hydrophobic species a drug analogues and monitor their release from the films as the main ibjective was to form biocompatible films. Then the release profiles could be associated with the type of structure. This would give the films biomedical relevance. Complementary to the studies presented here more experiments could be of interest to perform on the systems investigated. In the following some thoughts are given on future experiment, which could be of interest, using techniques different from those presented and employed in this work.

5.4.1 The films

A widely used method in the study of films, which has not been used in this work, is ellipsometry. In this optical technique the fact that the polarization of light is highly sensitive to the surface properties is utilised. The light polarised perpendicular to the plane of reflection (*s*-polarised) is reflected differently from the light polarised in the plane of reflection (*p*-polarised). This is what is utilised in the technique, which is well suited for following the kinetics of film formation at an interface as the changes in adsorption is easily investigated, whereas extracting absolute numbers from the technique is much more difficult [1, 2].

The technique has previously been applied to many polymer surfactant systems. It has for example been applied to study the thickness and refractive indices of a mixture of cationic surfactants and anionic polymers[3], to study the stability of film formed by oppositely charged polyelectrolyte and surfactant complexes [4] and to investigate the interactions between a polymer and a non-ionic surfactant [5]. These are just a few examples. This technique would be able to provide interesting additional information on the films and how they form with greater time resolution than neutron experiments.

Atomic force microscopy (AFM) is a real space imaging technique, which can also give information on the local elasticity or stiffness of the sample. However, this technique is normally only applied to structures on solid surfaces. However, it has also been demonstrated on film formed at an air-water interface [10]. The experiment can be performed in one of two modes; contact or non-contact mode. The general idea is that when the cantilever is close to the surface, this will then be deflected as a consequence of interaction forces and this deflection is detected. The deflection will when interpreted give a topographical image of the surface [11].

In contact mode the tip of the cantilever is kept in contact with surface, essentially dragging through the sample, whereby the topography of the sample is measured. Here, it should be noted that this way of performing an experiment will damage the sample if this is made from a soft material, like a polymer-surfactant film. Contrary, in non-contact or tapping mode the tip is kept at a definite distance from the sample at all times and no damage will be inflicted. However, the resolution of this method is lower, around an order of magnitude. Despite the loss of resolution one can also probe some surface properties, like the stiffness of the sample. This is an important characteristic of a film and can help to gain a better understanding of the film properties as a function of composition, which is of importance to this work and would therefore be a fruitful additional experiment to perform [11, 12]. The method has previously been used to study the thickness of spin-coated thin polymer films

[13] and also to study the elastic modulus and yielding strength of thin polymer films [14].

Furthermore, the quartz crystal microbalance technique (QCM) can be used to gain insight to the interaction between polymer micelle, provided one can be attached to a surface, and to self-assembly of surfactants or polymers in a solid surface. The technique works by having an oscillating quartz crystal and then measuring the frequency and dissipation of the crystal whereby the mass deposited on the surface can be determined. The crystal can be oscillated by an electrical current because quartz is piezoelectric element [15]. The technique has previously been used to study self-assembling systems. It has for example been used to study the incorporation of surfactant micelles in a polymer film [16] and to study the adsorption of phospholipids and triblock copolymers [17, 18]. Applying this technique to the system studied in this thesis may prove difficult though on the other hand interesting new insight may be gained.

5.4.2 The bulk phase

To further elucidate the behaviour of the subphase of CTAB and SB3-14 both in the presence and absents of polymer several other experiments could be performed. Real space analysis using transmission electron microscopy (TEM) could provide additional support to the micelle structure deduces form the small-angle scattering experiments. Further, one could also obtain supporting information on the mixed polymer surfactant system. However, there are several difficulties involved in performing this kind of experiment, the most pressing being the flash-freezing of the sample used in cryo-TEM. Here, possible defects can be induced in the system. Also, the structures investigated in this work may be difficult to visualise using TEM, as a consequence of their size, though micelles have previously been imaged [19-21].

Having obtained a satisfying sample one must be aware the in the TEM experiment only a subset of particles are investigated, contrary to solution small-angle scattering where the entire sample is evaluated. This means that one has to collect data on a large amount of subsets in order to extract statistical significant information from the experiment [19].

An interesting experiment in relation to the interaction between the micelles could be to perform a viscosity study as a function of surfactant concentration. Introducing particles to a liquid will change the viscosity of the system, as the flow patterns around the particles will change. By investigating the viscosity in the zero-share limit (at low concentration), the resulting viscosity is a consequence of particle diffusion [22, 23]. For a suspension of hard-sphere particles the intrinsic viscosity

can be interpreted as a function of two parameters, the first dominated by the shape and hydrodynamic properties of the particles and the second additionally affected by the interparticle interactions. Thus, information on hydrodynamics and interparticle interactions could be obtained for increasing salt concentrations to investigate the effect of electrostatics in the system [24, 25]. Anomalous SAXS experiments with tunable X-ray energy could further elucidate the positions of calcium and chloride ions when associated with SB3-14 micelles

5.5 References

1. Collins, R.W. and Y.T. Kim, *Ellipsometry for thin-film and surface analysis.* Analytical Chemistry, 1990. **62**(17): p. 887A-890A.
2. Taylor, D.J.F., R.K. Thomas, and J. Penfold, *Polymer/surfactant interactions at the air/water interface.* Advances in Colloid and Interface Science, 2007. **132**(2): p. 69-110.
3. Asnacios, A., D. Langevin, and J.F. Argillier, *Mixed monolayers of cationic surfactants and anionic polymers at the air-water interface: Surface tension and ellipsometry studies.* The European Physical Journal B - Condensed Matter and Complex Systems, 1998. **5**(4): p. 905-911.
4. Monteux, C., et al., *Adsorption of Oppositely Charged Polyelectrolyte/Surfactant Complexes at the Air/Water Interface: Formation of Interfacial Gels.* Langmuir, 2003. **20**(1): p. 57-63.
5. Robb, I.D. and P. Stevenson, *Interaction between Poly(acrylic acid) and an Ethoxylated Nonionic Surfactant.* Langmuir, 2000. **16**(18): p. 7168-7172.
6. Hönig, D. and D. Möbius, *Reflectometry at the Brewster angle and Brewster angle microscopy at the air-water interface.* Thin Solid Films, 1992. **210–211, Part 1**(0): p. 64-68.
7. Kaercher, T., D. Hönig, and D. Möbius, *Brewster angle microscopy.* International Ophthalmology, 1993. **17**(6): p. 341-348.
8. Mann, E.K., et al., *Polymer-surfactant films at the air-water interface. 1. Surface pressure, ellipsometry, and microscopic studies.* Macromolecules, 1993. **26**(25): p. 7037-7045.
9. de Mul, M.N.G. and J.A. Mann, *Determination of the Thickness and Optical Properties of a Langmuir Film from the Domain Morphology by Brewster Angle Microscopy.* Langmuir, 1998. **14**(9): p. 2455-2466.
10. Mate, C.M., M.R. Lorenz, and V.J. Novotny, *Atomic force microscopy of polymeric liquid films.* The Journal of Chemical Physics, 1989. **90**(12): p. 7550-7555.

11. Meyer, E., *Atomic force microscopy.* Progress in Surface Science, 1992. **41**(1): p. 3-49.
12. Krausch, G., *Surface induced self assembly in thin polymer films.* Materials Science and Engineering: R: Reports, 1995. **14**(1–2): p. v-94.
13. Ton-That, C., A.G. Shard, and R.H. Bradley, *Thickness of Spin-Cast Polymer Thin Films Determined by Angle-Resolved XPS and AFM Tip-Scratch Methods.* Langmuir, 2000. **16**(5): p. 2281-2284.
14. Du, B., et al., *Study of Elastic Modulus and Yield Strength of Polymer Thin Films Using Atomic Force Microscopy.* Langmuir, 2001. **17**(11): p. 3286-3291.
15. Marx, K.A., *Quartz Crystal Microbalance: A Useful Tool for Studying Thin Polymer Films and Complex Biomolecular Systems at the Solution−Surface Interface.* Biomacromolecules, 2003. **4**(5): p. 1099-1120.
16. Njue, C.K. and J.F. Rusling, *Controlling Catalytic Activity of a Polyion Scaffold on an Electrode via Microemulsion Composition.* Journal of the American Chemical Society, 2000. **122**(27): p. 6459-6463.
17. Stålgren, J.J.R., P.M. Claesson, and T. Wärnheim, *Adsorption of liposomes and emulsions studied with a quartz crystal microbalance.* Advances in Colloid and Interface Science, 2001. **89–90**(0): p. 383-394.
18. Johnsson, M., et al., *Adsorption of a PEO−PPO−PEO Triblock Copolymer on Small Unilamellar Vesicles: Equilibrium and Kinetic Properties and Correlation with Membrane Permeability.* Langmuir, 2001. **17**(13): p. 3902-3911.
19. Vinson, P.K., et al., *Direct imaging of surfactant micelles, vesicles, discs, and ripple phase structures by cryo-transmission electron microscopy.* Journal of Colloid and Interface Science, 1991. **142**(1): p. 74-91.
20. Won, Y.-Y., et al., *Cryogenic Transmission Electron Microscopy (Cryo-TEM) of Micelles and Vesicles Formed in Water by Poly(ethylene oxide)-Based Block Copolymers.* The Journal of Physical Chemistry B, 2002. **106**(13): p. 3354-3364.
21. Zheng, Y., et al., *Directly Resolved Core-Corona Structure of Block Copolymer Micelles by Cryo-Transmission Electron Microscopy.* The Journal of Physical Chemistry B, 1999. **103**(47): p. 10331-10334.
22. Holmberg, K., et al., *Surfactants and Polymers in Aqueous Solution. Chapter 15: An Introduction to the Rheology of Polymer and Surfactant Solutions, p. 317-336*. 2002: Wiley.
23. Bergenholtz, J. and N.J. Wagner, *The Huggins Coefficient for the Square-Well Colloidal Fluid.* Industrial & Engineering Chemistry Research, 1994. **33**(10): p. 2391-2397.
24. Wolfe, M.S. and C. Scopazzi, *Rheology of swellable microgel dispersions: Influence of crosslink density.* Journal of Colloid and Interface Science, 1989. **133**(1): p. 265-277.

25. Senff, H. and W. Richtering, *Influence of cross-link density on rheological properties of temperature-sensitive microgel suspensions.* Colloid & Polymer Science, 2000. **278**(9): p. 830-840.